SHOTS

Semi-Hydrogen Operating Turbofan Sustainable Aircraft

DSE Group 9

TUDelft

This page was intentionally left blank

SHOTS

Semi-Hydrogen Operating Turbofan Sustainable Aircraft

by

DSE Group 9

Name	Student number
A. Blomme	4551176
D.F. Cacais Pires	4643682
M.G. Dekkers	4533860
S. Eftekhar	4660714
B. García de Quevedo Suero	4678877
S. Hamza	4661281
J. Janissen	4444914
R. Kroon	4644220
V. Steenhuizen	4672372
S. Wen	4680537

Project duration: April 2020 - July 2020
Project supervisors: Dr. ir. R.C. Alderliesten
    Ir. A.F. Rius Vidales
    Dr. ir. A.S. Verma

TUDelft

Preface

"Once you have tasted flight, you will forever
walk the Earth with your eyes turned skyward,
for there you have been, and there you will
always long to return."

Leonardo da Vinci

This final report is the result of all the work performed for the 2020 Spring Design Synthesis Exercise (DSE) to obtain the Bachelor degree in Aerospace Engineering at Delft University of Technology. Normally, the DSE is seen as extremely challenging, however, the Coronavirus disease (COVID-19) crisis has introduced another trouble in this already difficult assignment.

Sustainable solutions have been implemented in various industries in the past years. Unfortunately, the aviation industry has not committed to this change and no significant changes for larger aircraft are expected in the coming years. Climate change and the depletion of fossil fuels are one of the most important issues that need to be addressed in the years to come. Another important aspect of the current sustainability strategies is the movement towards a circular economy. The aviation industry, with the introduction of advanced composites, requires special attention in order to bring about this change. Sustainable flying, both in terms of materials and energy sources, is possible and this is elaborated upon in this report in the design of the Semi-Hydrogen Operating Turbofan Sustainable (SHOTS) aircraft.

SHOTS is the solution to near-future green flying - Group 9

Executive Overview

This report presents the final result of the WeFlyCycle project: a Design Synthesis Exercise (DSE) performed by a group of 10 bachelor of Aerospace Engineering students at Delft University of Technology. Sustainability plays a major role in today's society and the aviation industry. With the growing demand for air transportation, the incremental design changes are no longer sufficient to overcome the environmental impact. This project is aimed at tackling this issue by setting two main goals: use of recyclable and/or recycled materials and the use of a propulsion principle greener than fossil fuels.

For this, the mission need statement and the project objective statement are defined as follows:

Mission Need Statement: Design an aircraft that promotes sustainable environmental practice through the implementation of recycling strategies and green propulsion.

Project Objective Statement: Develop and design a commercial (100-120 passengers) demonstrator aircraft manufactured from recycled and/or recyclable materials with propulsion principles greener than burning fossil fuels, by 10 students in 10 weeks [1].

Market Analysis

The aviation industry is facing unprecedented challenges with the Coronavirus disease (COVID) pandemic which acts as an accelerator for events that were bound to happen in the future. The recycling industry will have to expand its capacity to deal with the growing flux of end-of-life material. The increasing percentage of carbon fiber reinforced polymers on aircraft, in particular, introduces new challenges for the reverse supply chain. The industry will have to create versatile recovery channels that are able to re-introduce recycled fiber material to the market and build qualitative products out of them.

Concept Selection

The final report is the result of a project which has lasted approximately 10 weeks. During the baseline phase [2], the design option tree was presented. Based on this design option tree three different concepts were selected to be investigated during the midterm phase [3]. These three concepts are defined as follows:

- **Concept 1** has a propulsion system based on both biokerosene and hydrogen utilizing a tube and wing configuration. This concept has low, traditional, backward swept wings.
- **Concept 2** has a propulsion system only based on compressed hydrogen with a tube and wing configuration. This concept also has low, backward swept wings.
- **Concept 3** also has a propulsion system based on compressed hydrogen but utilizes a so called double-bubble configuration where the hydrogen tank is stored on top of the fuselage. This concept also has low, backward swept wings.

A trade-off was performed to find out that concept 1, the Semi-Hydrogen Operating Turbofan Sustainable (SHOTS) aircraft, seemed the most promising candidate. The trade-off criteria and rankings are presented in table 1 where RAMS is an abbreviation for reliability, availability, maintainability, and safety.

Table 1: Results of the performed trade-off (obtained from Midterm Report [3]).

Criteria	Weight	Concept 1	Concept 2	Concept 3
Max takeoff weight	0.40	5	1	1.12
Unit cost	0.23	3	1	5
RAMS	0.15	3.25	1.75	2
Market risk	0.09	4	1.67	1.33
Gas emissions	0.08	1	4.99	5
Noise	0.05	5	1	1.33
Total:		**3.87**	**1.49**	**2.48**
Rank:		**1**	**3**	**2**

System Integration Method

First, technical resource budgets for the mass and cost of the SHOTS aircraft were set up where a total mass budget of 71,474 kg and a total cost budget of $136.2 million were made. Then, a contingency was assigned to the range, MTOW, recyclability, cost and cruise altitude at different design and development phases as shown in table 2 for contingency management. Technical parameter measurement (TPM) is a technique that aims to ensure that the final product achieves its specified performance with acceptable consumption of resources. Figure 1 shows how the TPM variable changed throughout the entire design and development phase. Finally, to ensure that every design parameter was updated on time, a flow chart was constructed to show how different design parameters were interrelated.

Table 2: Contingency margins for key performance characteristics.

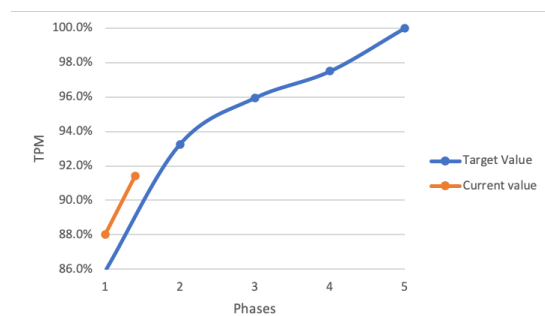| Design Phase	Range	MTOW	Recyclability	Cost	Cruise altitude
1-Conceptual	20%	20%	0%	15%	24%
Current value	**10%**	**13%**	**0%**	**7%**	**24%**
2-Preliminary	8%	10%	0%	5%	20%
3-Detailed	5%	7%	0%	3%	10%
4-Flight test	3%	5%	0%	2%	5%
5-Mass production	0%	0%	0%	0%	0%
Relative importance	25%	15%	25%	25%	10%

Figure 1: TPM at different phases in the design.

Materials

Materials that are generally used in aircraft were investigated for recyclability. Several considerations such as corrosion and lightning resistance were taken into account. In order to account for the economic feasibility of recycling, a model was used to estimate the recyclate resale value. Based on this analysis, the materials to be used in the primary structural components were ranked in a trade-off which was then used in the structural analysis. The use of novel materials such as flax for the aircraft interior was examined by investigating the flame/fire resistance and recyclability. The engines, landing gear, control surfaces, APU, and electronics can be certified for reuse [4][5]. An overview of the final material decisions for different aircraft parts, obtained after the analysis in *Structures*, is provided in table 3. Note that CFRP stands for Carbon Fiber Reinforced Polymer.

Table 3: Complete overview of selected materials for aircraft components and their End-of-Life solution.

Aircraft part	Material choice	End-of-Life solution
Fuselage skin, wing skin	T800S Carbon	Recycling/downcycling
Frames, stiffeners, ribs	Aluminum 2024-T3	Recycling/downcycling
Floor	T800S Carbon	Downcycling
Fasteners	Aluminum, steel	Recycling
Flaps and slats	Aluminum, CFRP	Recertify and reuse [1]
Windows	Plexiglass	Downcycling [6]
Overhead bins	Flax/ramie	Incineration
Seats	Flax/polyurethane foam	Polyurethane foam reused in other industries, flax incinerated
Cables	Copper	Recycling [5]
Paint	Chrome-free paint and primer [7]	Incineration

Weight Estimations

An initial static analysis was performed to find the weight of the hydrogen tank. Multiple materials were considered, of which Hexcel PV42/850 CFRP was the best material for the load carrying structure of the hydrogen tank, while high density polyethylene (HDPE) was used as a liner inside the tank. Detailed sizing of the tank including material trade-off was performed during detailed design. After that, an evaluation was performed on different engine models. It was found that, in order to meet the 105% unit cost requirement, two different engine models were required. It was opted to develop two aircraft types: SHOTS-1 and SHOTS-2. SHOTS-1 use

---

[1]Interview with the chief executive officer of AELS, D. van Heerden (10-06-2020)

PW1700G engines which have a low Specific Fuel Consumption (SFC) and hence low operational cost, but the higher unit cost makes it unable to fulfill the unit cost requirement. SHOTS-2, using PW1700G and CF34-10A engines, has a lower unit cost but higher operational cost. Finally, several iterations were performed to find the weight of all the subsystems for the class II weight estimation. The results can be seen in table 4.

Table 4: Determination of the subsystem weight according to the class II weight estimation.

Subsystem	Value	Unit	Value	Unit
Wing	17,461	[lbs]	7,920	[kg]
Horizontal Tail	739	[lbs]	335	[kg]
Vertical Tail	485	[lbs]	220	[kg]
Fuselage	12,743	[lbs]	5,780	[kg]
Landing Gear	5,326	[lbs]	2,416	[kg]
Nacelle	3,803	[lbs]	1,725	[kg]
Fixed Items	20,569	[lbs]	9,330	[kg]
Engine	15,203	[lbs]	6,896	[kg]
Tank	29,394	[lbs]	13,361	[kg]
Fuel	4,548/15,390	[lbs]	2,063/6,981	[kg]
Payload	27,079	[lbs]	12,283	[kg]
Operating Empty Weight	105,563	[lbs]	47,983	[kg]
Maximum Takeoff Weight	152,482	[lbs]	69,310	[kg]

Propulsion and Flight Performance

A hybrid propulsion system with four turbofan engines mounted under the wing has been designed. Half of the engines burn biokerosene and the other half burn hydrogen. A large emphasis was given to the consideration of possible safety concerns with the use of dual fuels, the selection of high-thrust, cost-efficient turbofan engines, as well as the optimization of the combustion chamber to accommodate the use of hydrogen fuel. Lean Direct Injection (LDI) and Micro Mix (MMX) combustion chambers are the most promising technologies to ensure high fuel efficiency and avoid a high risk of auto-ignition and flashback due to combustion of hydrogen in conventional combustion chambers. The nitrogen oxide (NO_x) emissions of both combustion chamber concepts, including five configurations of LDI combustors, were estimated. It was found that the LDI configuration 4 had the smallest NO_x emission of 60.6 parts per million (ppm). Hence, it was proposed to utilize LDI combustion in the PW1700G engines for burning hydrogen. Furthermore, the engine dimensions of PW1700G and CF34-10A were approximated by Jenkinson's method [8] with a fan diameter of 1.42 m and 1.4 m respectively. Then, the longitudinal and vertical positions of both engines with respect to the wing were calculated to check for ground clearance. The vertical position with respect to the wing for the PW1700G engine is 1.47 m and 0.855 m for the CF34-10A engine, hence complying with the ground clearance requirements.

There have been two design options considered in terms of engine types. SHOTS-1, was to use PW1700G type for all four engines, SHOTS-2, was to use two PW1700G and two CF-34-10A. This lead to some variations in terms of performance which are noted in table 5 and compared to E195-E2[2], with ROC at sea level with maximum takeoff thrust.

Table 5: Variations of performance parameters for the two design options compared to the Embraer E195-E2 [9].

Parameter	SHOTS-1	SHOTS-2	E195-E2
Range [km]	4,399	4,350	4,800
Take-off distance [m]	1,484	1,496	1,305
Landing distance [m]	1,452	1,451	1,290
ROC [m/s]	31	29	-
Ultimate load factor	4.5	4.5	-
Cumulative effective perceived noise (EPS) [dB]	260.5	269.4	257.4
CO2 emission [kg/s]	1.093	1.345	1.950
NOx emission [kg/s]	0.239	0.224	0.312

---

[2] https://www.embraercommercialaviation.com/commercial-jets/e195-e2-commercial-jet/ accessed 15-06-2020

Aerodynamics, Stability and Control

The wing has to be able to produce low induced drag values to maximize the lift-to-drag ratio. This resulted in a wing planform with a high aspect ratio of 9.65 optimized for elliptical lift distribution, while still providing enough space for high-lift device placement and landing gear storage by means of a yehudi (orthogonal trailing edge extension at the root). The aircraft's wing span remained below 36 m to ensure it was operable on smaller aerodromes according to International Civil Aviation Organization (ICAO) regulations [10]. The optimal cruise speed was Mach 0.79 at a cruise altitude of 11,000 m with a cruise lift-to-drag ratio of 18.89 and a wing design lift coefficient of 0.5419. The aircraft was able to perform a turn of 45 degrees in 1.4 seconds as required for class II aircraft according to ICAO regulations.

Since the large hydrogen tank is located in the rear section of the fuselage, it was important that the longitudinal stability of the aircraft was investigated in detail. Due to the relatively large tail arm of the aircraft, the horizontal stabilizer did not need to be disproportionately large. The final horizontal tail surface area turned out to be 32% of the wing surface area. Furthermore, the surface area of the vertical tail was also determined. This was done by analyzing the most critical flight condition, which is an engine failure during takeoff. By performing this analysis, it was found that the vertical tail requires a minimum surface area of 14% of the wing surface area. Finally, ground stability was analyzed. For this, the longitudinal placement of the landing gear was first determined such that the nose gear carried between 8% to 15% of the aircraft weight. Next, the lateral placement of the landing gear was chosen such that the aircraft would not roll-over if it made a sharp turn. Finally, the height of the landing gear was chosen such that the aircraft would have a tipback angle larger than 15 degrees and such that there was enough ground clearance underneath the engines. After the location and height of the landing gear were determined, it was found that the aircraft would not be able to take off without any passengers on board, since the requirement of having between 8 and 15 percent of the aircraft mass on the nose landing gear would not be met. This problem was solved by placing the only cargo hold all the way in front of the fuselage. By doing this, it was possible to shift the center of gravity within the limits by loading the cargo hold with the maximum cargo hold payload mass of 2,004 kg.

System Characteristics

The hydrogen system consists of three aspects: the tank, the refueling operations, and the engine's supply system. After initial sizing in *Weight Estimations*, a detailed sizing of the tank was performed, taking into account the fatigue behavior of the structure as a result of the cyclic loading and the damage tolerance of the tank. Four materials have been considered for the tank: T800S CFRP, Kevlar 49, PV42/850 CFRP, and 2800 maraging steel. The tanks with these four materials have been evaluated on their weight, unit cost, crashworthiness, and recyclability, as shown in table 6. Hexcel PV42/850 CFRP will be used to construct the tank.

Table 6: Final trade-off for the material selection of the hydrogen tank.

Criteria	Weight	T800S	Kevlar 49	PV42/850	2800 Steel
Tank mass	0.4	2	3	4	1
Unit cost	0.2	2	3	4	1
Damage tolerance	0.2	2	4	3	1
Recyclability	0.2	2	3	2	4
	Total	2	3.2	3.4	1.6
	Rank	3	2	1	4

For the refueling system, three options have been considered: 2 refueling trucks, 4 refueling trucks or a pipeline system. The benefit of using trucks is that the initial investments are much lower compared to pipelines. This is therefore feasible for smaller, secondary airports. The trucks carry a tank with 1380 kg compressed hydrogen at 875 bar. When the pressure of the truck and aircraft tank are equal, compressors are used to pump the remaining hydrogen into the aircraft. The pipelines supply hydrogen at a constant pressure of 875 bar. For all options, the refueling time has been calculated. Using 2 trucks, the refueling time is 5 hours and 26 minutes. Using 4 trucks, this decreases to 1 hour and 21 minutes. The pipelines are able to fill the tank in 53 seconds. For an Embraer E195-E2, the maximum refueling time is 16 minutes. Special attention has been given to the temperature of the gas in the aircraft tank during refueling. The safe temperature range is 15°C to 85°C. A temperature lower than 15°C can cause heating up and expansion of the gas, a temperature higher than 85°C

could result in exceeding the maximum allowable pressure in the aircraft tank. To make sure the temperature does not become too high, the initial temperature of the gas in the trucks and pipelines is 5°C.

Structures

The structural analysis focused on the buckling analysis, the fatigue characteristics of the material, the damage tolerance of the fuselage structure, and a drop test for crashworthiness. Finally, a trade-off for the different materials to be used in the structure was performed based on the material characteristics, cost, and weight. For both the fuselage and for the wing skin, carbon fiber T800S was selected based on the trade-off for the materials, illustrated in figure 7 for the wing and figure 8 for the fuselage. Other structural elements such as stringers, ribs, frames and, longerons will be made of Aluminum 2024-T3. A fiberglass layer can be used between these materials to prevent galvanic corrosion.

Table 7: Trade-off for wing design.

Criteria	Weight	Al 2024-T3	T800S	GLARE 2
Material score	0.3	4.4	3.55	3.15
Weight [kg]	0.5	1	5	1.76
Material cost [USD]	0.2	5	1	3.94
	Total	2.82	3.77	2.61
	Rank	2	1	3

Table 8: Trade-off for fuselage design.

Criteria	Weight	Al 2024-T3	T800S	GLARE 4
Material score	0.3	4.4	3.55	3.15
Weight [kg]	0.5	1	5	2.28
Material cost [USD]	0.2	5	1	3.37
	Total	2.82	3.77	2.76
	Rank	2	1	3

The chapter presents all calculations for the three different materials (Aluminum, Carbon fiber, and GLARE) but for the purpose of this summary the results are only listed for the carbon fiber T800S since this is the selected material. The allowable stresses were found based on the fatigue analysis to ensure the fuselage panels and lower wing can withstand 43,800 cycles without failure, as these are the parts that undergo cyclic tension loading. With regards to crashworthiness, figure 2 illustrates how the fuselage should break during impact and how the passengers are ensured to remain safe as the galley acts as the section which can break. A buckling analysis was also performed on a wing panel located near the root that consists of carbon fiber skin material. For this analysis, four different types of buckling were considered. Figure 3 illustrates how the different forms of buckling are dealt with by the structure. Only the last type of buckling (column buckling) is considered to be catastrophic for the entire system when the critical load is lower than the ultimate limit load sustained by the structure.
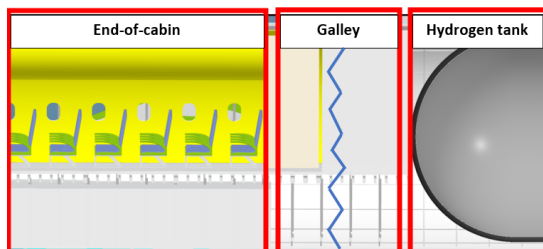

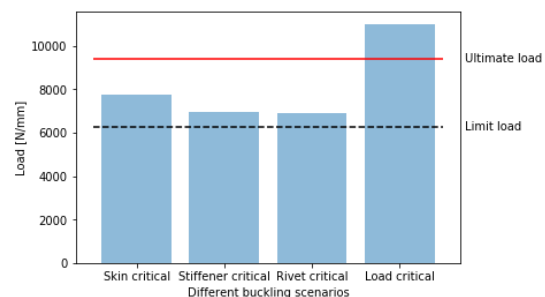Figure 2: Fracture between the cabin and the hydrogen tank.

Figure 3: T800S Carbon fiber buckling.

Based on the thicknesses obtained from the structural analysis, the damage tolerance of the fuselage was checked for all three materials. It was checked if the skin can withstand a crack of length 500 mm without failure, which is approximately the size between two frames.

Final Design Results

The most important parameters of the final design are summarized in table 9. Furthermore, the chapter outlines the different diagrams for proper operation of the aircraft.

Table 9: Parameters of the SHOTS aircraft.

Parameter	Value	Unit	Parameter	Value	Unit
Wing span	35.99	[m]	Payload weight	12,283	[kg]
Length	46.81	[m]	Fuel weight	6,981/2,063	[kg]
Wing area	132.57	[m^2]	Number of passengers	120	[−]
Aspect ratio	9.645	[−]	Engine type	PW1700G/CF34A	[−]
Airfoil	NASA SC(2) 00710	[−]	Number of engines	4	[−]
Maximum takeoff weight	69,310	[kg]	Stall speed	190	[km/h]
Operating empty weight	47,983	[kg]	Max cruise Mach number	0.82	[−]
Range	4,399	[km]			

Technical Sensitivity Analysis

To assess the robustness of the design, a sensitivity analysis was performed.

First, the hydrogen tank weight was increased by 10%. This had far reaching consequences in every major subsystem and a snowball effect was observed. Surprisingly, the engine selection was not affected because the engines have some margin with respect to the requirements. In conclusion, the MTOW increased with 2.9% to 71,314 kg, the range decreased with 6.1% to 4,131 km, and the stability was heavily affected. Because of this, the aircraft would not able to take off when less than 60% of the passengers are on board. To resolve this, the cabin layout can be optimized and higher strength materials such as T1100G CFRP can be used.

Secondly, the effect of changing the cruise altitude to 12,000 m is evaluated. To begin with, this increased the stress on the fuselage due to pressurization. The allowable crack length of the materials decreased by 12 %. However, the damage tolerance requirements were still met. Furthermore, the aerodynamic analysis changed dramatically: higher altitude means lower air density to generate lift. To keep the aircraft flying at this altitude, the airfoil design lift coefficient would need to increase from 0.73 to 0.85. This requires a complete redesign of the wing and airfoil, most likely increasing the sweep of the wing. Also, the cruise speed could be increased, at the expense of increased drag and fuel burn. A combination of increasing sweep and flying at higher speeds requires more investigation.

The WeFlyCycle Road map

For successful continuation of the project it is essential that proper further steps are taken. These steps are illustrated in figure 4.
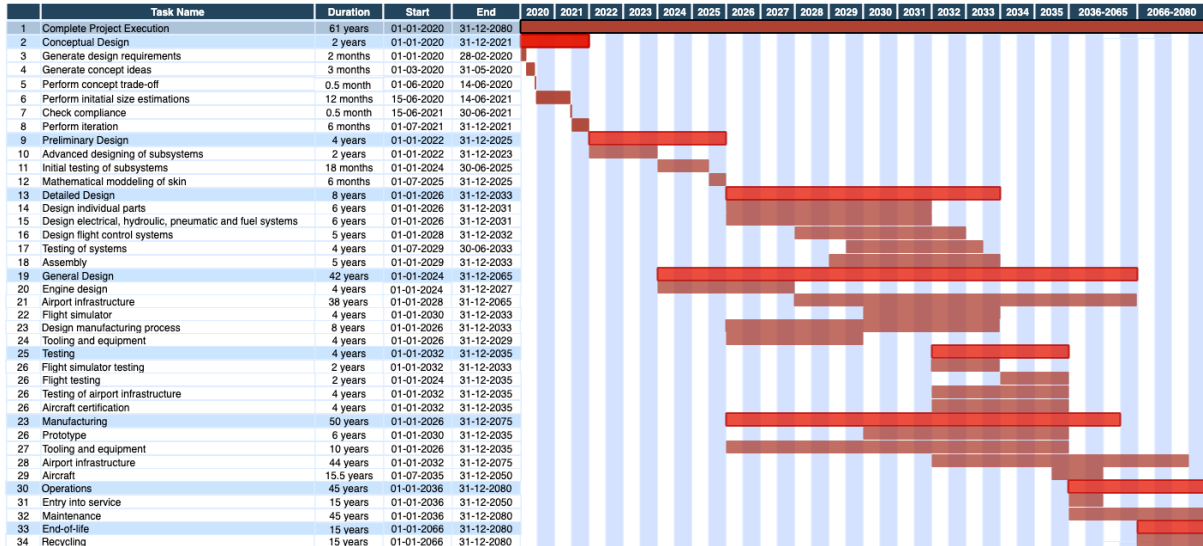

Figure 4: Overview of aircraft future design and operations.

The RAMS characteristics of the aircraft were also thoroughly analyzed:

- Reliability: the majority of the aspects are reliable due to the conventional design used. Nevertheless, the modular cabin, hydrogen tank, and the combustion chamber modifications lead to lower reliability when comparing to similar aircraft.
- Availability: when the airport infrastructure is not installed with pipelines to refuel the hydrogen, trucks must be used. The usage of trucks has the disadvantage of a long turnaround time.
- Maintainability: compared to similar aircraft, SHOTS has 2 additional engines that will require extra labor hours to inspect and maintain and therefore increase the maintenance time. Furthermore, the combustion chamber redesign will make it different to inspect compared to similar aircraft. However, the extensive use of composites in primary structural elements will decrease the maintenance time.
- Safety: the main point of concern is the high pressure hydrogen tank placed in the back of the aircraft, this is however thoroughly elaborated upon in this report in order to ensure the safety of the design.

For the implementation of the aircraft, the airport infrastructure is a limiting factor. An analysis showed that reference aircraft fly to destinations 2,000 km from the airline hub. For the implementation of the SHOTS aircraft, this could mean that refueling at a destination is not required and infrastructural investments are hence not needed at a destination. This would mean that the only location where infrastructure needs to adapt is the hub of the airline. On the other hand, it was also considered that the infrastructural problems were only an issue of time as hydrogen is expected to be introduced into the energy system.

The WeFlyCycle Business Model

The SHOTS aircraft has been built-up from the ground with recovery maximization at its root. This way, the goals stated by the Advisory Council for Aeronautics Research in Europe (ACARE) [11] can be reached and the sustainability philosophy is fulfilled. The SHOTS aircraft aims to be the successor to the Airbus A220 and profiles itself as a demonstrator aircraft for hydrogen technology while still providing a feeling of safety. Evolution rather than revolution is the core strategy. The development cost and the manufacturing cost form the two factors of the aircraft cost. To calculate the development cost, the per pound cost of each subsystem was estimated. This per pound cost was then multiplied by the weight of each subsystem and then finally added to get a total value of $2.69 billion. For the manufacturing costs the same approach was applied, where the cost of manufacturing each subsystem was multiplied by the subsystem weight. The cost of the 1st unit of option 1 with 7% contingency was $143.4 million whereas for option 2 it was $133.7 million. However, due to the learning curve, this manufacturing cost goes down as the number of aircraft produced goes up. Keeping in mind the manufacturing cost, the selling price set for option 1 is $80 million whereas for option 2 it is $78 million. This selling price is lower than the A220 hence giving a price advantage on the competitive aircraft. Selling at these prices the program will incur a loss for the first 126 units, after which, due to the learning curve, the manufacturing cost will go below the selling cost hence selling an aircraft will create a profit. The total investment required is therefore the development cost and the loss for the first 126 units, adding up to $ 3.55 billion. The project will hit its break even point after selling 717 aircraft after which it enters its profit phase. After selling a total of 1,200 aircraft, the profit is expected to be at $4.86 billion.

Sustainability Compliance Assessment

Sustainability has been a significant part of this project, with the top-level requirements being the use of recycled and/or recyclable material and the use of non-fossil fuel. Since the start of this project, this issue was considered in every design aspect. The steps taken were explained in every section and in the end, it was assessed whether the initial goals were achieved and what could be done in later phases. Using a model called Life Cycle Sustainability Assessment (LCSA) [12], two main phases, namely Design and Operations phase and End-Of-Life phase, were considered. It was found that the goals of having a recyclable aircraft and the use of non-fossil fuel were achieved. Recyclability has been assessed technically, but further investigation is required to prove economic feasibility. In addition to that, efforts in innovations and design changes for incorporating more sustainability in all three aspects of economic, social and environmental were conducted.

Conclusion and Recommendations

As one of the final steps, compliance of the requirements was listed and checked with the results from the analyses conducted thus far.
Finally, the report was concluded with the final results and recommendations for the future phases such

as:

- Aircraft parts that employ thermoset resin composites could potentially be replaced by thermoplastic composites, which have better recyclability potential. The use of thermoplastic composites has not yet been seen in primary structural parts but investments by Airbus on these materials show that advances are expected [3]. Thermoset composite parts that cannot be repaired could potentially be replaced for thermoplastic composites during the operational life of the aircraft to further improve recyclability. The use of thermoplastic composites could also be applied to rivets. By using similar materials for skin and rivets, the recyclability becomes easier compared to combinations of materials.
- Further research can be done on the use of biocomposites in aircraft parts. Currently, their use is limited to the cabin interior but the application to secondary structures can be investigated.
- Optimizing the required skin thickness of the four fuselage panels that are assembled during production. Each panel can be optimized for its critical load case as was done during the design of the Airbus A350 XWB [13].
- Extended market analysis into the reverse supply chain of CFRP to create demand for recycled aerospace composites. Performing market analysis to investigate the value of recycled CFRP for the sports industry. An assessment of the supply chain considering the volume of end-of-life aircraft waste and the specific recycling processes to be used is required. Furthermore, assessment of the relation between recyclate resale value and profit is needed.
- Analysis of possible tools to be used for attachment of fasteners for the hydrogen tank attachment and the access for removal. Furthermore, the specific fasteners to be used depend on a detailed analysis of the loading conditions in the hydrogen tank section.
- Design of a hybrid engine that can run on both hydrogen and biofuel to reduce the number of engines and save more weight and cost. Furthermore, this mitigates the risk that only half of the engines can be used because one of the fuels is unavailable.

An illustration of the aircraft is presented in figure 5.

Figure 5: A view of the SHOTS aircraft.

---

[3] https://www.airbus.com/newsroom/news/en/2015/01/airbus-focus-on-thermoplastic-composite-materials-brings-environmental-and-production-improvements.html (accessed 29-06-2020)

Contents

Nomenclature

List of Symbols

α	Angle of attack	rad
α_0	Zero lift angle	deg
α_s	Stall angle	rad
α_{trim}	Trim angle for optimal cruise	rad
δ_a	Maximum allowable deflection angle	deg
$\dot{m}$	Mass flow	kg/s
$\frac{T}{W}$	Thrust to Weight ratio	$-$
$\frac{W}{S}$	Wing loading	N/m^2
γ	Adiabatic index	$-$
λ	Taper ratio	$-$
$\Lambda_{c/2}$	Sweep angle at half chord	rad
$\Lambda_{c/4}$	Sweep angle at quarter chord	rad
Λ_{LE}	Sweep angle at leading edge	rad
μ	Bypass ratio	$-$
ϕ_{H_2}	Equivalence Ratio Hydrogen	$-$
ρ	Density	kg/m^3
σ	Stress	Pa
τ	Aileron effectiveness	$-$
τ	Residence time	$-$
A	Aspect ratio	$-$
a	Allowable crack length	mm
a	Speed of sound	m/s
b	Wing span	m
b_i	Location along the wing span	m
b_w	Height of the winglet	m
c	Chord	m
C_D	Drag coefficient of a finite wing	$-$
C_d	Drag coefficient of an airfoil	$-$
C_L	Lift coefficient of a finite wing	$-$
C_l	Lift coefficient of an airfoil	$-$
C_m	Moment coefficient	$-$

c_p	Specific heat capacity	$J/(kgK)$
c_r	Root chord	m
c_t	Tip chord	m
C_{D0}	Zero lift drag coefficient	$-$
C_{f_c}	Flat plate skin friction coefficient	$-$
$C_{l,des}$	Design lift coefficient	$-$
C_{L_α}	Finite wing lift gradient	$-$
C_{l_α}	Airfoil lift gradient	$-$
c_{pre}	Predicted costs	USD
CGR	Climb Gradient	$\%$
D	Drag	N
d	Distance	m
D_F	Fan diameter	m
E	Energy	J
E	Young's modulus	Pa
e	Oswald efficiency factor	$-$
E_r	Recycling energy	J
FF_c	Form factor component	$-$
g	Acceleration due to gravity	m/s^2
h	Wingbox height	m
h_c	Cruise height	m
I	Moment of inertia	m^4
IF_c	Interference factor component	$-$
k	Multiplication factor for the square of the lift coefficient	$-$
k_b	Burst safety factor	$-$
k_f	Safety factor for fiber translation efficiency	$-$
K_{Ic}	Fracture toughness	$Pa\sqrt{m}$
K_{inl}	Constant for weight estimations	$-$
L	Lift	N
M	Mach number	$-$
m	Mass	kg

$M^{\dagger}$	Technology factor for supercritical airfoils	$-$	t_{roll}	Free roll duration	s
m_p	Retained mechanical performance	$-$	t_{skin}	Skin thickness	m
m_x	Molecular weight nitrogen dioxide	kg	t_{spar}	Spar thickness	m
M_{crit}	Critical Mach number	$-$	TOP_{25}	Takeoff parameter	N/m^2
M_{cr}	Cruise Mach number	$-$	U	Internal energy	J
M_{dd}	Drag-divergence Mach number	$-$	V	Velocity	m/s
M_{MO}	Maximum operating Mach number	$-$	v	Flow velocity	m/s
N	Number of engines	$-$	W	Weight	N
n	Load factor	$-$	w	Wingbox width	m
P	Power	W	W_a	Total airflow at sea level	m
p	Atmospheric pressure	Pa	y	Length parallel to the fuselage	m
q	Dynamic pressure	Pa	Z	Compressibility factor of hydrogen	$-$

The table continues with the following entries (left column):

R	Specific gas constant	$J/(kgK)$
R	Stress ratio	$-$
r	Discount rate	$\%$
r	Radius	m
r_p	Percentage of reclaimed recyclable yield	$\%$
Re	Reynolds number	$-$
ROC	Rate of Climb	m/s
RV_0	Virgin material cost	USD
RV_i	Recycle value	USD
S	Stress	Pa
S	Wing surface	m^2
S_m	Material surface	m^2
S_{LFL}	Landing field length	m
S_{TOFL}	Takeoff field length	m
S_{UTS}	Ultimate tensile strength	Pa
T	Thrust	N
t	Thickness	m
t/c	Thickness to chord ratio	$-$
T_0	Inside tank temperature	K
T_3	Combustor inlet temperature	K
T_4	Combustor outlet temperature	K
T_e	Temperature	K
T_i	Outlet tank temperature	K
T_{eng}	Maximum static thrust	N

List of Abbreviations

ACARE	Advisory Council for Aeronautics Research in Europe	$-$
AELS	Aircraft End-of-Life Solutions	$-$
AEO	All Engines Operative	$-$
AFRA	Aircraft Fleet Recycling Association	$-$
APU	Auxiliary Power Unit	$-$
ATC	Air Traffic control	$-$
AVL	Athena Vortex Lattice	$-$
CFD	Computational Fluid Dynamics	$-$
CFRP	Carbon Fiber Reinforced Polymer	$-$
cg	Center of gravity	$-$
CO_2	Carbon Dioxide	$-$
COVID	Coronavirus Disease	$-$
DATCOM	USAF Stability and Control Data Compendium	$-$
DOE	United States Department of Energy	$-$
DOT	Design Option Tree	$-$
EASA	European Union Aviation Safety Agency	$-$
EI	Emission Index	$-$
EOL	End-of-Life	$-$
EPN	Effective Perceived Noise	dB
EU	European Union	$-$
GD	General Dynamics	$-$
GFRP	Glass-fiber reinforced polymer	$-$

GLARE	Glass-Reinforced aluminum laminate	−		ppm	Parts per million	−
HDPE	High Density Polyethylene	−		RAMS	Risk, Availability, Maintainability and Safety	−
HLD	High Lift Device	−		RQL	Rich-burn Quick-quench Lean-burn	−
ICAO	International Civil Aviation Organization	−		SFC	Specific Fuel Consumption	$lb/(lbfh)$
LCA	Life Cycle Assessment	−		SHOTS	Semi-Hydrogen Operating Turbofan Sustainable Aircraft	−
LCC	Life Cycle Costing	−		SLCA	Social Life Cycle Assessment	−
LCSA	Life Cycle Sustainability Assessment	−		SWOT	Strengths, Weaknesses, Opportunities and Threats	−
LDI	Lean Direction Injection	−				
LHV	Lower Heating Value	−		TE	Trailing Edge	−
MAC	Mean Aerodynamic Chord	m		TEI	Two Engines Inoperative	−
MLW	Maximum Landing Weight	kg		TO	Takeoff	−
MMX	Micro-Mix	−		TPM	Technical Parameter Measurement	−
MTOW	Maximum Takeoff Weight	kg		TRL	Technology Readiness Level	−
NO_x	Nitrogen Oxide	−		US	United States	−
OEI	One Engine Inoperative	−		USD	United States Dollar	−
OEM	Original Equipment Manufacturer	−		VOC	Volatile Organic Compound	−
OEW	Operational Empty Weight	kg		WFC	WeFlyCycle	−
PNNL	Pacific Northwest National Laboratory	−				

1
Introduction

Society has seen a rapid advancement in sustainable technologies in recent years. Due to global warming, severe air pollution, and international cooperation, it is expected that this trend towards a sustainable civilization is only at its beginning. Aviation, however, is an inherently reluctant industry to adopt change and has yet to start the transition to become more sustainable[1]. A severe reduction in greenhouse gasses is required, this is important in order to reach the goals stated by the International Air Transport Association (IATA)[2] to have a net reduction of 50% greenhouse gasses in 2050 compared to 2005. Recent events (such as the climate protests) have, nevertheless, struck the aviation industry with a demand from the public to see changes. Terms such as 'flight shame'[3] have become common but were unheard of several years ago. These movements have inspired many (such as Eviation[4] or Pipistrel[5]) in order to find ways to reduce the environmental footprint of aviation[6]; however, none of them have been very successful yet. The demand thus arises for a sustainable aircraft, with minimum or no global warming emissions, preferably also allowing for a circular economy.

This report reviews the Design Synthesis Exercise (DSE) WeFlyCycle project. This project is aimed at designing an aircraft which can transport 100-120 passengers with a range of 4000-4500 km, not utilizing fossil fuels in its propulsion system and manufactured from recycled and/or recyclable materials. A basic analysis for this aircraft, the Semi-Hydrogen Operating Turbofan Sustainable (SHOTS) aircraft, has already been performed during the midterm phase. This report aims to answer the question: What are the detailed characteristics of the SHOTS aircraft after the conceptual design? In order to answer this question, a thorough analysis is performed in order to research and analyze the different subsystems. Moreover, the feasibility of the SHOTS aircraft is also determined. Based on the relation between different design aspects the optimum combination of parameters is presented. Furthermore, with sustainability being a major part of the project, a strategy has been developed from the start of the design phase which was followed throughout the project. In the end, an assessment is conducted to check compliance with the outlined sustainability goals.

First, in chapter 2 the market is discussed. Chapter 3 gives an overview is given of what has already been performed before the final phase of the conceptual design. Then, in chapter 4, the system as a whole is introduced and the contingencies are elaborated upon. As a starting point for the design, chapter 5 elaborates on the estimated weight of the aircraft. Chapter 6 explains the material selection and trade-off criteria for different aircraft elements. Next, the flight performance and propulsion theory and calculations are outlined in chapter 7. After that, the aerodynamic properties of the aircraft, and its stability and controllability, are evaluated in chapter 8. The consecutive chapter, chapter 9, focuses on the hydrogen system from a detailed sizing of the tank to refueling characteristics and engine supply. The structural aspects of the design are then elaborated upon in chapter 10 which include buckling, fatigue, damage tolerance, and drop test. Chapter 11 then gives an overview of the complete design including the appropriate diagrams for software, hardware, et cetera. Chapter 12 evaluates how a certain change in design parameters influences the design. Chapter 13 then lays out the roadmap for the SHOTS aircraft. After that, the business model is discussed in chapter 14 and the profitability of the aircraft is illustrated. The sustainability of the design is then discussed in chapter 15. The ultimate chapter discusses all the requirements stated in the Baseline Report [2] and checks their compliance to the actual result. Finally, the report is concluded and future recommendations are listed in chapter 17.

---

[1] https://www.forbes.com/sites/blakemorgan/2019/09/25/how-far-are-we-from-flying-zero-emission-airplanes/#254a8e3c43f6 (accessed 20-05-2020)

[2] https://www.iata.org/en/policy/environment/climate-change/ (accessed 26-06-2020)

[3] https://www.bbc.com/news/business-49890057 (accessed 20-05-2020)

[4] https://www.eviation.co/ (accessed 26-06-2020)

[5] https://www.pipistrel-aircraft.com/ (accessed 26-06-2020)

[6] https://www.edf.org/climate/aviation (accessed 20-05-2020)

2
Market Analysis

The aviation industry has been extremely resilient in times of crisis, maintaining its economic growth in times of war, virus outbreaks or financial crashes. Its capability to adapt its business models and operations to socio-economic developments is creditworthy. However, with the ongoing COVID-19 pandemic, it has become clear that the industry will have to face unprecedented challenges in the near future. Section 2.1 reflects on the market devlopments that were laid out during the early stages of the WeFlyCycle project. A market forecast is touched upon in section 2.2 and more details regarding a reverse supply chain is further discussed in section 2.3. Last but not least, the WeFlyCycle project has certain market challenges which are assessed in section 2.4.

2.1. Market Developments

Recent developments in global climate awareness and the rising interest of climate youth activists, such as the Swedish environmental activist Greta Thunberg, have put air travel in a bad spotlight. The aviation industry is targeted in the wake of a global fight for a reduction in carbon dioxide emissions as well as other harmful greenhouse gasses such as nitrogen oxide. Both contributions are about 3% of the global production [11], which remains relatively low. However, the justification of air transportation is the culprit with people begging to reconsider other modes of travel. Airliners hope to provide a satisfactory response by offering optional footprint compensations on their ticket sales and by introducing recycled products in their waste streams, but this does not fulfil the need for structural change at the core of the industry.

The Advisory Council for Aeronautics Research in Europe (ACARE), in an effort to push for change, stated a strategy to mitigate the harmful factors originating from the aviation sector [14]. As stated earlier in the Baseline Report [2], the five goals to be achieved by 2050 are:

- CO_2 emissions per passenger kilometer have been reduced by 75%, NO_x emissions by 90% and perceived noise by 65%, all relative to the year 2000;
- Aircraft movements are emission-free when taxiing;
- Air vehicles are designed and manufactured to be recyclable;
- Europe is established as a center of excellence on sustainable alternative fuels, including those for aviation, based on a strong European energy policy;
- Europe is at the forefront of atmospheric research and takes the lead in formulating a prioritized environmental action plan and establishes global environmental standards.

The first and third target in particular justify the need for projects such as WeFlyCycle since it ascertains the bottlenecks in sustainability the industry has to overcome. Sustainability oversees many aspects of the society and the WeFlyCycle project aims to meet at least the ecological aspect. In this view, sustainability means the use of natural resources such that the carrying and regenerative capacities of the corresponding system are not jeopardized [15]. Section 2.3 explains how the market should incorporate this philosophy while chapter 15 discusses how the WeFlyCycle project complies with this sustainable approach.

2.2. Market Forecast

Where is the aviation industry headed and how will this affect the demand for airplanes? This is undoubtedly the most burning question in the sector at this time, which even the biggest experts have no answer to. The COVID-19 pandemic has become an accelerator of trends that were already lingering, for example the decommissioning of aircraft behemoths such as the Airbus A380 capable of transporting 800 passengers. This prestige project from the early 21st century is a clear example of overestimation of the market demand and

the introduction of the coronavirus has ended its lifetime prematurely[1]. The market analysis of the Baseline Report [2] predicted this development after performing a Strengths Weaknesses Opportunities and Threats (SWOT) analysis on the three fastest growing aviation markets, of which the findings are summarized in table 2.1.

Table 2.1: SWOT analysis of the fastest growing global aviation markets [2].

Asia-Pacific Market	
Strengths	**Weaknesses**
Middle-class wealth increasing rapidly	Young fleet of narrow-body aircraft Mediocre airport infrastructure
Opportunities	**Threats**
Increasing inter-regional tourism Expanding Tier 2 airports	Non-uniform aviation regulations across countries Chinese competitor will enter the market
North-America	
Strengths	**Weaknesses**
Large and resilient economy	Protectionism could harm future tourism & trade
Opportunities	**Threats**
High replacement demand Airlines looking for small narrow-body aircraft	TTIP negotiations Pilot shortage
Europe	
Strengths	**Weaknesses**
Stable market Large tourist influx by air	Tier 1 airports reaching maximum capacity
Opportunities	**Threats**
High replacement demand Point-to-point travel Hybrid full service/low cost carrier business model	Global pandemics Pilot shortage

The high replacement demand on the North-American and European market is the consequence of multiple factors. About 40% of the aircraft fleet on both markets has over 16 years of service and about 3,250 jets in the 60-150 segment (12% of the global fleet) are set out to retire by 2036 [16]. In addition, Embraer states that for North-American airlines, 45% of the flights undertaken by jets with 150 to 210 seats carry fewer than 130 passengers. The underutilized and aging fleet of the North-American market could certainly benefit from the smaller narrow-bodied aircraft [17]. Lastly, the demand from the general public to support the green revolution is growing and airlines are looking to renew their fleet. They are aware that once the dust settles and air travel is returning to former capacity, the few airlines that have succeeded in overcoming these financially difficult times will need to scrape the surface to convince the customer of their green ambitions or be replaced. Aircraft manufacturer Airbus is jumping on the cart as well, as the CEO Guillaume Faury recently reported that they are working on a hybrid-electric single-aisle jet intended to reach the market around 2035[2].

The downside of this evolution is the expected waste stream following these events. In the next two decades about 15,000 aircraft will be retired with an average of 700 per year, of which 152 aircraft are comparable to SHOTS[3]. This is the equivalent of 30,000 tons of scrap each year, yet this is negligible to the EOL weight coming from personal vehicles and industrial trucks. This limiting factor is explored in section 2.3. After the Second World War huge aircraft cemeteries, mainly located in the United States, started originating when all those airplanes went out of service in the 1980s. However, the cost of storage for a Boeing 747 at one of the USA's biggest cemeteries costs around 60,000 USD a month[3]. Henceforth, aircraft are increasingly shipped to recycling plants where they are stripped for parts and eventually everything that is not recovered ends up at a landfill in a third-world country.

---

[1] https://www.forbes.com/sites/jamesasquith/2020/04/03/will-most-airlines-ground-the-a380-forever-due-to-coronavirus/#1d466a9842e2 (accessed 22-06-2020)

[2] https://www.industryweek.com/leadership/article/22027751/airbus-may-make-the-next-version-of-its-topselling-jet-an-electric-hybrid (accessed 18-06-2020)

[3] https://edition.cnn.com/travel/article/retired-airplanes-upcycling-recycling/index.html (accessed 18-06-2020)

During the period from 2005-2007, Airbus France executed a European funded project called PAMELA - Process for Advanced Management of End of Life of Aircraft - to asses the percentage of an aircraft they were able to recycle. Not only did they manage to achieve a 70% re-use/recycling ratio in weight and reduce landfill waste to 15%, they decided to set up a service company as well to help airlines with EOL procedures [18]. TARMAC is a joint-interest of Suez, Safran and Airbus and it is a service company that provides storage, maintenance and recycling facilities. This is different from AELS, who buys the airplane entirely and facilitates the recycling process from start to end. Reportedly, TARMAC can now recycle 92% of an aircraft (85% recycling rate in 2012)[4]. Although these are positive news, one should remain critical when interpreting them. They provide no information on their reference system; hence, this could be based on weight, size, material value, et cetera. Secondly, the airplane of today is not the airplane of tomorrow. This is addressed more thoroughly in section 2.4. Take a look at the evolution of composite use in the Airbus A300-Series: 10% composite coverage for the early A300, 25% for the A380, and up to 52% for the A350 XWB. It is doubtful that TARMAC will be able to reach the same percentages when the first A350s start to decommission due to the high CFRP and GLARE percentages present in the design.

The advantages of composites are numerous and they sparked a small revolution in the Aerospace & Defence sector due to their strong tensile, stiffness and lightweight properties. Additionally, aircraft such as the Airbus A350 XWB require 50% fewer structural maintenance tasks, and the average threshold for an airframe check lies at 12 years compared to 8 years for the A380 [3]. However, the downside of the fiber composites is their fast decline in structural performance if not recycled properly. Although fiber composite recycling methods are now considered mature, the applications are still limited due to little economic drivers. The future is promising though with companies such as 'CFK Recycling' winning the Sustainable Industry Challenge 2020 in Germany for tremendous advances in the recycling of carbon fibers[5]. This year the request for CFRP is expected to reach 140,000 tonnes/year, almost 90% more compared to last year. The associated production and EOL waste amounts to 62,000 tonnes/year, of which 23,360 tonnes come from the aerospace industry. If not addressed, the accumulated mass from aerospace will supersede a staggering 408,000 tones by 2050. By the same year, EOL wind turbines will have accumulated 483,000 tonnes [19].

2.3. The Reverse Supply Chain
The efficiency of a product such as an aircraft can be evaluated with a life cycle assessment (LCA), it consists of 6 stages:

1. Raw material collection
2. Manufacturing
3. Packaging and distribution
4. Operations
5. EOL
6. Recycling

A LCA shows the facts and allows the designer/manufacturer to optimize the design cycle by taking goal-oriented decisions. This is detailed more extensively in chapter 15. Although the environmental impact of an airplane is most dominating during its operational phase, the real bottleneck for the WeFlyCycle project lies in the recycling phase or the reverse supply chain. Technically, everything in an airplane is recyclable if one puts in the budget and labor. Economically, this is not feasible as of yet. There exists a waste management hierarchy, discussed in section 6.3 and most of an airplane's residual value is attributed to the serviceable parts that can be re-certified and re-used with minor repairs if required. This process is fast and safe because shops exist that are specialized in certain ATA chapter parts. ATA Spec 100/iSpec 2200 is the industry's standard for aviation maintenance, repair and operations (MROs), published by Airlines for America, formerly known as the Air Transport Association (ATA)[6]. Often, the original equipment manufacturer (OEM) provides a re-certification service as well. Up to 95% of the EOL value is stored in those reuseable parts such as the landing gear, engines, APU, flaps, spoilers, et cetera, while only a marginal 5% comes from material recycling[7]. The recycle value over serviceable part value is close to 1/1,000. Some difficult to recycle parts are also re-introduced in simulators,

---

[4]Information obtained from Deutschen Gesellschaft für Luft- und Raumfahrt's webinar regarding 'Aircraft recycling and dismantling from design to execution' (accessed 17-06-2020)

[5]https://www.teijinaramid.com/en/cfk-recycling-wins-the-sustainable-industry-challenge-2020-and-launches-a-pilot-with-teijin-aramid/#:~:text=CFK%20Recycling%20wins%20the%20Sustainable%20Industry%20Challenge%202020%20and%20launches,for%20sustainably%20recycling%20carbon%20fibres. (accessed 18-06-2020)

[6]https://publications.airlines.org/CommerceProductDetail.aspx?Product=33 (accessed 18-06-2020)

[7]Interview with the chief executive officer of AELS, D. van Heerden (10-06-2020)

training environments for cabin personnel or aviation enthusiasts. Some excellent examples are shown in figure 2.1, where OEMs and airlines such as Lufthansa have started selling their own product line based on old aircraft material. Figure 2.1a shows a chair built out of an old Airbus A300 nosecone panel as well a wing rib variant and figure 2.1b are bags made out of recycled fabric from the cabin interior.

(a) Airbus - A Piece of Sky / The collection. [8]

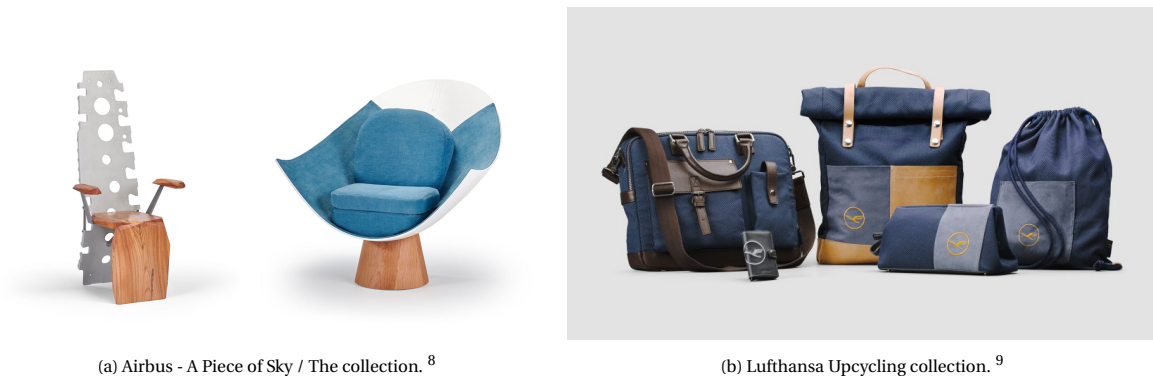(b) Lufthansa Upcycling collection. [9]

Figure 2.1: Specific reuse of aircraft parts.

Unfortunately, 10-15% of the aircraft weight still ends up at a landfill, most of which are composites. Not surprisingly, the primary waste management method for CFRP and glass-fiber reinforced polymer (GFRP) is landfill. The distribution of current practices is shown in figure 2.2.
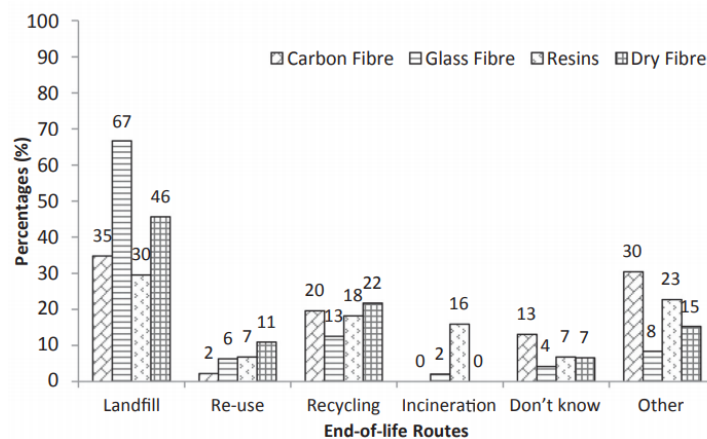

Figure 2.2: Distribution of current composites waste management practices [20].

The reason for this poor waste management is the inability to close the demand and supply chain gap for recycled fiber reinforced polymers. Although companies such as 'ELG Carbon Fiber', partner of Boeing, are providing recycled carbon fibers that are almost 40% less expensive than virgin fibers, the Aerospace & Defense sector still demands virgin fiber for most of its applications due to its inherent tensile strength and stiffness[10]. Secondly, the supply chain should be robust and provide high-volume with dedicated recovery channels for separation, shipment and customer profiling. AELS's CEO Derk-Jan van Heerden provides three requirements for a material to be recyclable: large enough volume, shipment operations to dedicated facilities and a customer that has a use for the end product. Once the cost is reduced below 300-350 €/ton, a sustainable model is accomplished. The problem of volume has to do with the fact that the aviation market is a niche market compared to the car industry. Take a look at table 2.2 for example[3].

---

[8] https://www.apieceofsky.airbus.com/?lang=en (accessed 18-06-2020)
[9] https://www.worldshop.eu/en/page/upcycling?p=AQ4RUMQQaDY (accessed 18-06-2020)
[10] https://www.compositesworld.com/articles/the-state-of-recycled-carbon-fiber (accessed 18-06-2020)

Table 2.2: Production, waste, material value and lifetime of products within the aviation and automotive industries.

2019	Aircraft company	Car company
Number of products	863	3.3 million
Amount of waste	30,200 tonnes	1.3 million tonnes
Material value	1x	17x
Lifetime	~25 years	~10 years

A leading company in the aviation industry such as Airbus produces about 863 airplanes in a year while an average car company can easily reach up to 3.3 million cars. The combined product waste therefore differs significantly, as well the value one is able to retrieve from the recycled material. Experts estimate this to differ by a factor of 17 [3]. In addition, the incentive to replace one's car is bigger than replacing one's aircraft and this is reflected in the operational lifetime of both products.

The customer base for recycled carbon fiber is growing as well. There are several companies that see opportunities for products such as sport equipment (surf boards, skis, bicycles, helmets, et cetera), lightweight interior and exterior cover, furniture, anti-corrosion seal caps and more. People are looking at the car industry to make a cross-link and start using aerospace recycled CFRP but the tipping point is yet to come. However, one should be cautious and target niche applications at the start in order to preserve the global supply of CFRP.

2.4. WeFlyCycle Market Challenges

The goal of the WFC project is to achieve a circular economy within the aerospace industry. For that to happen, several challenges need to be overcome and the biggest ones are listed below.

General

- **Draw the political landscape.** There should be a clear European political framework for requirement identification and allocated funding. Support new technology and implement mature solutions. Funding private projects of local companies is an effective way of tackling supply chain challenges as it can automatically flow back into the economy. This is visible for both Boeing and Airbus as well.
- **Introduce more restrictive regulations.** Reward companies that make use of the reverse supply chain. Apply environmental taxes.
- **Build versatile recovery channels.** The material of tomorrow can and will be different. Be ready to implement a solution for materials once they go out of service.
- **Tackle the Asian market boom.** The East-Pacific market is entering a phase of industrial wealth and the middle-class consumes increasingly more. The growth of aviation on the continent should go hand in hand with an efficient recycling program.

Challenges for OEMs

- **Configuration management.** The operational and maintenance state of an aircraft should be adapted for the introduction of recycled materials, airworthiness checks should be in place.
- **Material composition follow-up.** Report which materials are used and how to post-process them at EOL. Improve on knowledge regarding material handling and track material waste streams.
- **Anticipate recycling processes.** Prepare the reverse supply chain, manage the disposal of dangerous materials.

Note that the concept of 'level playing field' does not apply to aviation. Firms are free to handle their business according to local regulations. In this way, firms have advantages over others in waste processing. Global trade agreements that govern these processes are almost impossible to achieve. More legislation is bad according to Americans, but in Europe it is the other way around. Economic drivers will determine the progress made in the future. If Europe strengthens its leader role in the recycling business with respect to other continents, companies will be able to get more recycling value out of their product.

3

Concept Selection

This report is the result of a project which has lasted approximately 10 weeks. This logically means that a lot of work has already been done before this final phase of the conceptual design was initiated. This chapter sums up the most important information disclosed in the previous reports and lists the decisions made. First, the requirements are listed in section 3.1. Then the functional analysis is presented in section 3.2. After that, the design option trees are presented in section 3.3. Finally, the trade-off that has been performed in the Midterm Report [3] is presented in section 3.4.

3.1. Requirements
Requirements are the starting point for any design and therefore it is important to clearly phrase them. This section lists the most essential requirements for the design. Please note that these requirements stem from the baseline report [2].

3.1.1. Stakeholder needs
The essential stakeholder needs are listed below.

Client:

- Range between 4,000 and 4,500 km.
- Capacity for 100 to 120 passengers.
- Compliance with current safety and reliability requirements.
- Manufactured from recycled and/or recyclable materials.
- Green propulsion that is not based on fossil fuels.

Passengers:

- Sufficiently spacious cabin interior to allow passengers to board, disembark and sit comfortably during flight.
- Ensure safety of passengers during ground operations & flight.

Airport:

- Aircraft design compatible with airport infrastructure.

Airline:

- Similar maintenance and operational cost to conventional aircraft.

3.1.2. System requirements
A selection of the most important system requirements is listed below. These requirements are obtained from the Baseline Report [2].

Performance

- ***WFC-USER-PERF-01.1***: *The aircraft shall have a range of at least 4,000 km at maximum payload.*
- ***WFC-USER-PERF-02.1***: *The aircraft shall be able to transport 120 passengers.*
- ***WFC-PERF-01***: *The aircraft shall be able to transport all passenger's luggage.*
- ***WFC-PERF-02***: *The aircraft shall fly at a cruise altitude of at least 8,900 m.*
- ***WFC-PERF-03***: *The aircraft shall have an OEW/MTOW ratio of less than 0.6, excluding the tank weight from the OEW if hydrogen is used as fuel.*

- **WFC-PERF-04**: *The horizontal tail of the aircraft shall be sized to ensure longitudinal stability and controllability for the most aft and forward center of gravity (cg) positions encountered during operation.*
- **WFC-PERF-05**: *The energy consumption of the aircraft shall be similar to or less than similar existing aircraft.*
- **WFC-PERF-06**: *The aircraft shall be able to fly at a maximum cruise Mach number of 0.82.*
- **WFC-PERF-07**: *The ROC of the aircraft shall be no less than 17.8 m/s.*
- **WFC-PERF-08**: *The aircraft shall have a stall speed of no more than 190 km/hr.*
- **WFC-PERF-09**: *The aircraft shall be able to achieve a glide angle of at least 5.5 degrees.*

Operation

- **WFC-OP-01**: *The aircraft configuration shall comply with airport infrastructure present at the beginning of its operational life.*
- **WFC-OP-02**: *The runway length of the aircraft during takeoff and landing shall be no more than 1,500 m at sea level.*
- **WFC-OP-03**: *The aircraft shall be operational for the highest of at least 43,800 flights and 109,500 flight hours under an operational lifetime of 30 years.*
- **WFC-OP-04**: *The turnaround time of the aircraft shall be less than 40 minutes.*
- **WFC-OP-05**: *The hired maintenance crew shall be 5% more than for maintenance of conventional aircraft.*

Sustainability

- **WFC-USER-SUS-01**: *The aircraft shall be made of materials which are recycled and/or recyclable.*
- **WFC-USER-SUS-05**: *The propulsion system's energy source shall not rely on fossil fuels.*
- **WFC-SUS-01**: *The aircraft noise performance shall comply with the International Civil Aviation Organization's (ICAO) Annex 16 regulations [21].*
- **WFC-SUS-02**: *The aircraft shall generate less greenhouse gas emissions than similar existing aircraft.*
- **WFC-SUS-03**: *The cabin interior characteristics such as aisle width, seat pitch, cabin height and over-head baggage space shall be similar to similar existing aircraft.*
- **WFC-SUS-04**: *The noise level inside the cabin of the aircraft shall be similar to similar existing aircraft.*
- **WFC-SUS-05**: *The noise level outside the cabin of the aircraft during ground operations, take-off and landing shall be similar to similar existing aircraft.*
- **WFC-SUS-06**: *The end-of-life recycling procedures shall be accredited by AFRA.*

Safety and reliability

- **WFC-USER-SF-01.1**: *The certification of the aircraft shall comply with current safety and reliability requirements as specified in the European Union Aviation Safety Agency (EASA) CS25 regulations [22].*
- **WFC-SF-01**: *A factor of safety of 1.5 shall be applied to the prescribed limit load which are considered external loads on the structure.*
- **WFC-SF-02**: *The structure shall be able to support ultimate loads without failure for at least 3 seconds [22].*
- **WFC-SF-03**: *The aircraft shall use a propulsion technology with a TRL of at least 6, as defined by EU [23].*
- **WFC-SF-04**: *The aircraft shall have enough reserve energy to fly for 45 minutes at nominal cruise conditions after reaching its destination.*
- **WFC-SF-06**: *Manufacturing methods and materials shall ensure the safety of the workers during production and maintenance.*

Cost

- **WFC-USER-COST-01**: *The unit cost of the aircraft shall not be more than 105 % of similar existing aircraft.*
- **WFC-COST-01**: *The overall program cost of the aircraft shall be no more than 110 % of similar existing aircraft.*

Production

- **WFC-PD-01**: *The aircraft delivery rate shall be at least 5 aircraft/month.*
- **WFC-PD-01.1**: *The aircraft delivery rate shall be able to increase to 10 aircraft/month if there is a demand.*
- **WFC-PD-02**: *The aircraft shall be operational in 2036.*

- **WFC-PD-03**: *The aircraft shall be manufactured according to the lean manufacturing philosophy.*
- **WFC-PD-04**: *The assembly methods used for aircraft production shall allow part disassembly and retrofitting.*

From these essential requirements a few driving requirements can be identified. These driving requirements, as the name implies, drive the design more than average. The driving requirements for this design are **WFC-USER-SUS-05**, **WFC-USER-PERF-01.1**, **WFC-USER-PERF-02.1** and **WFC-PERF-05**.

3.2. Functional Analysis

To fully understand how a complex system such as the SHOTS aircraft has to function, a functional analysis is performed which results in a functional breakdown structure. These diagrams, in combination with the requirements discussed in section 3.1, form a basis for the different phases the aircraft has to go through. In figure 3.2 these phases are represented in the form of a functional flow diagram. Within this section, each phase is worked out in more detail in the form of a functional breakdown structure. The colors are defined as shown in figure 3.1.

Figure 3.1: Legend for the functional breakdown structure presented in the rest of this section.
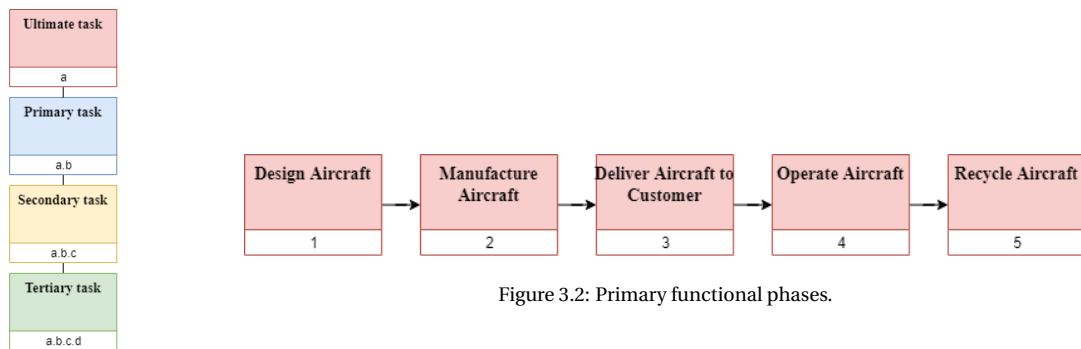
Figure 3.2: Primary functional phases.

Design phase

This is where it all starts: the design phase. Setting up requirements, creating concepts, and selecting one concept that can be worked out in full detail. The complete diagram is shown in figure 3.3. A prototype can be built and once it is certified the next phase can start, which is manufacturing the SHOTS aircraft for the clients.
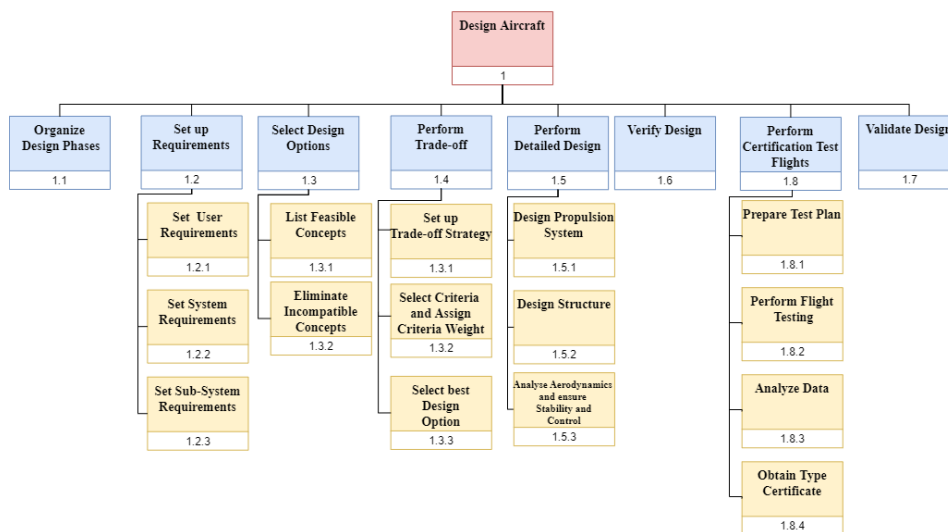
Figure 3.3: Functional breakdown structure for designing the SHOTS aircraft.

Manufacturing phase

The complete diagram for the manufacturing phase is shown in figure 3.4. Once an aircraft is fully assembled and meets all quality standards, the next phase can start which is delivering the aircraft to the customer.
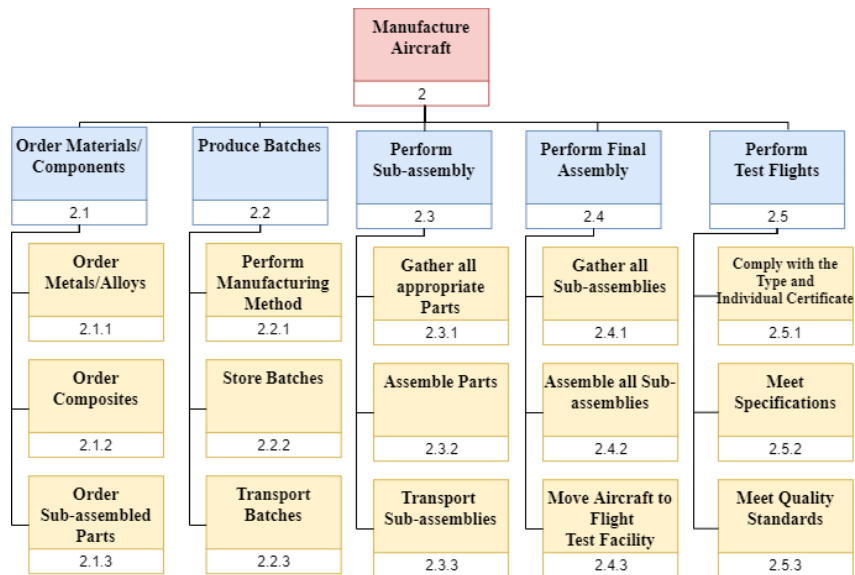
Figure 3.4: Functional breakdown structure for manufacturing the SHOTS aircraft.

Delivery phase

During the delivery phase, the technical acceptance process can start, and once completed, a transfer-of-title and ferry flight can be performed as shown in figure 3.5. After delivery of the SHOTS aircraft, the longest functional phase starts which is the operational phase of the aircraft.
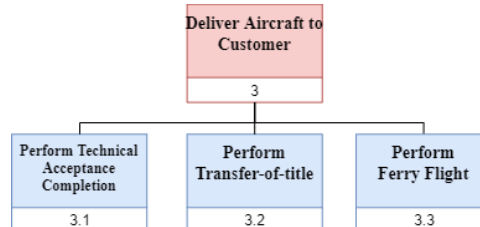
Figure 3.5: Functional breakdown structure for delivering the SHOTS aircraft.

Operational phase

The operational phase is the longest and most essential phase within the functional analysis. Its main focus is on transporting payload safely. The complete functional breakdown diagram of the operational phase is shown in figure 3.6. Once the aircraft needs to retire it will go into the final functional phase which is disposal.
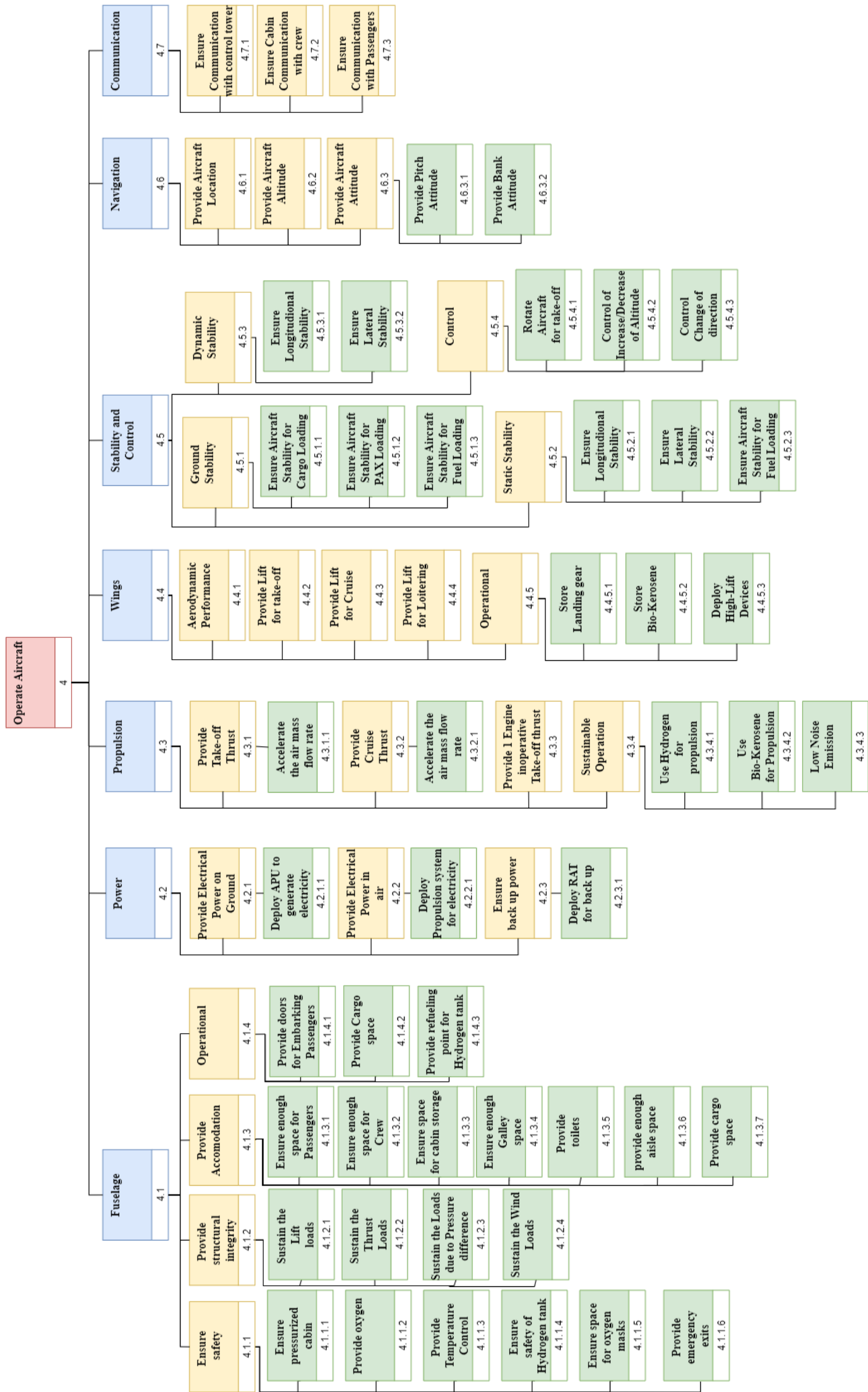
Figure 3.6: Functional breakdown structure for operating the SHOTS aircraft.

Disposal phase

The final functional phase is the disposal of the aircraft. Valuable components such as the engines and avionics are removed from the aircraft and brought back to the market as second hand components. The remainder of the aircraft is dismantled and the materials are recycled. The functional breakdown structure for the disposal phase is shown in 3.7.
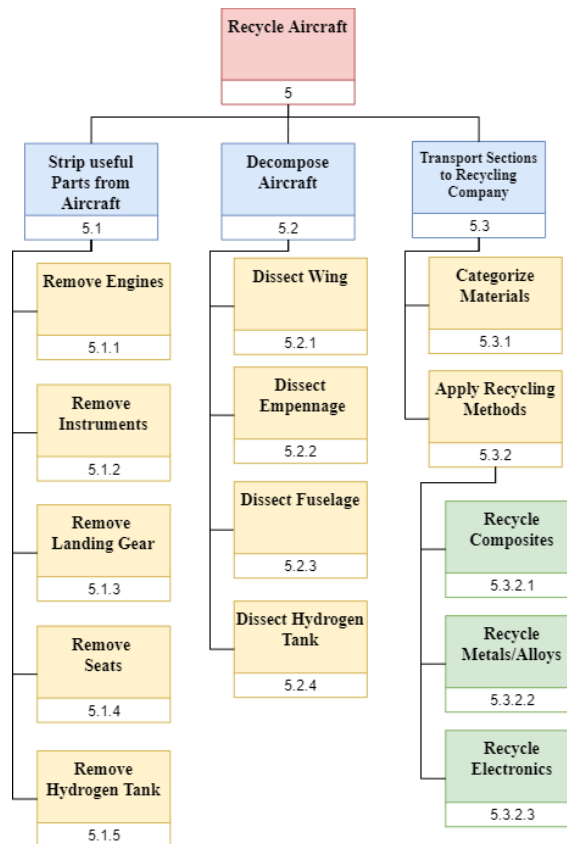
Figure 3.7: Functional breakdown structure for dismantling and recycling the SHOTS aircraft.

3.3. Design Option Tree

A design option tree (DOT) is a graphical aid to consider the options for the design. This section presents the DOT for the WeFlyCycle project. For more information about the DOT please consult the Baseline Report [2] or the Midterm Report [3]. Please note that a red box indicates an unfeasible considered option and a green box indicates a feasible considered option.

3.3.1. Aircraft configuration & energy source

Sustainability is a key aspect in the propulsion system design and therefore the energy source is the first element to be considered. The corresponding part of the design option tree is presented in 3.8. Please note that a hydrogen fuel cell is not considered feasible for several reasons:

- A hydrogen fuel cell in aircraft results in cooling problems for the required range of the SHOTS [24].
- A hydrogen fuel cell needs time to achieve its maximum power, therefore heavy batteries are required in order to compensate for this [24].
- A hydrogen fuel cell is extremely difficult to recycle and it therefore directly contradicts requirement **WFC-USER-SUS-01**.
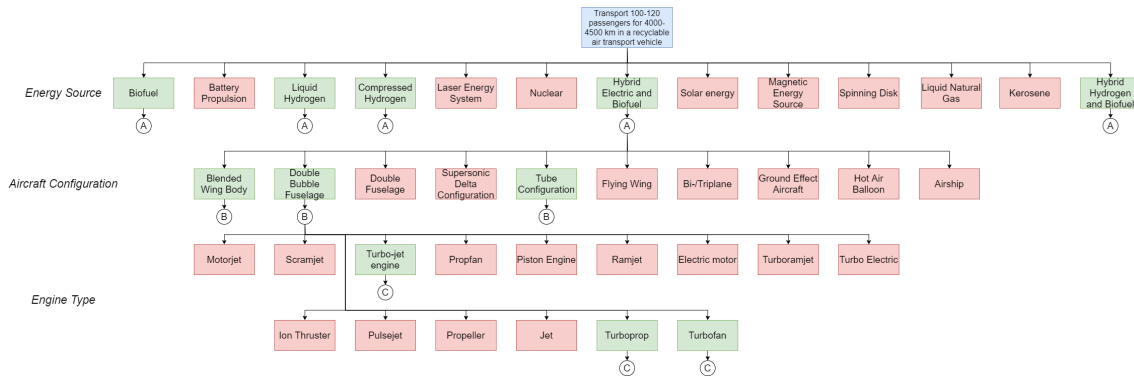
Figure 3.8: Design option tree for the energy source and the propulsion system (obtained from Midterm Report [3]).

3.3.2. Engine placement & wing selection

Engine placement and the wing planform are also decisions to be made. The design options are shown in figure 3.9.

Figure 3.9: Design option tree for the engine placement and the wing planform (obtained from Midterm Report [3]).

3.3.3. Tail & landing gear

A general decision also needs to be made for the tail and the landing gear, these are illustrated in figure 3.10.
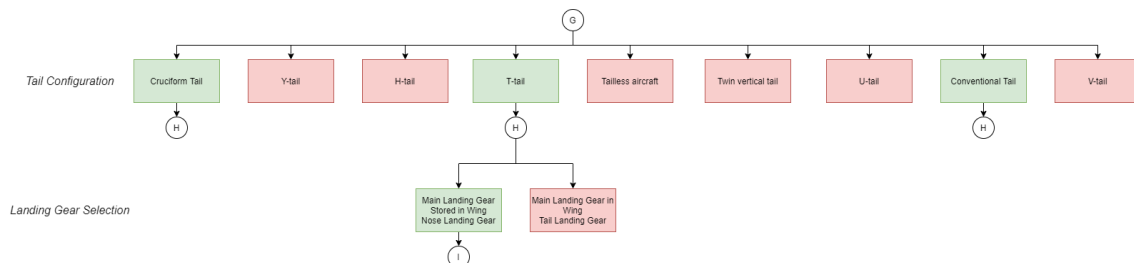
Figure 3.10: Design option tree for the tail and the landing gear (obtained from Midterm Report [3]).

3.3.4. Materials, structures & manufacturing

The last considerations for the design are the materials, structure and the manufacturing technique. These logically go hand in hand with one another. The options are presented in figure 3.11.

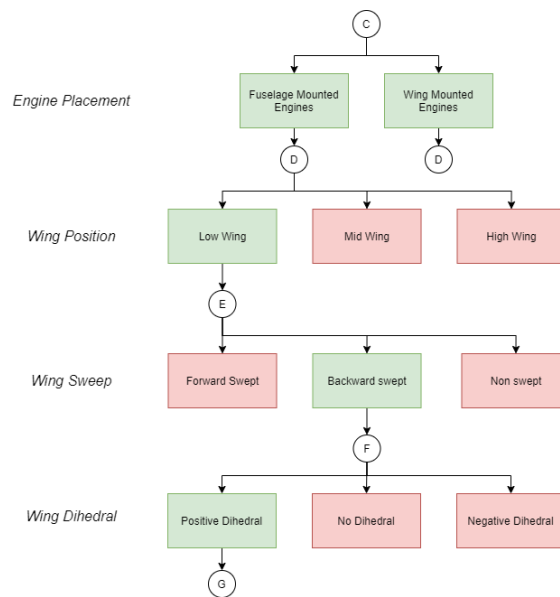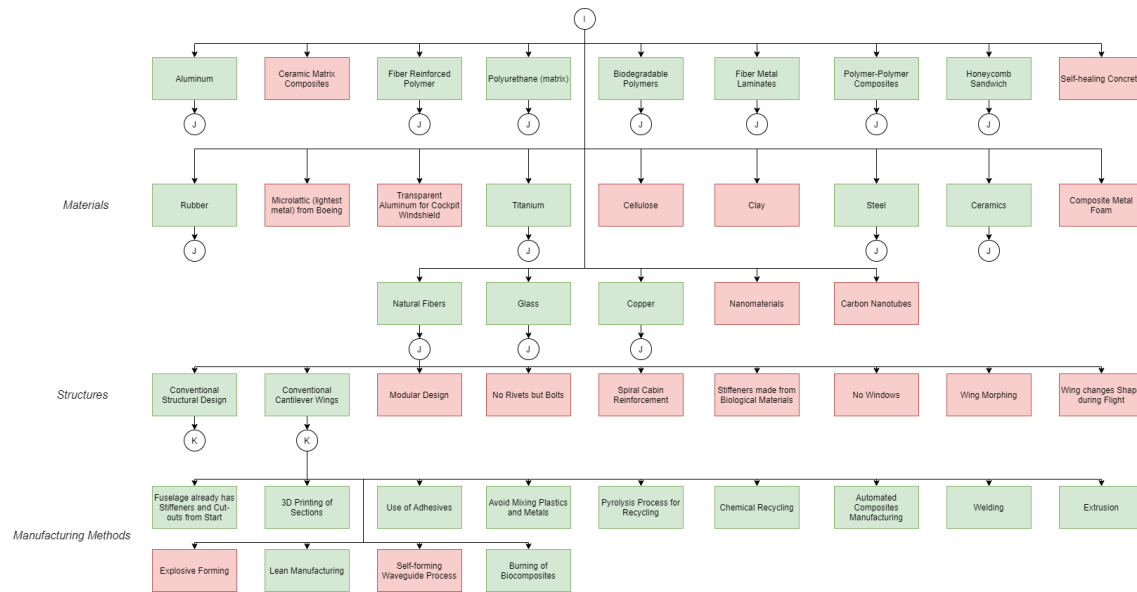Figure 3.11: Design option tree for the materials, structure and the manufacturing technique (obtained from Midterm Report [3]).

3.4. Concept Trade-off

In the baseline phase, three concepts were selected which were investigated in more detail during the midterm phase. The three different concepts that were evaluated are:

- **Concept 1** has a propulsion system based on both biokerosene and hydrogen. The configuration has low, traditional, backward swept wings and a pressure tube fuselage. The engines are wing-mounted.
- **Concept 2** has a propulsion system only based on compressed hydrogen. This concept also has low, backward swept wings and a pressure tube fuselage. The engines are fuselage-mounted.
- **Concept 3** also has a propulsion system based on compressed hydrogen but utilizes a so-called double-bubble configuration where the hydrogen tank is stored on top of the fuselage. This concept also has low, backward swept wings. The engines are wing-mounted.

After the detailed analysis of the three different concepts, a trade-off was performed. The result of this trade-off is shown in figure 3.1. Reliability, availability, maintenance, and safety (RAMS) was used as an operational trade-off criterion.

Table 3.1: Results of the performed trade-off for aircraft concept selection (obtained from Midterm Report [3]).

Criteria	Weight	Concept 1	Concept 2	Concept 3
Max take off weight	0.40	5	1	1.12
Unit cost	0.23	3	1	5
RAMS	0.15	3.25	1.75	2
Market risk	0.09	4	1.67	1.33
Gas emissions	0.08	1	4.99	5
Noise	0.05	5	1	1.33
	Total:	**3.87**	**1.49**	**2.48**
	Rank:	**1**	**3**	**2**

Concept 1, the SHOTS aircraft, was the clear winner. The rest of this report, reports the system and subsystem design and performance of the SHOTS.

System Integration Methods

A proper system integration is performed before a more detailed analysis is initiated. First, the resource allocation is discussed in section 4.1. This consists both of technical resource budgeting and contingency management. Finally, a chart is presented in section 4.2 which shows how different design parameters are interrelated.

4.1. Resource Allocation
During the development of the aircraft, several technical resources must be closely monitored as they are vital to the viability of the product and have a large influence on the total cost. For this analysis, results from the Midterm Report [3] are used to come up with resource budgets for mass and cost. This is discussed in subsection 4.1.1. Margins have to be considered within these budgets for contingency management. Moreover, while sizing for the range requirement **WFC-USER-PERF-01.1** translated from the user requirements, a contingency has to be considered as well, as discussed in subsection 4.1.2.

4.1.1. Technical Resource Budgets
To serve as a guideline during the detailed design process, a technical resource budget breakdown was made. Throughout the design process, a thorough check is performed to ensure that the design would comply with the technical resource budgets to reduce the chance of a significant increase in the mass or cost of the design. This section presents the preliminary budget breakdown of mass and cost of the SHOTS aircraft based on the calculations from the Midterm Report [3].

Mass: the MTOW is the first resource to evaluate. The average value from reference aircraft is 59,110 kg. It is expected that the OEW of the aircraft will be higher due to the hydrogen fuel tank. According to the class II weight estimation reported in the Midterm Report [3], the MTOW was estimated to be 71,474 kg. The mass budget for the MTOW is therefore set at 71,474 kg. Using the class II weight estimations in the Midterm Report [3], the mass budget breakdown can be found in table 4.1.

Cost: the unit cost is also a top-level client need which has been translated into a system requirement **WFC-USER-COST-01** based on delivery rate of 10 aircraft/month. In the Midterm report [3], the unit cost was estimated to be around $136 million in 2036 and this estimate will be used as the total cost budget for the entire aircraft using the typical cost per unit mass for each aircraft subsystem[25] and class II weight estimations. The preliminary cost budget breakdown can be found in table 4.1 as well.

Table 4.1: Technical resources budget breakdown.

Subsystems	Budgeted mass [kg]	Budgeted mass [%]	Acceptable error margin [± %]	Budgeted cost [mil$]	Budgeted cost [%]	Acceptable error margin [± %]
Wing	7,146	10.0	15	19.9	14.7	15
Empennage	496	0.7	15	3.6	2.7	15
Fuselage	6,046	8.5	15	18.0	13.3	15
Landing gear	2,416	3.4	5	1.6	1.2	5
Nacelle	1,592	2.2	10	-	-	-
Fixed items*	9,327	13.0	5	13.0	9.6	5
Engines and tank	23,329	32.6	15	48.0	35.4	15
OEW	**50,352**	**70.4**	**<0****	**10.1**	**7.4**	**<0**
Hydrogen fuel	1,858	2.6	15	-	-	-
Biokerosene fuel	6,981	9.8	15	-	-	-
Payload	12,283	17.2	5	21.4	15.8	5
Total	**71,471**	**100**	**<0****	**136.2**	**100**	**<0**

*It contains standard operational equipment such as the avionics, electrical system,APU and furnishing
**There is no positive error range, which means that a mass increase is not acceptable whereas a mass decrease is preferred.

For both the cost and mass budgets, the largest acceptable error of 15% was assigned to subsystems whose design are likely to be changed or iterated during this design phase including the wing, engines and so on. Same reasoning applies to the acceptable mass budget error for the fuel weights whereas the smallest acceptable error of 5% was assigned to the landing gear, fixed items and payload subsystems

as they generally remain the same. Moreover, the cost of the nacelle subsystem was taken into account in the engines and tank subsystems. Finally, the technical resource budget will be updated at the end of the detailed conceptual design (see section 11.2).

4.1.2. Contingency management

After determining the technical resource budget, a set of margins is determined for each allocated budget in order to take into account unexpected changes using a technique called Technical parameter measurement (TPM). TPM aims to ensure the final product achieves its specified performance with acceptable consumption of resources.

Range: the range was determined as a top level client needs to be at least 4,000 km. However, taking possible loitering into account the aircraft may need to stay airborne for longer. Furthermore, because the design is still in the conceptual phase, a margin is needed to ensure that the requirement will be met at the final development stages. By taking a loitering time of 45 minutes, designing for range with a margin of 10% is reasonable. This means the range margin at this stage will be 10%.

MTOW: during conceptual design, the aim for MTOW is 71,474 kg according to the class II weight estimation in the Midterm Report [3]. According to the Project Management and Systems Engineering in the DSE lecture slides [26], the typical weight growth during the detailed design phase is around 7% and during the flight test phase, it is around 5%. This means that in the detailed conceptual phase, a margin of 10% is reasonable for the MTOW.

Recyclability: given that recyclability is a top-level need of the client, the aim must be to have 100% built from recycled and/or recyclable material. There is no contingency margin for this resource. This means that from the conceptual design phase onwards, the goal will always be to use 100% recyclable materials. However, unlike cost or MTOW which can be quantified easily, it is difficult to have a quantitative measure of recyclability. Therefore, the way to monitor it is to ensure that the materials selected for each subsystem of the SHOTS aircraft can be recycled during the duration of the design phase as shown in chapter 6.

Cost: cost is also a top level need. During the preliminary conceptual design phase in the Baseline Report [2] a margin of 15% was taken into account. At this point, as the design is more refined and the cost breakdown will be more detailed and accurate, the margin is lowered to 7%.

Cruise altitude: a flight altitude requirement of higher than 8,900 m was generated due to EASA safety regulations [22]. A contingency of 24% is given, which means that the aircraft shall be sized to fly at 11,000 m.

In table 4.2 an overview of the contingency margins is presented. While designing the subsystems, the contingencies should be taken into account to ensure that the specified requirements will be met during the mass production phase. The TPM-parameter per phase is found by summing the product of the contingency and the relative importance. As the range, recyclability and cost requirements were specified by the customer, they have been given the highest relative importance which is 30%. The MTOW is essential for subsystem sizing as well as cost; hence, its relative importance only comes in second at 15%. Although the cruise altitude requirement regards safety regulations, a large contingency factor has already been given to ensure that the cruise altitude requirement; hence, its relative importance is slightly lower than the other parameters. Finally, the results are plotted in figure 4.1. As seen in the figure, the current TPM variables are higher than the target ones which means that the results are more accurate than expected.

Table 4.2: Contingency margins for key performance characteristics.

Design Phase	Range	MTOW	Recyclability	Cost	Cruise altitude
1-Conceptual	20%	20%	0%	15%	24%
Current value	**10%**	**13%**	**0%**	**7%**	**24%**
2-Preliminary	8%	10%	0%	5%	20%
3-Detailed	5%	7%	0%	3%	10%
4-Flight test	3%	5%	0%	2%	5%
5-Mass production	0%	0%	0%	0%	0%
Relative importance	25%	15%	25%	25%	10%

Figure 4.1: TPM at different phases in the design.

4.2. Design Process

To make the design process and the communication between the different departments successful, a flowchart with all the variables required by each department was created as shown in figure 4.2. This flowchart is of importance as it shows how a certain change of parameters influences the output of other departments. This same flowchart was used to decide where the design should start and how the iterative phase of the design will take place.
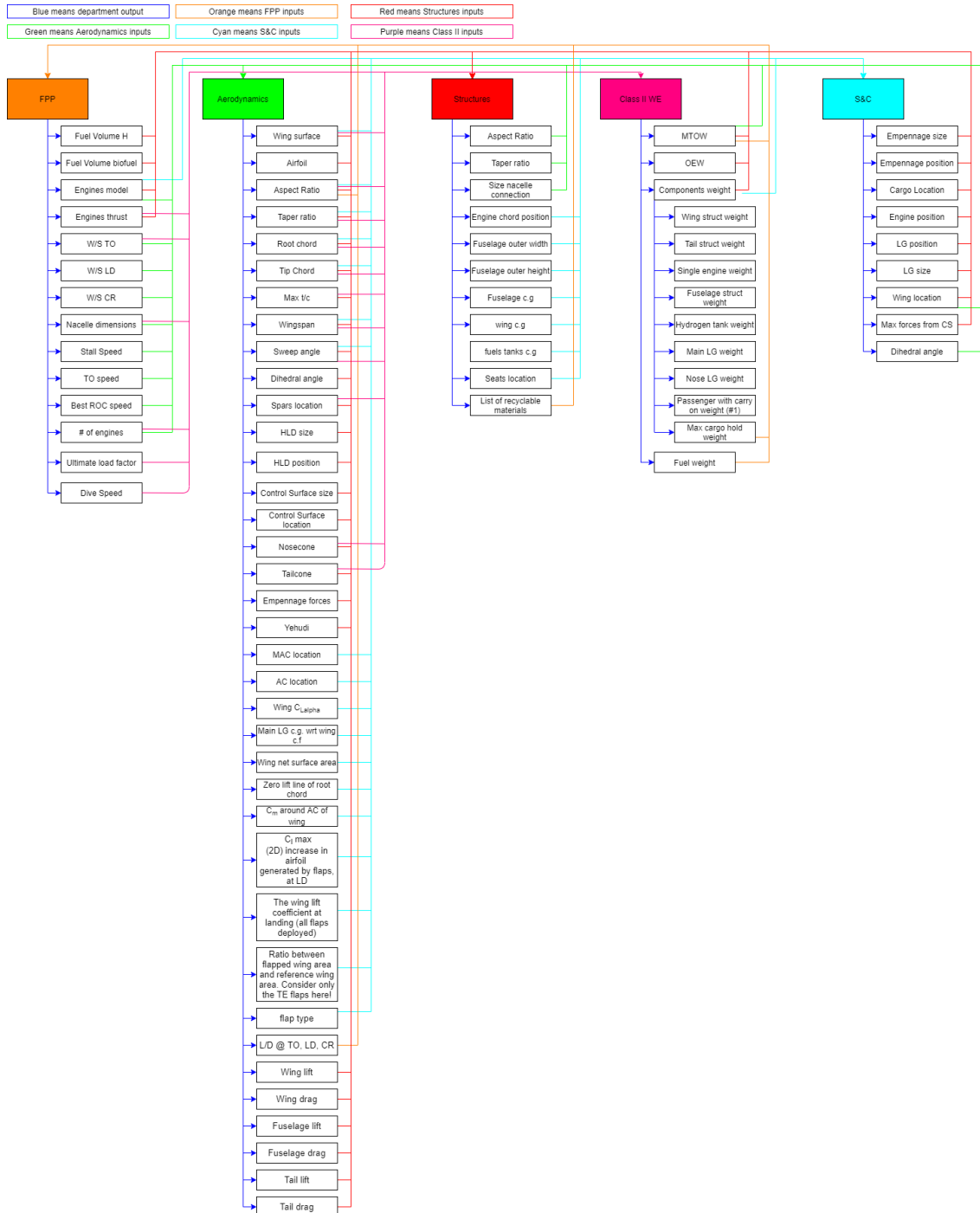
Figure 4.2: Flowchart of the variables from each department and their interdependencies.

<div align="right"><big>5</big></div>

Weight Estimations

As explained in the Midterm Report [3] the value for the class II weight estimation did not converge and therefore this requires more research. First, an initial determination of the tank weight is performed including a discussion of the materials in section 5.1. Second, the decision on the engine type is discussed again in order to find the most optimal combination of thrust requirement and engine type in section 5.2. Logically the tank mass and engine mass are required for the class II weight estimation to be performed properly. Third, in section 5.3 the class II weight estimation is reported. To obtain the final MTOW, several iterations have been performed to find the value it converges to.

5.1. Hydrogen Tank Weight

Since the hydrogen tank is an essential element in the design of this aircraft it is important to size it properly. During the midterm phase [3] it was sized assuming isotropic properties and using carbon fiber as a material. Logically, this did not yield an optimal result and it can hence be optimized by evaluating different materials. If composites are to be used, the fiber orientation can also be optimized to minimize the weight. The main functions of the tank are as follows:

- The tank has to accommodate all the hydrogen necessary for the mission in a safe way.
- The tank must be recycled when the aircraft has reached the end of its operational life.

The main requirements of the hydrogen tank are listed below.

- **WFC-TANK-01**: *The tank shall store 2063 kg of hydrogen at 700 bar.*
- **WFC-TANK-02**: *The tank shall fit inside the pressurized fuselage section, constraining its external radius to 1.80 meters.*

Several general assumptions have been made for the sizing of the tank:

- The tank is modelled as a thin-walled cylinder with hemispherical end caps,
- The thickness of the wall is constant throughout the tank,
- For composites, the fibers are placed for 2/3 using hoop winding and 1/3 using helical winding,
- For composites, the hoop stress is carried by the circumferential fiber layers and the longitudinal stress is carried by the longitudinal fiber layers. The final thickness is the summation of both these layers.
- For composites, the fiber translation efficiency is 80%, meaning a safety factor k_f of 1.25 is applied to account for sub-optimal fiber layout, manufacturing imperfections and other flaws that reduce the strength of the material[1].
- To prevent the hydrogen from escaping through the tank or causing hydrogen embrittlement of the material, a liner material is used[2,3]. This material is not load-bearing.
- The hydrogen is stored at a temperature of $25°C$.
- One layer of composite has a thickness of $0.001 m$.

5.1.1. Materials

Several important aspects need to be taken into account considering the hydrogen tank. The specific properties of the material are very important since weight needs to be minimized. Furthermore, the permeability of the material needs to be considered as well [27]. For the tank design, four different

---

[1]`https://hsecoe.org/models.html` (accessed 15-06-2020)

[2]`https://h2tools.org/bestpractices/material-selection` (accessed 08-06-2020)

[3]`https://www.dsm.com/corporate/news/news-archive/2017/2017-09-04-dsm-developing-novel-materials-solution-for-high-pressure-composite-tanks-for-hydrogen-storage.html` (accessed 08-06-2020)

materials are considered: carbon fiber T800S [28], Kevlar 49, Hexcel[4] PV42/850 (HS-CP-3300) carbon fiber [29] and 2800 Maraging Steel[5]. Composite materials have very good strength to sustain the high pressures, however their permeability needs some more attention. Composite wrapped tanks need a liner in order to prevent hydrogen gas escaping from the tank. For 2800 steel, hydrogen embrittlement can lead to a huge reduction of technical properties[6] [30]. Therefore, also for the steel tank a liner will be used. A material that is often used for this is high-density polyethylene (HDPE) with a density of 970 kg/m^3 [7]. According to Argonne[8] the liner thickness required for a 700 bar tank is 5 mm [31], this will hence be used in the calculations. Table 5.1 outlines the material characteristics which will be used to size the hydrogen tank.

Table 5.1: Material properties of the four considered materials.

Material property	T800S [28]	Kevlar 49[9]	Hexcel PV42/850[10]	2800 Maraging Steel[11]
Tensile strength $\sigma_{tensile}$ [MPa]	3290	3000	3378	2693
Density ρ [kg/m^3]	1800	1440	1790	8000
Assumed fiber volume [%]	60	60[12]	62	-

5.1.2. Tank design

For the design of a cylindrical pressure vessel there are two important stresses to take into account: the hoop stress shown in equation 5.1 and the longitudinal stress shown in equation 5.2 [32].

$$\sigma_{hoop} = \frac{pr}{t} \qquad (5.1) \qquad\qquad \sigma_{long} = \frac{pr}{2t} \qquad (5.2)$$

where σ denotes the stress in Pa, p denotes the pressure difference between the outside and inside of the tank in Pa, r the internal radius in m and t the thickness of the tank in m. The relation between the hoop and longitudinal stress is $\sigma_{hoop} = 2 \cdot \sigma_{long}$. This is important when the stress of the material used in the tank is carried by fibers. The orientation of these fibers can be optimized for this relation: 2/3 of the fibers are placed in circumferential direction to account for the hoop stress, 1/3 of the fibers are placed in axial direction to account for the longitudinal stress. To obtain the dimensions of the tank, the pressure is set at 700 bars. Using equation 5.3, the density of the hydrogen gas can be calculated. The required internal tank volume follows from equation 5.4.

$$\rho = \frac{p}{ZRT_e} \qquad (5.3) \qquad\qquad V = \rho \cdot m_h \qquad (5.4)$$

The pressure is denoted by p in Pa. R is the specific gas constant in $Nm/kg \cdot K$, for hydrogen 4157.2, and T_e is the temperature in K. Z denotes the compressibility factor of hydrogen. This value is a function of the pressure and is experimentally obtained by Colozza [33]: $Z = 0.99704 + 6.4149 \cdot 10^{-9} \cdot p$. In equation 5.4 m_h is the hydrogen fuel mass in kg.

The weight of the hydrogen tank is computed for all four materials. It should also be noted that the tank pressure difference compared to outside the tank is taken as 700 bars, therefore neglecting the very small pressure outside. This is a valid assumption since the pressure outside the tank is 3 orders of magnitude lower compared to the pressure inside.

Using this method, the required volume is 51.9 m^3. Furthermore, the tank needs to be fitted in the pressurized section of the fuselage. This means the external radius of the tank should be less than 1.8

---

[4] https://www.hexcel.com/ (accessed 03-06-2020)

[5] http://www.matweb.com/search/datasheet.aspx?matguid=de22e04486ff4598a26027abc48e6382&ckck=1 (accessed 03-06-2020)

[6] https://h2tools.org/bestpractices/material-selection (accessed 15-06-2020)

[7] https://www.plasticseurope.org/en/about-plastics/what-are-plastics/large-family/polyolefins#:~:text=The%20density%20of%20HDPE%20can,and%20tensile%20strength%20than%20LDPE.

[8] https://www.anl.gov/ (accessed 04-06-2020)

[9] http://www.matweb.com/search/datasheet.aspx?matguid=77b5205f0dcc43bb8cbe6fee7d36cbb5 (accessed 04-06-2020)

[10] http://www.matweb.com/search/datasheet.aspx?matguid=a9479c26ccfc4268830db6f5587abcb0 (accessed 04-06-2020)

[11] http://www.matweb.com/search/datasheet.aspx?matguid=de22e04486ff4598a26027abc48e6382&ckck=1 (accessed 04-06-2020)

[12] Not listed by manufacturer, for calculations 60% is assumed.

m. These are the two constraints for the static sizing of the tank. The static sizing ultimately determines the required wall thickness for the tank to make sure the tank does not burst during operation.

Equations 5.1 and 5.2 are rewritten such that the thicknesses in circumferential and longitudinal direction are straightforwardly calculated as shown in equations 5.5 and 5.6.

$$t_{hoop} = \frac{p \cdot R}{S_{UTS}} \qquad (5.5) \qquad\qquad t_{long} = \frac{p \cdot R}{2 \cdot S_{UTS}} \qquad (5.6)$$

In these equations, S_{UTS} denotes the ultimate tensile strength in Pa. This results in two thicknesses. For composites, these thicknesses are added because fibers can only carry loads in the same direction as they are oriented. For metals, simply the highest thickness is taken because the material is isotropic. Next, this required thickness t_{req} is multiplied with the layout and burst pressure safety factor k_b to obtain the ideal thickness t_{ideal}, as shown in equation 5.7. According to international standards, $k_b = 2.25$ [31].

$$t_{ideal} = k_f \cdot k_b \cdot t_{req} \qquad (5.7)$$

For composites, this value is rounded up to the nearest millimeter, resulting in a discrete amount of layers because one can not apply partial layers. For metals, this is not needed. This results in the final thickness t_{final} of the load carrying material, as reported in table 5.2.

Finally, the mass of the tank is calculated. This is done by calculating the total surface area of the material S_m of the fuel tank in equation 5.8, which is subsequently multiplied with the thickness and density of each material using equation 5.9. This results in the mass of the liner and the mass of the load carrying material. The results are reported in table 5.2.

$$S_m = 2\pi \cdot (r_{external} - \frac{1}{2} t_{final}) + 4\pi \cdot (r_{external} - \frac{1}{2} t_{final})^2 \quad (5.8) \qquad m = S_m \cdot t_{final} \cdot \rho \qquad (5.9)$$

$r_{external} - \frac{1}{2} t_{final}$ denotes the theoretical radius halfway the material. Because the structure is assumed to be thin-walled, this expression is valid to calculate the total surface. Equation 5.9 returns the mass of the liner and the mass of the composite by calculating the volume and multiplying it with the density of the materials. For the liner, this is always equal to 970 kg/m^3. The final result for all four materials is shown in table 5.2.

Table 5.2: Weight breakdown of the hydrogen tank for static loading conditions.

Parameter	T800S	Kevlar 49	PV42/850	2800 steel
Thickness liner t_{liner} [mm]	5	5	5	5
Thickness load carrying material t_{load} [mm]	101	109	88	62
Liner weight m_{liner} [kg]	374	376	370	363
Load carrying material weight m_{load} [kg]	15,147	14,632	12,992	34,995
Total tank weight m_{tank} [kg]	**15,520**	**15,008**	**13,361**	**35,358**

For the class II weight estimation, the lowest value has been used because this represents the optimal solution. A more detailed analysis of the hydrogen tank, including material trade-off and related systems is discussed in section 9.2.

5.2. Engine Selection

A preliminary engine selection was performed in the Midterm Report [3] where PW1700G engines have been chosen for the SHOTS aircraft. However, the unit cost of PW1700G (12 million USD) is rather high which might make it difficult to meet the unit cost requirement **WFC-USER-COST-01**. After comparing the operational fuel cost and engine cost of several engines, two design options are made with the main difference being the selected engines and the two design options are named SHOT-1 and SHOT-2 respectively. The details of the engine selection and the engines considered are elaborated in subsection 7.4.1. Table 5.3 shows the selected engine models and the total engine weights of SHOT-1 and SHOT-2 to be used as inputs for the class II weight estimations in the next section.

Table 5.3: Engine models and weights of the 2 design options

	SHOT-1	SHOT-2
Engine models	4 × PW1700G (2 burns biokerosene) (2 burns hydrogen)	2 × CF34-10A (burns biokerosene) 2 × PW1700G (burns hydrogen)
Engine weight [kg]	6,896	6,804

5.3. Class II Weight Estimations

In the detailed design of the other subsystems it is important to find out their approximate weight at an early stage, therefore a class II weight estimation is performed. This weight estimation is performed using the General Dynamics (GD) method described in Roskam [34]. The weight estimation is performed for five different subsystems, namely the wing, empennage, fuselage, landing gear and the nacelle. The fixed equipment weight is based on reference aircraft since many of the parameters on which it is based in the GD method are unknown at this stage. The propulsion and hydrogen tank weight are taken from sections 5.1 and 5.2 due to the irregular nature of the aircraft propulsion system. It should be noted that the GD method equations make use of the Imperial System. The component weights have been verified using the method from Torenbeek [34]. All values were within a 10 % difference, except for the landing gear weight. Therefore, the average of the Torenbeek method [34] and the GD method is used.

Table 5.4 illustrates the weights obtained using the explained method. These subsystem weights are used to update the mass budget that has been set up in section 4.1.1 and the updated mass budget can be found in section 11.2. Please note that the table includes both SI and imperial units since the equations make use of the Imperial System. For the fuel weight the first number describes the hydrogen while the second number denotes the biokerosene.

Table 5.4: Determination of the subsystem weight according to the Class II Weight Estimation.

Subsystem	Value	Unit	Value	Unit
Wing	17,461	[lbs]	7920	[kg]
Horizontal Tail	739	[lbs]	335	[kg]
Vertical Tail	485	[lbs]	220	[kg]
Fuselage	12,743	[lbs]	5,780	[kg]
Landing Gear	5,326	[lbs]	2,416	[kg]
Nacelle	3,803	[lbs]	1,725	[kg]
Fixed Items*	20,569	[lbs]	9,330	[kg]
Engine	15,203	[lbs]	6,896	[kg]
Tank	29,394	[lbs]	13,361	[kg]
Fuel	4,548/15,390	[lbs]	2,063/6,981	[kg]
Payload	27,079	[lbs]	12,283	[kg]
Operating Empty Weight	105,563	[lbs]	47,983	[kg]
Maximum Takeoff Weight	152,482	[lbs]	69,310	[kg]

*The fixed items subsystems contains standard operational
equipment such as the avionics, electrical system, APU and furnishing.*

The resulting MTOW in table 5.4 is the result of five iterations that were performed in order to make sure the MTOW converges. The result of this is figure 5.1 where it is clearly illustrated that the MTOW converges to a value that is within 1 % of the previous iteration.
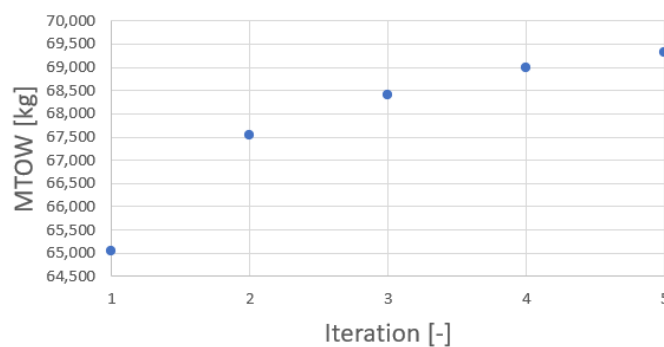
Figure 5.1: Graphical representation of the MTOW as a function of the iteration performed.

6

Materials

An essential part of the WeFlyCycle project is creating an aircraft that is recyclable and/or made out of recycled materials. Therefore, the material selection has to be more extensive than investigating the right material properties to deal with structural failure modes. Recyclability plays a big role in the material selection but is in itself a very broad topic. To give an example, an aircraft seat can be reused in another aircraft or the fabrics/metals can be recycled to produce new products with.

Since structures, materials and manufacturing are closely interrelated, a functional and requirements analysis is carried out for these three design aspects in sections 6.1 and 6.2 respectively. A definition of recycling and other end-of-life (EOL) procedures is provided in section 6.3 based on the waste hierarchy. The aircraft parts that can be re-certified for reuse in other aircraft are identified. The recyclability of materials of interest for the primary structures is assessed in section 6.4, followed by a recyclate resale value analysis in section 6.6. The considerations for aircraft interior materials are discussed in section 6.5. A trade-off is carried out to score the structural materials in 6.7. At the end, all findings regarding the materials are summarized and processed into an overview in section 6.8.

6.1. Functional Analysis

Figure 6.1 shows what functions the materials and structures of the aircraft have to fulfill throughout the lifetime of the airframe. The functions vary from the design of the aircraft to EOL of the aircraft.
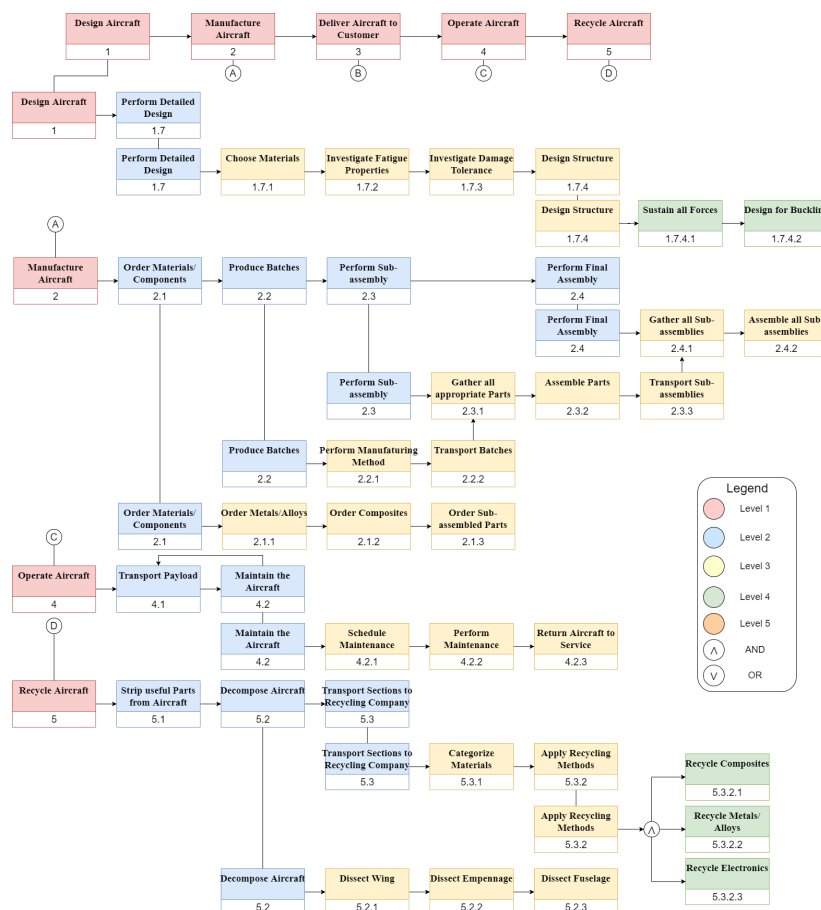
Figure 6.1: Functional analysis for the materials and structures.

6.2. Requirements Analysis

Requirements are an essential starting point for the analysis and design of a subsystem. The main system requirements are presented in section 3.1. The subsystem requirements are listed below:

- **WFC-MAT-01**: *The recyclate resale value of the material shall be higher than the landfill cost.*
- **WFC-MAT-02**: *Surface coatings shall protect the aircraft components from corrosion.*
- **WFC-MAT-03**: *Non-conductive materials shall employ a lightning strike protection system.*
- **WFC-MAT-04**: *Materials used shall withstand the thermal conditions experienced during aircraft operational life.*

6.3. Waste Hierarchy

The use of recycled and/or recyclable materials is one of the key requirements of the WeFlyCycle (WFC) project, as stated in **WFC-USER-SUS-01**. Thus, it is important to define exactly what is considered recyclable so compliance with the requirement can be verified. The materials used in the aviation industry are greatly constrained due to strict safety regulations. This means the use of recycled materials is generally avoided due to the deterioration in material properties, and thus are only considered for non-structural components used in the aircraft's interior. The definition of recycling in this report is "any recovery operation by which waste materials are reprocessed into products, materials or substances whether for the original or other purposes" [4].

For primary and secondary structural parts, the EOL solutions are assessed. These can be divided into four main categories that form a waste hierarchy: reuse, recycling, energy recovery and disposal [35]. These are ordered from most sustainable at the top to least sustainable at the bottom, and thus the reuse of aircraft components shall be prioritized and disposal in landfills shall be completely avoided. However, for some materials the recycling processes can be environmentally worse than landfilling, so a more detailed analysis of EOL solutions is required. Figure 6.2 shows the flow of EOL solutions.
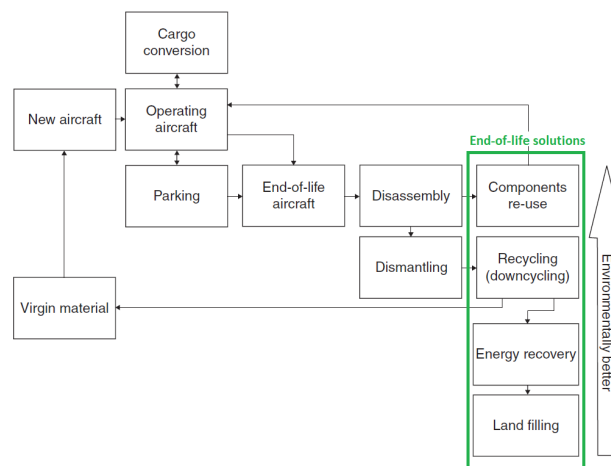
Figure 6.2: Aircraft end-of-life flowchart [35].

Reuse can refer to the reuse of the entire aircraft, as is the case for aircraft that have been parked for a definite period of time or passenger aircraft that are turned into freighters. This effectively increases the aircraft's operational life, but the fuel savings obtained with newer aircraft can easily compensate the negative environmental impact of old aircraft disposal [35]. Because of this, the focus is on reuse of aircraft components. Disassembly and re-certification for reuse is already a standard procedure in the aviation industry due to the high value of aircraft components. Additionally, a conventional design makes reuse of parts in other aircraft easier, thus increasing market opportunity. Parts that are generally disassembled and re-certified for reuse are engines, auxiliary power unit (APU), landing gears and avionics [4]. According to van Heerden, CEO of Aircraft-End-of-Life Solutions (AELS), flaps and slats made of carbon fiber reinforced polymers (CFRP) can also be reused in other aircraft[1].

---

[1]Interview with the chief executive officer of AELS, D. van Heerden (10-06-2020)

The next level in the waste hierarchy is recycling. As opposed to reuse, recycling does not maintain the original function of the material, but instead provides material of similar quality for production of new aircraft parts or downcycling for use in other industries where lower grade materials are used. The need for downcycling stems from issues such as recycling technology readiness, market opportunity, and use of complex materials. Recycling of EOL parts is also called secondary recycling [35].

Energy recovery refers to the burning of waste to generate heat or electricity [35]. Care must be taken when choosing energy recovery as an EOL solution, as in some cases the emissions from waste combustion are higher than the savings of energy recovery [36]. Generally, energy recovery is not considered a recycling method, but an exception is made for biomaterials. These materials can be considered to be carbon neutral as the carbon emissions from incineration are equal to the carbon absorbed during the plant's growth [37]. Nevertheless, the time scale of this solution could be an issue as the time it takes for a plant to absorb an equivalent quantity of carbon during its growth is much longer than the time it takes to release it during burning. Therefore, this option is limited to cabin interior solutions such that the materials can be sourced and managed in an environmentally responsible manner.

If the view is broadened outside of EOL solutions, the top tier of the waste hierarchy encompasses the reduction of material waste[2]. This can be achieved through primary recycling: recycling of materials during the production process [35]. This relates to the manufacturing methods available for each material and is considered in chapter 13.5. Material use reduction can also be achieved through the use of materials that provide substantial weight savings such as composites and fiber metal laminates.

6.4. Material Considerations

Several selection criteria have to be considered when it comes to aerospace materials. The desired properties greatly depend on the application. Resistance to fire, high heat, corrosion and lightning strikes are common requirements that vary greatly depending on the aircraft part. For this project, the recycling processes and their corresponding economic feasibility also need to be considered. Physical material properties such as ultimate strength, fatigue resistance, damage tolerance and density are implemented in the structural analysis of chapters 9 and 10.

Aluminum alloys have widespread use in the aviation industry. The aluminum recycling is already quite advanced and is even considered to be infinitely recyclable. Aluminum production has one of the largest energy differences between virgin and recycled material production [38], acting as an economic incentive. However, the accumulation of impurities may become an issue. Aluminum alloys used in the aviation industry are generally wrought alloys which contain a high aluminum content. For Aluminum 2024-T3 specifically, the chemical composition is 90.7-94.7 wt% Aluminum, 3.8-4.9 wt% Copper and 1.2-1.8 wt% Magnesium [3]. The different electrical conductivities and densities of these elements allow the use of technologies such as eddy current separation and sink float separation. The former is used widely in industry while the latter has around ten facilities in North America [38]. Shredding is generally used as a pre-recycling process to reduce part size and there are around 200 facilities in North America [38]. The recycling of metal alloys in the aviation industry is of commercial scale and can thus be assumed to have a Technology Readiness Level (TRL) of 9 [23]. With regards to thermal effects, aluminum alloys show a reduction in mechanical properties at temperatures of 100-150°C [39]. The nose, leading edges and skin are most affected by frictional heating at high speeds. However, this is not an issue for subsonic aircraft as temperature is not expected to go above 80-90°C [39].

Steel and titanium alloys are used for applications where resistance to high temperatures and pressure is required [5]. The use of steel in aircraft structures is limited due to its high density, which is 2.5 times higher than aluminum and 3.5 times higher than carbon-epoxy composite, and its low resistance to corrosion [40]. Typical applications are engine pylons and landing gear. Similarly, titanium alloys show excellent performance at high temperatures (500-600°C) [41]. Their main applications are jet engines and airframes, accounting for 9% and 10% of the structural weight of the Airbus A380 and Boeing 777 respectively [41]. The high cost and relatively high density are the main disadvantages.

Use of **advanced composites** in aircraft has been demonstrated in the Boeing B787, which uses T800 carbon composite for nearly half of its primary structure [42]. The high cost of carbon fibers is the

---

[2] https://www.epa.nsw.gov.au/your-environment/recycling-and-reuse/warr-strategy/the-waste-hierarchy (accessed 14-06-2020)

[3] http://asm.matweb.com/search/SpecificMaterial.asp?bassnum=MA2024T3 (accessed 14-06-2020)

main incentive for recycling. Mechanical recycling has a TRL of 6-7 for carbon fibers [43], however this results in large reduction of fiber length and mechanical properties. In this case, the recyclate can be reused in non-structural parts within the sports and automotive industry [44]. Relatively long fibers can be recovered with pyrolysis or solvolysis [44], which essentially dissolve the resin to leave fibers that maintain up to 90% of the original mechanical properties. The recovered fiber length obviously depends on the initial size of the part, which is generally large for aircraft skin panels, and the size of the chemical reactor [44]. The TRL of pyrolysis for carbon fibers is estimated to be 8 [45]. The commercial viability of pyrolysis has been proven by three companies processing 500-2,000 t/year of CFRP [46], but still most composite aircraft parts are currently sent to landfill at EOL [4] [20]. Nevertheless, the business case for pyrolysis recycling of carbon fibers is strong, as the net profit is believed to be 5 United States Dollar (USD)/kg [47]. For the Boeing B787 and Airbus A350 XWB, the total waste value is estimated to be approximately $275,000, with composite use in aircraft expected to grow in the next 20 years [47].

Glass reinforced aluminum (GLARE) waste in the next 40 years is expected to increase, as large quantities of EOL scrap are expected with the retirement of the Airbus A380 as well as the already present amount of production scrap [48]. The main advantages of this material are weight reduction and improved damage tolerance compared to aluminum alloys. Since GLARE is made of aluminum and glass prepreg layers, the main difficulty is the separation by removal of FM94 adhesive [48]. Mechanical separation and thermal delamination of GLARE have been investigated in scrap material, but still require advances in retained material quality and cost efficiency [48]. The TRL of these methods is assumed to be 3 [23], as the technology has been proven experimentally by Zhu [48]. Conventional recycling methods for aluminum and pyrolisis for fiber recovery can then be carried out post-separation.

Materials used in the outer skin of the aircraft must be able to conduct electrical charge in case of a lightning strike. This means that the material has to have high electrical conductivity [49]. For this reason, metal alloys such as Aluminum 2024-T3 have high resistance to lightning strikes, whereas carbon-epoxy composites require the addition of a metal mesh layer for protection. Corrosion is an important consideration for material selection. It accounts for roughly 25% of all metal component failures in aviation [50] and thus around $2 billion per year is spent on maintenance of metal parts damaged by corrosion [49]. Galvanic corrosion tends to occur at places where two materials mix. In the case of aluminum alloy and carbon-epoxy composite, an insulating layer of fiberglass laminate is used in assembly [50]. Nevertheless, the aircraft skin needs to be conductive and thus a different solution is required, usually in the form of corrosion-inhibiting primer and paint. If the chosen material does not have a high resistance to corrosion, protective coatings must be used such as anodised coating or Alclad for aluminum alloys [49].

The aircraft exterior is coated with primer and paint to protect it from corrosion. The paint should be durable, moisture-resistant and the primer contains corrosion-inhibiting chemicals for extra protection [49]. AkzoNobel Aerospace Coatings [7] offers chrome-free paint and primer solutions with low volatile organic compound (VOC) content for increased sustainability.

6.5. Interior Materials
The design of the interior of the aircraft is an essential element for passenger comfort. The major aspects of the design are twofold: the materials used should be as safe as possible (mainly fire/flame resistance) and the materials should be as comfortable for passengers as possible. The safety aspect of the materials goes hand in hand with strict regulations. Unfortunately, due to these regulations, sustainability does not always play a big role. According to Uddin [51] a small aircraft such as the SHOTS in this study contains about 3,300 kg (excluding carry-on luggage) of combustible materials. Of this 3,300 kg a small part is for items that are (almost) never used but are still subject to extreme safety regulations such as emergency slides, life vests or life rafts. About 1,455 kg of the combustible material is considered for use of more sustainable/better recyclable materials:

- **Seat shells** are currently manufactured from composites, mainly plastics and glass fibers[5]. Seat shells have the potential to adopt new technologies since they are not part of the primary structure. It is therefore opted to use flax biocomposites [52]. Zodiac Aerospace[6] has opted to use flax

[4] Interview with the chief executive officer of AELS, D. van Heerden (10-06-2020)
[5] https://www.aviationbusinessnews.com/cabin/composite-materials-aircraft/ (accessed 08-06-2020)
[6] https://www.zodiacaerospace.com/ (accessed 08-06-2020)

fibers with a PA11 resin [53] which can both be 100% bio-sourced. In a worst case scenario recycling is easy as well since the material can be burned and the emissions can be reused by the plants producing the materials in the first place, hence completing the cycle.

- **Cabin walls** are currently also manufactured from plastics and glass fibers. It is also opted to use flax fibers for this application.
- **Seat cushions** a seat cushion is often made from polyurethane foam [54]. This material is recyclable and actually used in other industries (such as mattresses or construction), therefore this material is considered sustainable in terms of recycling.
- **Aircraft radome**: radomes are often made from fiberglass[7] since, logically, the material should allow for electronic signals to pass through. A more sustainable material which can be used is kenaf fiber [52]. However, to aid the material in rain erosion a hybrid material should be used consisting of kenaf and glass fiber [52], this hybrid utilizes the best qualities of both materials. To properly recycle this the same technique used for GLARE can be applied.
- **Seat fabrics**: most seat fabrics are made from wool at the moment[8] which is considered to be a sustainable material which can easily be recycled in other industries. Special attention should however be given to the die used for colouring of the fabric.
- **Overhead bins**: according to the eco-compass research[9] and the Council for Scientific and Industrial Research (CSIR)[10] different materials should be considered for the overhead luggage bins such as flax or ramie. Special attention should be given to their fire/flame retardant properties by adding a substance in the matrix of the composite to reduce the hazard.
- **Carpet**: aircraft carpets are currently mainly made from nylon[11]. Technically nylon is fairly easy to recycle, economically however it can be quite difficult. Nylon is used in several other industries as well, such as fishing nets or sportswear. Due to the growing concern of recycling, it is expected that the recycling techniques concerning nylon will become significantly better, and cost effective, in the coming years.

6.6. Recyclate Resale Value

Since the difficulty with regards to material recyclability is related to the market and economic opportunity rather than the technological feasibility, an assessment of the recyclate resale value is presented based on work by Hagnell and Åkermo [55].

The model estimates the recyclate value RV_i at each recycling cycle i based on the following inputs: material value in previous recycling step RV_{i-1}, retained mechanical performance m_p, percentage of reclaimed recyclate yield r_p, and recycling processing cost P. For $i = 1$, the virgin material cost RV_0 is used. The relation is given by equation 6.1. The virgin material cost RV_0 is obtained from the raw material cost plus the production energy costs required to process these materials into a product. The recycling cost P cannot be obtained directly for some processes. In these cases, recycling energy E_r in MWh/kg is used in combination with the energy cost of a renewable energy source such as onshore wind energy which is assumed to be 41 USD/MWh [12]. A disposal cost of 0.4 USD/kg [13] is also added to take into account the transportation costs. Thus, P is obtained from equation 6.2.

$$RV_i = m_p r_p RV_{i-1} - P \qquad (6.1) \qquad\qquad P = 41 \cdot E_r + 0.4 \qquad (6.2)$$

The raw material costs of aluminum are assumed to be 3.5 USD/kg [56]. The values for CFRP show large variability, a mean value of 66.09 USD/kg is obtained from different sources [5] [44] [57]. If values of approximate relative material cost are used [58], the cost of a carbon-epoxy is estimated to be 63 USD/kg, 4.7% lower than the mean value. Taking a lower value for the calculation of resale value is a safer approach, so the relative material cost method is used.

For metal alloys, it is assumed the retained mechanical performance m_p is 1 and the reclaimed recyclate r_p is 0.95 to account for the added difficulty of separating the elements. For maraging steel specifically,

---

[7] https://www.azom.com/article.aspx?ArticleID=12107 (accessed 15-06-2020)

[8] https://www.spectra-ip.com/aircraft-products/aircraft-fabric/aircraft-upholstery-fabrics/ (accessed 15-06-2020)

[9] http://www.eco-compass.eu/ (accessed 15-06-2020)

[10] https://www.csir.co.za/ (accessed 15-06-2020)

[11] https://www.spectra-ip.com/ (accessed 21-06-2020)

[12] https://www.lazard.com/perspective/lcoe2019/ (accessed 01-06-2020)

[13] Interview with the chief executive officer of AELS, D. van Heerden (10-06-2020)

the cost is based on the current market price for steel[14] and a quotation at IndiaMart[15] and the recycling energy is assumed to be 30 times higher than for conventional steels to account for difficulties in recycling. For GLARE, a weighted average of the S-glass fibers and Aluminum 2024-T3 values is used assuming a ratio of 85:15, as this gives a virgin material cost close to 17.5 USD/kg as obtained from the relative material costs [58]. Values of S-glass fibers are for mechanical recycling. For carbon/epoxy composites, values are approximated for recycling via pyrolysis. The same values are assumed for recycling of aramid/epoxy composites. The inputs used for the analysis are shown in table 6.1 and the results are illustrated in figure 6.3.

Table 6.1: Inputs of resale value analysis.

Material	Aluminum 2024-T3	Carbon/ Epoxy	S-Glass fibers	GLARE	Maraging Steel	Titanium alloy	Aramid/ Epoxy
Relative material cost [-]	1 [58]	18 [58]	-	5 [58]	-	12 [58]	2 [58]
Material cost [USD/kg]	3.5 [38]	63 [16] [58]	-	17.5 [58]	-	42 [58]	7 [58]
Production energy [kWh/kg]	51.7 [38]	11.1 [49]	-	-	-	186.1 [47]	64.9 [59]
Virgin material cost RV_0 [USD/kg]	5.62	63.46	20	17.84	46.06 [14] [15]	49.63	9.66
Retained mechanical performance m_p [-]	1	0.88 [46]	1 [55]	1	1	1	0.88 [46]
Reclaimed recyclate r_p [-]	0.95	0.6 [60]	0.72 [55]	0.7545	0.95	0.95	0.6 [60]
Recycling energy E_r [kWh/kg]	4.17 [38]	8.33 [61]	-	-	83.33 [47]	70.83 [47]	8.33 [61]
Recycling cost P [USD/kg]	0.5708	0.7415	0.7 [55]	0.6806	3.8167	3.3042	0.7415
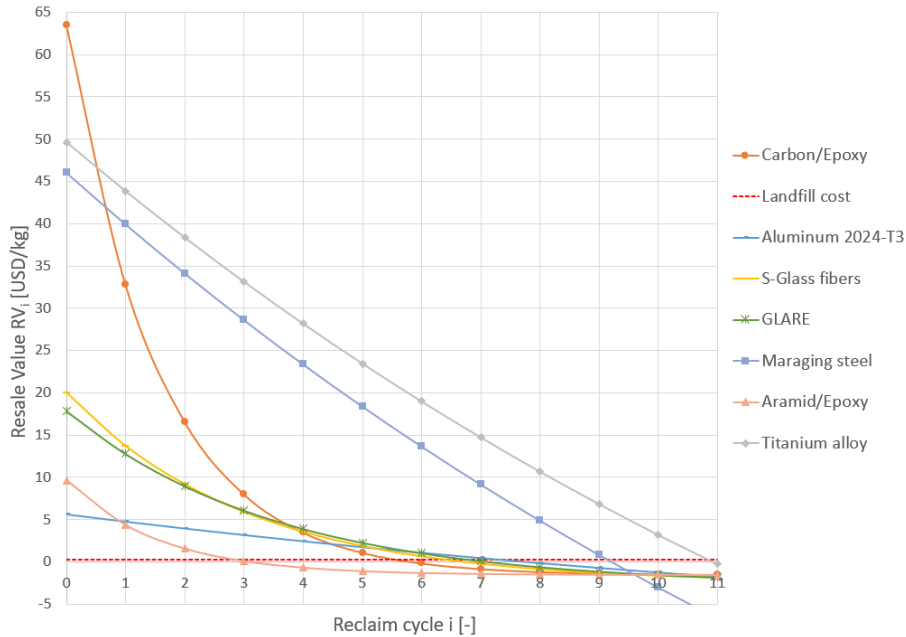
Figure 6.3: Resale value against number of recycling cycles for different materials.

Figure 6.3 shows that all materials have a higher resale value than the cost to landfill, which is assumed to be 0.25 USD/kg for all materials [46]. Furthermore, the analysis shows all materials have a higher resale value than the landfill cost for at least 5 reclaim cycles. This shows an increased market opportunity for recycling. The exception to this rule is aramid/epoxy composite which can only be reclaimed for 2 cycles.

Validation of these results is complicated due to the variability of material pricing due to supply and demand. This analysis aims to be a first order estimate of the value of recycled materials. However, it

[14]https://worldsteelprices.com/ (accessed 15-6-2020)

[15]https://dir.indiamart.com/impcat/maraging-steel.html (accessed 15-06-2020)

[16]Please note the large variability in CFRP costs depending on the final product (lay-up, complexity, fiber and resin choice).

is believed that the the net profit for recycled CFRP via pyrolysis is 5 USD/kg [47], 84% lower than the estimated recyclate value after one reclaim cycle. This discrepancy comes from the fact that the intrinsic material value does not scale directly with profit. Further analysis of this relation is required to prove that profit can be obtained from material recycling.

6.7. Trade-off on Primary Structure Materials

As discussed in section 6.4 the selection of materials depends on how well a material is able to resist against meteorological phenomena such as corrosion and lightning strikes. Furthermore, special attention is given to the feasibility of the recycling process. This is done by investigating the resale value after one recycling cycle and determining the TRL of the process itself. In order to understand how well a material performs on these criteria it is necessary to perform a trade-off. The material scores of this trade-off are used in chapter 10 as a basis for determining which material can best be used for the wing and fuselage, where the weight and cost of each component is also considered. In this way, the material properties and cost are included in the final material decision for the structure. The sensitivity of this trade-off is assessed in section 10.8.

The trade-off has a total of four criteria; resistance against lightning, resistance against corrosion, post-recycling value of a material and the TRL of a current recycling process. Since aspects of recyclability is of main importance within this project an overall weight of 75% is assigned to these criteria: 40% for the post-recycling value and 35% for the TRL of the recycling process. The weight for post-recycling is higher since an economically feasible product is more important than the TRL of a recycling process. The other 25% is distributed over the resistance against lightning (10%) and corrosion (15%) where the former is easier prevented than the latter [62].

The materials are given scores according to the following scale for lightning and corrosion resistance; 1: very bad, 2: bad, 3: satisfactory, 4: good, 5: excellent. The post-recycling value is measured in terms of RV_1/RV_0 as obtained from subsection 6.6 to account for the reduction in value after recycling. The scores are as follows; 1: 0-20%, 2: 21-40%, 3: 41-60%, 4: 61-80% and 5: 81-100%. Aluminum is given a 5 with 85%, T800S a 3 with 52% and GLARE a 4 with 72%. The TRL values assumed for the recycling methods are discussed in section 6.4 and scaled in a similar way; 1: TRL 1-2, 2: TRL 3-4, 3: TRL 5-6, 4: TRL 7-8, 5: TRL 9. The scores are multiplied by the weights and added to find a score out of 5.

Table 6.2: Material trade-off for primary structural components.

Criteria	Weight	Al 2024-T3	T800S	GLARE
Lightning resistance	0.10	5	2	4
Corrosion resistance	0.15	1	5	3
Post-recycling value	0.40	5	3	4
Recycling TRL	0.35	5	4	2
	Total	4.4	3.55	3.15
	Rank	1	2	3

6.8. Material Selection Overview

An overview of materials and corresponding EOL solutions for main aircraft parts is given in table 6.3.

Table 6.3: Complete overview of selected materials for aircraft components and its EOL solution.

Aircraft part	Material choice	EOL solution
Fuselage skin, Wing skin	Aluminium, CFRP, GLARE	Recycling/downcycling
Frames, Stiffeners, Ribs	Aluminium, CFRP	Recycling/downcycling
Fasteners	Aluminium, steel	Recycling
Windows	Plexiglass	Downcycling [6]
Overhead bins	Flax/ramie	Incineration
Seats	Flax/polyurethane foam	Polyurethane foam reused in other industries, flax incinerated
Floor	CFRP	Downcycling
Cables	Copper	Recycling [5]
Paint	Chrome-free paint and primer [7]	Incineration
Flaps and slats	Aluminum, CFRP	Recertify and reuse [17]
Engines	PW1700G/CF34-10A models	Recertify and reuse [4]
Landing gear	Steel	Recertify and reuse [4]
Avionics, APU, Electronics	-	Recertify and reuse [4][5]

---

[17] Interview with the chief executive officer of AELS, D. van Heerden (10-06-2020)

Propulsion and Flight Performance

One of the main objectives of the WeFlyCycle project is designing an aircraft that utilizes propulsion principles greener than fossil fuel. Therefore, extensive research has been conducted on different sustainable fuel options in the Midterm Report [3] regarding technical and economical feasibility. A hybrid propulsion system was proposed that consists of four turbofan engines which are mounted under the wing. Two out of four engines operate on biokerosene and the other two on gaseous hydrogen. As briefly discussed in section 5.2, there are two variants for the propulsion system design: SHOTS-1 has four PW1700G high-bypass ratio engines whereas SHOTS-2 has two PW1700G engines and two CF34-10A engines that have a lower bypass ratio and higher specific fuel consumption. As the propulsion principle of burning biokerosene is similar to that of burning kerosene, the main focus of the engine design is on how conventional turbofan engines can be modified such that they can operate on gaseous hydrogen.

This chapter presents the propulsion system characteristics and the performance of the aircraft. First, a functional analysis is performed in section 7.1 to identify the main functions that the propulsion system needs to fulfill, followed by the formulation of subsystem requirements in section 7.2. Section 7.3 discusses the main assumptions used to compute the characteristics of the propulsion system and to perform the performance analysis. Section 7.4 presents the propulsion system characteristics which include the engine selection, the type of APU, modifications on the combustion chamber for burning hydrogen, the implementation of a heat exchanger, estimation of engine size and positioning. Section 7.5 presents the performance analysis regarding range, takeoff, climb, and landing performance, load factor, as well as noise performance and gas emissions. As sustainability is an important aspect, section 7.6 presents the discussion about the sustainability of the propulsion system. Finally, section 7.7 presents the verification procedures and results of the calculations that were performed to determine the propulsion system characteristics in section 7.4 and performance analysis in section 7.5.

7.1. Functional Analysis

It is essential to understand the functions a propulsion system has to fulfill before designing it. Hence, a functional flow diagram that specifically demonstrates the functions that the propulsion system has to fulfill is shown in figure 7.1.
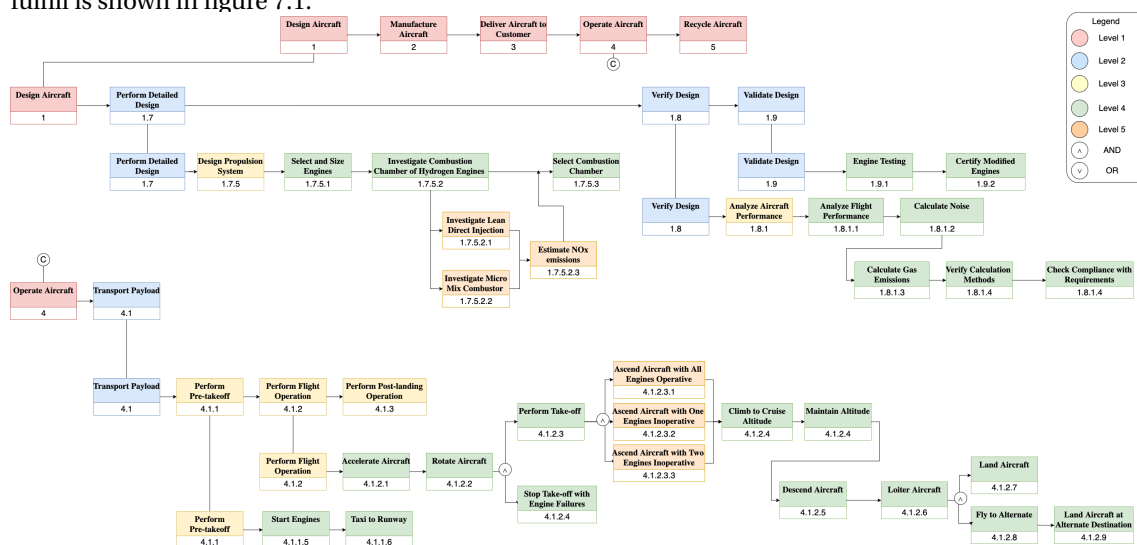

Figure 7.1: Functional analysis of the propulsion system.

The main focus at this stage is to design the propulsion system according to the stages in the "Perform Detailed Design" blocks in figure 7.1 and verify the design by analysing the aircraft performance. The main function of the propulsion system is to provide sufficient thrust to transport the passengers for a minimum distance of 4000 km. This range includes all phases during flight such as takeoff, climb, cruise, descent, loitering to reach alternate destination, and final landing.

7.2. Requirements Analysis

In order to analyze the flight performance of each concept, the requirements that the aircraft should fulfill need to be evaluated first. The main system requirements in section 3.1 that drive the design of the propulsion system are **WFC-USER-SUS-05**, **WFC-USER-PERF-01.1**, **WFC-USER-PERF-02.1**, **WFC-PERF-02**, **WFC-PERF-06**, **WFC-PERF-07**, **WFC-OP-02**, **WFC-SF-04** and **WFC-USER-COST-01**.

Besides the ones listed in section 3.1, some other important system requirements regarding the propulsion system which were defined in the Baseline Report [2] and Midterm Report [3] are listed below:

- ***WFC-SF-03****: The aircraft shall use a propulsion technology with a TRL of at least 6, as defined by European Union (EU) [23].* This aims to ensure low risk and cost. Because of this requirement, it was opted to select existing engines that have been manufactured and implemented on current commercial aircraft.
- ***WFC-PERF-09****: The aircraft shall be able to achieve a glide angle of at least 5.5 degrees.* This requirement ensures competitiveness with Airbus A220.
- ***WFC-USER-SF-01.2****: The landing climb gradient shall be at least 2.1 % for 2 engines, 2.4 % for 3 engines, and 2.7 % for 4 engines with one engine inoperative (OEI) at maximum landing weight (MLW) at 1.5 stall approach speed.* The requirement stems from the most critical climbing scenario of EASA CS25 regulations regarding climb performance in section 25.119 to 25.121 [22] [63].

Furthermore, by analysing these system requirements, the following subsystem requirements have been identified to ensure competitiveness with Embraer E195-E2 and Airbus A220-100:

- ***WFC-PROP-01****: The aircraft shall be able to reach a rate of climb of 17.8 m/s at sea level at MTOW.*
- ***WFC-PROP-02****: The aircraft shall have a stall speed of no more than 190 km/hr at takeoff at MTOW.*
- ***WFC-PROP-03****: The takeoff and landing runway field length of the aircraft shall be no more than 1,500 m at sea level at MTOW.*
- ***WFC-PROP-04:*** *The wing-mounted engines shall be placed in a position such that ground clearance is guaranteed to accommodate downward wing bending at landing with or without roll due to gust wind.* This requirement ensures sufficient ground clearance from the integration of the engines with the wing
- ***WFC-PROP-05:*** *The unit cost of the engines shall be no more than $48 million.* This requirement stems from the unit cost requirement **WFC-USER-COST-01**. This is to ensure the cost of selected engines is under the cost budget specified in section 4.1.1 to meet this requirement.

7.3. Main Assumptions

During the detailed conceptual design, several assumptions have been made for the computations of propulsion system characteristics. These include the required thrust and the flight performance analysis including the range calculation. The effects of these assumptions are discussed as well:

- SFC is assumed to be constant throughout the cruise phase. This is the main assumption of the Breguet range equation. In reality, SFC varies during flight, which will result in deviations of the calculated range value from the actual range the aircraft is able to achieve.
- The aircraft is flying at an altitude of 11,000 m during cruise. This is based on the cruise altitude of similar aircraft, such as the Airbus A220 and the maximum Mach number is defined at this altitude[1]. By applying this assumption, the aircraft is sized to fly at a cruise altitude which is 23.5% higher than the requirement of 8,900 m that was specified in **WFC-PERF-02**.
- During the computation of the takeoff field length, it is assumed that the aircraft takes off at MTOW. In reality, at takeoff, some fuel has already been used for warm-up and taxiing and hence, the aircraft weight is slightly smaller than MTOW. This leads to an overestimation of the takeoff field length. However, the used fuel weight is negligible compared to the magnitude of the overall

---

[1]`https://www.aerospace-technology.com/projects/airbus-a220-100-jetliner/` (accessed 20-05-2020)

aircraft weight; hence, the difference is considered insignificant.

7.4. Propulsion System Characteristics

This section presents the main propulsion system characteristics. First, section 7.4.1 presents the engine selection and a brief discussion of the APU used. Then, the modifications of the combustion chamber are discussed in section 7.4.2 such that the engine can burn gaseous hydrogen while emitting a low amount of nitrogen oxides (NO_x). Third, the implementation of the heat exchanger within the engine is discussed in subsection 7.4.3. Finally, subsections 7.4.4 and 7.4.5 present the estimation of the engine dimensions and the engine positions with regards to the wing.

7.4.1. Engine selection and design

As mentioned in section 5.2, a number of high-thrust turbofan engines with similar thrust levels, SFC, and weight have been looked into to select the suitable ones for the SHOTS aircraft. The main characteristics of the engines considered are listed in table 7.1. As the unit cost requirement **WFC-USER-COST-01** is one of the driving requirements and the considered engines have similar performance characteristics in terms of SFC, takeoff thrust and bypass ratio, the unit cost and operational cost of the considered engines are compared to select the most cost-effective engine models for the SHOTS aircraft. Note that the unit costs listed in table 7.1 do not account for the cost required to modify them into engines that can burn hydrogen. However, assuming that the cost for the modification is the same for all of these engine models, these unit costs are considered sufficiently accurate for the comparison.

Table 7.1: Engine characteristics of four different engines.[2] [3] [4] [64] [65] [66]

Engine characteristic	PW1700G	CF34-10A	RR Pearl 700	PW800
Takeoff Thrust [kN]	85.4	78.5	67.8	71.2
SFC [lb/(lbf h)]	0.52	0.65	0.57[5]	-
Dry weight [kg]	1,724	1,678	1,828.8	1,422.3
Bypass ratio [-]	9	5	6.5	5.5
Unit cost [million USD]	12	7.3	7	-

From table 7.1, one can see that the specific fuel consumption (SFC) of the PW1700G is the lowest which is desirable as it means that lower mass fuel flow is needed to generate the same thrust; however, its unit cost is very high compared to the other engines making it a very expensive option. CF34-10A has a lower unit cost and weight; however, its SFC is very high compared to the other 3 engines in table 7.1 which greatly impacts the operational costs of the aircraft. Moreover, RR Pearl 700 has a better SFC compared to CF34 10-A; however it is a heavier engine compared to the rest of the options. Finally, PW800 is the lightest engine; however, no information is provided regarding the SFC or the unit cost by the manufacturers. Hence, PW800 is not taken into account.

After analyzing each engine model, the engine cost, operational fuel cost and weight of six different engine configurations which consist of the aforementioned engine models are determined and the results can be found in table 7.2.

Table 7.2: Capital costs and life-time operating costs for engines.

Engine configurations	Option 1 4 × PW1700G	Option 2 4 × CF34-10A	Option 3 4 × RR Pearl 700	Option 4 2 ×PW1700G 2 × CF34-10A	Option 5 2 ×PW1700G 2 ×RR PEARL	Option 6 2 ×RR PEARL 2 × CF34-10A
Engine cost [million USD]	48	29.2	28	38.6	38	28.6
Fuel cost [million USD]	339	417	372	380	357	396
Dry weight [kg]	6,896	6,712	7,315	6,804	7,106	7,014

From the table, option 1 is clearly the best option with respect to operational cost. However, it comes with higher capital costs. This can increase the unit price of the complete aircraft to be more than 105% limit set by the customer. There is a significant drop in the engine cost for option 2 compared to option 1. Furthermore, the dry weight is lower as well. However, this benefit will be offset by an increase in the fuel weight, which will result in a heavier hydrogen tank and higher operating costs. Moving on to

---

[2] https://www.mtu.de/engines/commercial-aircraft-engines/narrowbody-and-regional-jets/gtf-engine-family/ (accessed 03-06-2020)

[3] https://aviationweek.com/business-aviation/gulfstream-unveils-new-g700-flagship-nbaa-bace (accessed 03-06-2020)

[4] http://www.deagel.com/Propulsion-Systems/BR715_a001711002.aspx (accessed 03-06-2020)

[5] Please note that this is a calculated value based on the percentage improvement compared to the previous generation of this engine [67].

option 3, it has the lowest engine cost, but it is also the heaviest option. Due to the increase in the engine weight, more hydrogen is required which also increases the tank mass.

Apart from using the engine model for all 4 engines, a mixed selection of 2 engine models have also been considered. Option 4 has two PW1700G and two CF34-10A engines and it has a lower engine cost at the expense of higher operating cost. Since PW1700G has the lowest SFC which means lower fuel weight and tank weight, it is best used for burning the hydrogen fuel. The next option explored, option 5, consists of two PW1700G engines with two RR Pearl engines. This option performs better when compared to option 4 in both the operating costs and engine costs. However, practically speaking, this configuration is not possible since the engines have a very high thrust difference. In order to provide same thrust PW1700G will have to be kept at thrust setting a lot lower than optimal which makes it inefficient [68]. This will hence increase the required hydrogen tank mass, further affecting the fuel costs and also the unit price of the aircraft. Finally, option 6 consists of two CF34-10A engines and two RR pearl engines. It has low engine costs, but the operating costs are very high. Furthermore, since RR Pearl will use the hydrogen fuel, the tank mass will increase as well which further increasing the aircraft mass.

Overall, two configurations have been chosen which are option 1 and option 4 in table 7.2. Even though option 1 has the highest engine cost, its fuel cost over the lifetime of the aircraft (30 years) is significantly lower. Option 4 has been chosen in case the customer is keen on maintaining the unit cost requirement as it is cheaper in terms of engine cost. The design with engine configuration option 1 is called SHOTS-1 and the one with option 4 is called SHOTS-2 as shown in table 7.3. Both options meet the requirement **WFC-PROP-05**.

Table 7.3: Engine models and takeoff thrust of the 2 design options: SHOTS-1 and SHOTS-2

	SHOTS-1	**SHOTS-2**
Engine configurations	4 × PW1700G (2 burns biokerosene and 2 burns hydrogen)	2 × CF34-10A (burns biokerosene) 2 × PW1700G (burns hydrogen)
Maximum takeoff thrust [kN]	341.6	327.8

To check whether the thrust generated by the chosen engine configuration meet the cruise speed requirement **WFC-PERF-06**, the rate of climb requirement **WFC-PROP-01**, the stall speed requirement **WFC-PROP-02**, the field lengths requirement **WFC-PROP-03** and the EASA landing climb gradient requirement **WFC-USER-SF-01.2** as discussed in section 7.2, a thrust-wing loading diagram has been constructed by using Roskam [63]. The thrust-wing loading diagram and the obtained results can be been in figure 7.2 and table 7.4 respectively. As seen in figure 7.2, the reason for the difference in the wing loading and thrust loading of the two designs SHOTS-1 and SHOTS-2 which are indicated as the green and red stars in the figure is due to the landing distance requirement. By comparing the required take-off thrust in table 7.4 and the maximum takeoff thrust in table 7.3, one can see that both SHOTS-1 and SHOTS-2 can produce higher thrust than the required thrust by a significant amount.

Table 7.4: Thrust-wing loading results.

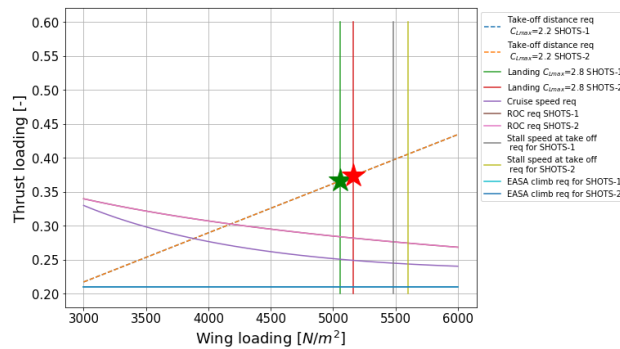| Parameter	SHOTS-1	SHOTS-2	Unit
Wing loading at takeoff	5,074.7	5166.1	N/m^2
Required thrust at takeoff	247.0	258.6	kN

Figure 7.2: Thrust-wing loading diagram of the SHOTS aircraft.

Besides the engines, an additional power source is required on-board of the aircraft to perform functions such as ground operations[69]. The power source is an APU and the one that is selected is a Honeywell 131-9A. It is connected to the biokerosene tank such that it can function properly.

7.4.2. Modification of combustion chamber

As discussed in section 5.2, one of the selected engines is PW1700G. This engine is a high-bypass ratio turbofan engine with a low SFC. As this engine originally uses kerosene as a fuel source, some design changes are required such that it can operate on gaseous hydrogen. One of the advantages of using biokerosene is that no changes need to be made to the engines that rely on it as a fuel source.

To accommodate the combustion of hydrogen, the conventional combustion chamber needs to be modified such that the hydrogen can burn efficiently as the properties of hydrogen are different from kerosene. Moreover, it should also ensure that the flame of the fuel is stable; hence, it should neither be too rich nor too lean. Compared to kerosene, hydrogen has the ability to burn leaner which means lower temperatures in the engine and also less fuel consumption. However, it is essential that the mixing intensity is increased such that the fuel is mixed properly and no local hot spots can be formed [70]. Furthermore, burning hydrogen in conventional combustors has an additional challenge which is the higher risk of flashback since its reaction rate is seven times higher compared to kerosene. There are two types of combustors that can be used for hydrogen combustion:the Lean Direct Injectors (LDI) and Micro-Mix combustors (MMX). Both these options have a TRL of 7 hence meeting the TRL requirement **WFC-SF-03** of at least 6 [71]. Due to requirement **WFC-SUS-02** it is necessary to reduce the harmful emissions. Therefore, the criterion for choosing between these two combustors depends on the amount of NO_x that each of these combustors emits.

First, the LDI combustors are analysed. The LDI combustors have five different configurations which can affect the performance of these combustors. All these combustors are safe to use since no flashback or auto-ignition occurs. Figure 7.3 shows how the combustor functions. The hydrogen and hot air passes through the combustors as it ignites them.
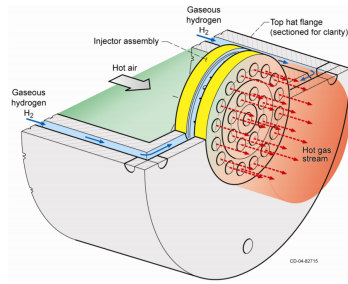
Figure 7.3: Combustor functioning [72].
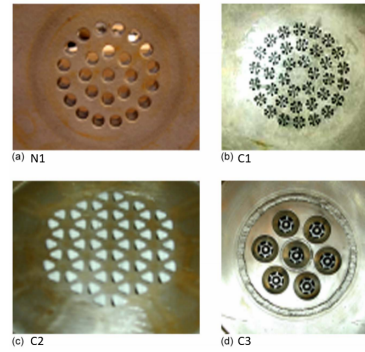
Figure 7.4: Different configurations of LDI combustors [72].

Figure 7.4 shows the design of different configurations that can be used as combustor. The first configuration is called the N1 injector. It contains 25 holes through which air can pass and 2 holes for hydrogen placed 180 degrees apart. The next one is configuration C1 which has 8 angled air holes surrounding each hydrogen hole. Figure 7.4c presents configuration C2 which is similar to N1, however, instead of circular holes it has triangular ones. Next is the configuration C3 which has a hydrogen nozzle at the center of each of the holes. Finally, configuration C4 which is not shown in figure 7.4 is a modification of C3 with the center hole replaced by small hydrogen jets.

The emissions of all the configurations are affected by some parameters. These parameters are the equivalence ratio ϕ, residence time τ, the combustor inlet temperature T_3, and the combustor inlet pressure P_3. Equation 7.1 shows how each of these parameters affects the NO_x emissions[72]. There are some other coefficients in this equation 7.1 which are specific to each configuration. These coefficients are A, a, b, c, d and e and are there to best fit the results which were found by NASA during the testing of the LDIs [72]. Hence, they do not have any physical meaning. These values are shown in the table 7.5. Note that the pressure loss $\Delta P/P$ is also different for each configuration since each configuration has different hole sizes, hence they are also shown in table 7.5.

$$ppm_{NO_x} = A(143P_3)^a (\phi_{H_2})^b (\tau)^c \exp\left(\frac{1.8T_3 - 460}{d}\right)\left(\frac{\Delta P}{P}\right)^e \tag{7.1}$$

Table 7.5: Coefficients for each configuration [72]

Configuration	A	a	b	c	d	e	P/P %
NASA N1	8.05E-06	2.98	1.15	0.579	645	0.658	4
C1	8.638	0	1.95	0.337	-794	1.45	12
C2	0.137	2.37	1.86	0.532	-127	0.496	4
C3	101	0	2.99	0.439	547	0.165	20
C4	9.355	0.275	4.12	0.455	211	-0.288	25

To use the equation 7.1 all the unknown parameters are calculated which is further discussed in this section. The equivalence ratio is the ratio between the actual air to fuel ratio and the stoichiometric air to fuel ratio for combustion[73]. It depends on the combustor inlet temperature and the outlet temperature. The equivalence ratio can be obtained by applying equation 7.2, where T_3 is the inlet temperature of the combustor and T_4 is the outlet temperature of the combustor.

$$\phi_{H_2} = 1.4 \cdot 10^{-4} \cdot (T_4 - T_3)^{1.157} \tag{7.2}$$

The residence time is the amount of time the gases stay in the combustion chamber[74]. Currently the residence times range between 10-20 milliseconds[75]. For the NO_x analysis, the worst case scenario is taken hence a residence time value of 20 milliseconds is used.

To obtain the inlet combustor pressure and temperature an ideal turbofan calculator[6] is used. The word ideal here indicates the combustion process is assumed to be ideal ,hence no heat is lost to the environment and there is no energy loss due to the friction of air with the engine surface[7]. For this stage in anlysis it is assumed that the affect on calculations due to these assumptions is negligible. The parameters required to calculate the combustor inlet temperature and pressure are the cruise mach number, ambient temperature, ambient pressure and the overall pressure ratio. The overall pressure ratio used is 45 [76], the Mach number is 0.79, ambient temperature used is 216 K and the ambient pressure is 22,632 Pa. Using these values, the combustion chamber inlet temperature is found to be 754 K whereas the inlet pressure is 1.5 MPa. Furthermore, the outlet temperature of the combustor during cruise for high bypass turbofan engines running on kerosene is 1,675 K [77]. However, hydrogen can provide the same amount of power at a lower temperature. Hence, this outlet temperature cannot be used. This is because the produced gases, when burning hydrogen, have a higher specific heat capacity (c_p) [J/kgK] value than the ones that are produced when burning kerosene. Figure 7.5 shows how c_p varies for different temperatures and the equation 7.3 shows how the output power of the turbine is affected by c_p and the the outlet temperature of the combustor (same as the inlet temperature of turbine). However, figure 7.5 does not show the c_p value at 1650 K. Therefore, the value for 1600 K is used, giving the c_p for kerosene at combustion chamber outlet to be 1,220 J/kgK. Finding the temperature for hydrogen is, however, not as straightforward and is further discussed.
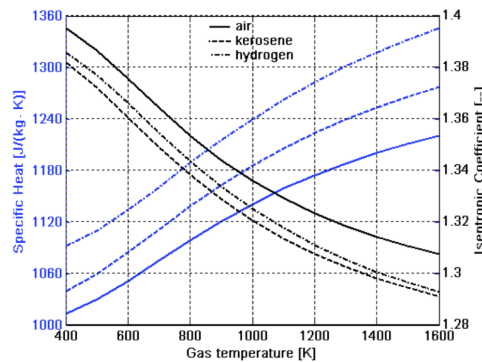
Figure 7.5: Specific heat and isentropic coefficient variation of air, kerosene and hydrogen with temperature.[78]

As mentioned before, hydrogen can deliver the same amount of power as kerosene at a lower operating temperature due to a change in specific heat. This effect can be analyzed by the use of equation 7.3[78].

$$P_{turb} = (\dot{m}_a + \dot{m}_f) \cdot c_p \cdot (T_{in} - T_{out}) \tag{7.3}$$

---

[6] https://www.particleincell.com/2014/turbofan-calculator/ (accessed 09-06-2020)

[7] http://www.ecourses.ou.edu/cgi-bin/ebook.cgi?topic=th&chap_sec=10.1&page=theory acessed 26-06-20

In the equation 7.3 the T_{in} and T_{out} denote the inlet and outlet temperature of the turbine and $\dot{m}_a$ and $\dot{m}_f$ are the mass flow rate of air and fuel respectively. Since the power produced by the turbine should stay the same, P_{turb} is kept constant. The turbine outlet temperature is calculated using the ideal turbofan calculator giving a value of 1160 K[8]. Moreover, the mass flow rate of air and the turbine outlet temperature is also kept constant. The mass flow rate of fuel is so small that changing it has negligible affect, therefore, it is ignored. Hence, there are only two variables left in equation 7.3. For air as mentioned, the turbine inlet temperature is 1675 K and c_p is 1220 J/kgK. Since the values of c_p is depending on temperature, the values are found by trial and error. By combining figure 7.5, the assumptions made and taking into account c_p and turbine inlet temperature of air, it is finally found that the c_p of hydrogen is 1335 J/kgK and the turbine inlet temperature is 1575 K.

Once the combustor outlet temperature (same as turbine inlet temperature) is calculated to be 1575 K, it can be used to find the equivalence ratio using equation 7.2 and the obtained inlet temperature of the combustor which is 754 K. Now all the input parameters are known for equation 7.1 and the NO_x emissions can be computed for all the configurations. However, these emissions are found in parts per million which are hard to compare when the emissions are compared with other reference aircraft. Therefore, it is important to convert it into emission index. Parts per million (ppm) is converted into emission index (EI_x) by applying equation 7.4.

$$EI_x = \frac{m_x}{m_e} \frac{1+f}{f} X \cdot 10^{-3} \tag{7.4}$$

In this equation, m_x is the molecular weight of nitrogen dioxide, m_e is the average molecular mass of the exhaust gas, f is the fuel to air ratio for hydrogen and X is the amount of NO_x emissions expressed in ppm. Since the exhaust gas of burning hydrogen is steam and nitrogen oxides, the average molecular mass of these gases is taken. In order to obtain the fuel to air ratio for hydrogen, equation 7.5 is used in combination with the acquired equivalence ratio.

$$f = 2.55 \cdot \phi_{H_2} \cdot 0.0292 \tag{7.5}$$

The results of this conversion, including the initial NO_x emissions in ppm, are presented in table 7.6 for the different combustor configurations.

Table 7.6: Produced NO_x emissions and the equivalent emission index for each configuration.

Configuration	NO_x [ppm]	$EINO_x$ [g/Kg]
NASA N1	1219.64	68.22
C1	36.80	2.06
C2	55.28	3.09
C3	140.76	7.87
C4	60.60	3.39

The second concept of hydrogen combustors is a Micro-Mix (MMX) combustor, which was investigated by Dahl and Suttrop [79]. They modified the kerosene gas turbine of an auxiliary power unit (APU) GTCP 36-300 into a hydrogen fueled one by applying MMX technology. As depicted by figure 7.6a, the main difference between a conventional combustor and a MMX combustor, in terms of configuration, is the addition of the ring segments near the exit of the combustion chamber. The MMX combustor utilizes the principle of miniaturized diffusion combustion to avoid the high temperature zones created by hydrogen combustion with large diffusive flames. The miniaturized diffusion combustion increases the number of local mixing zones between hydrogen and air compared to conventional combustors [79]. Miniaturized diffusion is done by having a large number of fuel/air injectors, as can be seen in figure 7.6b. The large number of fuel/air injectors allow heterogeneous mixing while taking a pressure loss of 3-4% into account, which results in numerous small diffusive flames. To enhance the mixing quality, the MMX combustor uses the fluid phenomenon of jet in-cross flow where the hydrogen is injected perpendicular to the flow of the air stream as shown in figure 7.6c [80]. As the emission of thermal NO_x is dependent on residence time of the flames, which proceeds at a significant rate at temperatures above 1850 K [81], the improved mixing quality decreases the emission by reducing the residence time at high temperatures and avoiding the formation of large, high-temperature diffusive flames.

---

[8]https://www.particleincell.com/2014/turbofan-calculator/ (accessed 09-06-2020)

(a) Conventional vs MMX combustors layout [82].

(b) Micro-Mix combustor prototype for APU GTCP 36-300 [83].

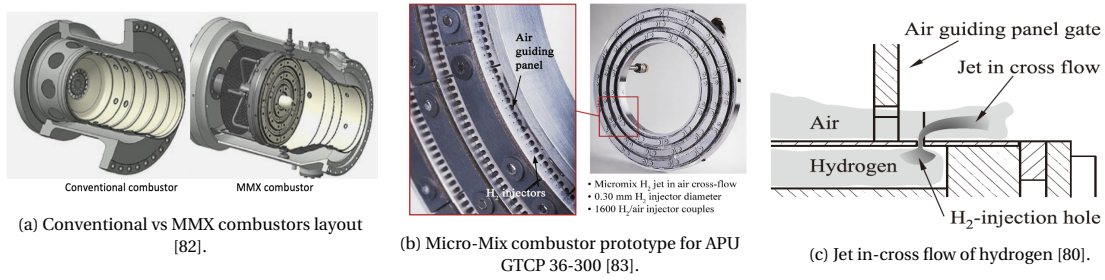(c) Jet in-cross flow of hydrogen [80].

Figure 7.6: Micro-mix combustor configuration.

Currently, the emissions of thermal NO_x from a MMX combustor have been computed from complex numerical simulation with STAR-CCM+ [9] software of CD-adapco and experimental data of MMX combustor integrated on specific gas turbines [80, 84, 85]. Such computations are outside of the scope of this DSE project; hence, to compute the NO_x emissions of a MMX combustor, a P_3-T_3 method is used [86]. Equation 7.6 shows that the P_3-T_3 method correlates sea level NO_x emission measurements and flight level measurements, based on the knowledge of the combustor operating environment at both altitudes [86], where $EINO_{x_{FL}}$ is the emission index at flight altitude, $P_{3_{FL}}$ is the inlet combustor pressure at the cruise altitude which is 1.5 MPa, $P_{3_{SL}}$ is the inlet pressure at sea level which 4.6 MPa, the exponent coefficients n and m are assumed to be 0.4 and 0 respectively since the engine-specific exponents are unknown, and finally, the fuel to air ratios at flight altitude and sea lvel (FAR_{FL} and FAR_{SL}) do not need to be computed as the exponent m equals to zero.

$$EINO_{x_{FL}} = EINO_{x_{SL}} \left(\frac{P_{3_F}}{P_{3_{SL}}} \right)^n \left(\frac{FAR_{FL}}{FAR_{SL}} \right)^m e^{19(h_{SL} - h_{FL})} \tag{7.6}$$

The ambient humidity is a function of altitude and the humidity at sea level h_{SL} is 6.344×10^{-5} kg H_2O per kg of dry air. It is found that at a cruise altitude of 11 km the ambient humidity is 2×10^{-5} kg H_2O per kg of dry air, with an ambient temperature of 216.65 K and a relative humidity of 15% [87] [10]. Since the combustor used in PW1700G is Talon X which was manufactured by Pratt and Whitney [88], it is used as the reference combustor in the calculation. The average value of NO_x emission index $EINO_{x_{SL}}$ of engines with Talon X is found from the ICAO emission databank [11].

Kyprianidis et al. [89] further derived a new, adaptable yet simple correlation that is sufficiently accurate to model the NO_x emissions of modern Rich-burn, Quick-quench, Lean-burn (RQL) combustors designed for advanced future cycles relative to current and future certification limits. Equation 7.7 can be used to estimate the NO_x emission index of turbofan engines with high overall pressure ratio with the default values of a = 8.4, b = 0.0209, c = 0.0082, d = 0.4, f = 19, P_3 = 3 MPa, ΔT_{ref} = 300 K, h = 6.344×10^{-5} kg H_2O per kg of dry air and TF = 0 for modern RQL combustor [89]. By using Kyprianidis et al.'s method and the conventional P3-T3 method, the $EINO_{x_{SL}}$ values of the MMX combustor at cruise condition are found and documented in table 7.7. Moreover, they can be converted to ppm by using equations 7.4 and 7.5. The values are shown in table 7.7.

$$EINO_x = (a + b \cdot e^{cT_3}) \left(\frac{P_3}{P_{3_{ref}}} \right)^d \left(\frac{\Delta T}{\Delta T_{ref}} \right)^{TF} e^{19(h_{SL} - h_{FL})} \tag{7.7}$$

Table 7.7: MMX NO_x emission results.

	P3-T3 method [86]	Kyprianidis et al. method [89]
$EINO_x$ [g/kg]	5.28	5.33
NO_x emission [ppm]	79.61	80.44

Tables 7.6 and 7.7 show the NO_x emissions for the LDI and MMX combustors respectively. It can be observed that configurations C1 and C2 perform the best in terms of emissions. However, they are not very durable[72] . Therefore, the next best configuration C4 is selected which emits slightly higher NO_x emissions but is durable since it does not fail at high temperatures.

7.4.3. Heat Exchanger

As evident by its name a heat exchanger is essentially used in an aircraft engine for heating up hydrogen before injection. Its point of action is on a temperature sensing device that influences alteration in fuel temperature[90]. This is done to improve the specific fuel consumption. There are three main positions where the heat exchanger can be integrated within the engine. One is that the heat exchanger can be placed on the main stream. The second possibility is that the heat exchanger can be placed right outside of the main stream. The third option is to place it right out of the engine where it is fed by an external aerodynamic stream [91]. For this engine, The first location was chosen since it calls for a small and light heat exchanger. More specifically, it was chosen to use a tube wrapped around the engine jet pipe. The added weight is less than 11 kg [92]. It should be noted that it was found in a study by Corchero, G. and Montañés, J. L the temperature of the engine should be 150-250 K in order to optimize the specific fuel consumption [91]. Although, in this design, the temperature of the stored gaseous hydrogen is 293 K and the inlet temperature is 754 K it was decided to still use a heat exchanger. The reasoning behind this is that the gas can expand in the pipes and its temperature can drop significantly. Therefore, to mitigate the risk of having very low temperature before combustion takes place, a heat exchanger is used. This risk was identified in section 13.3. A further modification on heat exchanger is recommended for the future phases.

7.4.4. Engine sizing

Since not all the dimensions of the engine are available from the manufacturer, a preliminary sizing was done using Jenkinson's method [8]. The results can be found in table 7.8, where W_a is the total airflow at see level, D_F is the fan diameter, μ is the bypass ratio, OPR stands for Overall Compression Ratio and M_{MO} is the maximum operating Mach number.

Table 7.8: Engine dimensions [8].

Parameter	Estimating relationship	PW1700G	CF34-10A	Unit
Intake highlight diameter (DIH)	$0.037W_a + 32.2$	1.93	1.58	[m]
Maximum height of main cowl (M_H)	$1.21D_F$	1.72	1.69	[m]
Main cowl length (LC)	$2.36D_F - 0.01(D_F M_{MO})^2$	2.82	2.78	[m]
Main cowl diameter at fan exit (DFO)	$(0.00036\mu W_a + 5.48)^2$	2.37	1.35	[m]
Gas generator cowl diameter at fan exit (DMG)	$(0.000475\mu W_a + 4.5)^2$	2.31	1.05	[m]
Gas generator cowl diameter at 'hot' nozzle exit (DJ)	$(18 + 55K)^{0.5}$, $K = (ln(\frac{1}{\mu+1})(\frac{W_a}{OPR}))^{2.2}$	0.21	0.24	[m]
Length of gas generator afterbody (LAB)	(DMG-DJ)0.23	0.48	0.18	[m]

The engine dimensions that are computed are further elaborated with figure 7.7.
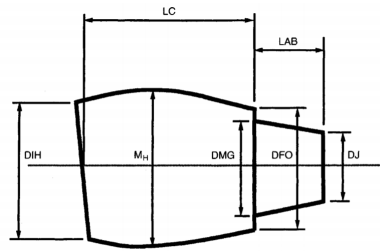
Figure 7.7: Engine design parameters [8].

7.4.5. Integration of the engine with the wing

The vertical position of the engine depends on the ground clearance requirements and aerodynamic interference between nacelle, pylon and the wing. To determine the longitudinal engine positioning under the wing a method from the Aerospace Design and System Engineering Elements 1 [93] was used. Based on the fact that the selected engines PW1700G and CF34-10A are long duct engines, $\frac{x_F}{c}$ is found to be around 0.13 with the use of figure 7.8a. Using equation 7.8, the longitudinal position H is found to be 0.21 m, which is visualized in figure 7.8b.

$$H/c = 0.07 + 0.03 cos\left[15\left(\frac{x_F}{c} + 0.03\right)\right] \tag{7.8}$$

(a) Engine positioning [93].

(b) Vertical position of the engine [93].

Figure 7.8: Longitudinal and vertical position of the engine.

Considering that the engine is installed as shown is figure 7.8b, an average of the dimensions DMG and DJ from table 7.8 is taken as the point of installation. Therefore, this gives for PW1700G a vertical position of 1.47 m and for CF34-10A a vertical position of 0.855 m. The reference point is as seen in figure 7.8 the point of installation on the wing for all measurements. Knowing that the main landing gear height is 3.1 m ,as is determined in section 8.6, this provides more than enough clearance to make sure that the engine does not hit the ground during operations and requirement **WFC-PROP-04** is met.

7.5. Performance Analysis

This section presents the performance analysis of the aircraft where subsection 7.5.1 presents the payload-range characteristics of the aircraft, subsection 7.5.2 presents the takeoff performance analysis, subsection 7.5.3 presents the discussion the rate of climb, subsection 7.5.4 discusses the landing performance, and subsection 7.5.5 presents the V-n load diagram. For the take-off performance, rate of climb and landing performance, three scenarios are considered: all engines operative (AEO), one engine inoperative (OEI), and two engines inoperative (TWI). Furthermore, the analyses of noise performance and gas emissions are also presented in subsections 7.5.6 and 7.5.7 respectively.

7.5.1. Payload-Range Diagrams

The payload range diagram of an aircraft shows the range of aircraft at maximum payload and after that how much it changes as the payload decreases. Equation 7.9 is used to find the range [63] and the cruise velocity is calculated by equation 7.10, where W_1 is the weight at the start of the mission phase, W_2 is the weight at the end of the phase, c_j is the specific fuel consumption, g is the gravitational acceleration, L/D_{cr} is the lift-to-drag ratio during cruise, M is the Mach number, γ is the specific heat ratio which is 1.4, R is gas constant of 287 $J/(K \cdot kg)$ and finally, and finally, T_e is the temperature at the flight altitude.

$$R = \frac{V}{g \cdot c_j} \cdot \left(\frac{L}{D}\right)_{cr} \cdot ln\frac{W_1}{W_2} \qquad (7.9) \qquad\qquad V = M \cdot a = M\sqrt{\gamma R T_e} \qquad (7.10)$$

The MTOW, OEW, payload and fuel weight, determined in section 5.3 by performing a class II weight estimation, are used to construct a payload range diagram as shown in figure 7.9.

(a) Payload-Range diagram for SHOTS-1

(b) Payload-Range diagram for SHOTS-2

Figure 7.9: Payload Range diagrams for SHOTS-1 and SHOTS-2

From figure 7.9a the range for SHOTS-1 with 120 passengers is 4,399 km and with 20 passengers it goes

up to 5,270 km. From figure 7.9b the range for option 2 with 120 passengers is 4,350 km and with 20 passengers it goes up to 5,241 km. Note that below 20 passengers the aircraft is does not have enough payload to be stable hence it can not take-off. So the maximum range occurs when at least 20 passengers are seated. More detail is provided in section 8.6.

7.5.2. Takeoff performance

The takeoff performance analysis consists of 3 segments: ground roll, transition to climb, and climb. During ground roll, the acceleration of the aircraft a is expressed as equation 7.11 [8],

$$a = \frac{dV}{dt} = \frac{T}{W} - \mu + \frac{1}{2}\rho V^2 \frac{S}{W}\left(C_L\mu - C_{D_0} - \frac{C_L^2}{\pi Ae}\right) \tag{7.11}$$

where T is the thrust, W is the aircraft wight, μ is the rolling frinction coefficient, ρ is the air density, V is the airspeed, S is the surface area, C_L is the lift coefficient, c_{D_0} is the zero lift coefficient, A is the aspect ratio, and e is the Oswald span efficiency factor. As the aircraft incidence will be constant during most of the ground run duration, C_L can be assumed to be constant and directly proportional to V^2. Hence, the following constants K_T and K_A are derived as shown in equations 7.13 and 7.12, where the takeoff thrust is examined to have a linear relation with velocity. Hence, during ground roll, the mean thrust T at a speed of 0.707 V is sufficiently accurate for the analysis [8].

$$K_T = \frac{T}{W} - \mu \qquad (7.12) \qquad\qquad K_A = 2\rho\left(C_L\mu - C_{D_0} - \frac{C_L^2}{\pi Ae}\right)\frac{W}{S} \qquad (7.13)$$

Using these constants and the relation that the lift-off velocity V_{LOF} equals to 1.1 times the stall speed at takeoff V_s, equation 7.11 is integrated between 0 and V_{LOF}, resulting in the derivation of equation 7.14.

$$s_g = \frac{1}{2gK_A}\ln\left(\frac{K_T + K_A V_{LOF}^2}{K_T}\right) \tag{7.14}$$

After the ground roll, the aircraft accelerates from V_{LOF} to the takeoff climb speed V_2. This is where the aircraft transitions from ground run to takeoff climb. The average speed during this transition to climb V_{TR} is given by $\frac{V_{LOF}+V_2}{2}$ where $V_2 = 1.2V_s$ and hence, $V_{TR}=1.15V_s$ [8]. Assuming the aircraft is flying along an arc, the radius of the arc R is calculated using equation 7.15 where the typical values for load factor n is 1.2 [8]. The climb gradient during the transition γ can be found using 7.16 assuming that there is zero acceleration. Consequently, the height h_T and ground distance s_T covered by the aircraft at the end of the transition can be calculated from equations 7.17 and 7.18 respectively.

$$R = \frac{V_{TR}^2}{g(n-1)} \quad (7.15) \qquad \gamma = \frac{T-D}{W} \quad (7.16) \qquad h_T = \frac{R\gamma^2}{2} \quad (7.17) \qquad s_T = R\gamma \quad (7.18)$$

According of EASA CS-25.113, the takeoff run on a dry runway is the distance between the start of the takeoff and the point where the aircraft reaches a screen height of 10.7 m (35 ft) above the takeoff surface at V_{LOF} velocity [22]. The screen height h_s may be exceeded during the transition. In that case, the ground distance covered by the aircraft s_s is defined by equation 7.19 [8].

$$s_s = \sqrt{(R+h_S)^2 - R^2} \tag{7.19}$$

At the end of the transition, the aircraft starts to climb away from the ground run as soon as its velocity reaches V_{LOF}. If the screen height has not been reached yet, the ground distance to the screen height at the end of the transition s_c can be calculated by equation 7.20, where s_c

$$s_c = \frac{h_s - h_T}{\tan(\gamma)} \tag{7.20}$$

The final takeoff field length is the sum of the aforementioned ground distances and this value is then factored by 1.15 to allow for pilot and operational variations according to CS25.113 regulation [22]. Since the maximum static thrust of the designed aircraft is quite high given the engine choices, it is found that only 44 % of the maximum static thrust setting for SHOTS-1 and 46 % for SHOTS-2 is required for the aircraft to take off at a field length of lower than 1500 m as specified by requirement **WFC-PROP-03**. Hence, the takeoff field length distance for these settings and the full takeoff climb thrust setting can be computed and found in table 7.9. The green color indicates that the takeoff field length requirement and

OEI second segment climb gradient are met whereas the orange color indicates that no requirements have been formulated.

In case of engine failures, the OEI scenario is first analyzed. After lift off, the takeoff climb begins and ends at 457 m (1500 ft) above the ground runway. For civil jet aircraft, the so called second-segment climb is more critical [8]. The second segment climb has landing gear up configuration at maximum takeoff thrust setting where a minimum climb gradient of 0.03 rad must be achieved at a velocity of $1.15V_s$ with OEI. Assume that the aircraft is climbing at a constant speed, the climb gradient is estimated by equation 7.16 where N is the number of working engines, T_{eng} is the maximum static thrust of each engine and the weight of the aircraft W is assumed to be MTOW.

$$\gamma = \frac{N \cdot T_{eng} - D}{W} \tag{7.21}$$

The total drag is a sum of the drag of the basic configuration and the asymmetric drag due to the failed engine which consists of the windmilling drag of the failed engine $C_{D_{failed}}$ and the additional trim drag $C_{D_{trimmed}}$ from the rudder/aileron required to counteract the asymmetric flight condition [8]. At preliminary design phase, the windmilling drag $C_{D_{failed}}$ can be estimated by equation 7.23 [8] where D_f is the fan diameter. For option 2, since PW1700G has a larger diameter and thrust, the most critical case would be the failure of one of these engines.

$$C_D = C_{D_{AEO}} + C_{D_{failed}} + C_{D_{trim}} = 1.05C_{D_{AEO}} + C_{D_{failed}} \tag{7.22} \qquad C_{D_{failed}} = \frac{0.3D_f}{S} \tag{7.23}$$

Moreover, since the aircraft uses dual fuels which is one of the main aspects that separates the aircraft design from conventional aircraft, it is important to assess the performance of the aircraft when one of the fuels cannot be used for safety concerns. In such cases, it would be considered as two engines inoperative scenarios as the inability to use one of the fuels means that two of the engines that are using this fuel cannot be used. Therefore, for SHOTS-1, the thrust will be half of the total thrust in the case of either one of the fuels cannot be used as all four engines are the same model and produce the same thrust whereas for design 2, the thrust level will depend on which fuel is accessible. If biokerosene is not accessible, the CF34-10A engines cannot be used and 52% of the total thrust in AEO scenario is available whereas if hydrogen is not accessible, then the PW1700G engines can not be used and 48 % of the total thrust in AEO scenario is available. Note that the results in table 7.9 are obtained for a takeoff climb thrust setting of 44% and 46% respectively for SHOTS-1 and SHOTS-2 as well as for a full takeoff climb thrust setting.

Table 7.9: Takeoff performance results.

Scenario	Parameter	SHOTS-1		SHOTS-2		Unit
For all scenarios	Takeoff thrust setting	44	100	46	100	[%]
AEO	Takeoff field length	1484.0	724.7	1495.7	753.8	[m]
OEI	Second segment climb gradient	0.075	0.249	0.071	0.234	[rad]
TEI: inaccessible biokerosene		0.019	0.141	0.027	0.143	[rad]
TEI: inaccessible hydrogen fuel		0.022	0.141	0.022	0.125	[rad]

Although the regulations for TEI scenarios have not been put in place yet, they may come about when the SHOTS aircraft enter into service due to safety concerns with using dual fuels. As seen in table 7.9, in TEI senarios with a thrust settings of 44% and 46% for SHOTS-1 and SHOTS-2 respectively, the second segment climb gradients are slightly below 0.03 rad (EASA CS25 regulation OEI requirement); however, they can be easily increased by increasing the thrust setting. Even under TEI situations, the lowest climb gradient is 0.125 rad for SHOTS-2 when PW1700G engines cannot operate where the climb gradient for SHOTS-1 is the same when the feed to either one of the fuels is lost as the engine models are the same.

7.5.3. Climb performance
Next, the climb performance is evaluated. The steady rate of climb of the aircraft at given altitude can be calculated by using equation 7.24 [94], where D is the drag force, P_a is the power available, and P_r is the required power. The thrust of the engines during climb reduces during the climb to the cruise altitude due to the effect of altitude and speed [95]. As the air density decreases with increasing altitude, the thrust will decrease and the thrust lapse which is the rate at which the thrust reduces will increase

slightly. The speed also influences the engines thrust. The effect of both factors can be computed by using equation 7.25 [95], where T is the current thrust level, λ is the bypass ratio and σ is the relative air density compared to sea level air density.

$$ROC_s = \frac{T-D}{W}V = \frac{P_a - P_r}{W} \tag{7.24}$$

$$\frac{T}{T_{max}} = K_1 + K_2\lambda + (K_3 + K_4\lambda)M\sigma^{0.7} \tag{7.25}$$

The constants K_1, K_2, K_3, and K_4 in equation 7.25 are different for different bypass ratio and Mach number. The constants in the first two rows of table 7.10 are used for the CF34-10A engines whereas the last two entries are used for the PW1700G engines. Note that the bypass ratio of engine PW1700G is 9 which is higher than 8 as listed in table 7.10, which might result in some inaccuracies. Using equations 7.24 and 7.25, figure 7.10a can be constructed for both design options to find the steady rate of climb at sea level. As seen in this figure, the power required is almost the same for both designs whereas the power available for SHOTS-2is slightly lower than for SHOTS-1 as the maximum takeoff thrust of SHOTS-2is lower. Dividing the difference between the power available and power required by the weight gives the steady rate of climb, which is plotted in figure 7.10b. One may notice a small kink in both figures 7.10a and 7.10b and this occurs due to the sudden change in the values of the constants listed in table 7.10 when the mach number reaches a Mach number of 0.4.

Table 7.10: Constants for equation 7.25 [95].

Bypass ratio	Mach number	K_1	K_2	K_3	K_4
3-6	0-0.4	1.0	0	-0.6	-0.04
3-6	0.4-0.9	0.88	-0.016	-0.30	0
8	0-0.4	1.0	0	-0.595	-0.03
8	0.4-0.9	0.89	-0.014	-0.30	0.005
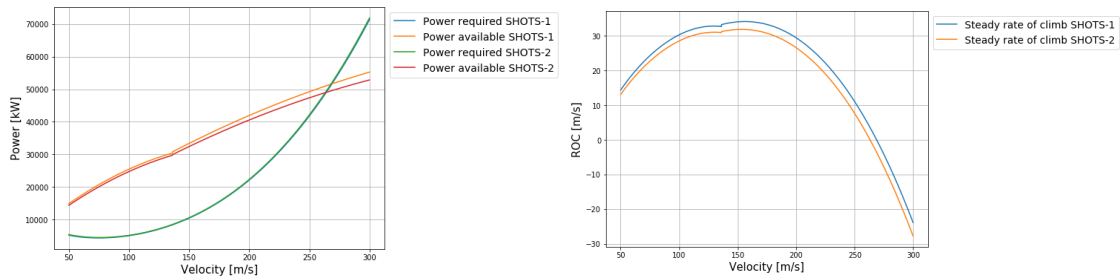
(a) Power available and power required at sea level.

(b) Steady rate of climb at sea level

Figure 7.10: Power required, power available and rate of climb vs speed graphs.

However, the steady rate of climb is only applicable to steady symmetric conditions, which is not representative of the real climb condition. Hence, the steady rate of climb ROC_S needs to be corrected to unsteady rate of climb ROC as shown in equation 7.26 [8] where the correction factor $\frac{VdV}{gdH}$ can be calculated by equation 7.27, where M is the Mach number and the value of ϕ depends on the flight-speed schedule [95] as defined in table 7.11 where the constant ζ equals to 0.190263 in the troposphere and 0 in the stratosphere.

Table 7.11: Values of ϕ at constant CAS and Mach number [95].

$$ROC = \frac{ROC_s}{1 + \frac{VdV}{gdH}} \tag{7.26}$$

$$\frac{VdV}{gdH} = 0.7M^2\phi \tag{7.27}$$

	Constant CAS	Constant Mach
ϕ	$-\zeta$	$\frac{(1+0.2M^2)^{3.5}-1}{0.7M^2(1+0.2M^2)^{2.5}} - \zeta$

Commercial flight operations typically consist of two segments: first, the aircraft will climb at constant calibrated airspeed (CAS) until it reaches the crossover height where the CAS matches a specified Mach number for the upper climb segment; then, it will climb at constant Mach until the cruise altitude is reached. Since the ROC at only the sea level is evaluated, the aircraft is assumed to fly at constant CAS. Hence, ϕ equalst to -0.190263. The unsteady rate of climb at different airspeed is calculated and plotted along with the steady rate of climb as shown in figure 7.11 where figure 7.11a shows the results for SHOTS-1 and figure 7.11b shows for SHOTS-2.
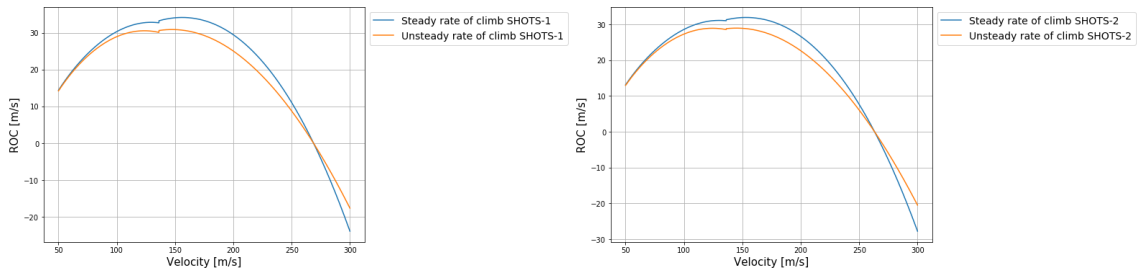
(a) Steady and unsteady rate of climb vs velocity for SHOTS-1 aircraft.　　(b) Steady and unsteady rate of climb vs velocity for SHOTS-2 aircraft.

Figure 7.11: Graphs steady and unsteady rate of climb vs velocity.

The maximum rate of climb of the aircraft at sea level is at the peak of unsteady rate of climb curve in figure 7.11a and the results are shown in table 7.12. Again, the OEI and TEI scenarios are both included in the analysis. The green color in the table indicates that the ROC requirement of 17.8 m/s set by **WFC-PROP-01** is met whereas the orange color indicates that it is not met.

Table 7.12: Climb performance results.

Scenario	Parameter	SHOTS-1	SHOTS-2	Unit
All engines operative	Maximum rate of climb	31.0	29.0	[m/s]
	Velocity at maximum rate of climb	147.2	144.7	[m/s]
One engine inoperative	Maximum rate of climb	19.8	18.1	[m/s]
(most critical: failed PW1700G engine)	Velocity at maximum rate of climb	112.9	101.4	[m/s]
Two engines inoperative	Maximum rate of climb	9.9	9.7	[m/s]
(inaccessible biokerosene fuel)	Velocity at maximum rate of climb	101.6	102.7	[m/s]
Two engines inoperative	Maximum rate of climb	9.9	8.3	[m/s]
(most critical: inaccessible hydrogen fuel)	Velocity at maximum rate of climb	101.4	100.6	[m/s]

7.5.4. Landing performance

The landing field length is evaluated in a similar manner as for the takeoff field length. According to CS25.125 regulation, the landing field length starts at the point where the aircraft descends to an obstacle height of 15.24 m (50 ft) and ends at the point where the aircraft's velocity becomes zero [22]. The landing field length consists of several segments that are defined in figure 7.12. Using the method as shown in table 7.13, the landing field length when all engines are operative is calculated by sizing to the glide angle requirement of no less than 5.5 deg.
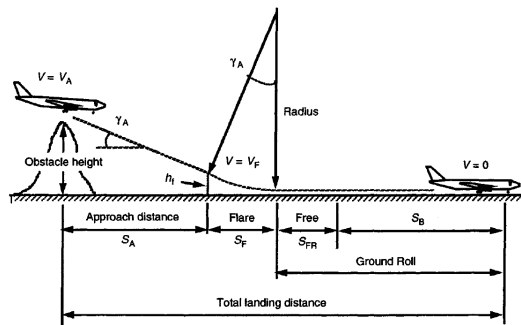

Figure 7.12: Definitions of landing distance [8].

Table 7.13: Landing distance calculation procedure and results for AEO [8].

Parameter	Symbol	Determination method	SHOTS-1	SHOTS-2	Unit
Approach angle	γ_A	Requirement **WFC-PERF-09** in section 3.1		5.5	[deg]
Load factor	n	Typical value during landing is used		1.2	[-]
Rolling friction	μ	Typical value for modern civil jet transports is assumed		-0.3	[m]
Free roll duration	t_{roll}	Airworthiness regulation		2	[s]
Landing stall speed	V_s	$V_s = \sqrt{\frac{2W}{\rho S C_{L_{maxTO}}}}$	49.49	49.48	[m/s]
Touch down speed	V_{TD}	$V_{TD} = 1.15 V_S$	56.91	56.90	[m/s]
Arc radius	R	$R = \frac{V_F^2}{g(n-1)}$	1873.8	1873.1	[m]
Flare height	h_F	$h_F = R\frac{\gamma_A^2}{2}$	8.63	8.62	[m]
Flare ground distance	s_F	$s_F = R\gamma_A$	179.9	179.8	[m]
Free roll distance	s_{FR}	$s_{FR} = tV_{TD}$	113.8	113.8	[m]
Braking distance constants	K_A, K_T	$K_A = -\rho C_{D_0}\frac{2W}{S}$ $\quad K_T = -\mu$	$-1.4\cdot10^{-5}$	$-1.414\cdot10^{-5}$	[m]
Braking distance	s_B	$s_B = \frac{1}{2gK_A}\ln\left(\frac{K_T+K_A V_{TD}^2}{K_T}\right)$	512.4	512.1	[m]
Landing field length	s_L	$s_L = 1.66(s_A + s_F + s_{FR} + s_B)$	1452	1451	[m]

The TEI scenario is also analyzed where the MLW will be different depending on which fuel is not accessible and the results can be found in table 7.14. The green color in the table indicates that the takeoff field length requirement and OEI second segment climb gradient are met whereas the orange color indicates that the requirement of 1,500 m set by **WFC-PROP-03** is not met. As seen in figure 7.13 and table 7.14, the most critical case is when biokerosene cannot be used as it will result in a higher MLW. According to the calculations, a higher landing distance than the requirement of 1,500 m set by **WFC-PROP-03** is the result.
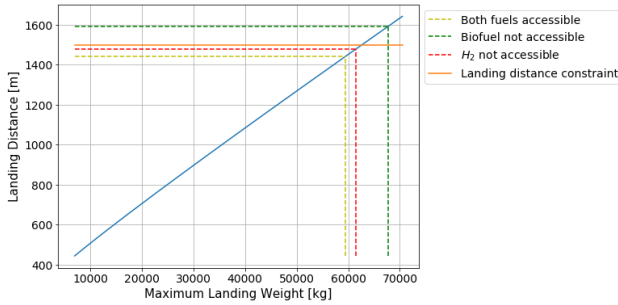

Figure 7.13: Landing field length vs velocity at sea level [95].

Table 7.14: Landing field length results for TWI scenarios.

	SHOTS-1	SHOTS-2	Unit
Hydrogen inaccessible	1482	1479	[m]
Biokerosene inaccessible	1571	1594	[m]

To ensure that the landing distance can be met even when biokerosene cannot be used, a thrust reverser can be installed to decelerate the aircraft during landing. One can Note that the OEI scenario has not be analyzed as this is considered to be less critical. Since the largest factor affecting the landing distance is the MLW, MLW for OEI scenario is assumed to be about the same for AEO scenario as both fuels can still be fed even when one engine is inoperative.

7.5.5. Load factor

In this part the load factor experienced during the flight is determined by constructing the load factor diagrams for both maneuver and gust loads. The stall speed at takeoff was previously determined to be 52.78 m/s. The cruise speed was also known to be 241.93 m/s. The corner speed or maneuver speed is found using equation7.28[96]:

$$V_C = \sqrt{\frac{2n_{max}}{\rho C_{L,max}}\frac{W}{S}} = \sqrt{\frac{2\cdot3}{1.225\cdot1.8}\cdot4843.47} = 114.8[m/s] \tag{7.28}$$

To calculate this velocity, n_{max} was assumed to be 3 based on values in [97]. Further, dive speed was assumed to be 50% higher than cruise speed [97] which was calculated to be 362.9 m/s. Knowing these, the maneuver V-n could be constructed. It is presented in figure7.14a.

(a) V-n maneuver diagram.
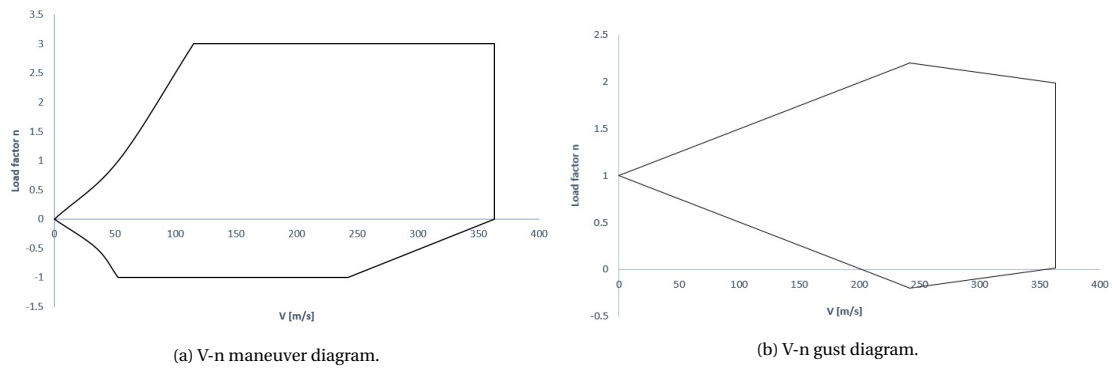

(b) V-n gust diagram.

Figure 7.14: V-n diagrams.

It is necessary that the V-n for gust loading is also constructed to account for loads that occur as a result of gust. For this the cruise speed, dive speed, and the maximum velocity that the aircraft can withstand in turbulence which is calculated to be 231.93 m/s, about 10 m/s (20 kts) less than the cruise speed[12]. The diagram is presented in figure 7.14b. The change is load factor due to gust was calculated using equation 7.5.5, where U is found using $U = KU_{de}$ and K is found with equation 7.5.5 for subsonic aircraft and U_{de} is assumed to be 9.1 m/s [97]. Lastly, μ represents mass ratio and is found using equation 7.5.5.

$$\Delta n = \frac{\rho U V C_{L_\alpha}}{2W/S} \qquad (7.29) \qquad K = \frac{0.88\mu}{5.3 + \mu} \qquad (7.30) \qquad \mu = \frac{2(W/S)}{\rho g \bar{c} C_{L_\alpha}} \qquad (7.31)$$

7.5.6. Noise

One of the regulations that is important for an aircraft to meet in order to get certified is the noise regulations set by ICAO. The noise of the aircraft is measured at three reference points as shown in figure 7.15a . The first point is lateral which is at a parallel distance of 450 m from the runway. The second reference point is flyover which is at 6500 m ahead of the takeoff point and finally, the approach reference point is at 2000 m before the runway [98]. The figure 7.15b shows how the EPNdb limit for lateral, approach and flyover varies with increase in MTOW.

(a) Noise measurement reference [99].

(b) Progression of ICAO Noise standards [13]
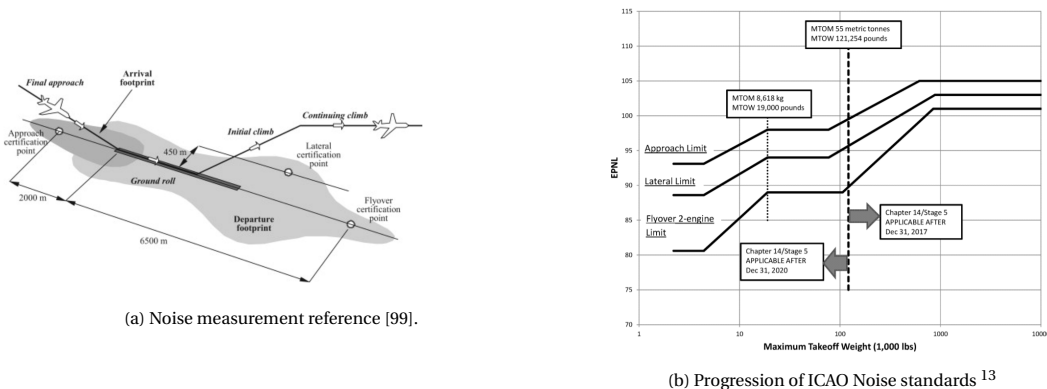
Figure 7.15: Noise regulations

The noise produced by the aircraft comprises of two main sources, the engine and the air frame [100]. The main source of noise during takeoff is the engine; however, during the approach, the air frame is the main contributor of noise [101]. Therefore, at the lateral and flyover reference points when the engines are operating at high thrust setting, only the engine noise is taken into account. For the approach reference point, only the air frame is taken into account. Taking this into account when using the noise database[14] for lateral and flyover reference points, the aircraft with the same reference engine is used.

---

[12]https://www.avweb.com/flight-safety/technique/turbulence-v-speeds (accessed 05-06-2020)

[13]https://www.federalregister.gov/documents/2017/10/04/2017-21092/stage-5-airplane-noise-standards (accessed 12-06-2020)

[14]http://noisedb.stac.aviation-civile.gouv.fr/find.php (accessed 12-05-2020)

For the approach reference point, the aircraft with similar MTOW is used. Finally, the cumulative effective perceived noise (EPN) in decibels is calculated by simply adding the lateral, flyover and approach noise levels.

Since there are two variants of the aircraft, both of them are analysed separately. First option uses all PW1700G engines, so the flyover and lateral EPNdB of the Embraer E195-E2 [9] are used giving the values of 76.5dB and 85.6 dB respectively. However, the Embraer E195-E2 has two engines compared to the first variant which has four engines. Hence, the EPNdB values are multiplied by two on the decibel scale to account for the change in the amount of engines. For the approach reference point, the Airbus A320 is used with a MTOW of 70 tons [102]. Table 7.15 shows clearly that the aircraft meets the noise requirement for all three reference points and the cumulative EPNdB is 27.2 dB.

Table 7.15: Noise level at all the reference points for SHOTS-1.

	Lateral	Approach	Flyover	Cumulative
Noise Level (EPNdB)	88.6	92.4	79.5	260.5
Noise Limit (EPNdB)	96.5	100.2	91	287.7
Margin (EPNdB)	7.9	7.8	11.5	27.2

The second variant uses two PW1700G and two CF34-10A engines. For the PW1700G, when estimating EPNdB for flyover and lateral reference point, the same Embraer E195-E2 is used. For the CF34-10A engine model, the only reference aircraft is the Comac ARJ21 which is not available in the ICAO database. Hence, the engine model CF34-10E is used for the analysis. This engine is slightly bigger than the CF34-10A version and is installed on the Embraer ERJ 190-100. Using the values from this aircraft the flyover EPNdB is determined to be 83.6 dB and the lateral EPNdB is 92.6 dB. Similar to SHOTS-1, the EPNdB for PW1700G and CF34-10E are added together on the decibel scale for the final values. Finally, for the approach reference point the same values for SHOTS-1 are used since both the variants use the same air frame. Table 7.16 shows the final results for option 2. It is important to note that for estimating these results a bigger engine is used hence it is very likely the lateral and flyover noise levels are overestimated. However, even with the overestimation the option 2 comfortably meets the noise requirement with cumulative margin of 18.3 dB.

Table 7.16: Noise level at all the reference points for SHOTS-2.

	Lateral	Approach	Flyover	Cumulative
Noise Level (EPNdB)	92.6	92.4	84.4	269.4
Noise Limit (EPNdB)	96.5	100.2	91	287.7
Margin (EPNdB)	3.9	7.8	6.6	18.3

Table 7.17 shows the noise performance for the Embraer E195-E2[15]. The results are quite similar to SHOTS-1, however, the Embraer E195-E2 is considerably quieter than option 2.

Table 7.17: Noise level at all the reference points for the Embraer E195-E2.

	Lateral	Approach	Flyover	Cumulative
Noise Level (EPNdB)	86.1	91.7	79.6	257.4
Noise Limit (EPNdB)	96.1	99.9	90.4	286.4
Margin (EPNdB)	10	8.2	10.8	29

Finally, the cabin noise levels during the cruise are estimated for both the design variants. During cruise, the engine noise and frame noise are equally important [103]. The total cabin noise for the reference aircraft is found by Zevitas et al. [103]. It is assumed that 50% of the noise for the reference aircraft is due to frame and the rest is due to the engine. The Embraer E190 is used as a reference aircraft for the engines, reporting a value of 78.7 dB. Since only 50% of the total noise is the engine noise, the value halved on the dB scale. However, as SHOTS-1 uses four engines, the noise is doubled again, resulting in 78.7 dB.

The next source of noise is the air frame. The Airbus A320 has been used, reporting a total noise of 82.7 dB. This value is halved to estimate the air frame noise of the Airbus A320, resulting in 79.7 dB. Finally, the noise level due to engine that is 78.7 dB and air frame that is 79.7dB are added together. The cabin noise level during the cruise for SHOTS-1 is estimated to be 82.2 dB.

---

[15]http://noisedb.stac.aviation-civile.gouv.fr/pdf.php?id=12410 (accessed 15-06-2020)

For option 2, since no information is provided for the reference aircraft, the cabin noise is estimated comparatively to SHOTS-1. The air frame noise for this option stays the same at 79.7 dB. However, the engine noise is expected to be higher. From the tables 7.15 and 7.16 it can be seen that when the engine noise is the main source of noise the noise level is on average 4.5 dB higher. Hence 4.5 dB is added to the engine noise of SHOTS-1 giving the value 83.2 dB. Finally, adding the air frame and engine noise shows that the cabin noise during cruise is 84.5 dB. It is important to note that since the noise level for engine is overestimated for option 2 (as already explained previously). The inaccuracy is carried over to the cabin noise as well, resulting in a higher value.

7.5.7. Gas emissions

Another important requirement for the aircraft is regarding the gas emissions. The harmful emission due to burning Hydrogen is the NO_x while burning biokerosene mainly emits NO_x and carbon dioxide (CO_2). For burning hydrogen the NO_x emission index is already calculated in section 7.4.2. Using the equation 7.32, the mass flow rate of air can be calculated in the combustion chamber during the cruise where $\dot{M}_{fuel}$ is the mass flow rate of fuel, LHV_f is the lower heating value (LHV) of fuel which is 143 MJ/kg for hydrogen, ΔT is the change in temperature, cp_{air} is the specific heat coefficient of air at combustion chamber at constant pressure which is taken as 1075 J/(kg·K).

$$\dot{M}_{air} = \frac{\dot{M}_{fuel} \cdot LHV_f}{\Delta T \cdot cp_{air}} \tag{7.32}$$

The change in temperature is the increase of temperature due to the combustion of hydrogen hence the difference of inlet combustion chamber temperature (754K) and outlet combustion chamber (1576K) already stated in 7.4.2. Finally, for the mass flow rate of fuel equations 7.33 and equation 7.34 are used. The SFC for PW1700G is 0.52 lb/lbf·hrs [16] as already stated in section 5.3. These values are converted into SI units. This gives the SFC in kg/Ns. To find the fuel consumed for the whole aircraft, it is multiplied by the thrust required during cruise as shown in equation 7.33. This is divided by four to get the mass of kerosene consumed by each engine per second. To convert this mass flow rate of kerosene into the mass flow rate of hydrogen the equation 7.34 is used.

$$\dot{M}_{kerosene} = \frac{T}{4} \cdot SFC_{\frac{kg}{Ns}} \tag{7.33} \qquad \dot{M}_{fuel} = \frac{\text{Energy density Hydrogen}}{\text{Energy density Kerosene}} \cdot \dot{M}_{Kerosene} \tag{7.34}$$

The mass flow rate of hydrogen during cruise is calculated to be 0.063 kg/s. For SHOTS-1 the mass flow rate of biokerosene is 0.176 kg/s where as for option 2 it is 0.217 kg/s. The mass flow rate of air is calculated to be 10.15 kg/s and the Emission index of Nitrogen oxide the emissions of nitrogen for each engine running on hydrogen is calculated to be 28 g/s.

Next the ICAO database[17] is used to find the emission index of nitrogen oxide for the PW1700G and CF34-10A engines when burning biokerosene. The values are taken for approach conditions since the mass flow rate during takeoff and climb out is too high and hence do not represent the cruise conditions accurately. The emission index for PW1700G is 10.7 g/kg whereas for the CF34-10A it is 7.97 g/kg. Using equation 7.32 again the mass flow of air per second is calculated for PW1700G and CF34-10A to get the final results. The NO_x emission for PW1700G is found to be 91.6 g/s and for CF34-10A the NO_x emission is found to be 83.9 g/s Finally for the carbon dioxide emissions of PW1700G and CF34-10A the chemical reaction as shown in equation 7.35 is used. Calculating the mass flow rate of biokerosene using equation 7.33 and finding mass ratio of kerosene to carbon dioxide using equation 7.35 the emissions are calculated.

$$C_{12}H_{26} + 18.5\,(O_2 + 3.76\,N_2) \longrightarrow 13\,H_2O + 12\,CO_2 + 69.56\,N_2 \tag{7.35}$$
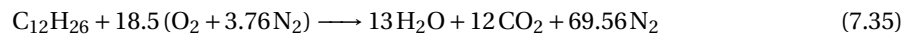
Finally, the emission for the Embraer E195-E2 and Airbus A220-100 is also calculated to analyze how well the designs perform compared to it. The ICAO database is used to find emission index for PW1919G which is used on the Embraer E195-E2 and PW1521G for Airbus A220-100. Furthermore taking into account the mass of these aircraft and assuming same flight conditions, the NO_x emissions are calculated.

---

[16] http://www.jet-engine.net/civtfspec.html (accessed 18-05-2020)

[17] https://www.easa.europa.eu/domains/environment/icao-aircraft-engine-emissions-databank (accessed 09-06-2020)

For carbon dioxide emissions the method explained is used for calculations. The final results of NO_x and CO_2 emissions for each option are shown in table 7.18.

Table 7.18: Gas emission in kilogram per second by the aircraft.

Gas emitted	SHOTS-1	SHOTS-2	Embraer E195-E2	Airbus A220-100
Carbon dioxide [kg/s]	1.093	1.345	1.950	1.930
Nitrogen oxide [kg/s]	0.239	0.224	0.312	0.296

7.6. Sustainability

Propulsion system was a significant part of sustainability within the project, with one of the top-level requirements being use of non-fossil fuel. Therefore, hydrogen and biokerosene were chosen as fuel. Further, two types of engine were selected, Pratt & Whitney PW1700G and CF34-10A which resulted in a cheaper design in comparison to using PW1700G for all 4 engines, which helps in achieving economic sustainability. To accommodate burning hydrogen within the engine the combustion chamber needed to be altered to reduce NO_x emissions. LDI and MMX combustion chambers were considered. For LDI, five configurations were analyzed in terms of NO_x emissions and it was found that the LDI configuration 4 has the smallest NO_x emission of 60.6 ppm. Therefore, it was proposed to utilize LDI combustion in the PW1700G engines for burning hydrogen. Further, noise emission was considered as it is important for social sustainability. Noise calculations were done on the two design options namely, using two different types of engine, PW1700G and CF34-10A or using only PW1700G. Both resulted in less noise level than the allowed by regulations. Despite the fact that the former has a lower level, it was chosen since it was the cheaper option, which in return helped with economic sustainability.

Another important improvement was in gas emissions. Based on the calculations both design options have significantly less CO_2 and NO_x emissions in comparison to the reference aircraft Embraer E195-E2. The design option which uses two types of engine was the final selection and it emits 1.345 kg/s of CO_2 and 0.224 kg/s of NO_x. Furthermore, an APU is used for providing the electricity needed in ground operations which runs on biokerosene; however, the emissions can be further reduced by using hydrogen instead. This can be a recommendation for further phases in order to help with sustainability even more. Lastly, it should be noted that the propulsion system is highly recyclable/reusable.

7.7. Verification and Validation

This section presents the verification procedures of the computation models that were used to estimate the NO_x gas emssions of LDI and MMX combustor chambers, the noise levels, total emissions of NO_x and CO_2, and finally, the flight performance calculations in the payload-range diagram, takeoff and landing distance, and rate of climb.

7.7.1. Combustor emission

For the LDI, a unit test is first carried out to check whether the equivalence ratio calculated is correct. The results are shown in table 7.19.

Table 7.19: Equivalence ratio verification.

T	Real equivalence ratio	Code equivalence ratio
700	0.28	0.27
900	0.38	0.37
1100	0.45	0.46

A system check is also carried out to see if the ppm NO_x calculated is accurate. In order to do so the results shown in figure 7.16 are used. The figure shows how the NO_x emission vary with the change in outlet temperature. For this figure the inlet temperature is 700 K, the loss of pressure is 4 %, the residence time is 2 millisecond and the inlet pressure used in 0.7 MPa. Keeping the same inputs the code is used to calculate the NO_x emissions. The figure 7.17 shows the NO_x emissions for different outlet temperatures. Comparing the figure 7.16 and figure 7.17 show that the values are accurate.
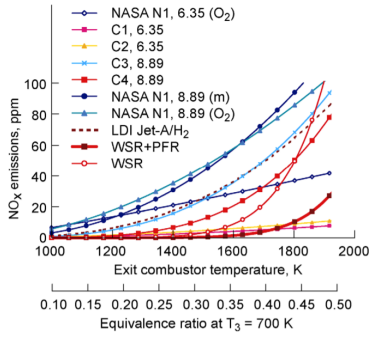
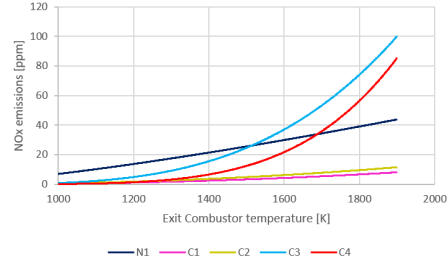Figure 7.16: Experimental results of LDI combustor [72].

Figure 7.17: results of LDI combustor calculated using code

For the NO_x emission of the MMX combustor, the experimental results and atmospheric conditions of a modified MMX combustor integrated in the APU GTCP 36300 gas turbine [104] are used to verify the computed results in section 7.3. The experimental data were obtained with a combustor inlet temperature of 300K and a pressure of 1.6 MPa. Assuming that the outlet temperature is 1600K under full power output condition, an estimation of the $N0_x$ emission for this combustor is made using both the P3-T3 method and Kyprianidis et al.'s method. Then, the results are compared with the experimental results of the modified hydrogen MMX combustor, which is the bottom line displayed in figure 7.18.
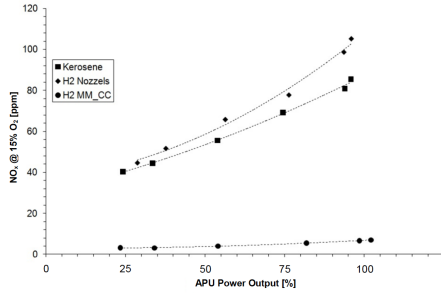

Figure 7.18: Experimental results of NO_x emissions of a modified MMX combustor integrated in APU GTCP 36300 gas turbine [104].

Table 7.20: MMX combustor NO_x emission verification results.

Method	Simulated results	Experimental data [104]	Unit	Difference
P3-T3 method [86]	8.3	9.5	[ppm]	-13.1%
Kyprianidis et al.'s method [89]	9.0	9.5	[ppm]	-5.3%

As shown in table 7.20, the emission estimated by Kyprianidis et al.'s method [89] has the smallest deviation from the experimental data which is 5.3 %. Both methods seem to underestimate the NO_x emissions considerably; however, due to the assumptions made in the computation, the differences are considered acceptable. Finally, since the MMX combustor is still in a development stage and has not been applied in a large scale yet, there are no validation data available for MMX combustors that are applicable to large turbofan engines. Hence, validation of the results is not possible at this stage.

7.7.2. Flight Performance

For the payload range diagram the code is verified by using it to calculate the range for an existing aircraft. Hence the Airbus A220-100 is used which has MTOW of 63.1 tonnes and MZFW of 50.4 tonnes[18], it is calculated that the range is 6,196 km compared to the actual range that is 6,297 km.

To verify the takeoff, climb, descent and landing performance calculations, the parameters of the Embraer E190, that are presented in table 7.21, are used as input in the python code and the simulated results are compared with the performance data of the aircraft as shown in table 7.22. As seen in table 7.22, the differences are quite small where both the takeoff and landing field lengths as well as the ROC have been slightly overestimated.

---

[18]https://www.airbus.com/aircraft/passenger-aircraft/a220-family/a220-100.html (accessed 16-06-2020)

Table 7.21: Parameters of the Embraer E190[19][20] [105].

Parameter	Dimension	Unit
Maximum takeoff weight	51,800	[kg]
Maximum landing weight	44,000	[kg]
Fuel weight	12,971	[kg]
Wing area	92.5	$[m^2]$
Wing span	28.72	[m]
Fan diameter	1.864	[m]
Bypass ratio	5.4	[-]

Table 7.22: Takeoff, landing, and climb performance calculation verification[19][21].

Parameter	Simulated result	Actual data	Unit	Difference	Verification Method
Takeoff field length	1,290	1,267	[m]	1.8%	Input parameters of similar aircraft into programme
Landing field length	1,233	1,226	[m]	0.6 %	
Rate of climb	17.8	17.3	[m/s]	2.8 %	

7.7.3. Noise and gas emissions

For the sound performance, the EPNdB values are taken from the ICAO database. Hence, they are already verified. Moreover, in the section 7.5.6, the noise performance is compared to the Embraer E195-E2 which verifies that the estimated values are accurate.

For the gas emissions, the NO_x emission index values taken from the ICAO database and from the section 7.4.2 are multiplied by the mass flow of air to find the emissions in kg/s. Hence, it is important to verify the calculations of the mass flow rate. Hence, the code is tested by comparing the results with the real values for different engines in the market. The input values for the engines are used to find mass flow rate. The mass flow of air during cruise is verified by substituting values for other engines. Table 7.23 shows the results.

Table 7.23: Mass flow rate of air validation.

	CFM 56 3C1	PW4056	PW JTD-219	RR TAY 651
Real mass flow rate [lb/s]	707	1,705	488	426
Calculated mass flow rate [lb/s]	675	1,645	468	423

---

[19]https://www.embraercommercialaviation.com/commercial-jets/e190/ (accessed 21-06-2020)

[20]http://www.flugzeuginfo.net/acdata_php/acdata_emb190_en.php(accessed 21-06-2020)

[21]https://contentzone.eurocontrol.int/aircraftperformance/details.aspx?ICAO=E190& (accessed 21-06-2020)

Aerodynamics, Stability & Control

Although the aerodynamic performance and handling qualities of the aircraft are not the main focus of the WeFlyCycle project, the underlying subsystems should be designed meticulously to ensure optimal performance and passenger comfort. Section 8.1 presents an analysis of the functionality that should be provided by the subsystem and the resulting requirements are discussed in section 8.2. Section 8.3 presents a summary of the final wing geometry parameters resulting from the design approach discussed in the Midterm Report on wing geometry and airfoil selection [3]. The lift and drag characteristics of the entire aircraft are considered in section 8.4. The aerodynamic subsystem analysis is concluded with section 8.5 on the sizing of the high-lift devices (HLDs) and aileron surfaces. Section 8.6 continues with the stability analysis, followed by the control characteristics of the airplane. Finally, a clarification of the verification and validation procedures applied throughout the final design phase is presented in section 8.7 .

8.1. Functional Analysis

The functional breakdown of the aerodynamic, stability and control subsystems is relatively simple for a standard jet airliner. Figure 8.1 shows a snippet of the entire functional flow diagram shown in chapter 3. The relevant functions basically comprise the mission profile of the aircraft. The aircraft is required to rotate, ascend, cruise, descend, loiter and land all in a stable and controlled manner.
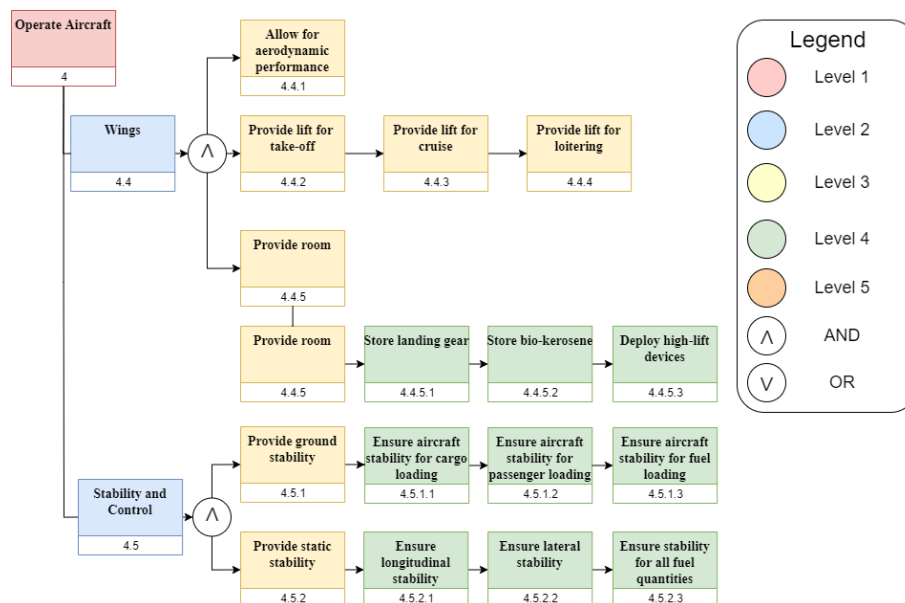

Figure 8.1: Functions governing the design of the aerodynamic, stability and control subsystems.

The actual design considerations are generated once the user requirements are taken into account. It's not what but how (well) the subsystem should enable the aircraft to fulfil its functionality. Please refer to section 8.2 where all the relevant requirements are listed.

8.2. Requirements Analysis

The subsystems regarding aerodynamic performance and stability should comply with multiple system and subsystem requirements. Several system requirements were already identified in the Baseline report [2]. They are listed in section 3.1 on concept selection.

8.2.1. Subsystem requirements

During the detailed design phase, several additional subsystem requirements were identified. They are subdivided in wing, aerodynamic, stability and control requirements and listed below.

- *WFC-WING-1: The wing structure shall accommodate for safe storage of the main landing gear.* This requirement stems from the stability analysis and the lateral as well as longitudinal position of the landing gear.
- *WFC-WING-2: The wing span shall not exceed 36 m.* This requirement stems from the operability of the aircraft on secondary aerodromes according to ICAO regulations annex 14 [10].
- *WFC-AERO-01: The aircraft's angle of attack during landing shall not exceed 15 degrees.* This requirement stems from safety reasons to ensure runway visibility for the pilots.
- *WFC-AERO-02: The high-lift devices installed on the wing will accommodate for the required increase in lift coefficient to sustain flight at stall-speed.*
- *WFC-AERO-03: The high-lift devices installed on the wing will ensure that the aircraft is able to perform roll, yaw and pitch manoeuvres at stall speed.*
- *WFC-AERO-04: The aspect ratio of the wing will be sufficiently high such that drag production remains within limits to ensure safe climb should one engine fail during takeoff.*
- *WFC-CONT-01: The ailerons will be able to induce a steady state roll rate of minimum 32.14 degrees/s, according to ICAO regulations for class II aircraft [106].*
- *WFC-STAB-01: The horizontal tail shall be large enough to keep the aircraft stable during all flight configurations.*
- *WFC-STAB-02: The horizontal tail shall be large enough to keep the aircraft controllable during all flight configurations.*
- *WFC-STAB-03: The vertical tail shall be large enough to keep the aircraft stable if one of the outer engines fails during takeoff at a minimum speed of $1.13V_{mc}$.*
- *WFC-STAB-04: Landing gear shall be placed in such a way that the aircraft is stable on the ground.*
- *WFC-STAB-05: The landing gear shall be sized in such a way that the aircraft has enough ground clearance.*

8.3. Final Wing Geometry

The design of the wing lay-out has been an iterative process. It soon became clear that the trapezoidal wing assumption made in the Midterm Report trade-off [3], would have to be altered to accommodate for landing gear storage as well as increase flap efficiency to meet the lift coefficient requirements discussed further in section 8.5. This has been accomplished by splitting up the geometry in two parts. The trapezoidal section and the triangular area that is added to the trailing edge (TE) of the wing. The exact approach to designing a trapezoidal wing for transonic flight was discussed in the Midterm report [3], but the following paragraph briefly summarizes the major design decisions.

The aspect ratio, based on the average of the Embraer E195-E2 and the Airbus A220 [67], has changed after the midterm phase. The initial estimate of 9.95 is too high if the aircraft wants to have a wingspan below 36 m; therefore, the aspect ratio was changed to 9.65. The Performance department confirmed that the drag production is within limits should one engine fail during climb, hence requirement **WFC-AERO-04** is met. Moreover, the Structures department reported no issues with respect to the required structural stiffening. In accordance with requirement **WFC-PERF-02**, the cruise altitude was set to 11,000 m to maximize engine efficiency with a cruise Mach number of 0.79. This will allow the aircraft to fly at a maximum Mach number of 0.82, the drag divergence Mach number, after which compressibility effects will become apparent as excessive wave drag will set in. This way, requirement **WFC-PERF-06** is met and the aircraft can compete with the Airbus A220 in terms of speed. The required sweep angles as well as the maximum thickness-to-chord ratio (t/c) to avoid sonic conditions were calculated using relations from Torenbeek [107]. Lastly, the taper ratio, reportedly laying between 0.2-0.3 for swept wings to approach elliptical lift distribution, was set to 0.22 after looking at modern aircraft configurations [3].

Values below 0.2 are to be avoided should one want to minimize the risk of the wing tips stalling before the root [97]. With the information provided above and some geometrical relationships one is able to construct the trapezoidal wing.

However, the final wing design adds a yehudi to the TE of the wing. This triangular section was sized carefully in conjunction with stability and control. Because the aspect ratio, wing span and taper are fixed, an iterative process is performed where the size of the yehudi is altered to fit the landing gear storage and to allow for enough flap spacing. This changes the longitudinal wing position as well, which is discussed in section 8.6. The trapezoidal section is sized accordingly such that the area together with the added area of the yehudi totals the required wing surface area. The required wing surface area is known by looking at the wing loading diagram in section 7.5 and the estimated MTOW from chapter 5. Equations 8.1-8.2, which estimate the size and the location of the mean aerodynamic chord, had to be supplemented by equation 8.3 (the integral approach [108]) to ensure a correct computation of lift and drag values in section 8.4.

$$MAC = \left(\frac{2}{3}\right) c_r \left(\frac{1 + \lambda + \lambda^2}{1 + \lambda}\right) \qquad (8.1) \qquad \qquad y_{MAC} = y_r + \left(\frac{b}{6}\right)\left(\frac{1 + 2\lambda}{1 + \lambda}\right) \qquad (8.2)$$

The root chord is defined by c_r, c_t is the tip chord, MAC is the mean aerodynamic chord, y_{MAC} is the location of the MAC along the semi-span $b/2$ and y_r is the coordinate of a root chord.

$$MAC = \frac{\sum_{i=1}^{n} MAC_i \cdot S_i}{\sum_{i=1}^{n} S_i} = \frac{MAC_1 \cdot S_1 + MAC_2 \cdot S_2 + MAC_3 \cdot S_3 + \ldots + MAC_n \cdot S_n}{S_1 + S_2 + S_3 + \ldots + S_n} \qquad (8.3)$$

S_i is the area of individual sections. The span-wise location y_{MAC} can be computed by replacing all the instances of MAC by the y-coordinate.

The final wing geometry parameters are grouped in table 8.1. One will notice that the spar locations have been added for completeness. Their location depends on the size of the HLDs, discussed in section 8.5, as well as the location of the landing gear, explained in section 8.6. The dihedral angle follows from the stability analysis as well.

Table 8.1: Final wing geometry.

Parameter	Value	Unit	Parameter	Value	Unit
Wing area	132.57	[m^2]	Root chord with yehudi	7.788	[m]
Aspect ratio	9.65	[-]	Root chord trapezoidal	4.398	[m]
Wing span	35.99	[m]	Tip chord	1.715	[m]
Sweep angle LE	32.77	[deg]	Yehudi root extension	3.390	[m]
Sweep angle c/4	31.22	[deg]	Yehudi span	13.738	[m]
Sweep angle c/2	29.62	[deg]	MAC length	4.502	[m]
Sweep angle TE	26.27	[deg]	MAC y-location	6.694	[m]
Dihedral angle	6.00	[deg]	Location front spar	0.175*	[x/c]
Taper ratio	0.20	[-]	Location middle spar	0.580*	[x/c]
Max thickness-to-chord	0.13	[-]	Location back spar	0.800**	[x/c]

*The front and middle spar chord location percentages are expressed wrt. the trapezoidal chord as they are aligned with the sweep angle.	**The back spar's percentage is expressed wrt. the root chord with the yehudi because it's oriented orthogonally to the fuselage and intersects with the middle beam.

8.4. Lift and Drag Characteristics

The lift and drag performance of the aircraft should be tailored according to the mission profile. For a transonic jet airliner, the emphasis is laid on high speed and low drag during cruise. The design point is the lift coefficient of the wing during cruise $C_{L,des}$, which can be recovered from equation 8.4.

$$C_{L,des} = \frac{1.1 \cdot W_{cr}}{q_{des} \cdot S} \qquad (8.4)$$

The factor 1.1 accounts for the negative lift contribution of the tail, W_{cr} is the average weight during cruise, q_{des} is the dynamic pressure at the cruise Mach number and selected cruise altitude and S is the wing surface area. The wing design lift coefficient can be related to the airfoil design lift coefficient $C_{l,des}$ by correcting it for sweep using equations 8.4-8.6.

$$L = qSC_{L,des} \cong q_{eff}SC_{l,des}$$

$$q_{eff} = \frac{1}{2}\rho V_{eff}^2 \qquad (8.5) \qquad\qquad V_{eff} = V_\infty \cos \Lambda_{c/4} \qquad (8.6)$$

The free-stream density is given by ρ and $\Lambda_{c/4}$ is the quarter-chord sweep angle.

8.4.1. Airfoil characteristics

During the Midterm [3], the NASA SC(2)-0710 supercritical airfoil was selected as the primary geometry for the wing after a rigorous trade-off. Only supercritical airfoils were considered due to their excellent performance in the transonic regime. Please consult appendix A for an explanation of the weighting process. The NASA SC(2)-0710 showed excellent lift-over-drag (L/D) performance close to the $C_{l,des}$ point, while remaining below the upper limit on thickness-to-chord ratio (t/c).

Table 8.2 lists the most important characteristics of the NASA SC(2)-0710 airfoil. Most of the values were obtained from experimental data [109], the maximum lift coefficient and stall angle were approximated with numerical data from Xfoil. The applicability and trust-worthiness of the data obtained from Xfoil were validated with experimental data in the Midterm Report [3]. The data is plotted in figure 8.2.
It should be noted that Xfoil tends to overestimate the lift coefficient at high angles of attack. This is due to the fact that Xfoil takes the wake trajectory from the inviscid solution and does not correct for the change in trajectory which occurs when the flow becomes viscid [110]. As can be seen in figure 8.2, the predicted $C_{l,max}$ is around 2.1. To account for the overestimation made by Xfoil, the actual lift coefficient is assumed to be 15% below the calculated value which means that a final $C_{l,max}$ of 1.8 is obtained for the NASA SC(2)-0710 airfoil. Finally, as explained in the verification and validation chapter of the Midterm Report [3], the actual stall angle of attack will also be lower than the value found by Xfoil, which is currently 17 degrees. The actual value is assumed to be approximately 15 degrees.

Table 8.2: NASA SC(2)-0710 airfoil characteristics at $Re = 20.4\text{x}10^6$.

	(t/c)	$C_{l,0}$	α_0 [deg]	$C_{l,max}$	α_s [deg]	$C_{d,min}$	$C_{l,des}$	$(C_l/C_d)_{max}$	$C_{m,cruise}$
NASA SC(2)-0710	0.10	0.52	-4	1.8	15	0.006	0.7	90	-0.12
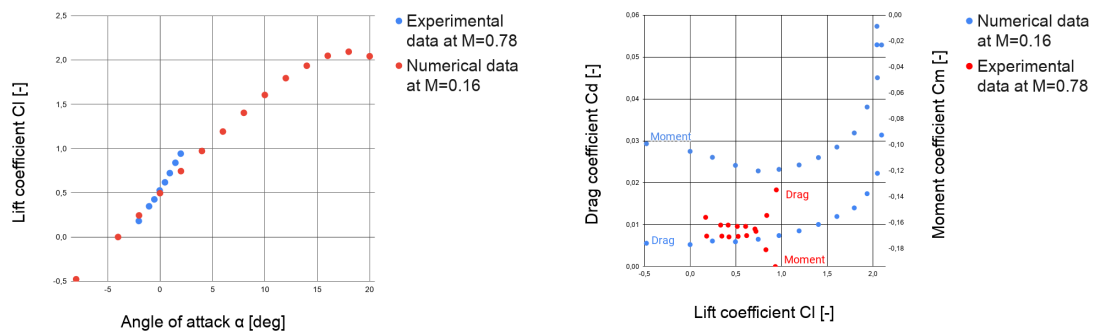
Figure 8.2: Experimental and numerical data from the NASA SC(2)-0710 supercritical airfoil, on the left the lift coefficient is plotted as a function of angle of attack and on the right figure the lift coefficient is given as a function of the drag and moment coefficient [109].

8.4.2. Lift characteristics

This section analyzes the lift capacity of the aircraft for several load scenarios that are crucial for safe flight operations. The aerodynamic performance from the aircraft depends on the fluid flow behavior,

which can be quantified using the Reynolds number. The final Reynolds numbers for different flight conditions are reported in table 8.3.

Table 8.3: Reynolds number of the different flight conditions.

Flight condition	Cruise	Landing	Takeoff	Best ROC
Reynolds number	$26.9 \cdot 10^6$	$20.4 \cdot 10^6$	$24.4 \cdot 10^6$	$20.3 \cdot 10^6$

Different flight conditions result in different lift curve gradients. The C_{l_α} for any given airfoil and non-compressible flow is often close to 2π [1/rad]. One has to correct for compressibility by applying the Prandtl-Glauert correctional factor given by equation 8.7. One will notice that the lift gradient increases with the Mach number. Secondly, if one wants to extend the analysis to a a finite wing, then equation 8.8 from the United States Air Force Stability and Control Data Compendium (DATCOM) [97] provides an estimate based on the aspect ratio A, the Mach number M and sweep angle $\Lambda_{c/2}$.

$$C_{l_\alpha} = \frac{2\pi}{\sqrt{1-M^2}} \quad (8.7) \qquad C_{L_\alpha} = \frac{2\pi A}{2 + \sqrt{\frac{A^2(1-M^2)}{k^2}\left[1 + \frac{\tan^2 \Lambda_{c/2}}{(1-M^2)}\right] + 4}} \quad (8.8)$$

The airfoil efficiency factor k is assumed to be 0.95 unless the 2D-lift curve slope is known for that particular Reynolds number and one can compute this more accurately.

The trim angle for cruise conditions can be calculated using equation 8.9 and the zero lift angle of the airfoil α_{0L}. The maximum achievable lift coefficient in clean configuration follows from equation 8.10 where information on $\left[\frac{C_{Lmax}}{C_{lmax}}\right]$ is provided by the DATCOM method as well [97].

$$\alpha_{trim} = \frac{C_{Ldes}}{C_{L\alpha}} + \alpha_{0L} \quad (8.9) \qquad C_{Lmax} = \left[\frac{C_{Lmax}}{C_{lmax}}\right] C_{lmax} \quad (8.10)$$

The aerodynamic performance of an airplane is expressed via the lift coefficient of the wing for that particular flight condition, several of which are on the limit of the flight envelope. According to requirement **WFC-OP-02**, the aircraft should be able to take off within 1,500 m. Equation 8.11 provides a relationship between the takeoff parameter TOP and $C_{L_{TO}}$. Figure 8.3 provides an estimate on TOP based on the takeoff distance and the number of engines.
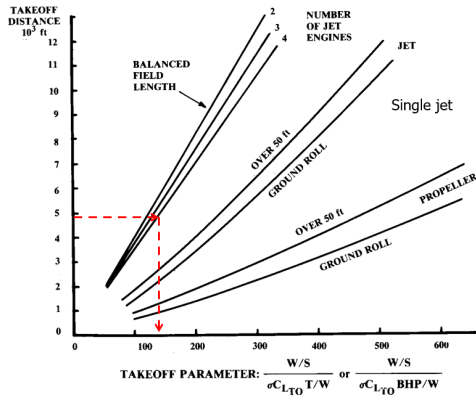
$$TOP_{jet} = \left(\frac{W}{S}\right)_{TO} \cdot \left(\frac{W}{T}\right)_{TO} \cdot \frac{1}{C_{L_{TO}}} \cdot \frac{\rho_0}{\rho} \quad (8.11)$$

Figure 8.3: Takeoff distance over TOP in lbs/ft^2 [97].

In order to meet requirement **WFC-PERF-08** on stall speed V_S, equation 8.12 is used to compute the required $C_{L_{max}}$ for $\left(\frac{W}{S}\right)_{TO}$ (in case of an emergency right after takeoff) and $\left(\frac{W}{S}\right)_{land}$ to check whether the approach angle is within limits according to requirement **WFC-AERO-01**.

$$\frac{W}{S} = \frac{1}{2} \cdot \rho \cdot V_S^2 \cdot C_{L_{max}} \quad (8.12)$$

Once the required lift coefficients are known, targets should be established to ensure that the aircraft remains controllable should it reach the limit of the flight envelope. The target C_L was established by adding an additional 0.1 margin to every $C_{L_{max}}$ which should allow the airplane to maneuver safely, thus satisfying requirement **WFC-AERO-03**. Table 8.4 provides an overview of the design lift characteristics. It should come as no surprise that the wing lift coefficient is not sufficient to deal with the critical flight operations. The HLDs, discussed in section 8.5, will supplement the remaining ΔC_L.

Table 8.4: Final aerodynamic parameters.

Parameter	Value	Unit	Parameter	Value	Unit
$C_{L,des}$	0.5419	[-]	Prandtl factor cruise	0.61	[-]
$C_{l,des}$	0.7347	[-]	C_{l_α} cruise	0.19	[1/deg]
$C_{l_{max}}$	1.8010	[-]	C_{L_α} cruise	0.10	[1/deg]
$C_{L_{max}}$ clean	1.9080	[-]	C_{l_α} landing	0.11	[1/deg]
$C_{L_{max}}$ takeoff	2.2210	[-]	C_{L_α} landing	0.07	[1/deg]
$C_{L_{max}}$ stall at W_{TO}	2.6823	[-]	α_{stall} clean	22.09	[deg]
$C_{L_{max}}$ stall at W_{LD}	2.9544	[-]	α_{trim} cruise	1.39	[deg]

8.4.3. Drag characteristics

All systems waste energy and an airplane is no different. In aviation, the energy of the flow that cannot be used to perform work is called drag. Drag originates from various sources and has multiple sub-components. For the conceptual design, drag is modelled with a drag polar that varies quadratically with lift, modelled by equation 8.13 for cambered airfoils. This is not entirely accurate but deemed sufficient for this stage of the design.

$$C_D = C_{D_{\min}} + \frac{1}{\pi Ae}\left(C_L - C_{L_{\min}}\right)^2 \tag{8.13}$$

$C_{D_{min}}$ is the minimum drag of the structure, $C_{L_{min}}$ shifts the drag polar because the minimum drag for cambered airfoils is usually not reached for $C_L = 0$ and e is the Oswald efficiency factor to account for the non-elliptical lift distribution. The first term on the right of the equation comprises the inherent drag of the airplane: skin friction, form drag, interference drag, base drag, excrescence drag, ram drag etc. The second term on the right is called the induced drag, drag as a result of lift: viscous and inviscid drag-due-to-lift, trim drag, wave drag etc.

8.4.3.1. Zero-lift drag

There are multiple ways to calculate the parasite drag of an aircraft. Some are faster than others. Two methods from Raymer have been implemented and averaged to increase accuracy [97]. This provides a contingency margin for performance in terms of range, as the actual drag values would probably be a bit lower.

Firstly, the fast approach based on historical C_D values and the component wetted area relative to the total wetted area are given by equation 8.14 and equations 8.15-8.16 on the wetted areas.

$$C_{D_0} = \frac{1}{S_{ref}} \sum_c C_{D_c} A_c + C_{D_{misc}} \tag{8.14}$$

Parameter	CDc
Wing	0.0030
Fuselage	0.0024
Nacelles	0.0060
Tailplane	0.0025
$C_{D_{misc}}$	Add 10% to C_{D_0}

$$
\begin{aligned}
S_{W_{wet}} &= 1.07 \times 2 \times S_{W_{exp}} \\
S_{HT_{wet}} &= 1.05 \times 2 \times S_{HT_{exp}} \\
S_{VT_{wet}} &= 1.05 \times 2 \times S_{VT_{exp}}
\end{aligned} \tag{8.15}
$$

$$S_{F_{wet}} = \frac{\pi D}{4}\left(\frac{1}{3L_{nose}^2}\left[\left(4L_{nose}^2 + \frac{D^2}{4}\right)^{1.5} - \frac{D^3}{8}\right] - D + 4L_{cabin} + 2\sqrt{L_{tail}^2 + \frac{D^2}{4}}\right) \tag{8.16}$$

L_{nose} is the length of the nose cone, L_{cab} the length of the cabin section and L_{tail} the length of the tail cone.

The second approach is the component build-up method that estimates every component's subsonic parasite drag using equation 8.17.

$$C_{D_0} = \frac{1}{S_{ref}} \sum_c C_{f_c} \times FF_c \times IF_c \times S_{wet_c} + C_{D_{misc}} \tag{8.17}$$

C_{f_c} is the component flat plate skin friction coefficient, FF_c is the component form factor and IF_c is the component interference factor.

Once the percentage of laminar/turbulent flow over the component is known, C_{f_c} can be estimated using equations 8.18-8.19. The form factors can be approximated using equations 8.20-8.23.

$$C_{f_{laminar}} = \frac{1.328}{\sqrt{\mathrm{Re}}} \tag{8.18} \qquad C_{f_{turbulent}} = \frac{0.455}{\left(\log_{10}(\mathrm{Re})\right)^{2.58} \left(1 + 0.144 M^2\right)^{0.65}} \tag{8.19}$$

$$FF_{wing} = FF_{tailplane} = \left[1 + \frac{0.6}{(x/c)_m} \left(\frac{t}{c}\right) + 100 \left(\frac{t}{c}\right)^4\right] \left[1.34 M^{0.18} (\cos \Lambda_m)^{0.28}\right] \tag{8.20}$$

The location of the airfoil maximum thickness is given by $(x/c)_m$ and (t/c) is the average thickness-to-chord ratio.

$$FF_{fuselage} = \left(1 + \frac{60}{f^3} + \frac{f}{400}\right) \tag{8.21} \quad FF_{nacelle} = 1 + \frac{0.35}{f} \tag{8.22} \quad f = \frac{l}{d} = \frac{l}{\sqrt{(4/\pi) A_{\max}}} \tag{8.23}$$

The interference factors for various components can be found in Raymer [97].

Additionally, several miscellaneous drag contributions have been added due to fuselage upsweep, fuselage base drag, landing gear, flap deflection, excrescence and wave drag. Table 8.5 provides a summary of the estimated drag values and table 8.6 lists all the different wetted areas as well as the wetted-over-wing-area ratio.

Table 8.5: Overview of the zero-lift drag estimations.

Zero-lift drag coefficient	Method 1	Method 2	Average
C_{D_0} clean	0.0200	0.0148	0.0174
C_{D_0} takeoff*	0.0550	0.0441	0.0495
C_{D_0} landing**	0.1050	0.0810	0.0930

* *Extra drag is present due to landing gear deployment and flap setting of 15 degrees.*
** *Extra drag is present due to landing gear deployment and flap setting of 40 degrees.*

Table 8.6: Overview of the different wetted areas.

Wetted area	Value	Unit
Fuselage	477.93	[m^2]
Wing	224.35	[m^2]
Horizontal stabilizer	68.09	[m^2]
Vertical stabilizer	30.02	[m^2]
Nacelles	56.82	[m^2]
Total	857.21	[m^2]
S_{wet}/S_{wing}	6.47	[-]

8.4.3.2. Induced drag

In order to calculate the drag due to lift, it is required to have an estimate on the Oswald efficiency factor e. Equation 8.24 provides an accurate estimate based on Mach number, aspect ratio, sweep, number of engines and a taper function given by equation 8.25 [111]. When flaps are extended, it is required to enhance the efficiency factor by a certain fraction depending on the flap angle, using equation 8.26 from Roskam [63]. Similarly, twisting the wing has to be accounted for with equation 8.27. The final total drag coefficient values together with their components and the efficiency factor are listed in table 8.7.

$$e = (1 + 0.12 M^6) \left[1 + \frac{0.142 + f(\lambda) A (10 t/c)^{0.33}}{(\cos \Lambda_{c/4})^2} + \frac{0.1 (3 N_e + 1)}{(4 + A)^{0.8}}\right] \tag{8.24}$$

where $f(\lambda)$ is a taper function and N_e is the number of engines.

$$f(\lambda) = 0.005 \left[1 + 1.5(\lambda - 0.6)^2\right] \tag{8.25} \quad \frac{\Delta e}{\Delta \delta_f} = 0.0046 \tag{8.26} \quad \Delta C_{D_i} = 0.00004 \left(\phi_{tip} - \phi_{MAC}\right) \tag{8.27}$$

Table 8.7: Overview of the total drag coefficients.

Flight operation	C_{D_0}	C_{D_i}	C_D	e
Cruise	0.0174	0.0123	0.0297	0.703
Takeoff*	0.0495	0.1746	0.2240	0.772
Landing**	0.0930	0.2374	0.3303	0.887

*Extra drag is present due to landing gear
deployment and flap setting of 15 degrees.
**Extra drag is present due to landing gear
deployment and flap setting of 40 degrees.*

8.4.4. Aircraft aerodynamic performance

Based on the findings in the previous sections, it is now possible to measure the aerodynamic performance of the plane during takeoff, cruise and landing. Table 8.8 clearly shows that the fuel-intensive stages of the mission profile occur during takeoff and landing. However, during cruise we are able to reach a high lift-over-drag ratio of 18.64 which indicates excellent aerodynamic performance for a single-aisle jet. Section 8.7 details this further.

Table 8.8: Overview of the lift and drag characteristics of the aircraft.

Flight operation	Lift [N]	Drag [N]	L/D [-]
Cruise	707,213	37,929	18.64
Takeoff	903,736	95,742	9.44
Landing	618,341	113,266	5.46

8.5. High-Lift Devices and Aileron Control Surfaces

The implementation of mobile surfaces on the wing is a meticulous process that requires special attention due to the space constraints on the wing. There is limited space to fit landing gear, engine nacelles, wing tip devices, flaps and slats.

8.5.1. High-lift device sizing

The HLDs on the leading and trailing edge of a wing serve multiple purposes. They allow the aircraft to perform at optimal conditions during cruise: small wing surface area, small camber and low induced drag, while providing the extra lifting capabilities needed during takeoff and landing as well as runway visibility (hence lift for low angles of attack). As can been seen in section 8.4.2, the wing needs to be able to produce an additional ΔC_L of 1.0464. This will be distributed among the slats and flaps. The main purpose of the slats (slotted leading edge flaps) is to delay stall by decreasing the effective angle of attack and reducing the suction peak that causes flow separation. Because they are slotted, they provide a marginal increase in lift curve slope. The trailing edge flaps provide the real lift increase by increasing the wing surface area and wing camber significantly. This will extend and steepen the lift curve. Additionally, if a single-slotted Fowler flap is chosen, the airfoil curve will be shifted to the left as the flow will generate a fresh, thin and stable boundary layer on the extended flap element, effectively delaying flow separation as well. The flaps were sized using the DATCOM method from Raymer [97]. Equation 8.28 allows calculation of the contribution of a high-lift device and equation 8.29 computes the shift of the lift curve.

$$\Delta C_{L\max} = 0.9 \Delta C_{l\max} \frac{Swf}{S} \cos \Lambda_{\text{hinge\_line}} \tag{8.28}$$

$$\Delta \alpha_{0L} = (\Delta \alpha_{0l})_{\text{airfoil}} \frac{Swf}{S} \cos \Lambda_{\text{hinge\_line}} \tag{8.29}$$

$\Delta C_{l\max}$ depends on the specific HLD type, Swf is the reference wing flapped surface area and $\Lambda_{\text{hinge\_line}}$ is the sweep angle of the connection line of the HLDs, often assumed to equal the sweep of the spars. $\Delta \alpha_{0l}$ is a specific airfoil lift curve shift due to HLD deployment. The contribution of the flaps/slats to

the lift curve slope is calculated with equation 8.30 based on the increased wing surface area due to the extended HLDs, given by equation 8.31,where $\frac{c'}{c}$ is the chord extension ratio of the wing.

$$C_{L\alpha-flapped} = \frac{S'}{S}C_{L\alpha-clean} \qquad (8.30) \qquad\qquad \frac{S'}{S} = 1 + \frac{Swf}{S}(\frac{c'}{c} - 1) \qquad (8.31)$$

The results of the calculations are visualized in figure 8.4. The wing is able to reach the $C_{L_{max}}$ of 2.6823 during landing and stall speed at an angle of attack of 14.5 degrees with a wing incidence angle of 1 degree. This is within the limit of 15 degrees for runway visibility reported by literature [112] and thus the aircraft meets requirement **WFC-AERO-01**. Secondly, the ultimate lift coefficient equals 2.9561 which means the aircraft is able to sustain flight at stall speed with MTOW. The remaining parameters are detailed in table 8.9.
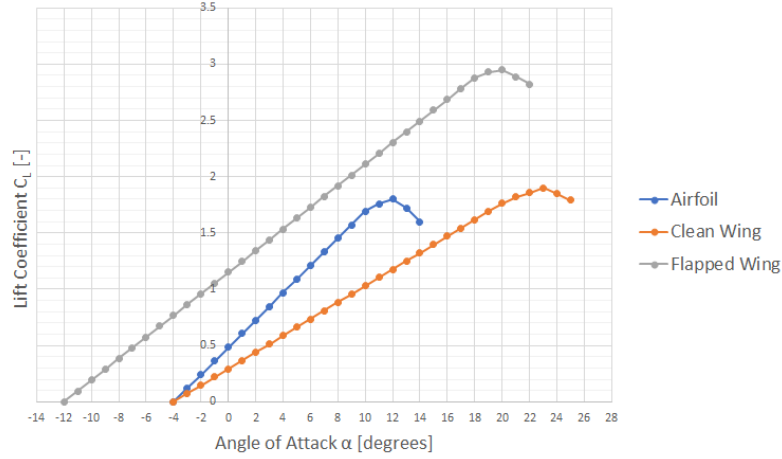

Figure 8.4: Lift curves of the airfoil, clean and flapped wing.

Table 8.9: Final high-lift device parameters.

Parameter	Value	Unit	Parameter	Value	Unit
Flap chord	0.35 [1]	[x/c]	Wetted area flaps	73.28	[m^2]
Slat chord	0.1	[x/c]	Wetted area slats	94.26	[m^2]
Max extended chord ratio flap	1.27	[c'/c]	Increased wing surface ratio flaps	1.15	[-]
Max extended chord ratio slat	1.05	[c'/c]	Increased wing surface ratio slats	1.07	[-]
Max ΔC_L flap	0.821	[-]	Flaps start at	1.94	[m]
Max ΔC_L slat	0.226	[-]	Flaps end at	10.70	[m]
Sweep hinge line flap	29.62	[deg]	Slats start at	2.51	[m]
Sweep hinge line slat	32.77	[deg]	Slats end at	19.93	[m]
Shift in α_0 due to flap	-8.29	[deg]	Flap deflection takeoff	15	[deg]
C_{L_a} fully flapped wing	0.10	[1/deg]	Flap deflection landing	40	[deg]

8.5.2. Aileron sizing

The ailerons are sized to conform with requirement **WFC-CONT-01**. The aircraft's steady state roll rate P can be calculated with equation 8.32. The roll moment coefficient $C_{l_{\delta a}}$ can be found with equation 8.33 and likewise, the roll damping coefficient C_{l_p} is retrieved from equation 8.34.

$$P = -\frac{C_{l_{\delta a}}}{C_{l_p}}\delta_a\left(\frac{2V}{b}\right) \qquad (8.32)$$

$$C_{l_{\delta a}} = \frac{2c_{l\alpha}\tau}{S_{ref}b}\int_{b_1}^{b_2} c(y)y\,dy \qquad (8.33) \qquad C_{l_p} = -\frac{4\left(c_{l\alpha} + c_{d_0}\right)}{S_{ref}b^2}\int_0^{b/2} y^2 c(y)\,dy \qquad (8.34)$$

---

[1]Over the entire span of the yehudi, the flap-to-chord ratio at the TE of the wing equals 0.2 due to landing gear placement and spar location. This is not a problem because the flaps are more effective with a zero-angle hinge line and will make up for the loss in lift.

The maximum allowable deflection angle is given by δ_a, c_{l_α} is the lift curve slope of the airfoil at stall speed (as we size for the most critical case), c_{d_0} is the airfoil's zero-lift drag coefficient, τ is the aileron effectiveness estimated to equal 0.59 based on literature [113], b_i is the location along the wing span, y is the orthogonal distance from the root chord and $c(y)$ is the span-wise chord length as a function of the distance to the root chord. After iterating several times in conjunction with the HLD geometry, the final ailerons are capable of providing a steady roll rate of 32.58 m/s. Several other aileron parameters are listed in table 8.10.

Table 8.10: Final aileron parameters.

Parameter	Value	Unit
Aileron chord	0.39	[x/c]
Wetted area ailerons	28.38	[m^2]
Aileron starts at	10.96	[m]
Aileron ends at	16.93	[m]
Max deflection of the aileron	25	[deg]
$C_{l_{\delta a}}$	0.3015	[-]
C_{l_p}	-0.6830	[-]
Aircraft steady state roll rate	32.58	[deg/s]

8.6. Stability and Control

In order to perform the sizing of the horizontal tail properly, it is first necessary to determine all the possible locations of the center of gravity of the aircraft. This is done by generating the loading diagram of the aircraft which is explained further in subsection 8.6.1. Next, it is possible to calculate the required horizontal tail area for longitudinal stability and control of the aircraft. This is explained in subsections 8.6.2 and 8.6.3. The sizing of the vertical tail is considered in subsection 8.6.4 and the placement of the landing gear is explained in subsection 8.6.5. Finally, the scissor plot and the final values for stability and control are shown in subsection 8.6.6.

8.6.1. Loading diagram

The first step in determining all possible locations of the center of gravity of the aircraft is to determine the center of gravity of the aircraft operational empty weight, which is done by making use of equation 8.35.

$$x_{cg} = \frac{\sum\limits_{i=0}^{n} x_i m_i}{\sum\limits_{i=0}^{n} x_i} \tag{8.35}$$

Here, x_i is the location of the center of gravity of the i-th subsystem relative to the nose of the aircraft and m_i is the mass of the corresponding subsystem, which follows directly from the class II weight estimation described in section 5.3. An overview of all subsystem weights and locations, as well as the final operational empty weight and the aircraft center of gravity are given in table 8.11 below.

The center of gravity range can now be determined by creating the loading diagram of the aircraft. This is done by plotting the center of gravity of the aircraft for all possible ways in which the payload and the fuel can be loaded onto the plane. Equation 8.35 can again be used to calculate the new center of gravity of the aircraft when the passengers, cargo and fuel are loaded onto the aircraft. An overview of the payload and fuel masses and their corresponding locations is shown below in table 8.12.

Table 8.11: Mass and location of center of gravity of each subsystem contributing to the operational empty weight of the aircraft.

Element	Mass [kg]	Location [m]
Fuselage structure	5,780	21.26
Wing stucture	7,920	25.28
Inner engines	4,310.5	20.48
Outer engines	4,310.5	24.03
Empennage	555	40.34
Hydrogen tank	13,361	29.33
Nose landing gear	676	3.5
Main landing gear	1,740	24.58
Other	9,330	12.4
Total	47,983	22.87

Table 8.12: Mass and location of center of gravity of all payloads and fuels.

Element	Mass [kg]	Location [m]
Passenger	81,9	9.39 - 24.11
Cargo hold	2,004	10.81
Hydrogen	2,063	29.33
Biokerosene	6,981	24.04

The final loading diagram can now be plotted by showing where all centers of gravity lie relative to the mean aerodynamic chord and is shown below in figure 8.5. A free body diagram of the aircraft during flight is shown in figure 8.6.
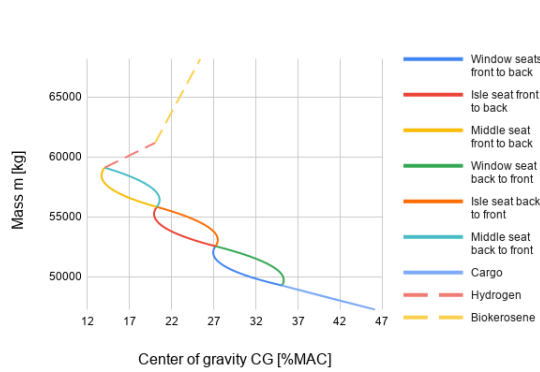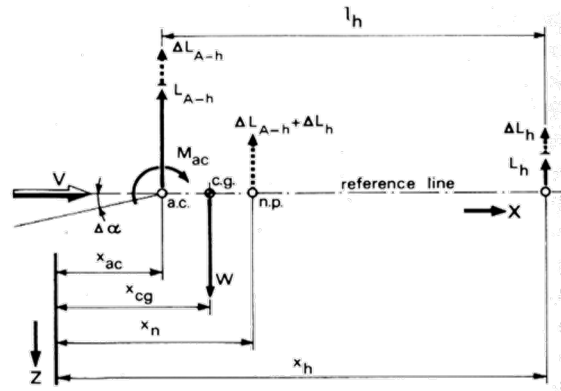

Figure 8.5: Loading diagram of aircraft.

Figure 8.6: Free body diagram of the aircraft during flight [107].

8.6.2. Stability

Now that the most forward and aft centers of gravity are known, it is possible to set up a equation that can provide the horizontal tail size required for stability. This is done by making use of figure 8.6.

To ensure that the aircraft is longitudinally stable, it is required that if the aircraft is perturbed in any direction, the aircraft generates a moment opposite to this perturbation. This means that the aircraft should produce a pitch down moment to any increase in angle of attack. This is mathematically described by equation 8.36.

$$\frac{dC_m}{d\alpha} < 0 \tag{8.36}$$

On any aircraft there exists a point, called the neutral point, around which no change in moment occurs due to a change in angle of attack. Looking at figure 8.6, it becomes evident that in order to comply with equation 8.36, the center of gravity should always lie in front of the neutral point. In this way, if the angle of attack is increased, resulting in a positive change in lift, the aircraft generates a pitch down moment. By taking the moments around neutral point created by the changes in lift, and setting this equal to zero since by definition there is no moment created due to a change in angle of attack, equation 8.37 is obtained.

$$\Delta L_{A-h} \left(\bar{x}_{np} - \bar{x}_{ac} \right) - \Delta L_h \left(\bar{x}_h - \bar{x}_{np} \right) = 0 \tag{8.37}$$

ΔL_{A-h} and ΔL_h are given by equation 8.38 and 8.39 respectively, and the dashes above the x's indicate that the location is divided by the mean aerodynamic chord $\bar{c}$.

$$\Delta L_{A-h} = C_{L_{\alpha_{A-h}}} \Delta\alpha \frac{1}{2}\rho V^2 S \tag{8.38} \qquad \Delta L_h = C_{L_{\alpha_h}} (\Delta\alpha - \Delta\epsilon) \frac{1}{2}\rho V_h^2 S_h \tag{8.39}$$

Substituting these equations into equation 8.37, and rewriting it results in equation 8.40.

63

$$\bar{x}_{np} = \bar{x}_{ac} + \frac{C_{L_{\alpha_h}}}{C_{L_{\alpha_{A-h}}}} \left(1 - \frac{d\epsilon}{d\alpha}\right) \frac{S_h l_h}{S\bar{c}} \left(\frac{V_h}{V}\right)^2 \tag{8.40}$$

Since the center of gravity must stay ahead of the neutral point, it is wise to introduce a static stability margin $SM = \bar{x}_{np} - \bar{x}_{cg}$ which is usually set to 5% [97]. Substituting equation 8.40 into this formula and rewriting results in equation 8.41 which gives the most aft allowed center of gravity of the aircraft.

$$\frac{S_h}{S} = \frac{1}{\frac{C_{L_{\alpha_h}}}{C_{L_{\alpha_{A-h}}}} \left(1 - \frac{d\epsilon}{d\alpha}\right) \frac{l_h}{\bar{c}} \left(\frac{V_h}{V}\right)^2} \bar{x}_{c.g.} - \frac{\bar{x}_{ac} - 0.05}{\frac{C_{L_{\alpha_h}}}{C_{L_{\alpha_{A-h}}}} \left(1 - \frac{d\epsilon}{d\alpha}\right) \frac{l_h}{\bar{c}} \left(\frac{V_h}{V}\right)^2} \tag{8.41}$$

An extensive overview of all formulas used to determine the parameters in equation 8.41 is given in appendix B.

8.6.3. Control

To determine the required horizontal tail area in order to keep the aircraft controllable, the trim condition is considered during the landing, since that is the most critical flight condition for the controllability of the aircraft. The trim condition is the equilibrium condition of the aircraft which means that all moments are zero. Taking the moments around the aerodynamic center in figure 8.6 results in equation 8.42.

$$M = M_{ac} + W(x_{cg} - x_{ac}) - L_h l_h \tag{8.42}$$

After assuming $W = L_{A-h}$ and making equation 8.42 dimensionless, equation 8.43 is obtained.

$$C_m = C_{m_{ac}} + C_{L_{A-h}}(\bar{x}_{cg} - \bar{x}_{ac}) - \frac{C_{L_h} S_h l_h}{S\bar{c}} \left(\frac{V_h}{V}\right)^2 = 0 \tag{8.43}$$

Since all moments are zero in the trim condition, this equation can be set to zero as well. It is now possible to rewrite equation 8.43 to find the relative horizontal tail area required for controllability. The result is shown below in equation 8.44.

$$\frac{S_h}{S} = \frac{1}{\frac{C_{L_h}}{C_{L_{A-h}}} \frac{l_h}{\bar{c}} \left(\frac{V_h}{V}\right)^2} \bar{x}_{cg} + \frac{\frac{C_{m_{ac}}}{C_{L_{A-h}}} - \bar{x}_{ac}}{\frac{C_{L_h}}{C_{L_{A-h}}} \frac{l_h}{\bar{c}} \left(\frac{V_h}{V}\right)^2} \tag{8.44}$$

The formulas used to determine all parameters in equation 8.44 can again be found in appendix B.

8.6.4. Lateral stability

In order to size the vertical tail of the aircraft, the most critical flight condition must be analysed. For an aircraft with wing mounted engines, this condition is during takeoff with one engine inoperative. The following equation is obtained from Torenbeek [107] and it calculates the vertical tail area required to counteract the moment created by the engines which are still operative.

$$\frac{S_v}{S} = \frac{1}{\eta_v C_{Y_{v_\alpha}}} \frac{C_L \frac{Y_e}{l_v} \frac{\Delta T_e}{W} + \beta C_{n_{\beta_{A-h}}} \frac{b}{l_v}}{\tau_v \delta_r - (\beta - \sigma_v)} \tag{8.45}$$

The definition of the variables in equation 8.45 can be found in appendix B.

8.6.5. Ground stability

The aircraft should not only be stable during flight, but also when it is on the ground. An example of a situation which needs to be avoided at all times is having the center of gravity of the aircraft behind the main landing gear, since this would mean that the aircraft will tip backwards. To avoid this, the main landing gear should be placed behind the most aft center of gravity of the aircraft. Furthermore, the main landing gear should also not be placed too far aft, since that would mean that the nose landing gear will carry a large portion of the aircraft weight. This is unwanted since that would require a very large and heavy landing gear. The optimum location for the main landing gear is such that the weight on the nose landing gear is between 8% and 15% of the total aircraft weight for the most aft and forward center of gravity respectively [97]. To calculate where the most forward and aft center of gravity may be in order to satisfy this requirement, figure 8.7 is used. By setting the distance between the nose landing gear and the nose of the aircraft to d_N, the distance between the main landing gear and the nose of the

aircraft to d_M and taking the moments around the nose of the aircraft, equation 8.46 is found. After dividing both sides by W, equation 8.47 is obtained.

$$d_N F_N + d_M F_M = x_{cg} W \quad\quad (8.46) \quad\quad\quad d_N \frac{F_N}{W} + d_M \frac{F_M}{W} = x_{cg} \quad\quad (8.47)$$

As aforementioned, for the most forward center of gravity $\frac{F_N}{W}$ should be equal to 0.15, which automatically means that $\frac{F_M}{W} = 0.85$ and for the most aft center of gravity, $\frac{F_N}{W}$ should be equal to 0.08 and $\frac{F_M}{W} = 0.92$. Furthermore, assuming the nose landing gear to be located 3.5 m from the nose, and the main landing gear at 80% of the root chord, the center of gravity limits can be calculated.

For the lateral placement of the landing gear, figure 8.8 is used. From Raymer [97] it is obtained that the turn-over angle Ψ should be less than 55 degrees. Furthermore, the landing gear height can be determined from figure 8.9. In order for the aircraft to meet with certification specifications regarding the injection of foreign objects into the engines, the ground clearance angles Φ_0 and Φ_1 should be more than 5 and 8 degrees. Finally, the landing landing gear should also be long enough to make sure that the tip-back angle required for a tail strike is more than 15 degrees.
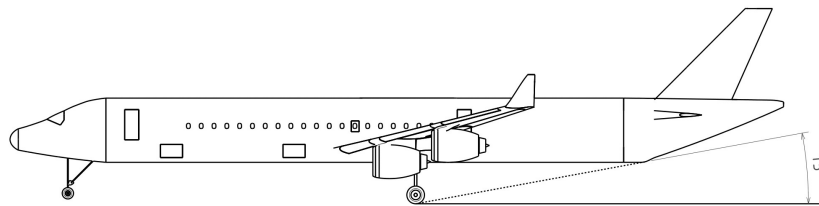

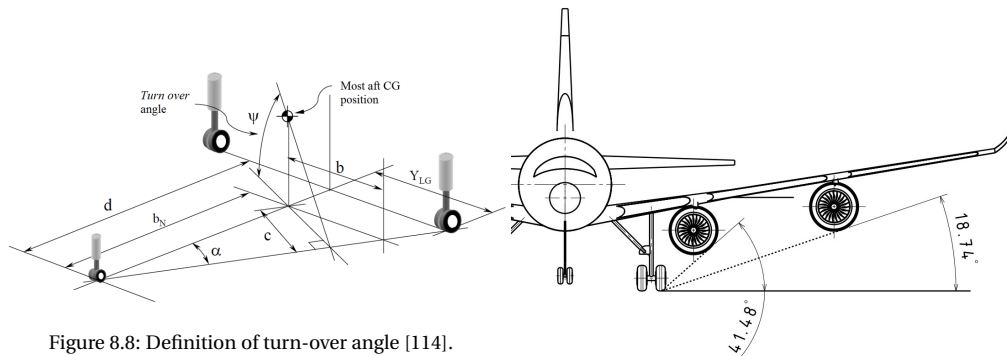Figure 8.7: Free body diagram of an aircraft on the ground

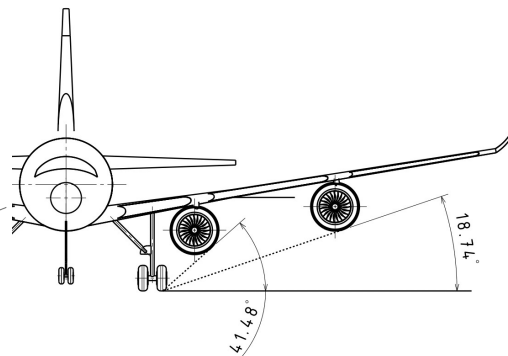Figure 8.8: Definition of turn-over angle [114].

Figure 8.9: Ground clearances of the engines.

8.6.6. Scissor plots

Now that equations 8.41 and 8.44, which describe the relative horizontal tail area as a function of the aircraft center of gravity, as well as equation 8.47, which sets the center of gravity limits for ground stability, have been obtained, it is possible to plot the scissor plot of the aircraft. The result is shown in figure 8.10. In this figure, the most forward and aft center of gravity locations of the aircraft obtained from figure 8.5 are also shown. In order for the aircraft to be stable, all possible centers of gravity must lie to the right of the stability line. Whilst in order for the aircraft to be controllable, all possible centers of gravity of the aircraft must lie to the right of the control line. As can be seen from figure 8.5, the smallest possible horizontal tail area for which these requirements hold is 32 % of the main wing area.

The most aft and forward centers of gravity of the aircraft as obtained from figure 8.10 are for the case where the aircraft is carrying its maximum payload weight. However, there will also be times when the aircraft is not fully loaded and in some cases it might even be completely empty. The loading diagram of the aircraft when the fuel is loaded first is shown in figure 8.11. In this diagram, the most forward and aft allowed center of gravity limits for ground stability are shown as well. As can be seen, if the aircraft

is only loaded with fuel, the aircraft center of gravity exceeds the most aft allowed center of gravity for ground stability. This means that the aircraft cannot take off with only fuel on board. If the aircraft thus need to be flown without passengers, the cargo hold needs to be filled with a mass of 2000 kg since this shifts the aircraft center of gravity within the limits. During flight, when the aircraft is burning up fuel, the center of gravity will shift even further forwards, making the aircraft more stable. Finally, if there is no cargo on board and the passengers need to disembark quickly, the aircraft will not run into stability problems since the center of gravity of the aircraft lies in front of the main landing gear in all loading configurations.

An overview of the most important parameters obtained from the stability and control analysis is shown in table 8.13 below.

Table 8.13: Overview of most important parameters obtained from the stability and control analysis.

Parameter	Value	Unit	Comment
Horizontal tail area	42.4	[m^2]	
Vertical tail area	18.3	[m^2]	
Longitudinal location of mean aerodynamic chord	20.81	[m]	Measured from the nose of the aircraft
Longitudinal location of nose landing gear	3.5	[m]	Measured from the nose of the aircraft
Longitudinal location of main landing gear	24.55	[m]	Measured from the nose of the aircraft
Lateral location of main landing gear	3.6	[m]	Measured from center line
Landing gear height	3.1	[m]	Distance from ground to wing center line
Horizontal tail arm	15.04	[m]	Distance between aerodynamic centers
Vertical tail arm	12.16	[m]	Distance between aerodynamic centers
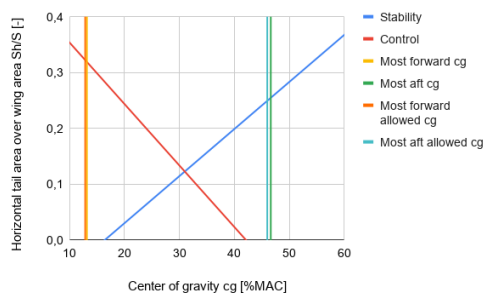
Figure 8.10: Scissor plot of the aircraft when loading payload first
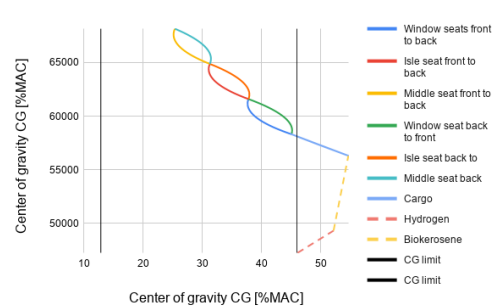
Figure 8.11: Loading diagram of aircraft with fuel loaded first

8.7. Verification and Validation

In the process of analyzing a certain system, it is important to perform verification and validation of the methodology applied throughout the analysis. In this section, the verification and validation of the aerodynamic analysis is explained in subsection 8.7.1 and the verification and validation of the stability and control analysis is described in subsection 8.7.2.

8.7.1. Aerodynamic performance

The lift and drag characteristics of the airplane, discussed in section 8.4, have been verified in multiple ways. For example, by comparing the C_D values with historical data from Roskam[63] and simulating the lift distribution in vortex lattice models such as the Athena Vortex Lattice (AVL) software, created by Prof. Mark Drela[2]. The results of the C_D comparison are shown in table 8.14.

---

[2] http://web.mit.edu/drela/Public/web/avl/

Table 8.14: Verification of the drag coefficients [63].

Flight operation	C_{D_0}	Roskam	C_{D_i}	Roskam
Cruise	0.0174	0.0168	0.0123	0.0111
Takeoff	0.0495	0.0518	0.1746	0.1633
Landing	0.0930	0.1018	0.2374	0.2409

The computed drag characteristics of the airplane stay within 5% of the values provided by Roskam, hence are deemed feasible. Moreover, the lift-over-drag ratio was verified with a publication of the International Civil Aviation Organization on the environmental outlook of aviation [115]. Figure 8.12 showcases the historical trend in lift-over-drag performance for single- and double-aisle aircraft for the past 50 years. Single-aisle aircraft upon entry into service in 2020 will have an L/D ratio close to 18. By 2036, when the SHOTS aircraft is expected to enter the market, it should be feasible to reach an L/D ratio of 18.64. It is believed that the increasing use of CFRP in design will lead to bigger parts build out of one-piece and smoother surface transitions, therefore optimizing the drag performance even better[3].
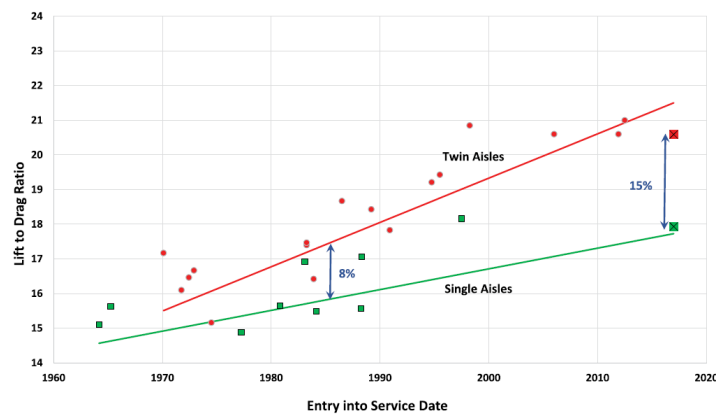
Figure 8.12: Historical trend in lift-over-drag ratio [115].

Figure 8.13 and figure 8.14 show the Trefftz-plane analysis of the lift distribution and induced angle of attack for different wing geometries. The trapezoidal wing's local C_l curve clearly indicates increased wing tip loading due to sweep, yet the lift distribution (the C_l curve normalized with respect to the MAC) closely resembles an elliptical distribution but with a dip at the center due to interference. By adding a yehudi, the lift magnitude at the center gets a sharp increase and wing tip loading is decreased. This will be beneficial to overcome drag interference of the fuselage which is not modelled here. Lastly, by adding wing tip devices (wing + wtd curve), the induced drag of the wing is reduced. This is clearly visible in figure 8.14 at the span edges where the induced angle of attack is reduced significantly. This will add to the aileron effectiveness as well. The estimated C_{D_i} for the wing at Mach cruise without winglets is 0.0113, which complies with the values from table 8.14. Adding the winglets would result in a further reduction, leading to a C_{D_i} value of 0.0086. Because the aircraft is limited in span due to <36 m span constraint, it is therefore justified to install winglets on the wing if proper structural integration is applied in the process.

---

[3]Information obtained from Deutschen Gesellschaft für Luft- und Raumfahrt's webinar regarding 'Aircraft recycling and dismantling from design to execution' (accessed 17-06-2020)

Figure 8.13: Trefftz-plane analysis of the lift distribution.

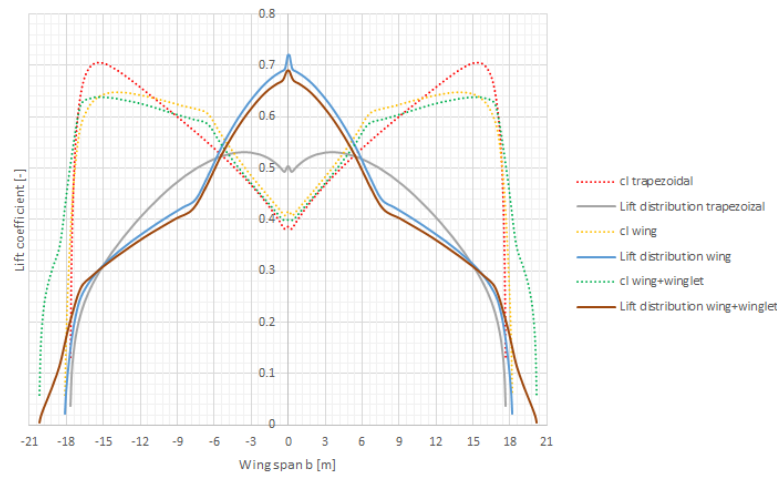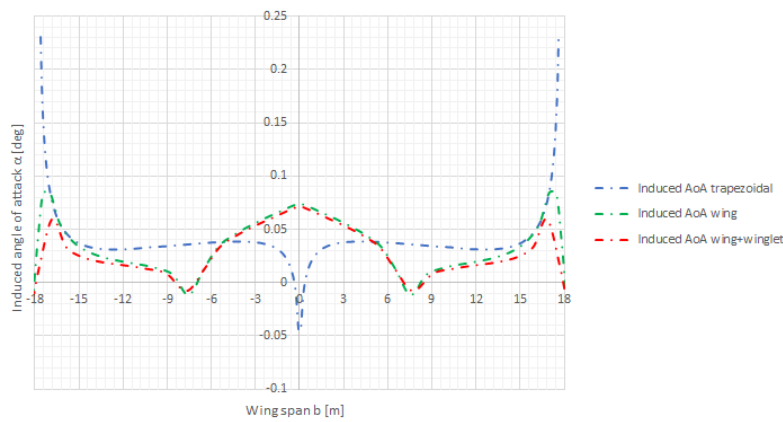Figure 8.14: Trefftz-plane analysis of the induced angle of attack.

8.7.2. Stability

In order to verify the method used to size the horizontal and vertical tail and the landing gear position, the Airbus A220-100 was also analysed. The loading diagram is shown in figure 8.15, where all required data was obtained from the Airbus A220-100 Airport planning publication [116] and the Airbus A220-100 Aircraft recovery publication [117]. From the loading diagram it is seen that the aircraft center of gravity always lies within the limits, except when only the forward cargo hold is loaded. This does not result in any problems, since it is very easy to distribute the cargo over the forward and aft cargo holds.

Next, the scissor plot was created which is shown in figure 8.16. In this figure, the most forward and aft centers of gravity allowed for takeoff are also shown. From the Airbus A220-100 Airport planning publication [116] it is found that the horizontal tail surface area of the Airbus A220 is 32.6 % of the wing surface area. Looking at figure 8.16 is can be seen that this puts a forward limit on the aircraft center of gravity of about 12 % MAC. Furthermore, it can be seen that the most aft allowed center of gravity for ground stability is approximately 30 % MAC.

From the Airbus A220 Aircraft recovery publication [117] the actual center of gravity limits are obtained and shown in figure 8.17. As can be seen, the most forward center of gravity limit is 12 % MAC, just as expected from the scissor plot shown in figure 8.16. Furthermore, the most aft allowed center of gravity during takeoff is between 26 and 36 % MAC. This also corresponds to the most aft allowed center of gravity calculated. The only difference between the calculated center of gravity limit and the actual center of gravity limit of the Airbus A220 is that the actual allowed center of gravity limit shifts backwards with increasing aircraft weight. This can be appointed to the fact that for the most aft allowed center of gravity calculation, a minimum weight fraction of 8 % on the nose landing gear was assumed. This is to ensure that there is enough friction between the nose landing gear and the ground. However, if the

68

aircraft becomes heavier, the weight on the nose landing gear increases as well. Even if the center of gravity shifts backwards, thus reducing the fraction of the weight on the nose landing gear below 8%, there will still be enough friction for ground control. A final important observation to be made is the fact that there is an aft limit to the aircraft center of gravity of 37 % MAC. This might be set due to the fact that if the center of gravity moves further backwards, the drag produced by the horizontal tail becomes too large.
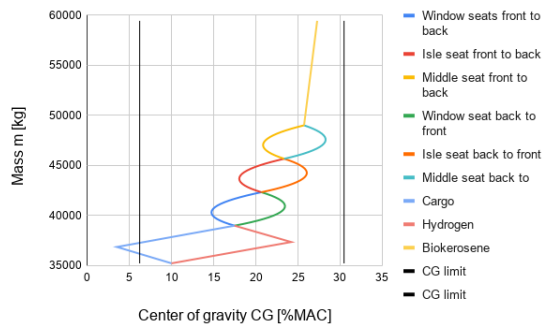

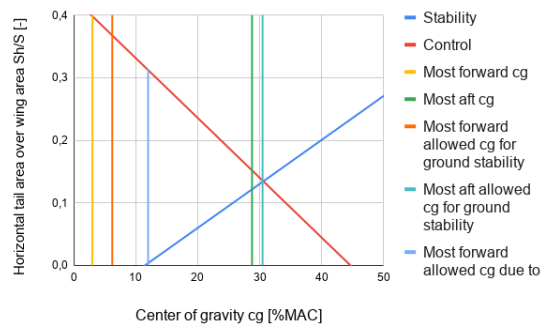Figure 8.15: Loading diagram of Airbus A220.
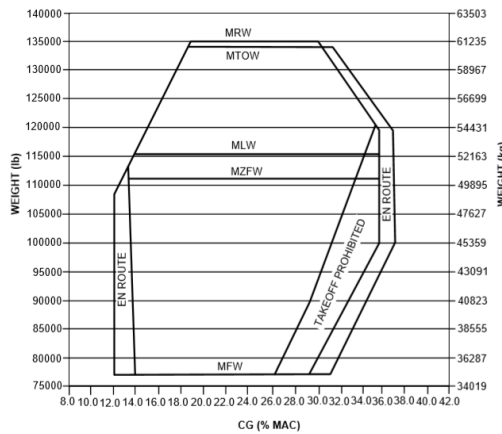

Figure 8.16: Scissor plot of Airbus A220.

Figure 8.17: Airbus A220-100 center of gravity limits [117].

69

<div align="right">

9

</div>

System Characteristics

In this chapter, two systems in the SHOTS aircraft are discussed in more detail. These two systems are the hydrogen tank and the modular design, both of which are significantly different from conventional aircraft. First, the hydrogen tank requirements are discussed in section 9.2. Second, fatigue and damage tolerance are taken into account to size the hydrogen tank in detail, as discussed in section 9.2. This section uses the initial sizing of the hydrogen tank as a basis, which was discussed in subsection 5.1.2. Then, the safety aspects of the hydrogen tank and the refueling process are examined in section 9.3 and section 9.4 respectively. The fifth topic is the modular design which is discussed in section 9.5. This design focuses on the removal of the tail cone from the fuselage such that the hydrogen tank can be removed for inspection and maintenance. Lastly, the hydrogen tank sizing and refueling process are verified and validated in section 9.6.

9.1. Hydrogen Tank Requirements

One of the key elements of the SHOTS aircraft is the hydrogen propulsion system which makes the design different from conventional aircraft. The main functions of the hydrogen system are as follows:

- The tank stores the hydrogen for use during operations.
- The piping system transports the hydrogen to the engines.
- The refueling system resupplies the hydrogen on the ground.

Based on these functionalities, the following requirements can be formulated in addition to the ones listed in section 5.1.

- ***WFC-TANK-03****: The tank shall operate for the complete operational life of the aircraft, which is assumed to be 43,800 cycles.* This stems from the market analysis. Furthermore, it is not very practical to replace the tank multiple times during operations.
- ***WFC-TANK-04****: The tank shall sustain structural damage done to the tank in the form of bullets and small cracks up to 50 millimeters.* This stems from the ISO/TS 15869 requirements.
- ***WFC-TANK-05****: The materials used for the tank shall be recycled for 100%.* This holds for both the load carrying material and the liner.
- ***WFC-TANK-06-1****: The refueling system shall refuel 80% of the tank within 16 minutes.* This ensures competitiveness with the Embraer E195-E2 [118].
- ***WFC-TANK-07****: The engine supply system shall be able to transport the hydrogen from tank to engine also in case of malfunctioning.* From chapter 7, it was concluded that unavailability of the hydrogen propulsion system has a very negative impact on the performance of the aircraft.

9.2. Hydrogen Tank Fatigue and Damage Tolerance

In section 5.1 only the static loading case was considered for the hydrogen tank. Therefore, in this section, the tank is analyzed in more detail. The same general requirements and assumptions as listed in section 5.1 hold. In subsection 9.2.1 the hydrogen tank fatigue sizing is discussed. This is followed by damage tolerance considerations specifically for the tank in subsection 9.2.2. Then, a material trade-off for the tank is performed in subsection 9.2.3 based on tank mass, unit cost and allowable crack size.

9.2.1. Fatigue sizing

Here, the hydrogen tank is sized for fatigue or cyclic loading condition. The fatigue sizing ultimately determines the required tank wall thickness to fulfill the requirement that the tank can be used for the

complete operational lifetime of the aircraft: 43,800 cycles.

For this, several assumptions are made:

- The tank wall is only loaded in tension.
- The loading of the tank ranges between 0 and the maximum applied load. This means that the stress ratio R, defined as $R = \frac{S_{min}}{S_{max}}$, equals zero.
- The tank is fully pressurized and depressurized during one cycle.
- For composites, the maximum allowable stress amplitude reduces by 20% over 10 million cycles. For CFRP this is accurate [119]. For Kevlar, this is slightly conservative [120], [121]. This means that the fatigue strength $S_f = 0.8 \cdot S_{UTS}$ where S_{UTS} denotes the ultimate tensile strength.
- For 2800 Steel, a fatigue ratio S_f/S_{UTS} of 0.3 is assumed for 1 million cycles. This is based on similar (though lower strength) steel alloys [122] and that the ratio decreases as S_{UTS} increases[1] [123]. This assumption is on the safe side, as Wang et al. [124] found a ratio of 0.41667.
- The design number of cycles is multiplied with a safety factor of 8 for metals and 16 for composites to account for the spread observed in S-N curves. The design number of cycles is 43,800. Therefore, the allowable stress amplitude for metals occurs at 350,400 cycles and for composites at 700,800 cycles.

For the tank sizing, the same approach is used as in subsection 5.1.2. However, there is one difference: the allowable stress for the static sizing is equal to S_y. For fatigue, this stress is first calculated based on the fatigue analysis. The allowable stress of composites and materials for a given number of cycles can be determined by using a Wöhler curve [123]. Because Wöhler curves for the four tank materials do not exist, they are constructed following the method in Schijve [123]. This method is also used in section 10.5. The Wöhler curves show the relation between the stress amplitude S_a and the number of cycles N using a log-log scale. In this way, the relation can be approximated by two horizontal asymptotes and a linear middle region. The linear region can be approximated by the Basquin relation [123] in equation 9.1.

$$S_a^k \cdot N = \text{constant} \tag{9.1}$$

First, the upper asymptote is determined by the S_{UTS} of each material, so $S_a = S_{UTS}$. Then for metals, S_a is constant up to 100 cycles and then linearly decreases to the fatigue limit at 1 million cycles for steels and 10 million cycles for aluminum alloys [123]. For composites, the curve decreases linearly to the fatigue limit at 10 million cycles. The fatigue limit is found by $S_f = \alpha \cdot S_{UTS}$. For high-strength steels $\alpha \approx 0.3$, for aluminium alloys $\alpha \approx 0.35$ and for composites $\alpha \approx 0.8$.

Secondly, the previous steps are valid when the mean stress S_m is 0. If the mean stress is not zero the asymptotes have to be adjusted accordingly. The upper asymptote is defined by $S_a = S_{UTS} - S_m$ and the lower asymptote is calculated using the Goodman relation [123]. This relation assumes fatigue strength decreases linearly with increasing S_m, as shown in figure 9.1. The new value of S_f is found at the intersection of the Goodman curve and the curve for $S_m = S_a$.
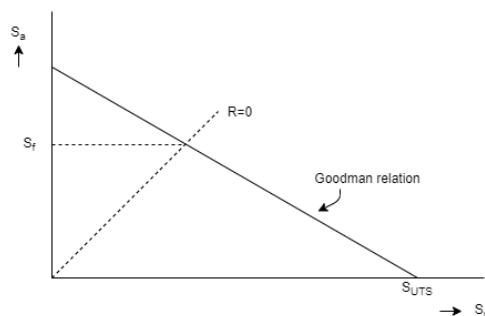
Figure 9.1: Fatigue strength determination for R = 0. Adapted from Schijve. [123]

Thirdly, the effect of notches in the materials is taken into account with the notch factor K_t [123]. Depending on the notch size, the factor K_t has to be adjusted for metals and then K_f is used. K_f is defined

---

[1] `https://www.engineeringtoolbox.com/steel-endurance-limit-d_1781.html` (accessed 09-06-2020)

by the notch sensitivity q, which is obtained graphically from Schijve [123]. Using equation 9.2 K_f is calculated.

$$q = \frac{K_f - 1}{K_t - 1} \qquad (9.2)$$

Composites generally have high notch sensitivity, which means $q \approx 1$ and $K_t \approx K_f$. For fiber metal laminates such as GLARE, the average q of the metal and composite layers is used. For metals, K_t or K_f only applies for the reduction of the fatigue limit by this factor, while the upper asymptote remains unaffected. For composites, both the asymptotes are reduced.

The value of K_t depends on loading conditions. For the fatigue analysis of the fuel tank, tensile bi-axial loading is assumed, resulting in $K_t = 2.5$.

For the four materials used for the tank sizing, figure 9.2 shows the constructed Wöhler curves. On the x-axis, N denotes the amount of cycles. On the Y-axis, S_a denotes the amplitude of the stress.
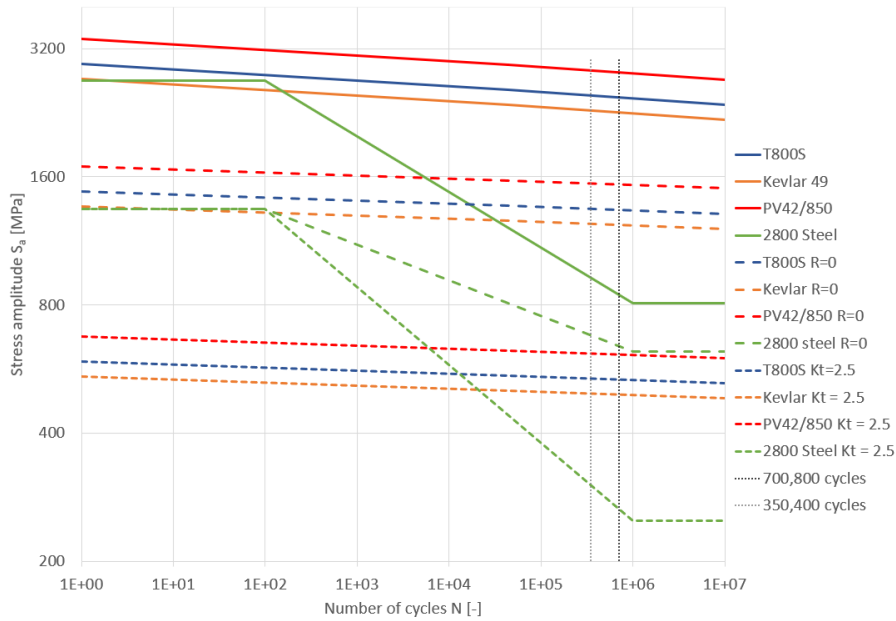
Figure 9.2: Wöhler curves for four materials used for the tank. Blue is T800S, orange is Kevlar 49, red is PV42/850 and green is 2800 Steel. The vertical dotted lines denote the number of cycles for which the material is designed.

For 2800 Steel, the allowable stress amplitude at 350,400 cycles equals 349 MPa. For T800S, Kevlar 49 and PV42/850 at 700,800 cycles the allowable stress amplitude is 535 MPa, 494 MPa and 613 MPa respectively. The relation between stress amplitude and applied stress is shown in equation 9.3.

$$S_a = \frac{S_{max} - S_{min}}{2} \qquad (9.3)$$

Due to the cyclic pressurization loading, $S_{min} = 0$ and thus the maximum allowable stress S_{max} is simply twice the stress amplitude S_a. The maximum allowable stresses are input for the fatigue sizing of the tank, resulting in the load-carrying material thickness as reported in table 9.1.

Table 9.1 shows the weight breakdown of the hydrogen tank for all four materials. The values for the total tank weight **in bold** denote the design weight, either defined by the static or the fatigue sizing.

Table 9.1: Weight breakdown for hydrogen tank containing 2063 kg of hydrogen under a pressure of 700 bar.

Parameter	Toray T800S		DuPont Kevlar 49		Hexcel PV42/850		2800 maraging steel	
	Static	Fatigue	Static	Fatigue	Static	Fatigue	Static	Fatigue
Thickness liner [mm]	5	5	5	5	5	5	5	5
Thickness load carrying material [mm]	101	99	109	107	88	86	60	100
Liner weight [kg]	374	373	376	375	370	370	363	373
Load carrying material weight [kg]	15,147	14,678	14,632	14,221	12,992	12,686	34,995	61,721
Total tank weight [kg]	**15,520**	15,050	**15,008**	14,586	**13,361**	13,055	35,358	**62,093**

9.2.2. Damage tolerance sizing

The damage tolerance indicates how well the structure can sustain certain damage, for example a fan blade of the engine piercing through the wall. Furthermore, in chapter 13 the risk of a tank rupture due to ground impact is discussed. The tank must be able to sustain a crack due to this impact. Because the tank is already protected by the fuselage, the tank does not need to fulfill the same requirement, but cracks due to bullet holes can still occur.

For the damage tolerance, the fracture toughness of the material plays a vital role. By obtaining the fracture toughness, one is able to give a more sophisticated prediction of the remaining strength of the material [32][125]. In this analysis, only the fracture toughness associated with mode I cracks has been evaluated. This corresponds with the situation shown in figure 9.3 that an object pierces through the skin that is loaded in tension.
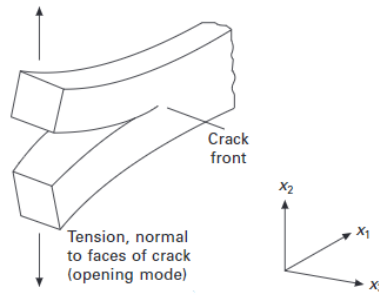
Figure 9.3: A mode I crack (obtained from *Introduction to Aerospace Materials* [126]).

The fracture toughness of a material is defined by equation 9.4 [32].

$$K_{Ic} = S_{crit}\sqrt{\pi a_{crit}} \tag{9.4}$$

Mouritz [126] provides ranges for the values of K_{Ic} for metals and composites. Furthermore, a study from NASA using the CODSTRAN model [127] is also used to obtain the values for K_{Ic} of composites. It should be noted that the values from NASA [127] are a factor 10 higher than found in Mouritz [126]. This is realistic because the crack propagation through the material will not be comparable to metal, where all the stress intensity is found at the tip of the crack. In contrast, Wisnom et al. found that due to the strong fibers the crack will deflect and split along the fibers [128]. This effectively increases the area of the crack, hence lowering the stress intensity. For this, it is vital that the layers of fiber are alternating in orientation. Therefore, hoop winding and helical winding need to be alternated during production. Using the hoop stress present in the material due to pressurization, the critical crack length $2a$ can be obtained. These are reported in table 9.2.

Table 9.2: Damage tolerance analysis.

Parameter		T800S	Kevlar 49	PV42-850	2800 Steel	Unit
Skin thickness	t	101	109	88	100	[mm]
Fracture toughness	K_{Ic}	460	460	460	150	[MPa$\sqrt{m}$]
Hoop stress	σ_{hoop}	1,171	1,079	1,352	1,178	[MPa]
Allowable crack size	2a	98	116	74	10	[mm]

Table 9.2 shows that the tank can withstand certain impacts without failure. This is deemed sufficient because the fuel tank is also protected by the fuselage. Furthermore, the fracture toughness can be increased by changing the matrix composition. Companies such as Hexcel have developed custom made epoxy resins like HexPly 8552 just for this purpose[2].

9.2.3. Tank material trade-off

Four materials have been considered for the construction of the hydrogen tank. These materials will be evaluated based on four criteria, after which the optimal material for the tank is selected. The trade-off criteria are the weight of the tank, the cost, the safety and the recyclability of the tank.

Tank weight: for each material the tank has a different weight, because the thickness and the density of the load carrying material changes. The weight is a vital criterion because it influences the performance of the aircraft and also has a direct effect on the operational cost. Calculations have shown that for every 1,000 kg reduced, the operational costs lower by approximately 5 million USD. Furthermore, because the tank is located in the back, weight is important to consider as it has a strong influence on the stability of the aircraft as discussed in section 8.6.

Tank unit cost: for the cost of the production of one fuel tank, data from Composite World[34], Lucintel [129], Industry Experts [130] and CEMAC [131] is used. These sources report the price of composite pressure vessels in different ways: /L, /kg_{tank} and /kg_{H_2}. Based on these references, the cost for the three composite fuel tanks is estimated. For steel, the cost is based on the current market price for steel[5] and a quotation at IndiaMart[6].

Safety: the safety of the tank is assessed based on the damage tolerance as discussed in subsection 9.2.2. The allowable crack length per material is used to evaluate this.

Recyclability: the recyclability of the material used for the fuel tank is very important. Not only the technical feasibility is investigated, but also the economics. The following questions are used to investigate the economics: Are there companies making money by recycling these materials? Is the recycled material of the same quality as before or is the material downcycled?

The weight, cost and damage tolerance of each tank is summarized in table 9.3.

Table 9.3: Tank mass, unit cost and allowable crack size of the tank for four different materials.

Criterion	T800S	Kevlar 49	PV42/850	2800 Steel
Tank mass [kg]	15,520	15,008	13,361	61,957
Unit cost [$]	681,300	667,500	628,520	1,625,000
Allowable crack size [mm]	98	116	74	10

For the recyclability of the material, the information from chapter 6 is used and this is combined with a material-specific market analysis.

For T800S and PV42/850, recycling the material is technically possible but because of the high cost and lack of demand, companies such as AELS are currently not recycling their CFRP [35]. However, with the enormous increase in demand for CFRP in both aerospace and pressure vessel industry [131], the authors expect that when the aircraft comes to the market, this will be economically viable. In conclusion, both CFRPs receive a score of 2 for recycling.

For Kevlar 49, there is a large market for recycled material. This is because the pulp that is produced during recycling can be used in safety equipment[7] [132] and as a replacement for asbestos[8]. However, this is considered downcycling because the material cannot be used for the same application. Therefore, the score for Kevlar is 3.

---

[2]hexcel.com/user_area/content_media/raw/HexPly_8552_eu_DataSheet.pdf (accessed 18-06-2020)
[3]https://www.compositesworld.com/articles/pressure-vessel-tank-types (accessed 15-06-2020)
[4]https://www.compositesworld.com/articles/next-generation-pressure-vessels (accessed 15-06-2020)
[5]https://worldsteelprices.com/ (accessed 15-06-2020)
[6]https://dir.indiamart.com/impcat/maraging-steel.html (accessed 15-06-2020)
[7]https://www.brentindustries.com/aramid/ (accessed 15-06-2020)
[8]https://www.teijinaramid.com/nl/over-ons/duurzaamheid/recycling/ (accessed 15-06-2020)

For 2800 Steel, similar to other metals, the material is simply 'put back in the smelter' after which new products can be made with the same properties. Recycling this kind of first grade scrap is easy [35]. Therefore, this material receives a score of 4.

The final trade-off is shown in table 9.4.

Table 9.4: Final trade-off for the material selection.

Criteria	Weight	T800S	Kevlar 49	PV42/850	2800 Steel
Tank mass	0.4	2	3	4	1
Unit cost	0.2	2	3	4	1
Damage tolerance	0.2	2	4	3	1
Recyclability	0.2	2	3	2	4
	Total	**2**	**3.2**	**3.4**	**1.6**
	Rank	**3**	**2**	**1**	**4**

To assess the robustness of the trade-off, a sensitivity analysis has been performed.

First, the criteria are taken out one by one by setting their weights to zero. For both the tank mass and unit cost, this changed the ranking of the material. By taking out the tank mass criterion, Kevlar 49 is now the preferred material with a score of 3.3, followed by PV42/850 with 3.0. By taking out the unit cost criterion, Kevlar 49 and PV42/850 share the first place with a score of 3.25.

Secondly, the weights of the criteria have been increased by 0.2 one by one. By increasing the damage tolerance to 0.4, Kevlar 49 is now the best material with a score of 3.4, followed by PV42/850 with 3.3. By increasing the recyclability criterion to 0.4, Kevlar 49 is the best material with a score of 3.15, followed by PV42/850 with 3.05.

It is shown that Kevlar 49 has a very similar performance to the Hexcel PV42/850. Therefore, it will also be certified as tank material. This makes sure that when the Hexcel CFRP is unavailable or that when the trade-off criteria weights change during later stages in the design, a good back-up material is available. The material used for the design is Hexcel PV42/850 CFRP with HDPE as liner.

9.3. Safety of the Hydrogen Tank

The final aspect is the safety of the hydrogen tank. Tests in order to determine how safe the pressure vessels are differ from dropping it from a certain height to firing a bullet at the tank[9]. The ability of the hydrogen tank to sustain certain damage has been analyzed in subsection 9.2.2. Now, additional safety measures to protect the airframe and passengers are explained. These stem from the risk analysis as discussed in section 13.3.

Failure of the hydrogen tank could pose a serious risk for the safety of the passengers. To mitigate this risk, five aspects of the integration of the hydrogen tank in the aircraft have been considered.

To begin with, the most risky part of the hydrogen tank, the opening with the valves, is pointed to the back of the aircraft. In case the valves shear of the tank, the stream of hydrogen is pointed backwards, away from the passengers. However, this poses the risk of the tank moving forward as a reaction, turning into a rocket (just like this video [10]). The initial force of the hydrogen escaping at the back is estimated by $F = p \cdot A$ with p being the pressure difference between the inside and outside of the tank, in this case 700 bar or $7 \cdot 10^7$ Pa, and A the cross sectional area of the opening in m^2. It is assumed that the valves shear of at the root, meaning $A = \pi r^2$ with r the radius of the opening in m. This results in a net propulsive force of 8.8 MN. To account for this, it is recommended that the specialized frames that support the tank are designed for this load. Furthermore, the wall is connected to the cabin floor which is a very stiff structure, therefore it is assumed that the structure is able to sustain the static force exerted by the tank. Finally, the wall between cabin and tank will be positioned very close to the tank, such that the tank has no room to accelerate.

Secondly, the fuselage will be designed in such a way that when the aircraft crash lands and the fuselage fails, the fuselage will tear between the passenger section and the hydrogen tank. This is discussed in more detail in section 10.7.

---

[9]https://www.energy.gov/eere/fuelcells/high-pressure-hydrogen-tank-testing (accessed 04-06-2020)
[10]https://www.youtube.com/watch?v=C4kb-8CjVYg (accessed 16-06-2020)

Thirdly, the hydrogen tank is positioned aft of the wing. This means that when a fan blade of one of the engines flies off, it will not hit the hydrogen tank. The smallest angle between one of the fans and the tank is calculated to be 19°.

Fourthly, by design, the aircraft is equipped with a set of pressurization valves. These valves regulate the pressure inside the cabin. The main outflow valve is unchanged, but the emergency pressure release valves are positioned in the same fuselage section as the tank. The nominal pressure differential at cruise altitude is 48 kPa. These valves will be pneumatically designed to open at a pressure differential of 62 kPa[11]. For this pressure differential, direct spring pressure release valves are used [133]. These valves ensure that an increase in fuselage pressure due to escaping hydrogen is immediately relieved. This prevents structural damage to the fuselage. The wall between tank and cabin ensures the safety of the passengers.

Finally, the wall between the passenger cabin and tank is also designed for fire protection. Raymer [97] advises a 0.4 mm thick stainless steel sheet between the tank and passengers. This adds 33 kg to the fuselage.

9.4. Hydrogen Refueling
In this section, the refueling operations at airports are considered. To analyze this, several assumptions have been made:

- For the refueling process three different scenarios are considered. The use of four hydrogen trucks, two hydrogen trucks and pipelines.
- For the use of pipelines, the reservoir is much larger than the hydrogen tank itself, meaning there is no pressure drop in the pipelines.
- The initial pressure within the refueling trucks and pipelines is 875 bar.
- The tank of a refueling truck has a volume of 36.7 m^3.
- Each refueling truck is connected to one compressor.
- The tank material has a low thermal conductivity and therefore the heat transfer between the inside of the tank and its surroundings can be neglected.
- The refueling hose is assumed to have a constant cross sectional area.
- During refueling, the mass flow rate is constant.
- The refueling process is an isenthalpic process and the temperature changes are analyzed by use of the Jonson-Thomson principle [134].

The assumed values regarding the refueling trucks are based on an actual truck trailer that can hold 1100 kg of gaseous hydrogen at a pressure of 500 bar [12]. It is expected that in the future there will be an increase in the storage pressure by using stronger materials. Thus, being able to store compressed hydrogen at 875 bar. This larger pressure results in a larger pressure difference between the refueling unit and the hydrogen tank on-board of the aircraft. Since gaseous hydrogen flows faster when the pressure difference is increased, the refueling time will be shorter and therefore improved. A compressor is used to further improve the refueling time. The one that is selected is the ionic compressor IC90 [135].

To obtain the right amount of fuel and pressure after refueling, it is important to consider the temperature range inside the tank. Following the analysis presented by Maus et al. [136], the temperature inside the tank must be between 15 °C and 85 °C to avoid overfilling. When the temperature is below 15 °C the hydrogen would heat up and expand which results in an increase in pressure. If the temperature is above 85 °C, the tank would have a higher pressure than the maximum allowed pressure which would violate the safety criteria as shown in figure 9.4. To prevent excessive temperature increases during refueling, the hydrogen is cooled down in the refueling unit before it enters the tank. During flight, the hydrogen should remain between -40°C and 85 °C.

---

[11]http://www.b737.org.uk/pressurisation.htm (accessed 18-06-2020)
[12]https://www.linde.nl/en/news_and_media/press_releases/news_20130925.html (accessed 08-06-2020)
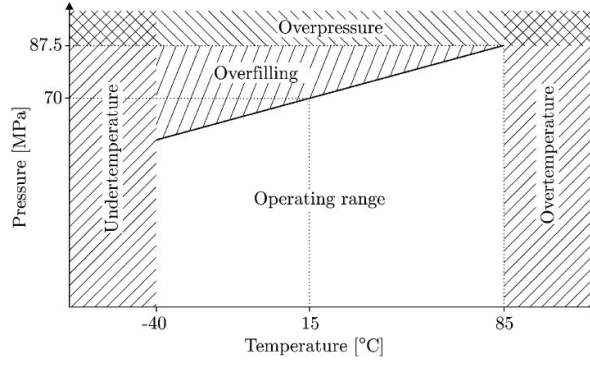
Figure 9.4: Temperature versus pressure diagram for safe refueling of the 700 bar pressure tank [136].

To understand the temperature change inside the tank, the refueling process is analyzed in more detail. As pressurized hydrogen at 875 bar is pumped inside the tank, it has the ability to expand at first and therefore the pressure of the gas decreases. However, as the refueling process proceeds, the gas gets compressed and this leads to a temperature increase inside the tank. During flight, when the fuel is used, the amount of hydrogen decreases and due to a constant tank volume this results into a temperature decrease. Various experiments have been performed for type IV tanks of a smaller size compared to the one used in the SHOTS aircraft. An example of such research is presented by Bourgeois et al. [137], where a 90.5 L tank is analyzed. For this tank, a temperature increase of 80 °C is found when refueling it, having an initial tank temperature of 3.3 °C and an inlet temperature of 9.4 °C. The fill rate of this tank was 1.5 bar/s and it took 200 seconds to fill the tank. As this experiment uses a constant pressure flow, this same data can also be reproduced applying some changes to the code as the pressure rate will be constant.

To analyze the refueling time, pressure variation and temperature inside the tank, the principle of conservation of mass is used: the outflow mass of the trucks or pipelines is equal to the inflow in the tank. This leads to equation 9.5.

$$\frac{v_0^2}{2} + \frac{\gamma}{\gamma - 1} \cdot \frac{p_0}{\rho_0} = \frac{v_1^2}{2} + \frac{\gamma}{\gamma - 1} \cdot \frac{p_1}{\rho_1} = \text{constant} \tag{9.5}$$

In this equation, v denotes the velocity in m/s and γ denotes the heat capacity ratio. The pressure and density of the gas are denoted by p in MPa and ρ in kg/m^3, respectively. The index 0 indicates the conditions inside the truck tank and the index 1 indicates the conditions inside the aircraft tank. Since the velocity at the inlet of the truck is 0 at the start of the process, both the pressures and densities inside the truck and the aircraft tank are known. It is possible to rearrange equation 9.5 to find the velocity at the outlet inside the aircraft tank.

To obtain the mass flow rate, equation 9.6 can be used in combination with the obtained velocity v at the outlet inside the aircraft tank, the cross sectional area A of the refueling hose and the density ρ of hydrogen. Integrating over time and adjusting the pressure and density both inside the aircraft and truck trailer, the new velocity at the outlet inside the aircraft can be found. This process is performed until the pressure inside the truck and aircraft tanks are equal resulting in a pressure balance. After this step, the compressors must be turned on and compress the hydrogen to 1000 bars to feed the aircraft tank with a mass rate of 67.2 kg/hr.

$$\dot{m} = v \cdot A \cdot \rho \tag{9.6}$$

The refueling is completed once the desired mass of hydrogen is inside the tank. This can be monitored using a pressure and a temperature sensor to compute the actual mass inside the tank. Equation 9.7 retrieved from the work done by Sapre et al. [134] shows the temperature rise inside the hydrogen tank as a function of time where T_0 is the temperature inside the tank, T_i the gas temperature at the outlet in the tank, m_0 the initial mass present inside the tank and $m(t)$ the total mass inside the tank at a given time t.

$$T_e(t) = T_0 + T_i \cdot (\gamma - 1) \cdot \left(1 - \frac{m_0}{m(t)}\right) \tag{9.7}$$

By using equation 9.5 the velocity of the gas at the outlet can be found using the pipe diameter. This velocity can then be used to find the mass flow rate by applying equation 9.6. A program was created in order to simulate the refueling process. Within this program a step time of 1 s is used and at each time interval the mass inside of the tank is evaluated. Since the volume inside of the tank is known, the density inside the tank can be found by dividing the mass present inside the tank by the tank volume. Finally, to find the pressure inside the tank, equation 9.8 is used [13].

$$p = 0.0203 \cdot \rho^2 + 1.0076 \cdot \rho + 0.4401 \qquad (9.8)$$

This equation was obtained by plotting the hydrogen pressure against the density at 25 °C and using a function to best fit the data to extrapolate the data between points.

Finally, the refueling time of all the three methods can be calculated. The results can be seen in figures 9.5, 9.7 and 9.6 and show that using pipelines as refueling method is the fastest option. The difference between using 4 and 2 trucks can also be seen in figure 9.6 and 9.7 respectively when it comes to pressure balance difference. This value depends on the amount of trucks as all trucks have the same initial pressure and will transfer mass to the aircraft tank. Therefore, the total volume and mass available increase with the amount of trucks. When a given amount of mass has been transferred to the aircraft, there will be a pressure reduction in the trucks. This pressure decrease will be lower with the higher number of trucks.
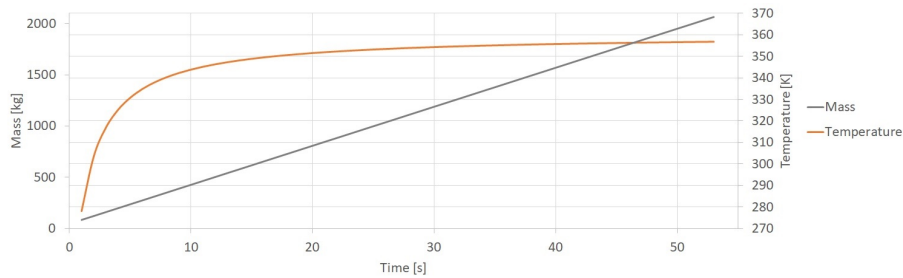
Figure 9.5: Hydrogen fuel inside the aircraft and temperature over time for the use of pipelines.
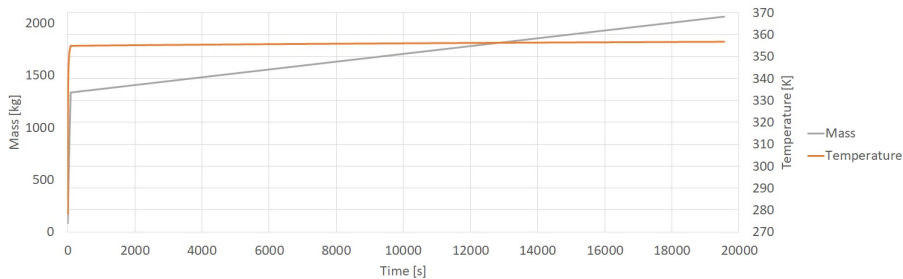

Figure 9.6: Hydrogen fuel inside the aircraft and temperature over time for the use of four trucks with compressors.
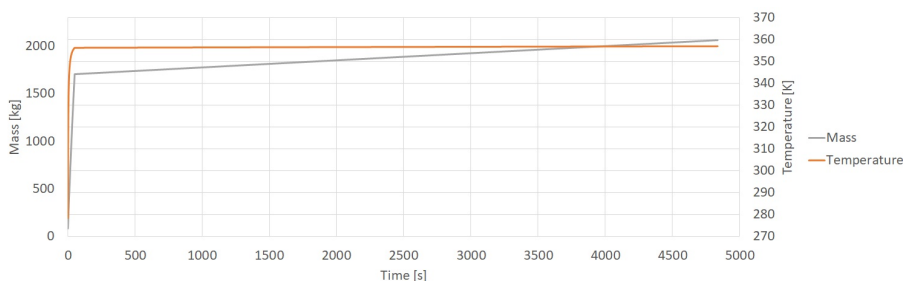

Figure 9.7: Hydrogen fuel inside the aircraft and temperature over time for the use of two trucks with compressors.

[13]https://h2tools.org/hyarc/hydrogen-data/hydrogen-density-different-temperatures-and-pressures (accessed 11-06-2020)

An overview of all results is presented in table 9.5 where the first three columns show the results obtained by using the pressure balance principle. For the pipeline method, this is limited by the moment when the tank is filled with 2063 kg of hydrogen. However, for the other two methods the compressors need to be used once a pressure balance is obtained such that the rest of the required hydrogen can be pumped into the tank until a mass of 2063 kg is reached. The transfer process performed by the compressors can be seen in the last two columns, where the four and two compressors columns represent the refueling method of using four and two trucks respectively. For comparison, the maximum refueling time of the Embraer E195-E2 is 16 minutes [118].

Table 9.5: Results from different refueling methods.

Method	Pipeline	Four Trucks	Two Trucks	Four Compressors	Two Compressors
Initial pressure [bar]	20.5	20.5	20.5	513	369.8
Initial temperature [K]	278.15	278.15	278.15	356	355
Gas flow temperature [K]	200	200	200	200	200
Final pressure [bar]	670	513	369.8	670	670
Final mass [kg]	2,063	1,706	1,336	2,063	2,063
Final density [kg/m^3]	37.58	31.07	24.3	37.58	37.58
Final temperature [K]	356.8	356	355	356.8	356.8
Elapsed time [s]	53	51	88	4,783	19,469

During turn around, 80% of the fuel needs to be refueled (the rest is back-up and not used during normal operations) [118]. As shown in table 9.5, the pipeline and the 4 trucks scenario are able to reach > 80% within one minute. This is 10 minutes faster than the Embraer E195-E2 [118].

9.4.1. Engine supply system
For safety, each engine will have two fuel lines coming from the fuel tank with each line fitted with valves at each end that will monitor the pressures. If there is a failure, the pressure difference will trigger the action of closing both valves such that the given line will not have hydrogen inside and the engines can still be operational using the backup fuel line. Based on the data provided by the propulsion group, it will the required to provide each engine with 0.1782 kg/s of hydrogen and it should be delivered at a pressure of 15 bar. In case the pressure inside the fuel tank decreases below this pressure, compressors need to be used at the exit of the tank, such that the engine can continue running smoothly. By rewriting equation 9.5 the diameter of the piping connection of the tank to the engines can be determined and results in equation 9.9.

$$d = \sqrt{\frac{p}{\pi} \cdot \frac{\dot{m}}{\rho \cdot \sqrt{\frac{\gamma}{\gamma-1} \cdot \left(\frac{p_0}{\rho_0} - \frac{p}{\rho}\right) \cdot 2}}} \tag{9.9}$$

By plugging in p as 15 bars, $\dot{m}$ as 0.1782 kg/s, ρ as 1.32 kg/m^3, γ as 1.41 and P_0 and ρ_0 as the condition where the pressure at the compressor is 20 bar and the density is 1.69 kg/m^3, the final inner diameter is found to be 18 mm.

9.4.2. Hydrogen system layout
The main layout of the hydrogen fuel system is presented in figure 9.8. The red lines are fuel lines which feed gaseous hydrogen to the engines and in blue the refueling lines are illustrated. When the hydrogen tank is refueled by the use of four refueling trucks, there need to be four connections for the refueling hoses. However, when only two trucks are used the refueling time takes twice as long if the same connections would be used. To solve this issue, two wider connections are available on the refueling panel which have the same total cross sectional area as the four smaller connections. The result of this refueling panel is shown in figure 9.8 too. Besides refueling connections, there are also two data connectors to allow communication between the refueling infrastructure and the hydrogen tank. Information is provided on important parameters such as pressure, temperature, and the amount of hydrogen inside the tank.
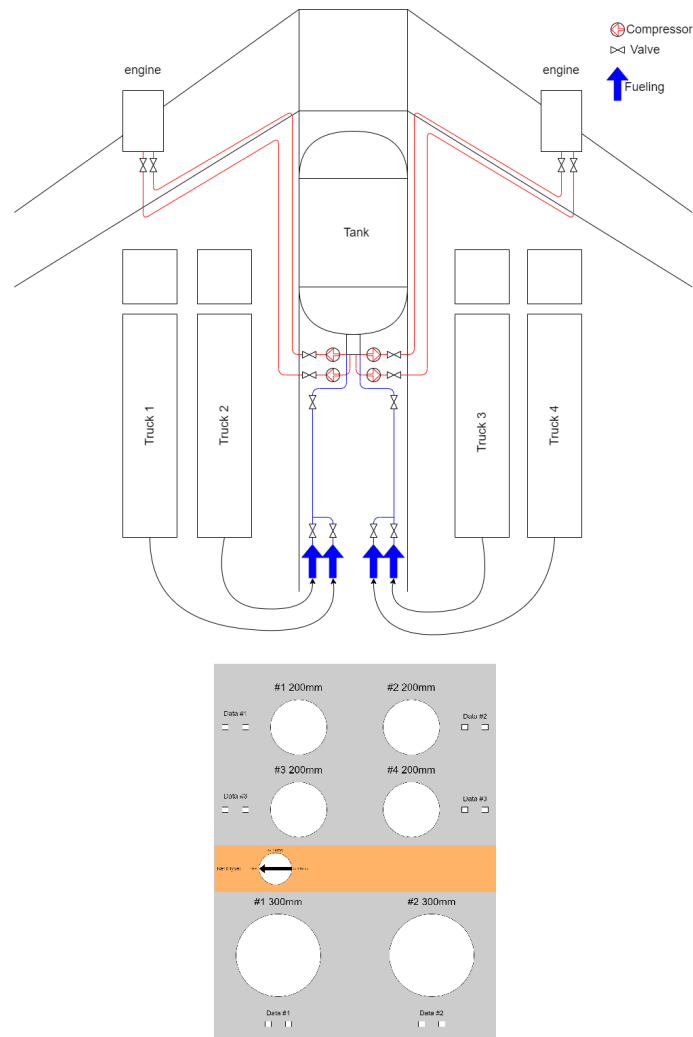
Figure 9.8: Schematic illustration of the hydrogen fuel system layout (please note that the diagram is for illustrative purposes only and is not to scale).

9.5. Modular Design

To improve the efficiency on the ground when a D-check needs to be performed, a modular system in the back of the aircraft is implemented. This system will allow for an easier removal of the hydrogen tank for inspection, or reuse at the end of life. To perform this task, the tail cone section has to be removed. Before the tail cone can be removed, the hydraulic lines and fuel lines first need to be disconnected. This is required because these lines come from both the main hydraulic system to feed the control surfaces in the tail line and from the biokerosene tank inside the wing to provide fuel to the APU. Additionally, the electric power line needs to be disconnected from the the APU to the fuselage. Last but not least, the data cables that provide the controls to the APU and the activation valves in the hydraulic system need to be detached as well. All these steps can be performed by accessing the tail cone due to a hatch that is placed behind the bulkhead. The next step will be to strap the tail cone with the aid of a crane such that no damage is done during the separation of the tail cone and the rest of the fuselage. This is shown in figure 9.9a.

The tail cone and the rest of the fuselage are connected by a specially designed frame. By unfastening one side of this frame, the tail cone can be separated from the rest of the fuselage as illustrated in figure 9.9b. This step can done with the help of a mobile or roof crane. The weight of this section is estimated to be around 2.5 t (150 kg APU, 335 kg horizontal tail, 220 kg vertical tail and 1800 kg skin).

Once the tail cone is removed, the bulkhead will be accessible as seen in figure 9.9c. To access the inside of the bulkhead, a hatch in the bottom part of the fuselage near the tank connection can be used.

Furthermore the bulkhead has a diameter of 3.81 m and the attachments in the fuselage have a diameter of 3.62 m leaving a margin of 3 cm between the tank and the fuselage supports. The bulkhead has an outer support which is fixed to the fuselage. In this step the screws holding the bulkhead to the outer support are removed to extract the bulkhead which can be seen in figure 9.9d.

Now that the hydrogen tank is visible, the fixations that keeps it in place can be removed and a gripping tool can be attached to remove it as seen in figure 9.9e.

Finally the tank can be slid out of the fuselage as illustrated by figure 9.9f and 9.9g. The result is a fuselage that is fully accessible from the back as seen in figure 9.9h. To simplify this task further analysis needs to be done, for instance what kind of support to use to facilitate the tank removal: lie rollers or an arm that will take the tank out without damaging the fuselage.

(a) Tail cone ready for removal.

(b) Removal of the tail cone.

(c) Access to the bulkhead for unscrewing.

(d) Removal of the bulkhead.

(e) Access to the hydrogen tank for supports removal.

(f) Hydrogen tank removal through the back, part 1.

(g) Hydrogen tank removal through the back, part 2.

(h) Fuselage without hydrogen tank and tail cone.
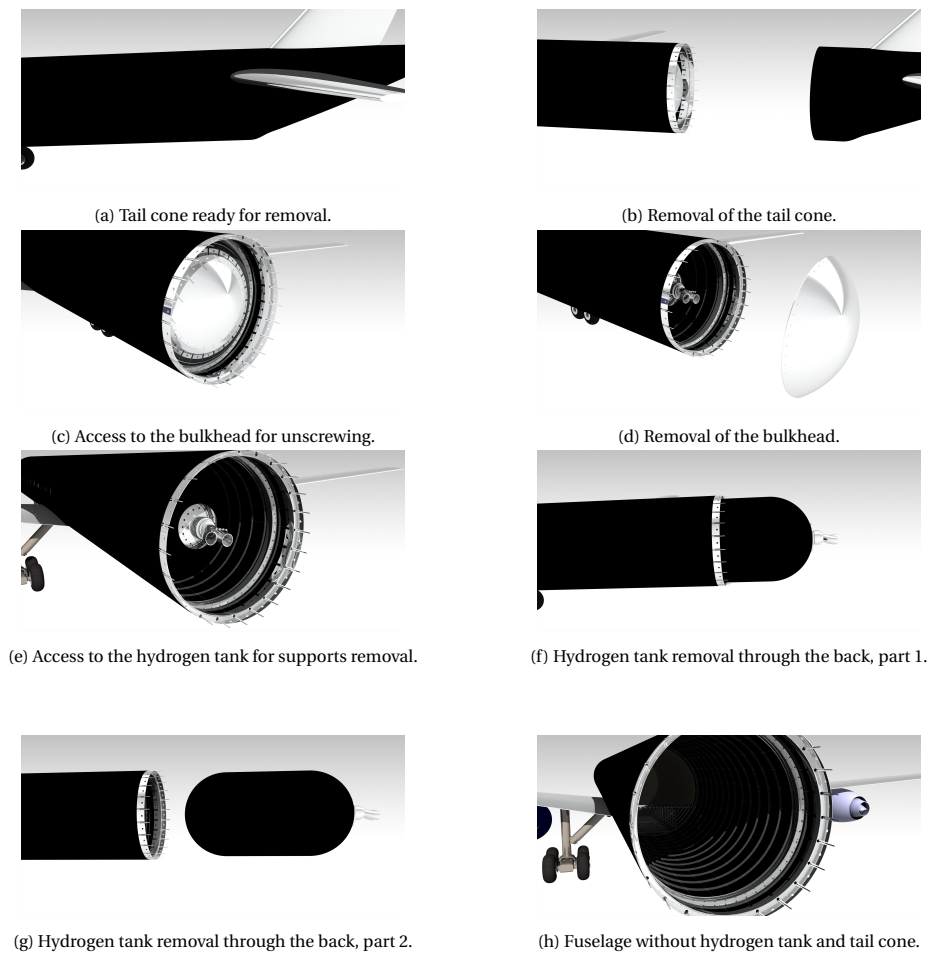
Figure 9.9: Steps to remove the hydrogen tank from the aircraft. (cont.)

Further development of this modular concept can be done to exploit its potential for a faster replacement of cabin elements such as seats, floor, interior fittings, toilets and galleys.

9.6. Verification and Validation
This section discusses the verification and validation of the calculations performed for the hydrogen tank sizing in section 5.1 and section 9.2 and the calculations performed for the refueling system in section 9.4.

9.6.1. Hydrogen tank sizing verification
To verify the calculations done for the hydrogen tank sizing, three methods have been used.

To begin with, unit tests were performed on several parts of the calculation model. The density of the hydrogen gas has been compared to a database of the National Institute of Standards and Technology[14]. The required volume of the material was checked by hand calculations.

Secondly, system tests were performed with a computational model developed by the Pacific Northwest National Laboratory (PNNL) [138]. For this, the model had to be adjusted to be able to change the material properties. The tank volume, required wall thickness and tank mass have been compared for Hexcel PV42/850 CFRP. Furthermore, this model also gives a preliminary cost estimation based on material cost only. Using the information of CEMAC [131], it is possible to estimate the complete tank cost for the PNNL model. CEMAC estimates that 90% of the tank costs are material cost. Therefore, the result from PNNL is multiplied with 1.11 and adjusted for inflation. The complete verification is shown in table 9.6.

Table 9.6: Comparison between WeFlyCycle and PNNL model.

Model	Required volume [m^3]	Load carrying material thickness [mm]	Tank mass [kg]	Tank unit cost [$]
WeFlyCycle	51.911	88	13,361	628,520
PNNL	53	100	12,770	647,145
Difference	-2.1 %	-12 %	4.6 %	-2.9 %

To verify the calculation of the fatigue sizing, a different computational model from the Structures department has been used. It was possible to do this because this department chose a different approach for the fatigue sizing of both wing and fuselage. First, the Wöhler curves were compared graphically. Then, the allowable stress amplitudes S_a obtained from the two models were compared. The difference between the models was found to be 0.099 %. Please consult section 10.5 for further elaboration on the computational model used for fatigue sizing of both wing and fuselage.

9.6.2. Hydrogen tank sizing validation

At this moment, validating a tank that is not commercially available anywhere can only be done by extrapolating data from pressure vessels with much smaller storage capacity. For this, linear relations are assumed. The United States (US) Department of Energy (DOE) has provided estimates for the volumetric and gravimetric efficiency of such a tank [139]. Furthermore, the DOE provides values for the cost per kWh, based on a 5.6 kg tank. This is used to validate the cost estimation. To compare, the efficiencies of the tank are all calculated in kWh. The amount of energy stored in the tank is 81,374 kWh. All three comparisons are shown in table 9.7.

Table 9.7: Validation of the hydrogen tank.

Model	Volumetric efficiency [kWh/L]	Gravimetric efficiency [kWh/kg$_{system}$]	Cost estimation [$]
WeFlyCycle	1.6	6.1	628,520
US DOE	2.3	2.5	550,000-651,000
Difference	-30 %	144 %	Within range

Very large differences are observed when comparing the values for a 5.6 kg hydrogen tank to the fuel tank. This is of course a logical consequence of the extrapolation from a very small tank to an extremely big one. Moreover, since the materials in aviation are of extremely high quality this could explain the difference as well.

9.6.3. Hydrogen refueling verification

As the main issue with refueling hydrogen tanks is the temperature increase inside the tank, the verification was performed by changing the computed parameters by actual experimental data in the created program. These values come from an experiment by Galassi et al. [140]. The data obtained in the experiment is plotted against the simulated data in figure 9.10.

---

[14]https://h2tools.org/hyarc/hydrogen-data/hydrogen-density-different-temperatures-and-pressures (accessed 21-06-2020)
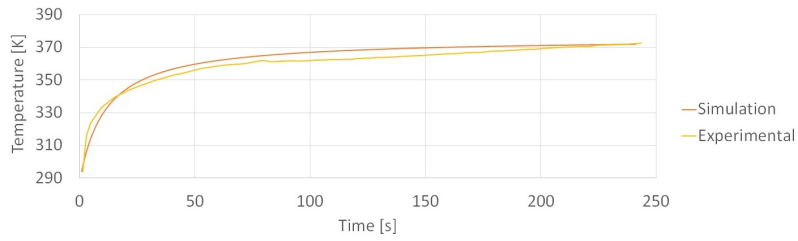
Figure 9.10: Temperature evolution inside the hydrogen tank during the refueling process.

As can be seen in figure 9.10, there are differences between the simulated data and the data obtained from the experiment by Galassi et al. [140]. This is due to the fact that in the simulation, no heat is exchanged with the environment as it was assumed the tank walls have a low thermal conductivity. Furthermore, the refueling process is assumed to be isenthalpic.

9.6.4. Hydrogen refuelling validation

To validate the obtained mass and temperature changes during the refueling process, a comparison is made between figure 9.5 and an experiment performed by Galassi et al. [140]. The pipeline simulation and the part of figures 9.6 and 9.7 where no compressors are working is used for the comparison. It can be seen that the curve from figure 9.11 matches those of the mass of the experiments and simulations in figures 9.5, 9.6, 9.7 since the pressure evolution over time is the same as the mass evolution.
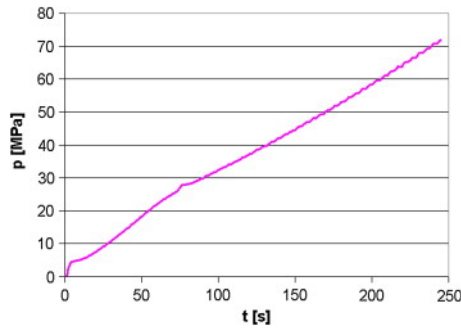
Figure 9.11: Validation pressure rise inside the tank [140].

<div align="right">

10
Structures

</div>

During the Midterm Report [3], the structural design of the fuselage and wing was focused on how these structures support internal bending moments within the structure. However, these structures also need to fulfill other functions as presented in section 10.1. From the functional analysis, a set of subsystem requirements is made and listed in section 10.2. The structural analysis approach is briefly discussed in section 10.3 and stems from the Midterm Report [3]. The buckling of the wing is further analyzed in section 10.4, resulting in the required skin thickness, stringer dimensions and rib spacing. Then the wing and fuselage skin are sized to sustain fatigue loads in section 10.5 to comply with requirement **WFC-OP-3**. Furthermore, the fuselage skin requires to sustain a crack of 500 mm and the structure as a whole needs to protect the passengers on-board if the aircraft would drop on the ground due to an emergency. These analyses are discussed in section 10.6 and 10.7 respectively. A trade-off is performed in section 10.8 to select the best material for the wing and fuselage skin regarding structural weight, material cost and material performance from section 6.7. Lastly, the calculations are verified and validated in section 10.9.

10.1. Functional Analysis
Since structures go hand in hand with the selected materials, the functional analysis for structures is presented in chapter 6, section 6.1.

10.2. Requirements Analysis
The main system requirements are presented in section 3.1. To aid the design process, the subsystem requirements are set up as follows.

- ***WFC-STRUC-01****: The aircraft's primary structural components that are accessible for inspection shall withstand total or partial failure for a period of un-repaired use after failure [32].* This requirement stems from the need for passenger safety.
- ***WFC-STRUC-02****: Aircraft parts that cannot be accessed for inspection shall be designed according to safe-life philosophy.* Again, this requirement stems from the need for passenger safety.
- ***WFC-STRUC-03****: The aircraft's primary structural components shall withstand fatigue cyclical loading without failure for a lifetime equivalent to 43,800 flight cycles.* This requirement stems from the estimated operational lifetime of the aircraft.
- ***WFC-STRUC-04****: The fuselage skin shall withstand ultimate loads for a through-the-thickness mode I crack of length 500 mm without failure.* This requirement stems from the possibility of an engine failure creating a crack in the fuselage.
- ***WFC-STRUC-05****: The fuselage skin thickness shall be lower than 7 mm.* This limit has been set because the Airbus A350 XWB's fuselage consists out of CFRP skin panels with a thickness of 1.27 mm. This thickness is increased by a factor of 5 around door cut-outs [13].
- ***WFC-STRUC-07****: Local skin buckling, local stiffener buckling and inter-rivet buckling critical loads shall be higher than the limit load.* Requirements on buckling stem from the possibility of this failure mode and the need for passenger safety.
- ***WFC-STRUC-08****: The column buckling critical load shall be higher than the ultimate load.*
- ***WFC-STRUC-09****: The lower fuselage panel shall not deflect more than 1.62 m when withstanding an impact load of 9.5g during a drop test.* This requirement stems from the need for passenger safety. The deflection needs to be lower than the floor height so as to not harm the passengers.
- ***WFC-STRUC-10****: During a drop test the fuselage shall break only behind the cabin section.* This requirement is set so that the hydrogen tank and passengers are separated in case of a crash.
- ***WFC-STRUC-11****: The structural weight of the fuselage shall be lower than 5,780 kg.* Requirements on structural weight stem from the class II weight estimation performed in section 5.3.

• **WFC-STRUC-12**: *The structural weight of the wing shall be lower than 7,920 kg.*

10.3. Approach Structural Analysis

A structural analysis is performed on the fuselage and wing structure in order to determine their structural weight. The bending stresses are found and the thickness is chosen accordingly in order for the structures to support the maximum stresses. Thus, the structural weight is found for three different materials discussed in section 6.7. The analysis is based on beam theory and therefore, some assumptions and simplifications have been made:

- The wing and fuselage are modelled as thin-walled beams subjected to pure bending.
- All loads act along the vertical plane of symmetry of fuselage and wing and thus no torsional loads are introduced. In reality, there might be coupling between bending and torsional loads but this is neglected at this stage.
- "Plane cross-sections of the beam remain plane and normal to the longitudinal fibers of the beam after bending" [141].
- "The wall thickness is assumed to be much smaller than the other representative dimensions of the cross-section"[142]. This means higher orders of thickness are neglected in the calculations.
- Wing is modelled as a cantilever beam, with one clamped end and one free end.
- Fuselage is modelled as a free beam (both ends free).
- Landing gear weight, engine weight and wing loading on the fuselage are assumed to be point loads. All other weight loads are assumed to have a uniform distribution.
- Lift distribution on the wing is assumed to be elliptical and continues to the center of the aircraft. This is a reasonable assumption for subsonic flight conditions [97].
- The carbon fiber composite, which consists out of T800S carbon fibers, is assumed to be quasi-isotropic. This can be achieved by manufacturing a [0/45/90/-45/0] lay-up.
- The composite material GLARE 2 is placed such that its fibers are directed in a spanwise direction due to the fact that the main load path in the wing corresponds to bending loads in the spanwise direction. Therefore, the material properties in the longitudinal direction can be applied [143].
- The composite material GLARE 4 is placed such that its fibers are directed in the fuselage length direction due to the fact that the main load path is in this direction, corresponding to bending loads. Therefore, the longitudinal material properties are applied in the fuselage length direction and the transverse material properties in the circumferential direction [143].

10.4. Buckling

For the buckling analysis of the wing, four different forms of buckling are considered: local skin buckling, local stiffener buckling, inter-rivet buckling and column buckling. The first three of the buckling modes are considered to be non-catastrophic while the last one is considered to be catastrophic because the top wing panel becomes unstable and can collapse due to the ultimate bending stress. A wing panel that is located near the root is selected for this analysis. The bending stress at this location is at its maximum and therefore the four forms of buckling are most critical. Hat stringers are applied to stiffen this wing panel and are selected due to their weight efficiency [144]. Furthermore, countersunk rivets are used in order to attach stringers to the skin. This type of rivet is selected since it improves the aerodynamic performance of the wing. The equations in this section only assume a first buckle (i.e. $n = 1$).

10.4.1. Local skin buckling

Local skin buckling, as the name implies, happens at the skin. It is hence a failure mode which does not involve the geometry of the stringer itself, except the spacing between stringers. The critical skin buckling stress can be calculated using equation 10.1 [141]:

$$\sigma_{cr} = \frac{\pi^2 kE}{12(1-\nu^2)}\left(\frac{t}{b}\right)^2 \tag{10.1}$$

where k is the buckling coefficient, E the Young's modulus, ν the Poisson's ratio of the material, t the thickness of the skin and b the spacing between the stringers.

10.4.2. Local stiffener buckling

To compute the critical stiffener buckling stress the same approach is taken as for the local skin buckling. The main difference is the value of k which depends on the boundary conditions the hat stiffener's

web/flange is subjected to. The critical stress for local stiffener buckling can hence be calculated using equation 10.1.

10.4.3. Inter-rivet buckling

Equation 10.2 is used to compute the stress for inter-rivet buckling and is very similar to a thin-plate, the difference being that k is replaced by C which depends on the type of rivet used and the stringer spacing b is replaced by the rivet spacing s [141]:

$$\sigma_v = \frac{\pi^2 CE}{12(1 - v^2)} \left(\frac{t}{s}\right)^2 \tag{10.2}$$

10.4.4. Column buckling

The critical load where the section will fail due to column buckling is estimated using equation 10.3 [141]:

$$P_{cr} = \frac{\pi^2 EI_{xx}}{l_e^2} \tag{10.3}$$

It should be noted that the moment of inertia I_{xx} is not the moment of inertia of the stiffener, but of both stiffener and a small part of the skin (with width $w = 30t$) which adds a contribution.

10.4.5. Normalization

In order to compare these failure modes, a normalization needs to be performed in order to find the load per unit width N_x. To do this a new variable, the equivalent thickness t^* is defined in equation 10.4. To convert the stress and load to load per unit width, one can use equation 10.5.

$$t^* = \frac{A_{st}}{b} + t_{skin} \tag{10.4} \qquad\qquad N_x = \sigma_{cr} t^* = \frac{P}{b} \tag{10.5}$$

10.4.6. Results

In order to size the selected panel's characteristics, such as skin thickness and stringer dimensions, it is essential that the four different forms of buckling do not occur below either the limit load or the ultimate load. Local skin buckling, local stiffener buckling and inter-rivet buckling may not take place before the panel is loaded at the limit load whereas column buckling may not occur before the panel is loaded at the ultimate load. These loading limits are obtained by using the results of the structural analysis from the Midterm Report [3]. By applying the values of required skin thickness, maximum internal bending moment and location from the centroid, the limit and ultimate load limits could be determined and normalized by the use of equation 10.5.

Since the stringers are attached to the skin by countersunk rivets an end fixity coefficient C of 1.5 is used. The different boundary conditions of the plate and stringers lead to a buckling coefficient k of 4.0 for a simply supported plate and 0.43 for a plate with three simply supported and one free edge [141]. Furthermore, different materials are evaluated during the analysis. An assumption has been made on the Poisson's ratio of the composite materials. However, note that for the composite materials, a range of Poisson's ratios have been applied from 0.1 to 0.5 to make sure that the a change in Poisson's ratio does not lead to a form of buckling occurring below either the limit or ultimate load. An overview of the results is shown in table 10.1 and figure 10.1.

Table 10.1: Results of the wing buckling analysis for different materials.

Parameters	Al 2024 T3	T800S	GLARE 2	Unit
Young's modulus	73.1	294	67	[GPa]
Poisson ratio	0.33	0.3	0.3	[-]
Buckling coefficient	4.0 / 0.43	4.0 / 0.43	4.0 / 0.43	[-]
End fixity coefficient	1.5	1.5	1.5	[-]
Normalized limit stress	876	6,281	2,396	[N/mm]
Normalized ultimate stress	1,314	9,421	3,594	[N/mm]
Skin thickness	3.5	3.9	4.2	[mm]
Stringer thickness	1.7	2	2.1	[mm]
Stringer's hat width	30	30	35	[mm]
Stringer height	65	65	55	[mm]
Stringer total width	70	70	70	[mm]
Number of stringers	13	15	17	[-]
Stringer spacing	140	120	110	[mm]
Rib spacing	1,100	975	700	[mm]
Rivet spacing	120	110	95	[mm]

(a) Aluminum 2024-T3.

(b) T800S Carbon.

(c) GLARE 2.
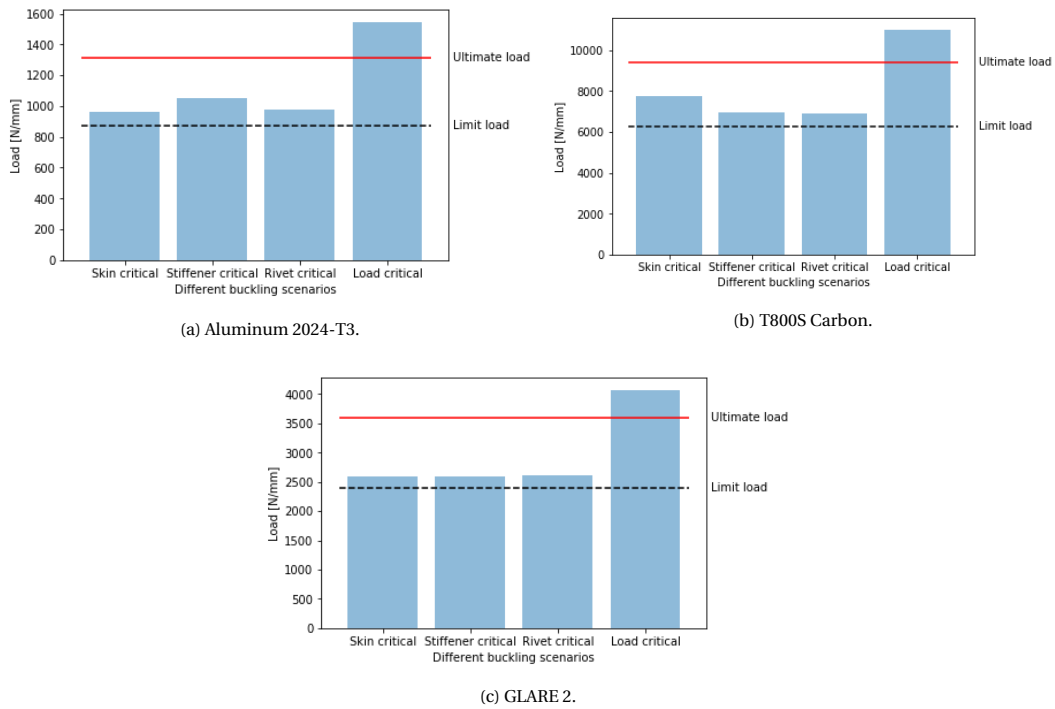
Figure 10.1: Required loads for appearance of four buckling modes for different materials.

10.5. Fatigue

As described in **WFC-STRUC-03**, the primary structural components have to be able to withstand the fatigue loading conditions experienced during the aircraft's operational life. The method followed for fatigue analysis is based on the construction of Wöhler curves as described in subsection 9.2.1. For cyclical pressurization loading, the assumption of constant amplitude load cycles is reasonable, as is the case with the pressurized fuel tank and fuselage cabin. However, wing load cycles are defined by an arbitrary spectrum [32]. For the purposes of this analysis, it is assumed that all load cycles have the same stress amplitude and mean stress for both the fuselage and wing. It is assumed that the maximum stress is equal to the ultimate tensile strength of the material and the minimum stress is zero for a conservative approach.

The fatigue limit of a given material is obtained from $S_f = \alpha \cdot S_u$ [123]. For aluminum alloys $\alpha \approx 0.35$. For composites, it is assumed that under tension loading $S_f = 0.8 \cdot S_u$ after 10 million cycles. The curves are then adjusted according to the Goodman relation for a stress ratio $R = 0$, meaning $S_{min} = 0$ is assumed for both fuselage and wing. In reality, this is not true for the wing, which is subjected to tension loading during cruise and compression during landing. This means S_{min} is negative which would lead to higher allowable stresses. Thus, taking $S_{min} = 0$ is a conservative approach.

As explained in subsection 9.2.1, K_t depends on the loading conditions. A value of 2.5 can be assumed for purely pressurized structures, so this is used for the fuselage side panels. For the top and bottom, the bending stresses need to be considered. The top panel is loaded in tension during flight, increasing the longitudinal stress with respect to the hoop stress, and thus K_t is reduced to 2. On the other hand, the compression on the bottom panel means $K_t \approx 3$. The latter is also assumed for the lower wing. For the upper wing, most of the load cycle occurs in compression. Under these conditions a fatigue crack is closed and the loading can be assumed to be non-damaging [123].

With regards to notch sensitivity, q is obtained graphically from Schijve [123] and is assumed to be 0.8 for aluminum alloys, corresponding to a notch size of 2 mm. For composites such as T800s, $q \approx 1$. For GLARE, an average of the aluminum and composite layers is taken as 0.9.

Following the procedure presented in subsection 9.2.1 the Wöhler curves are constructed and shown in figures 10.2 and 10.3 for the fuselage and wing respectively. On the right side of both figures more information can be found regarding what each line stands for.
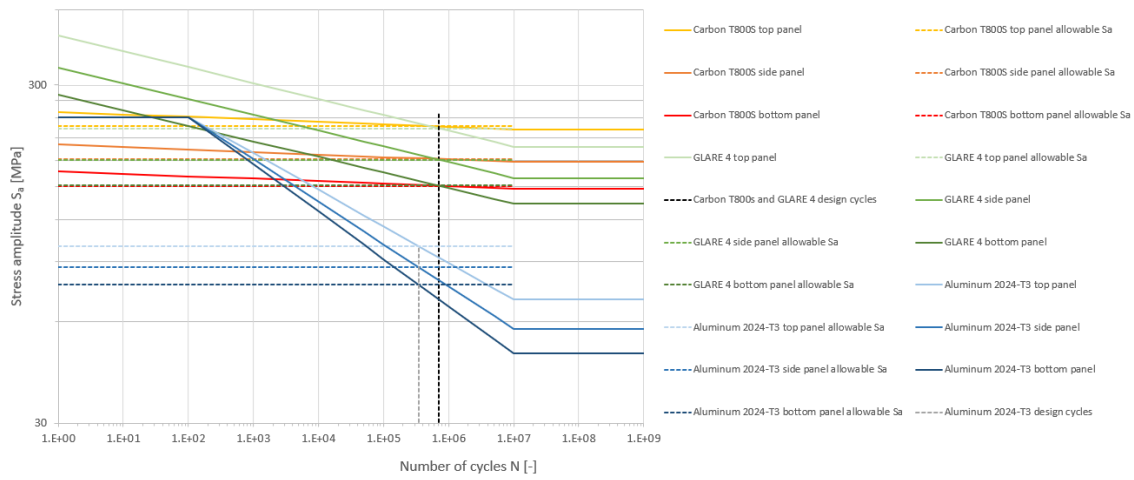
Figure 10.2: Wöhler curves for different panels and materials of the fuselage.
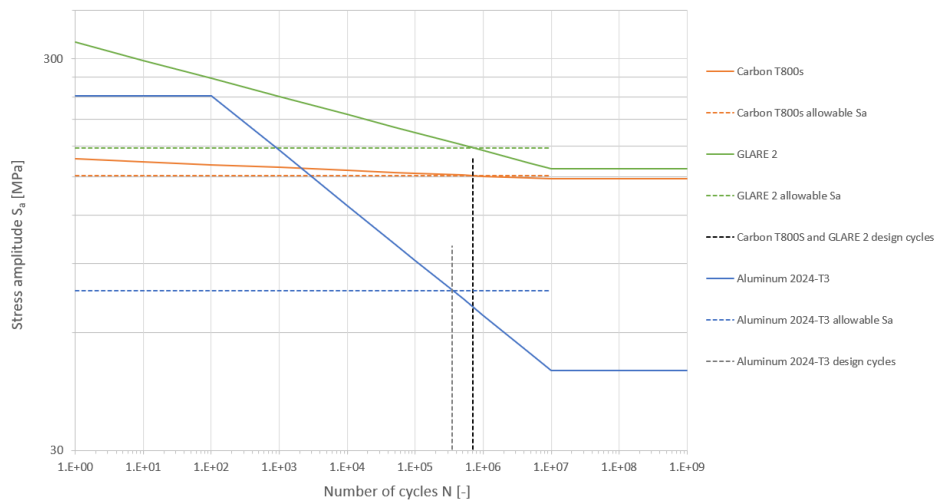
Figure 10.3: Wöhler curves for different materials for the lower wing.

From figure 10.2, it is clear that the fuselage skin thickness has to be designed based on the allowable stress amplitude of the bottom panel as this is the most critical section in fatigue. Due to the cyclical pressure loading on the fuselage, $S_{min} = 0$ and $S_{max} = 2 \cdot S_a$.

Although $S_{min} = 0$ is assumed to construct the Wöhler curve of the wing, the allowable stress on the wing is given by $S_{max} - S_{min} = 2 \cdot S_a$ in reality. The maximum and minimum loading conditions on the wing correspond to cruise and landing respectively. This means the values obtained are slightly conservative.

The allowable stresses are used to perform the structural analysis as discussed in section 10.3 to ensure the aircraft structure can sustain the fatigue loads for the duration of its operational lifetime. A contingency margin of 8.5% is applied to the allowable stress amplitude so the input values for the analysis are lower than the calculated values. The result is a restriction on the minimal required skin thickness used within the fuselage and wing structure. The amplitude stress values obtained graphically, the values with the applied contingency margin and the required skin thickness are shown in table 10.2.

Table 10.2: Maximum allowable stress amplitude and required skin thickness for fuselage and wing considering different materials.

Parameters	Unit	Fuselage 2024-T3	T800S Carbon	GLARE 4	Wing 2024-T3	T800S Carbon	GLARE 2
Ultimate tensile strength	[MPa]	483 [1]	1,000 [145]	843 [143]	483 [1]	1,000 [145]	992 [143]
Allowable stress amplitude S_a with 8.5% margin	[MPa]	70.46	138.28	138.44	70.46	138.21	162.82]
Skin thickness t	[mm]	2.0	1.6	1.5	4.4	4.6	4.0

10.6. Damage Tolerance

The damage tolerance philosophy is defined as "the ability of the structure to sustain anticipated loads in the presence of fatigue, corrosion or accidental damage until such damage is detected through inspections or malfunctions and is repaired" [32]. For a given fuselage thickness, it is checked if the material can support the hoop stresses when a crack of length $2a = 500$ mm is present. The hoop stress is multiplied by a load factor of 2 to obtain the maximum applied stress S_{max}. This value must be lower than the critical stress S_{crit} obtained from equation 9.4 to sustain the defined crack length.

The fracture toughness K_{Ic} of Aluminum 2024-T3 is approximately 40 MPa$\sqrt{m}$ [32]. However, correction factors can be applied to account for the effects of fuselage curvature and presence of frames and stringers [146], resulting in a new K_{Ic} of 90.8 MPa$\sqrt{m}$ which is used for the analysis [147].

For composites and fiber metal laminates, K_{Ic} depends greatly on the lay-up used. CFRPs have a fracture toughness of 32-45 MPa$\sqrt{m}$ [126], similar to aluminum alloys. However, the value is adjusted to take into account the presence of stiffening elements and the special crack propagation described in subsection 9.2.2, and a value of 138.6 MPa$\sqrt{m}$ is used.

For GLARE, work by Rodi [148] shows that the residual strength is independent of sheet width but dependent on lay-up. By assuming a linear relationship between residual strength and lay-up thickness, the K_{Ic} range for GLARE 4 is obtained for 2/1-0.4 up to 8/7-0.4 lay-up, and is equal to 110-120 MPa$\sqrt{m}$. The K_{Ic} value is scaled similarly to Aluminum 2024-T3 to account for the presence of frames and stringers, resulting in an average of 270.7 MPa$\sqrt{m}$ is used.

The cruise altitude is assumed to be 11,000 m rather than 8,900 m for contingency, as a higher cruise altitude means a higher pressure difference and thus hoop stress. Assuming a cabin altitude of 2,500 m, an inner fuselage radius of 1.81 m, and taking the thickness values obtained from table 10.2, the hoop stresses on the fuselage are calculated. Initially, S_{crit} is obtained from equation 9.4 assuming $a = 500$ mm. By setting $S_{crit} = S_{ult}$ the maximum allowable crack size is obtained as shown in table 10.3. The values are rounded down to the nearest integer.

Table 10.3: Fuselage damage tolerance results for different materials.

Parameter	Aluminum 2024-T3	T800S Carbon	GLARE 4	Unit
Critical stress S_{crit}	102.5	138.6	305.4	[MPa]
Maximum applied stress S_{max}	94.2	117.8	125.6	[MPa]
Allowable crack size $2a$	591	881	2,956	[mm]

Table 10.3 shows that requirement **WFC-STRUC-04** is met for all materials. This means the required thickness in terms of damage tolerance could even be decreased, but this is limited by the drop test and buckling requirements. As expected, GLARE 4 has the best performance for damage tolerance.

10.7. Drop Test

A common method to test the crashworthiness of aircraft is by performing a drop test. This section performs a very simplified approach to the drop test. First, the steps behind the drop test itself are described, then a formula for the deflection of a curved beam is introduced and analyzed and finally, the design is actually analyzed using the formulas. Several assumptions are made for the analysis:

- The frames all take equal load and are assumed to be continuous throughout the length of the cabin (cutouts such as doors/cargo doors are not considered).
- Only the frames in the cylindrical part of the fuselage are assumed to carry the impact loads.
- The beam is assumed to act linear-elastically throughout its entire deflection.

10.7.1. Approach

The simplified drop test is performed on a section of the fuselage such that the end results can be verified by data from the Boeing 707 [149]. The main purpose of this test is to ensure passenger safety which means that the floor on which the cabin seats are attached to must stay intact and that after impact the cabin is separated from the hydrogen tank section to prevent a hazardous situation. Therefore, this analysis focuses on the lower part of the fuselage and the stiffness between fuselage sections. The structure of the bottom fuselage consists of multiple components such as frames and struts as seen in

---

[1]`http://asm.matweb.com/search/SpecificMaterial.asp?bassnum=MA2024T3` (accessed 20-06-2020)

figure 10.4a. When the fuselage drops down, its potential energy is converted into kinetic energy. At the moment of impact, this energy is transferred into the structure and 60% of the energy is absorbed by the frames of the fuselage [150]. Furthermore, the cargo floor undergoes a bending deformation which risks the safety of the passengers as can be seen in figure 10.4b. To protect the passengers, the structure can be modified by changing the number of frames used in the fuselage and the location of the struts. The bending deformation of the cargo floor and its supports is analyzed by applying Castigliano's second theorem.

(a) Structural breakdown of the bottom fuselage [151].

(b) Bending deformation of the cargo floor and supports after impact[152].
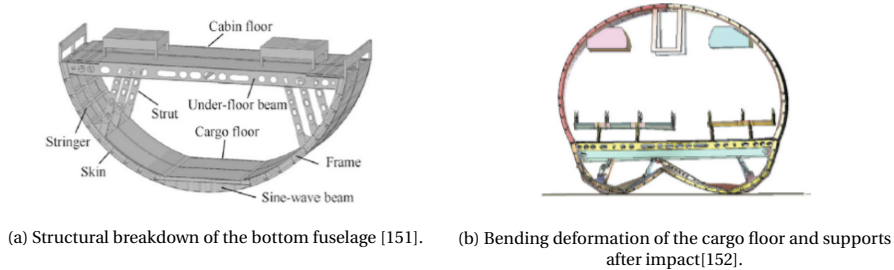
Figure 10.4: Lower fuselage structure and its deformed shape after a drop test.

10.7.2. Castigliano's Second Theorem

An equation needs to be found in order to properly analyze the deflection of the bottom half of the frames. For this several assumptions are made:

- The height of the frame is negligible compared to the radius of the fuselage.
- The bottom part of the fuselage is modelled as two separate circular beams. Normally these are logically fixed to one another so the normal bending properties of the frames are better compared to the performed analysis.

The structure is idealized as shown in figure 10.5.
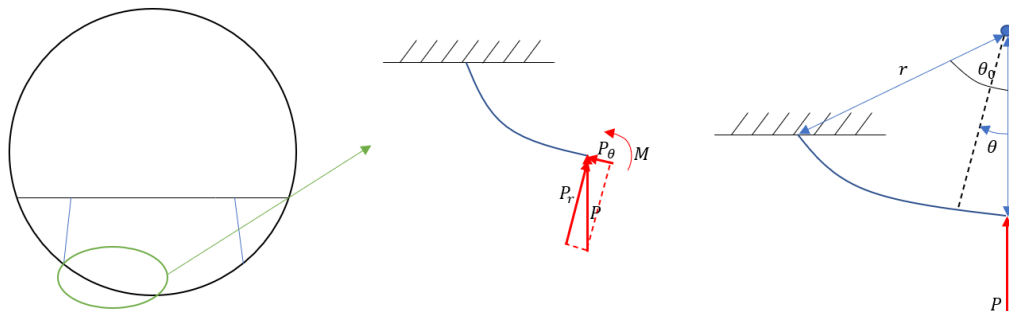
Figure 10.5: Idealization of the frame for the drop test.

Making the change to internal forces and polar coordinates yields the following forces and moment [153]:

$$P_r = P\cos(\theta) \quad (10.6) \qquad P_\theta = P\sin(\theta) \quad (10.7) \qquad M = PR\sin(\theta) \quad (10.8)$$

The strain energy in the beam consists of four different components [153]:

- Strain energy due to the bending moment

$$U_1 = \int_0^{\theta_0} \frac{M^2 R}{2EI}\, d\theta \tag{10.9}$$

- Strain energy due to the axial force F_θ:

$$U_2 = \int_0^{\theta_0} \frac{P_\theta^2 R}{2AE}\, d\theta \tag{10.10}$$

- Strain energy due to the moment generated by force F_θ:

$$U_3 = \int_0^{\theta_0} \frac{MP_\theta}{AE} d\theta \tag{10.11}$$

- Strain energy caused by the shear force F_r:

$$U_4 = \int_0^{\theta_0} \frac{P_r^2 CR}{2AG} d\theta \tag{10.12}$$

where C denotes the correction factor for the cross-section [153].

The deflection at the point where force P is introduced can now be found using Castigliano's second Theorem [153]:

$$\delta = \frac{\partial U}{\partial P} = \frac{\partial U_1}{\partial P} + \frac{\partial U_2}{\partial P} + \frac{\partial U_3}{\partial P} + \frac{\partial U_4}{\partial P} \tag{10.13}$$

Simplifying this equation, using the polar coordinates definitions for the internal forces, yields:

$$\delta = \left(\frac{PR^3}{2EI} - \frac{PR}{2AE} \right) \left(\theta_0 - \frac{1}{2} \sin(2\theta_0) \right) + \frac{PCR^3}{2AG} \left(\theta_0 + \frac{1}{2} \sin(2\theta_0) \right) \tag{10.14}$$

10.7.3. Results

By applying the formulas from subsection 10.7.2 the deflection of a bottom frame could be computed if the aircraft would drop down with an acceleration of 9.5g. By installing 80 frames within the fuselage, the bottom deflection of a frame is 0.98 m which is well below the floor height of 1.62 m and therefore, meeting requirement **WFC-STRUC-09**. An overview of the results and the dimensions of the frame can be seen in table 10.4 and figure 10.6 respectively.

Table 10.4: Drop test results.

Parameter	Value	Unit
Fuselage radius r	1.81	[m]
Floor height	1.62	[m]
Number of frames	80	[-]
Frame spacing	500	[mm]
MTOW	69,310	[kg]
θ_0	0.21π	[rad]
Moment of inertia frame	1.88E-7	[m^4]
Deflection	0.98	[m]
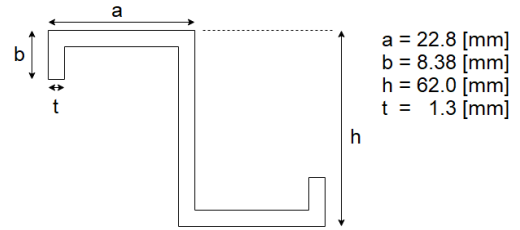
Figure 10.6: Fuselage frame dimensions.

Lastly, an inspection has been performed on the stiffness between the cabin and the hydrogen tank fuselage section to ensure that after impact both sections separate from each other. Figure 10.7 presents the division of an end-of-cabin, galley and hydrogen tank part. Since the wing-fuselage connection and the hydrogen tank are stiff components compared to the galley, it is expected that fracture would occur between the end-of-cabin and hydrogen tank section as indicated by the blue line in figure 10.7. This ensures passenger safety in case the hydrogen tank structure would fail at impact as discussed in the risk assessment in section 13.3.
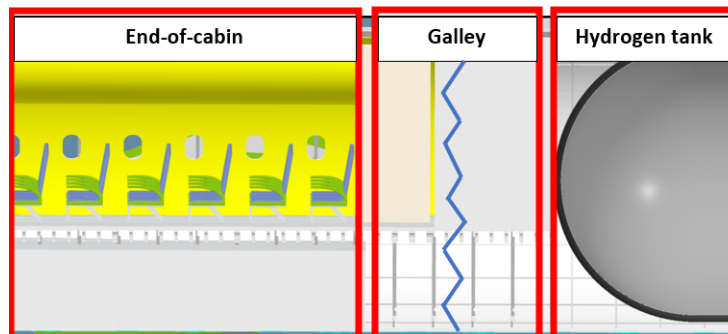
Figure 10.7: Fracture between fuselage sections due to a drop test.

10.8. Structures Trade-off

For the structural design of the wing and fuselage, it has been determined that applying Aluminum 2024-T3 for stiffening components such as stringers, ribs and frames enhances the resistance against lightning strikes and gives the opportunity to apply metals or composites for the skin panels. The total structural weight is computed by combining the results for the required skin thickness, stringer dimensions and frame dimensions. The cost for the material is then obtained by using the virgin material cost from table 6.1. The results of the total weight and material cost of the wing and fuselage for the different materials are shown in table 10.5.

Table 10.5: The results of the fuselage and wing weight and material cost.

Parameters	Unit	Fuselage			Wing		
		2024-T3	T800S Carbon	GLARE 4	2024-T3	T800S Carbon	GLARE 2
Weight	[kg]	11,734	5,628	9,785	4,366	1,788	3,878
Material cost	[USD]	65,945	306,716	163,909	24,537	184,161	66,745

The criterion weights are assigned as follows. For the material score, a relatively high importance is given as this criterion considers the recyclability of the material and other considerations which affect cost. A weight of 0.3 is assigned. The highest weight of 0.5 is given to the structural weight. Reductions in weight are one of the most efficient ways to reduce operational costs and improve sustainability through the reduction in required fuel. A weight of 0.2 is given to the material cost. Although this might seem like a low trade-off weight, the maintenance costs over the operational life of an aircraft are around 2-3 times greater than the initial material cost [49]. The ease of maintenance is considered in the material score through the corrosion resistance, thus consolidating the criterion weight choices.

The material scores are taken directly from section 6.7. The scores for weight and material cost are based on the results from table 10.5. The highest weight or cost is given a score of 1, while the lowest is given a 5. The middle value is found using linear interpolation.

The results of the trade-off for wing and fuselage are presented in tables 10.6 and 10.7 respectively.

Table 10.6: Trade-off for wing design.

Criteria	Weight	Al 2024-T3	T800S	GLARE 2
Material score	0.3	4.4	3.55	3.15
Weight [kg]	0.5	1	5	1.76
Material cost [USD]	0.2	5	1	3.94
		Total	2.82	3.77	2.61
		Rank	2	1	3

Table 10.7: Trade-off for fuselage design.

Criteria	Weight	Al 2024-T3	T800S	GLARE 4
Material score	0.3	4.4	3.55	3.15
Weight [kg]	0.5	1	5	2.28
Material cost [USD]	0.2	5	1	3.37
		Total	2.82	3.77	2.76
		Rank	2	1	3

Sensitivity of the trade-off is assessed in three ways: changing weights of structures trade-off, weights of materials trade-off of section 6.7 and scores on materials trade-off of section 6.7. First, the weights used in the structures trade-off are varied to see the effect on the results. The weights of material score and cost are increased while the one for structural weight is decreased to check if T800S is still the winner. For combinations of material score/weight/material cost of 0.45/0.35/0.2, 0.4/0.35/0.25 and 0.3/0.4/0.3, the rank is the same for all three materials for both wing and fuselage. Secondly, the weights of the materials trade-off are changed to see the change in rank of the structures trade-off. Since the material score is used in the structures trade-off with a relatively low criterion weight, the effect on the structures trade-off total scores is barely noticeable even for large changes in material trade-off weights. The rank is thus unchanged. Finally, the same effect is observed when the scores of the materials trade-off are adjusted.

The result of the trade-off is the use of T800S Carbon for the fuselage and wing skin with Aluminum 2024-T3 frames, longerons, ribs and stiffeners.

10.9. Verification and Validation

Verification and validation are essential to find out whether results are logical and actually trustworthy. This section focuses on performing the verification and validation for the elements discussed in this chapter.

10.9.1. Fatigue

To verify the calculation of the structural fatigue sizing, the computational model from the hydrogen tank fatigue sizing in subsection 9.2.1 is used. The two departments chose a different approach to the

fatigue sizing. First, the Wöhler curves are compared graphically. The input values used for the calculation of allowable stress amplitude in the fuel tank for T800S material are put into the structural fatigue program. A percentage difference of 0.099% is found. Such a small difference can be attributed to computer rounding errors. The calculation of fatigue stress adjusted to $R = 0$ was also verified by hand calculations using trigonometry and the same values were obtained.

In order to validate the fatigue calculations, the analytical results are compared to experimental data. The maximum allowable stress values are compared for Aluminum 2024-T3 alloy at 350,400 cycles. The experimental data obtained from Rice et al. [154] presents graphs for $K_t = 2$, $q = 0.92$ and $K_t = 3$, $q = 0.75$. The experimental values are found to be higher than the ones obtained analytically, which is expected due to the conservative approach used when constructing the Wöhler curves in section 10.5. The validation results are presented in table 10.8.

Table 10.8: Validation of fatigue calculations for Aluminum 2024-T3.

| Parameter | Unit | Kt = 2, q = 0.92, N=350,400 | | | Kt = 3, q = 0.75, N = 350,400 | | |
		Analytical	Experimental	Error	Analytical	Experimental	Error
Allowable stress amplitude S_a	[MPa]	95.47	99.97	-3.79%	65.74	68.95	-4.66%

10.9.2. Damage tolerance

The results obtained for the damage tolerance analysis are verified at several stages using hand calculations. The errors observed are documented in tables 10.9, 10.10 and 10.11 for Aluminum 2024-T3, CFRP and GLARE 4 respectively. These errors can be attributed to the allowable number of decimal places on a calculator, proving the computer program to be more accurate.

Table 10.9: Damage tolerance results verification for Aluminum 2024-T3.

Parameter	Unit	Computer program	Hand calculations	Percentage error [%]
Pressure at 11,000 m	[Pa]	22,632.0639734629	22,632.06397	1.53E-08
Pressure at 2,500 m	[Pa]	74,682.5336614574	74,682.53366	1.95E-09
Hoop stress	[MPa]	47.105675067635	47.10567507	-5.02E-09
S_{crit} for $2a = 500$ mm	[MPa]	102.456828372273	102.4568284	-2.71E-08
Allowable crack length $2a$	[mm]	591.351039620601	591.3510396	3.48E-09

Table 10.10: Damage tolerance results verification for CFRP.

Parameter	Unit	Computer program	Hand calculations	Percentage error[%]
Pressure at 11,000 m	[Pa]	22,632.0639734629	22,632.06397	1.53E-08%
Pressure at 2,500 m	[Pa]	74,682.5336614574	74,682.53366	1.95E-09%
Hoop stress	[MPa]	58.8820938345438	58.88209383	7.72E-09 %
S_{crit} for $2a = 500$ mm	[MPa]	156.3933525594380	156.39335256	-3.59E-10 %
Allowable crack length $2a$	[mm]	881.8203199806070	881.82031998	6.88E-11 %

Table 10.11: Damage tolerance results verification for GLARE 4.

Parameter	Unit	Computer program	Hand calculations	Percentage error [%]
Pressure at 11,000 m	[Pa]	22,632.0639734629	22,632.06397	1.53E-08
Pressure at 2,500 m	[Pa]	74,682.5336614574	74,682.53366	1.95E-09
Hoop stress	[MPa]	62.8075667568467	62.80756676	-5.02E-09
S_{crit} for $2a = 500$ mm	[MPa]	305.4323810594140	305.43238106	-1.92E-10
Allowable crack length $2a$	[mm]	2,956.0803283861600	2,956.08032839	-1.30E-10

10.9.3. Drop test

Verification of the drop test is performed using data from the Boeing 707 frames [149]. This data can be found in table 10.12. As mentioned in the table the moment of inertia is based on figure 10.8, the exact dimensions used in the figure are obtained from NASA [149].

Table 10.12: Properties of the Boeing 707 aircraft for the drop test [149]

Parameter	Value	Unit	Assumption
Fuselage radius r	1.77	[m]	
Floor height	1.77	[m]	The same as the radius.
Number of frames	78	[-]	85% of the length of the plane is able to have circular impact resisting frames.
Frame spacing	500	[mm]	According to Johnson et al [149].
MTOW	99,880	[kg]	
θ_0	0.25π	[rad]	Based on similar aircraft cross-sections.
Moment of inertia frame	2.15E-7	[m^4]	Based on frame dimensions (figure 10.8), excluding crown and keel.
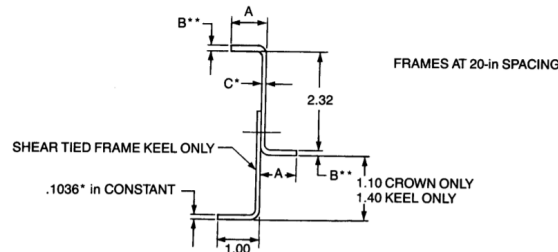
Figure 10.8: Frame used on the Boeing 707 (obtained from NASA [149])

Using the same assumptions as in section 10.7 the deflection of the lower fuselage is found to be 1.78 m, which is approximately the same value as the floor height. Due to the large number of assumptions made the 1 cm excessive deflection is deemed to be negligible and the passengers are thus safe for this specific test. The method is hence verified.

10.9.4. Structural weight and skin thickness

The validation of the wing structural weight and required skin thickness is performed by using data of a modified McDonnell Douglas MD 90-40X aircraft. The modification was performed by NASA in a research project to find out how composite materials such as CFRP influence the structural integrity and weight of the wing [155]. In table 10.13, the wing characteristics are present and as can be seen the wing weight of the SHOTS aircraft is in the same order of magnitude as the wing weight of the modified McDonnell Douglas MD 90-40X. However, since the required skin thickness of T800S is determined in a conservative manner the value is substantially higher than for the modified McDonnell Douglas MD 90-40X. Therefore, further research and testing is required to optimize the thickness of the wing panels. Regarding the fuselage skin thickness, the Airbus A350 XWB's fuselage skin is 1.27 mm, therefore, validating the thickness of 1.6 mm presented in table 10.2 for T800S Carbon. Lastly, the fuselage structural weight of the Airbus A350 XWB is 4,082 kg[2] which is 38% ligher than the 5,628 kg for the fuselage structure of the SHOTS aircraft. Since Aluminum 2024-T3 is selected for stiffening components, instead of an aluminum-lithium composite used in the Airbus A350 XWB [67], the structural weight is higher but acceptable and compliant with requirement **WFC-STRUC-11**.

Table 10.13: Wing structural weight and skin thickness validation [155] [156] [145].

Parameter	MD 90-40X	SHOTS*	Unit
Wing area	134.43	132.57	[m^2]
Wing span	35.05	35.99	[m]
Aspect ratio	9.137	9.645	[-]
Max distance between spars	2.85	3.15	[m]
Material stringer	T800	Al 2024-T3	[-]
Material wing panel skin	DMS-2436-D	T800S	[-]
Density stringer material	1,800	2,780	[kg/m^3]
Density skin material	2,000	1,800	[kg/m^3]
Ultimate stress skin composite	996	1,000	[MPa]
Operational altitude	10,600	11,000	[m]
Cruise Mach	0.76	0.79	[-]
Wing weight	1,823	1,788	[kg]
Required skin thickness	1.4	4.6	[mm]

* SHOTS-1 and SHOTS-2 have the same wing characteristics.

[2] https://www.compositesworld.com/articles/a350-xwb-update-smart-manufacturing (accessed 29-06-2020)

Final Design Results

This chapter lists the overall results of the SHOTS aircraft. This includes information on the basic dimensions of the aircraft, the airfoil and the weight of the aircraft, among other things in section 11.1. Then, section 11.2 presents the updated technical resource budgets for the cost and mass of the aircraft subsystems. Moreover, section 11.3 presents the system interface consisting of the hard- and software diagrams, data handling block diagram, electrical block diagram, and communication flow diagram.

11.1. Design Overview

The main parameters of the SHOTS aircraft are provided in table 11.1. Please note that the results of both design options SHOTS-1 and SHOTS-2 are given. Furthermore, the engine type also denotes the engine models selected for SHOT-1 and SHOT-2. Detailed CATIA drawings are made to depict the aircraft design in a holistic manner for SHOT-1 only as the main difference in the aircraft configuration between SHOTS-1 and SHOTS-2 is the selected engine models. Figure 11.1 presents the render image of the aircraft at cruise, figure 11.2 shows the exploded view of the aircraft, and finally, figure 11.3 shows the cross section of the fuselage to depict the layout of cabin. Finally, figures 11.5, 11.6 and 11.7 show the 3 view drawings of SHOTS.

Table 11.1: Parameters of the SHOTS aircraft.

Parameter	SHOTS-1	SHOTS-2	Parameter	SHOTS-1	SHOTS-2
Wing area [m^2]	132.57	132.57	Engine type [-]	PW1700G	PW1700G/CF34A*
Max wing loading [kg/m^2]	522.82	533.80	Number of engines [-]	4	4
Aspect ratio [-]	9.645	9.645	Max cruise Mach number [-]	0.82	0.82
Wing span [m]	35.99	35.99	Max ROC [km/h]	111.6	104.4
Length [m]	46.81	46.81	Takeoff distance [m]	1484	1495.7
Airfoil [-]	NASA SC(2) 00710	NASA SC(2) 00710	Landing distance [m]	1452	1451
Range [km]	4,399	4,350	Stall speed [km/h]	190	190
Pax [-]	120	120	Max thrust loading [kg/kN]	256.8	272.9
MTOW [kg]	69,310	70,710	CO_2 emissions [kg/s]	1.093	1.345
OEW [kg]	47,983	47,983	NO_x emissions [kg/s]	0.239	0.224
Max payload [kg]	12,283	12,283	Refueling time [min]	5.9	7.2
Max fuel [kg]	2,063/6,890 **	2,063/8,390	Turnaround time [min]	18	18

* *SHOTS-2 uses two PW1700G and two CF34A engines.*
** *Fuel weight consists of hydrogen/biokerosene weight.*

Figure 11.1: Render of SHOTS at cruise.

Figure 11.2: Render of SHOTS in exploded view.

Figure 11.3: Seats map of SHOTS.

Figure 11.4: Cabin layout of SHOTS.

Figure 11.5: Front view drawing of SHOTS.

Figure 11.6: Top view drawing of SHOTS.

Figure 11.7: Left view drawing of SHOTS.

11.2. Technical Resource Budget Breakdown

With a detailed conceptual design, the technical budget breakdown in section 4.1 can be reevaluated and updated as shown in table 11.2. The budgeted mass and cost of each subsystem with its corresponding acceptable error margin were set up in section 4.1. The current mass estimates are obtained from the class II weights in section 5.3. The current subsystem cost estimates are obtained using the current class II weight estimates and the typical cost per unit mass for every aircraft subsystem [157] adapted to year 2020 (more details are elaborated in section 14.2). A contingency of 7% which was defined in section 4.1.2 is added to the total cost estimate. The actual error margin is the percentage difference between the budget and the estimate value and if it falls under the acceptable error margin, the mass budget is considered to be met which is indicated by the green color whereas the orange color indicates that the mass budget is exceeded but is considered tolerable.

Table 11.2: Technical resource budget breakdown.

Subsystems	Budgeted mass [kg]	Current mass estimate [kg]	Acceptable error margin [±%]	Actual error margin [%]	Budgeted cost [mil$]	Current cost estimate [mil$]	Acceptable error margin [±%]	Actual error margin [%]
Wing	7,146	7,920	15	10.8	19.9	19.1	15	-4.0
Empennage	496	555	15	11.9	3.6	3.8	15	5.6
Fuselage	6,046	5,780	10	-4.4	18.0	13.3	15	-16.1
Landing gear	2,416	2,416	5	0	1.6	1.6	5	0
Nacelle	1,592	1,725	10	8.4	-	-	-	-
Fixed items*	9,327	9,330	5	0.03	12.4	12.4	5	0
Engines and tank**	23,329	20,257/20,165	15	-13.2/-13.6	48.0	48.6/38.6	10	1.3/-18.3
OEW**	**50,352**	**47,983/47891**	**<0***	**-4.7/-4.9**	**10.1**	**9.1/9.1**	**<0***	**-11.0/-11.0**
Hydrogen fuel	1,858	2,063	15	11.0	-	-	-	-
Biokerosene fuel**	6,981	6,981/8,324	15	0/19.2	-	-	-	-
Payload	12,283	12,283	5	0	21.4	20.3	5	-5.1
Total**	**71,471**	**69,310/70,561****	**<0***	**-3.0/-1.3**	**136.2**	**143.4/133.7**	**<0***	**5.8/-1.4**

*It contains standard operational equipment such as the avionics, electrical system, APU and furnishing
**Two different values are shown for SHOTS-1 and SHOTS-2 with the first one for SHOTS-1 and second one for SHOTS-2 with the rest of the values being equal for both options
***There is no positive error range, which means that a mass increase is avoided whereas a mass decrease is preferred.

Most of the subsystems meet the mass budget except for the biokerosene fuel of SHOTS-2 where the mass estimates exceeds the mass budget significantly by 19.2% outside the acceptable range of 15%.

The reason for the large increase in the biokerosene fuel mass of SHOTS-2 is due to the replacement of two PW1700G engines with two CF34-10A engines which have high specific fuel consumption than PW1700G. SHOTS-2 needs more biokerosene on-board to generate enough thrust and meet the range requirement. Overall, as the total mass (or MTOW) meets the mass budget, this increase in the mass of biokerosene fuel is considered acceptable. For the cost budget, the cost of the landing gear subsystem reduces significantly and the change is outsi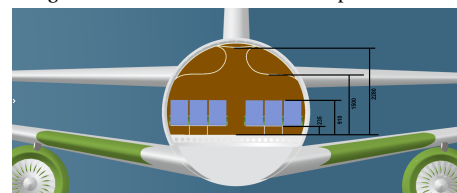de of the acceptable error margin of 15%; however, since a decrease in cost is desirable, this is deemed acceptable. The engines and tank cost of SHOTS-1 is significantly lower due to replacement of two PW1700G engines with two cheaper CF34-10A engines. Again, this is desirable and hence, it is acceptable. Overall, the total cost of option 1 exceeds the cost budget; however, since a contingency has been used, this discrepancy is deemed tolerable. In contrast, the total cost of option 2 is below the budget. Finally, the current mass and cost estimates will be used as the new budgets for the later design phases.

11.3. System Interfaces

In this section, the different diagrams that define the systems inside SHOTS are presented. More precisely, the hardware and software diagrams, followed by the electrical diagram, data handling diagram and finally, the communication flow diagram are presented.

Hardware and software diagrams

First, the hardware diagram is presented in figure 11.8. In this figure, the different top-level systems are shown in their respective locations in the aircraft and the arrows show the flow of data between the systems where the red arrows show the primary flow of data into the flight computers and the black arrows show the secondary flow of data to each top-level system.
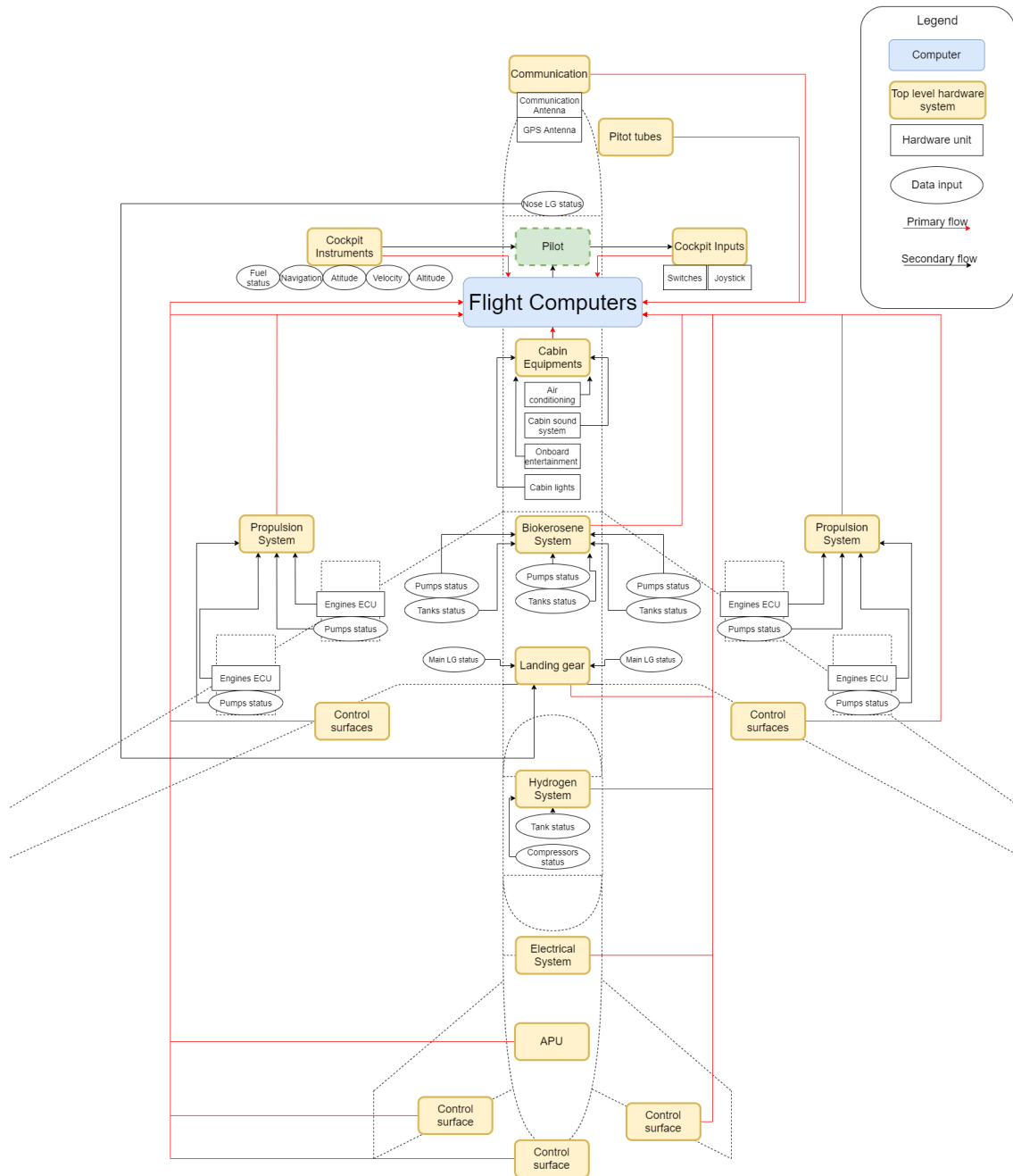
Figure 11.8: Hardware diagram SHOTS.

Next, the software diagrams are presented. Figure 11.9 shows the overview of the different software installed in the aircraft and how they communicate with each other in a flow-down structure.
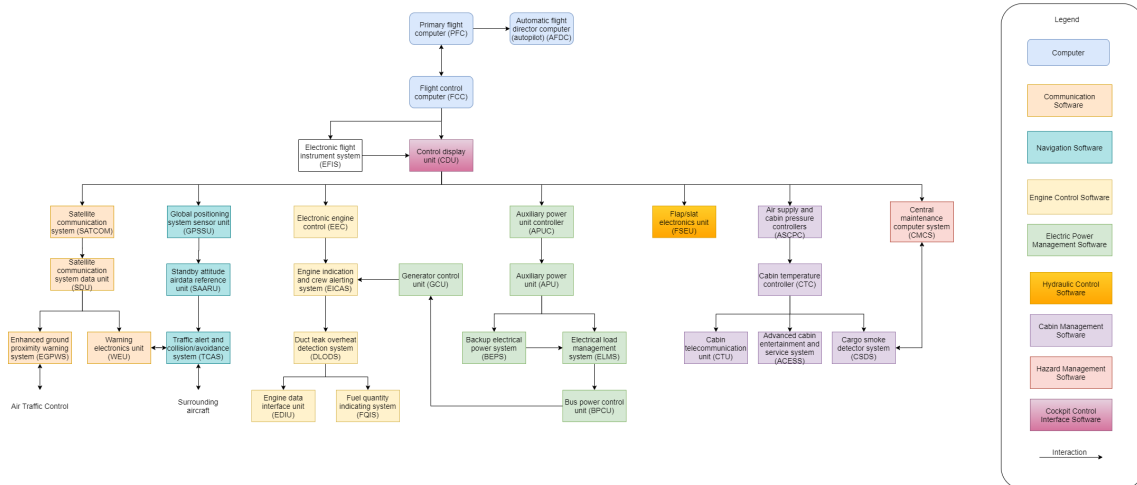
Figure 11.9: Software diagram for the SHOTS aircraft displaying the main software units.

Figure 11.10 illustrates the interactions between different software programs. The main computers, sensors and actuators on the aircraft are shown in the figure as well as the data flow where the arrow indicates when an input is given to a given subsystem, for example, engines and hydraulics.
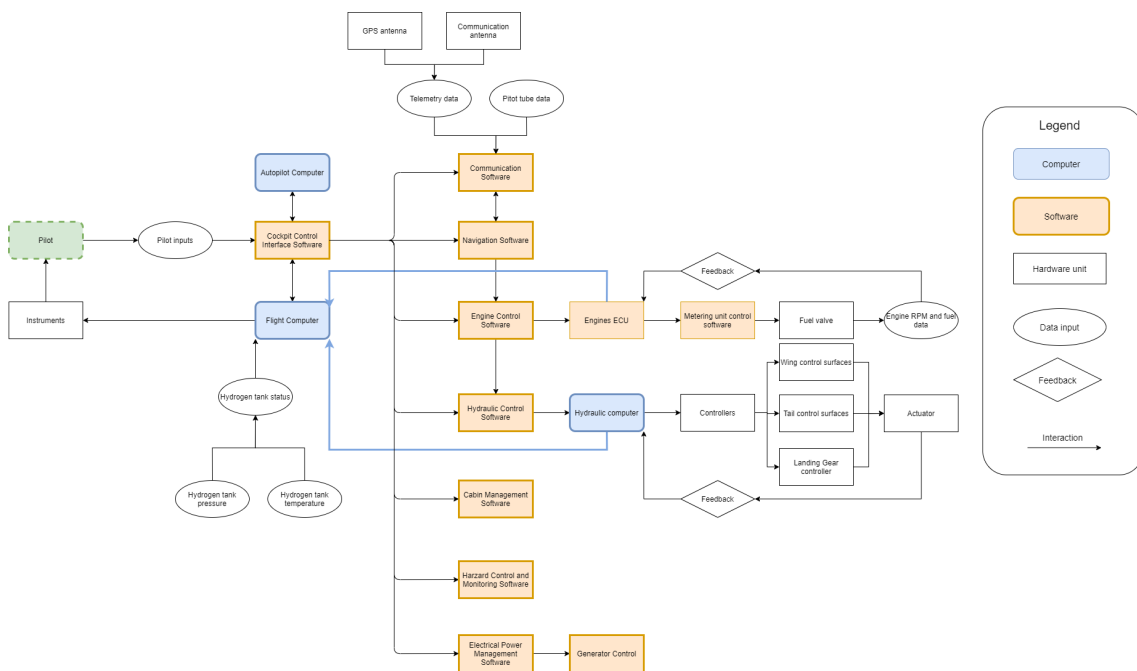
Figure 11.10: Software diagram for the SHOTS aircraft displaying the main interactions between different software units.

Electrical block diagram

Figure 11.11 gives an overview of the electrical system which shows both the main power lines and the backup power. The very top blocks are the electrical load management system, generator control unit, bus power control unit. The central maintenance computer system represent a computer with the respective software running, and as this can be a critical point in case of failure, these software run in multiple devices such that in case of failure from the main one, a backup device can take over. A white block represents a physical hardware/system where as a dashed block represents a group of software programs.
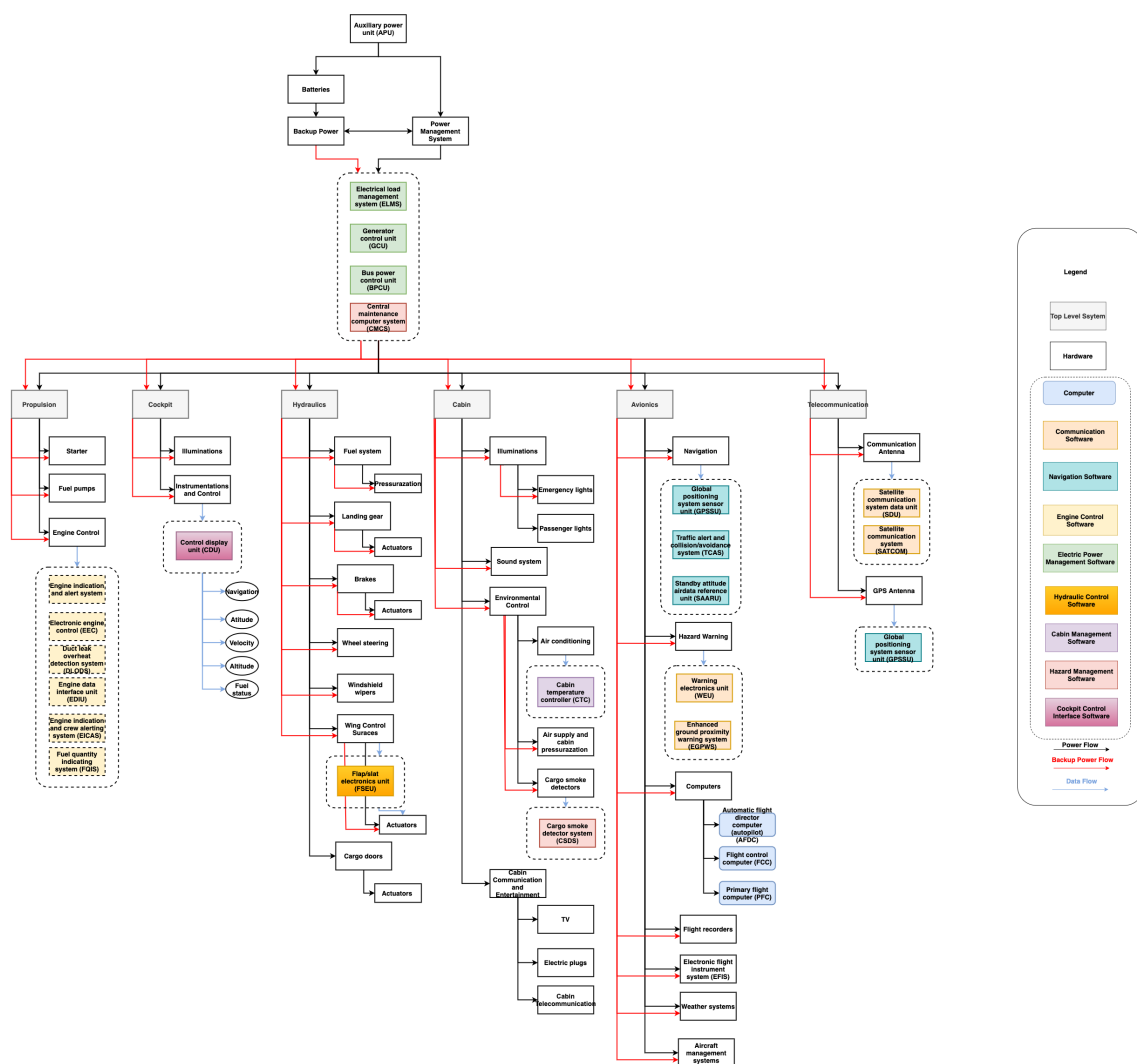
Figure 11.11: Electrical block diagram of the SHOTS aircraft.

Data handling block diagram

The data handling diagram, as shown in figure 11.12, gives an overview of how data flows from different systems and locations flow within the aircraft. Each block represents a location/system, from which the data is transmitted to the cockpit (blue lines) and/or to the black-box (red lines) in the aircraft. How the data is transmitted to the ground station is also demonstrated in the diagram.
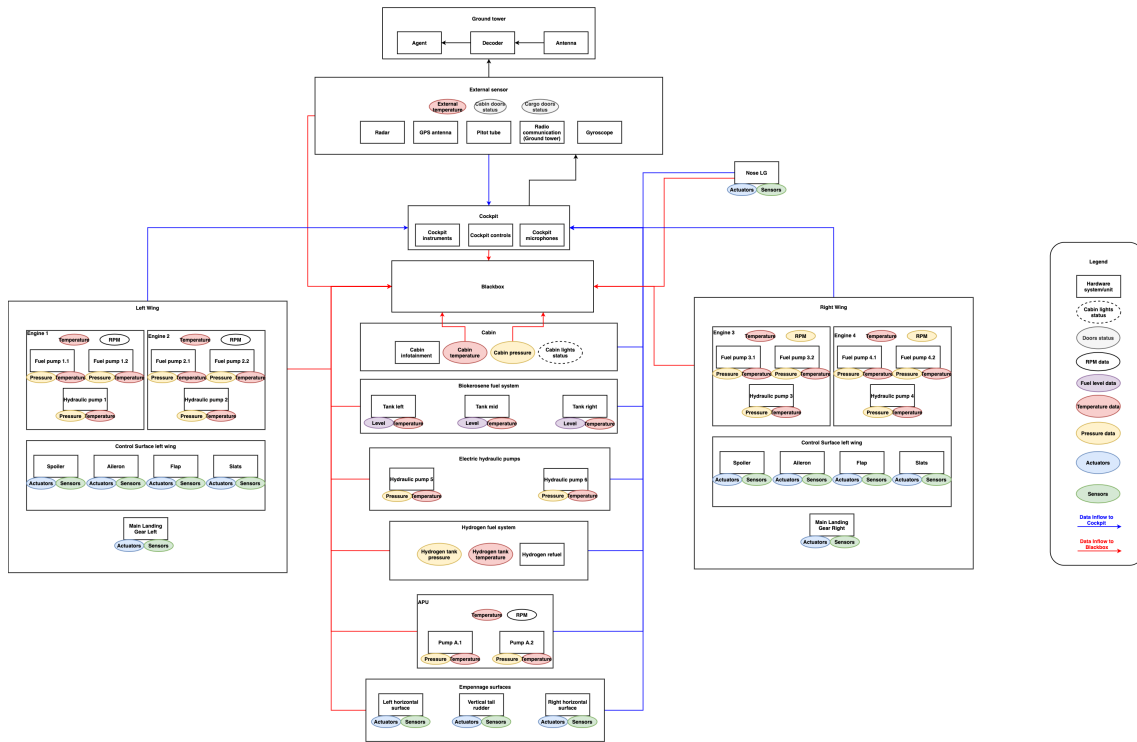
Figure 11.12: Data handling block diagram of the SHOTS aircraft.

Communication flow diagram.

Finally, the communication flow diagram can be found in figure 11.13. In this diagram, the information seen by the pilot in the cockpit instruments can be found as well as the origin of the data used by the instruments to indicate the final results. Hence, the pilot can have sufficient and accurate information to make commands to different systems such as the hydraulics system to operate the aircraft. Furthermore, the communication with the Air Traffic Control (ATC) is done in the 123.5 Mhz AM band [1].

Figure 11.13: Communication flow diagram of the SHOTS aircraft.

---

[1] https://wiki.radioreference.com/index.php/Aircraft#:~:text=In%20the%20US%20the%20civil,and%20136.5%2D136.875%20MHz%20ranges. (accessed 26-06-2020)

12

Technical Sensitivity Analysis

In this chapter, the technical sensitivity analysis of the design is performed. The technical sensitivity discusses several technical parameter changes in the design that affect the related subsystem and the aircraft system as a whole. By performing the analysis, one is able to gather insights on how well the design can cope with changes. Section 12.1 discusses the effects of increasing the hydrogen tank weight in the aircraft design whereas section 12.2 discusses the effects of changing the cruise altitude.

12.1. Modification in Hydrogen Tank Weight

The integration of the tank in the fuselage has only been discussed briefly, therefore it is possible that more material is needed to support the tank inside the fuselage. To investigate the sensitivity of the design, a weight increase of 10% is applied to the structural weight of the hydrogen tank. Having additional weight on-board of the aircraft leads to changes within the aircraft design.

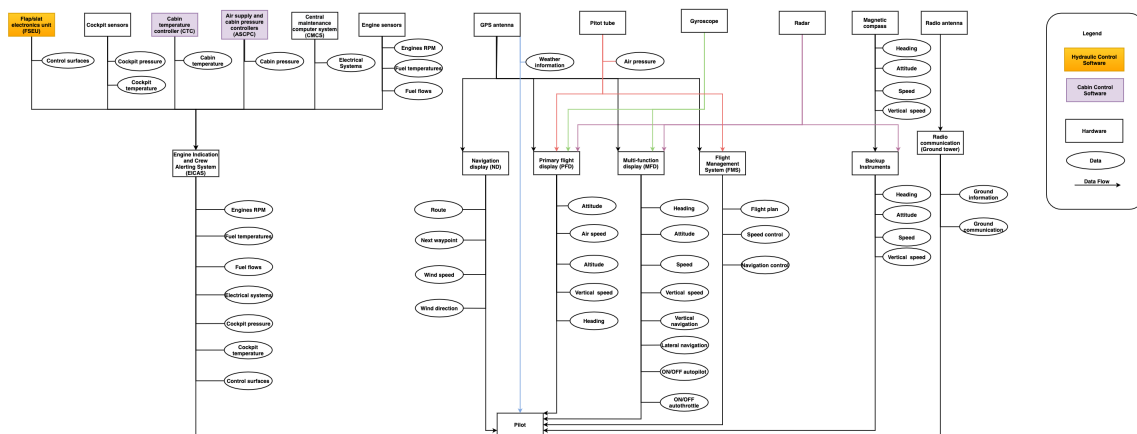The first change is clearly visible in the class II weight estimation. Due to a 10% increase in the structural weight of the hydrogen tank, there is an increase in fuselage, landing gear, tail and wing weight. Combining all these components results in a 2.9% increase in MTOW. In order to maintain the same wing loading, a larger wing area is required which impacts the produced drag and required thrust. The required thrust increases from 247 kN to 255.3 kN. However, the selected engine combinations of either four PW1700G engines or two PW1700G and two CF34 engines provide a maximum static thrust of 341.6 kN and 327.8 kN respectively. Thus, the selected engines can overcome the drag penalty; however, in order to do this, a higher thrust setting is required. More fuel needs to be burned, limiting the range of the aircraft from 4,399 km to 4,131 km, but the aircraft still complies with the **WFC-USER-PERF-01.1** requirement.

A second adjustment is regarding the increased wing area which is actually beneficial for the aerodynamic performance. An increase from 132 m^2 to 138 m^2 occurs and therefore, the wing can generate a larger amount of lift at for instance takeoff as can be seen in table 12.1. Furthermore, positioning the HLDs and other subsystems becomes easier due to the added surface area.

Lastly, since the hydrogen tank is located in the back of the fuselage, a weight increase of 1,336 kg has an immense impact on the stability of the aircraft. A special loading sequence is required and the aircraft would be unable to take off if less than 60% of the available seats are occupied.

An overview of the main parameter changes can be seen in table 12.1.

Table 12.1: Critical parameters changes due to an increase of 10% in tank structural weight.

Parameter	Unit	Current values	Effect of hydrogen tank mass increase of 10 %	Difference
Hydrogen tank weight	[kg]	13,361	14,697	+10 %
MTOW	[kg]	69,310	71,314	+2.8 %
Range	[km]	4,399	4,131	-6.1 %
Lift at takeoff	[N]	903,736	944,882	+4.6
Ground stability	[-]	Nominal, no issues	Special loading sequence necessary, unable to take off with less than 60% of the available seats occupied	

Based on table 12.1, it can be concluded that the stability is very sensitive to hydrogen tank weight changes. Because the other requirements are still met, the total aircraft is not very sensitive to this change. It is recommended for future development that the spacial integration of the tank in the fuselage is further optimized. Secondly, thorough investigation has to be done into composites that have a higher

S_{UTS} because this will lower the tank structural mass. For this, newly developed Toray T1100G CFRP can be considered [158]. This will increase the design margin and resolve the stability problems.

12.2. New Regulation on Cruise Altitude

In the coming 20 years, the amount of aircraft flying is expected to double [159]. To make sure all the aircraft can operate in a safe way, regulations could change, mandating aircraft to fly at higher cruise altitudes. To inspect the robustness of the design to such a change, the cruise altitude of the aircraft is increased from 11,000 to 12,000 m.

First of all, due to a change in cruise altitude, there is a decrease in outside pressure, meaning that the pressure differential between cabin and the outside increases. This means that the stress in the fuselage skin increases. The new maximum allowable crack lengths for each material are given in table 12.2.

Table 12.2: Sensitivity analysis on damage tolerance calculations: new allowable crack length for 12,000 m cruise altitude.

Parameter	Unit	Aluminum 2024-T3	T800S Carbon	GLARE 4
Allowable crack length $2a$	[mm]	522	778	2,609

It is found that the values decrease by 11.7% with respect to the 11,000 m cruise altitude. Nevertheless, all three materials still comply with requirement **WFC-STRUC-04**. Although these values are still preliminary and more extensive analysis is required with the aid of experimental results, this shows the material selection of the aircraft can be maintained despite a new cruise altitude regulation.

Secondly, the aerodynamic performance of the aircraft is heavily affected. Because the air density is lower, a higher value of the airfoil design lift coefficient $C_{l_{des}}$ is required to meet the cruise speed requirement **WFC-PERF-06**. The required $C_{l_{des}}$ increases from 0.73 to 0.85. Currently, no transonic commercial airliner comparable to the SHOTS aircraft is flying with airfoils that deliver such a high $C_{l_{des}}$. This adjustment requires an iteration in the airfoil selection by selecting an airfoil that can provide the required $C_{l_{des}}$. The problem of this iteration is that a larger pressure difference is required to provide the design lift coefficient. For this, a thicker airfoil is needed which results in issues with the critical Mach number. To solve this, the sweep angle must be increased. However, this will negatively impact the elliptical lift distribution and add structural weight to the wing. In short, a snowball effect takes place which could lead to a total redesign of the wing and other subsystems. One other way to mitigate this is to increase the cruise speed to 242 m/s, or M_{cr} conditions. This would lead to increased drag, but the required $C_{l_{des}}$ lowers from 0.85 to 0.79. Further investigation into airfoils that can deliver a $C_{l_{des}}$ of 0.79 is necessary. Additionally, the engines must be able to provide enough thrust in the thinner air. However, because the SHOTS aircraft utilizes 4 engines, this is assumed to be possible.

In conclusion, the system is very sensitive to an increase in cruise altitude. It is it not able to fly at optimal conditions. Two different mitigation strategies are to increase the wing sweep or to fly faster. Also, a combination of these strategies can be adopted. Further research is necessary to investigate this.

The WeFlyCycle Roadmap

Once the initial design of an aircraft is completed, subsequent design phases of the project can start. This is followed by the flight testing and certification, after which the aircraft may enter into service. In this chapter, an overview is given of the entire life-cycle of the SHOTS aircraft. In section 13.1 the project gantt chart is provided. The following sections are based on each of the project phases shown in the gantt chart. The conceptual, preliminary and detailed design of the SHOTS aircraft is described in section 13.2. Next, the technical risk assessment is discussed in section 13.3. The production plan is described in section 13.5, followed by the operations and logistics which is described in section 13.6. Finally, the aircraft EOL phase is described in section 13.6.5.

13.1. Project Gantt Chart

The time between the initial mission statement and the disassembly of an aircraft is often multiple decades; designing the aircraft and manufacturing it takes around eight years, flight testing and certification another year and an aircraft can be serviceable for over 30 years. In figure 13.1 an overview of all the project phases of the SHOTS aircraft is shown.
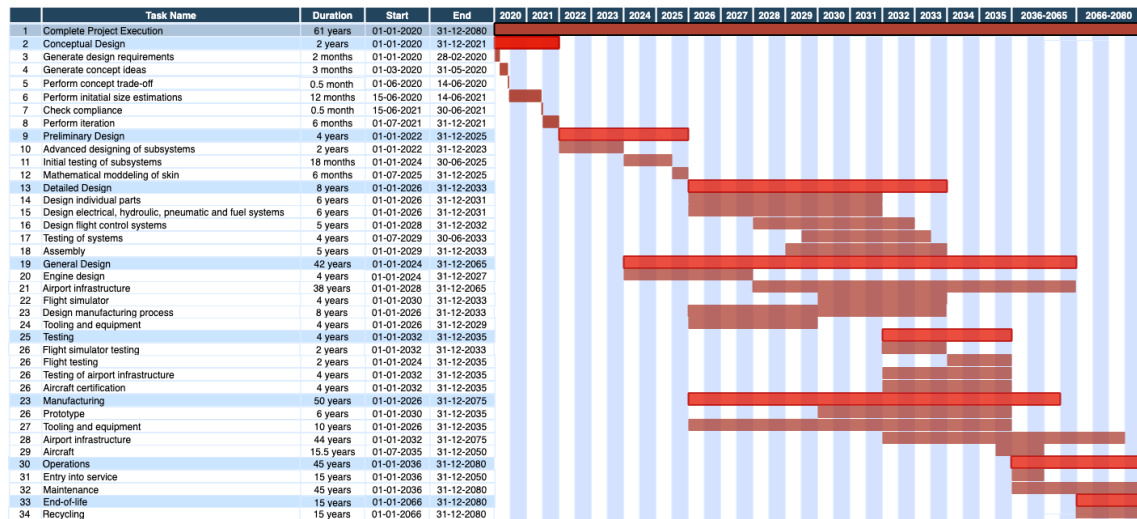
#	Task Name	Duration	Start	End
1	Complete Project Execution	61 years	01-01-2020	31-12-2080
2	Conceptual Design	2 years	01-01-2020	31-12-2021
3	Generate design requirements	2 months	01-01-2020	28-02-2020
4	Generate concept ideas	3 months	01-03-2020	31-05-2020
5	Perform concept trade-off	0.5 month	01-06-2020	14-06-2020
6	Perform initatial size estimations	12 months	15-06-2020	14-06-2021
7	Check compliance	0.5 month	15-06-2021	30-06-2021
8	Perform iteration	6 months	01-07-2021	31-12-2021
9	Preliminary Design	4 years	01-01-2022	31-12-2025
10	Advanced designing of subsystems	2 years	01-01-2022	31-12-2023
11	Initial testing of subsystems	18 months	01-01-2024	30-06-2025
12	Mathematical moddeling of skin	6 months	01-07-2025	31-12-2025
13	Detailed Design	8 years	01-01-2026	31-12-2033
14	Design individual parts	6 years	01-01-2026	31-12-2031
15	Design electrical, hydraulic, pneumatic and fuel systems	6 years	01-01-2026	31-12-2031
16	Design flight control systems	5 years	01-01-2028	31-12-2032
17	Testing of systems	4 years	01-07-2029	30-06-2033
18	Assembly	5 years	01-01-2029	31-12-2033
19	General Design	42 years	01-01-2024	31-12-2065
20	Engine design	4 years	01-01-2024	31-12-2027
21	Airport infrastructure	38 years	01-01-2028	31-12-2065
22	Flight simulator	4 years	01-01-2030	31-12-2033
23	Design manufacturing process	8 years	01-01-2026	31-12-2033
24	Tooling and equipment	4 years	01-01-2026	31-12-2029
25	Testing	4 years	01-01-2032	31-12-2033
26	Flight simulator testing	2 years	01-01-2032	31-12-2033
26	Flight testing	2 years	01-01-2034	31-12-2035
26	Testing of airport infrastructure	4 years	01-01-2032	31-12-2035
26	Aircraft certification	4 years	01-01-2032	31-12-2035
23	Manufacturing	50 years	01-01-2026	31-12-2075
26	Prototype	6 years	01-01-2030	31-12-2035
27	Tooling and equipment	10 years	01-01-2026	31-12-2035
28	Airport infrastructure	44 years	01-01-2032	31-12-2075
29	Aircraft	15.5 years	01-07-2035	31-12-2050
30	Operations	45 years	01-01-2036	31-12-2080
31	Entry into service	15 years	01-01-2036	31-12-2050
32	Maintenance	45 years	01-01-2036	31-12-2080
33	End-of-life	15 years	01-01-2066	31-12-2080
34	Recycling	15 years	01-01-2066	31-12-2080

Figure 13.1: Overview of aircraft future design and operations.

13.2. Design Phases

The design of an aircraft can be split into three phases: the conceptual design phase which is described in subsection 13.2.1, the preliminary design phase which is described in subsection 13.2.2 and the detailed design phase is described in subsection 13.2.3.

13.2.1. Conceptual design

In the conceptual design phase, the concept is chosen which best fits the user requirements. This is the design phase in which the SHOTS aircraft currently is at. The conceptual design starts with translating the top level requirements from the customer into technical requirements. After an overview of all possible concepts is generated, a trade-off is performed in order to choose the most suitable concept. The general aircraft parameters are then determined, after which it is checked that the concept meets all requirements. If this is not the case, an iteration on the concept's subsystems needs to be performed. It might even be required to review the concepts overview and choose an entirely different concept. An

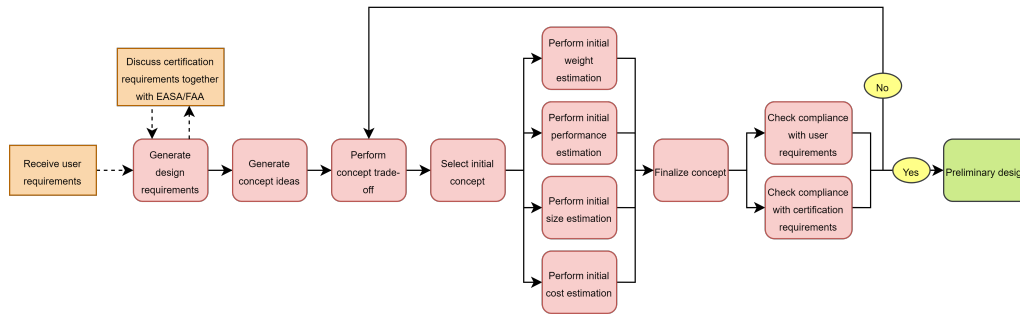overview of the SHOTS conceptual design phase is provided in figure 13.2.

Figure 13.2: Overview of the conceptual design phase.

13.2.2. Preliminary design

After the most suitable concept is chosen, the preliminary design phase begins. During this phase, no significant changes are allowed to the design. Furthermore, the first testing of subsystems is performed which might be done by using computer software or actual scale models. The preliminary design phase is concluded with the decision from the customer to continue the program or not. This decision is sometimes referred to as 'you bet your company' since it might occur that the sales of the aircraft will not be high enough to reach the break-even point [97]. If the customer chooses to continue the program, the concept goes into the detailed design phase. The overview of the preliminary design phase of the SHOTS aircraft project is shown in figure 13.3.
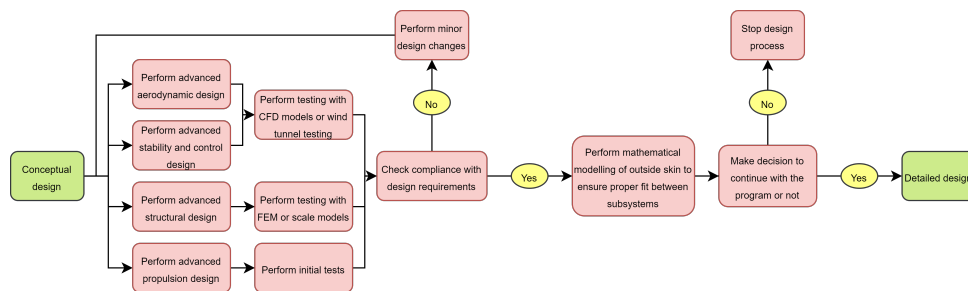

Figure 13.3: Overview of preliminary design phase.

13.2.3. Detailed design

If the customer decides to continue the program after the preliminary design phase, the concept enters the detailed design phase. This design phase takes the longest time of all three phases. In this phase, all parts are being designed in full detail. Furthermore, the production process of the aircraft will be designed, as well as the tools and jigs required for the manufacturing of the aircraft. Concurrent to this, the electrical, hydraulic, pneumatic, fuel and flight control systems are fully designed and tested. Once all parts of a subsystem are designed and manufactured, it is possible to assemble these subsystems and perform full scale testing. Finally, once all subsystems are individually tested, the entire aircraft can be assembled and the certification process of the complete aircraft can start. The overview of the detailed design phase of the SHOTS aircraft project is presented in figure 13.4.
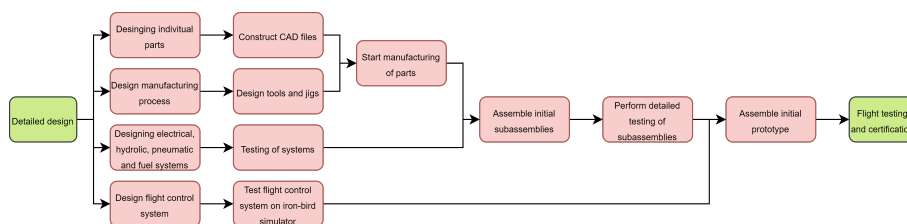

Figure 13.4: Overview of detailed design phase.

13.3. Technical Risk Assessment

This section discusses the identification, assessment and mitigation of technical risks. For a more elaborate discussion on the project's related risks, the Baseline [2] and Midterm Report [3] can be consulted.

The probability and impact of a risk are scored by using 5-point scales as shown in table 13.1. It should be noted that these scores mainly apply to operational risks. For the probability estimation of other design risks, the TRL of a given technology has also been taken into account. Similarly, while several risks have a clear impact on the aircraft and its passengers, some risks relate more to the design process itself. The risks in table 13.2 are selected based on the fact that important system requirements and design consideration are based on them. DES, PROD and OPS denote the design, production and operational risks respectively. In table 13.3, system risks are discussed. These system risks provide important safety requirements in the design of the subsystems. References to these sections is added in the fifth column. Mitigation measures are briefly summarized from these design sections.

Table 13.1: Probability and impact scales for risk assessment.

| Probability	Explanation	Impact	Explanation
1: very low	Basically never happens	1: very low	Project or aircraft and passengers unaffected
2: low	Unlikely to happen	2: low	Project or aircraft slightly affected
3: moderate	Happens once during operational lifetime	3: moderate	Mission continues, aircraft and passengers affected
4: high	Likely to happen within 1,000 flight cycles	4: severe	Mission failure, non-lethal damage to passengers
5: inevitable	Likely to happen soon	5: catastrophic	(Partial) destruction of aircraft and lethal damage to passengers

Table 13.2: Process risk identification and assessment.

	Identifier	Risk	Probability	Impact	Mitigation strategy
1	R-DES/PROD/OPS-1	Loss of funding or demand due to bankruptcy of customer or contact breach	2	4	Contract multiple customers and ask for advance payment, Close collaboration with customers to incorporate their needs
2	R-DES-8	Less optimal final design due to bad design choices caused by insufficient concept analysis, wrong trade-offs or assumptions	4	4	Perform literature study and contact experts to identify driving and killer requirements. Discuss design choices with external experts to get feedback on these choices
3	R-PROD-8-9	Depletion of natural resources because recycled and recyclable materials can not be used due to unavailability or underperformance	3	4	Perform in-depth market analysis into materials, reducing probability that this will happen. Find and certify back-up materials
4	R-PROD-14/OPS-9	Health problems due to manufacturing or maintenance of new recyclable materials	3	3	Perform weekly health checks, Wear protective gear
5	R-OPS-8	Decrease in demand because aircraft cannot be upgraded with new parts as there is no room for system swapping or lack of resources	3	3	Flexible design that allows for easy subsystem swaps, Adopt easy-access assembly methods

Table 13.3: System risk identification and assessment.

	Identifier	Risk	Probability	Impact	Reference	Mitigation strategy
6	R-SYS-1	In flight hydrogen tank burst, leading to sudden release of compressed hydrogen. This could cause failure of the fuselage because the internal pressure becomes too high.	2	5	section 9.3	Installation of emergency release valves in the fuselage section where the tank is located.
7	R-SYS-2	Failure of hydrogen engine supply, only biokerosene available for propulsion	3	4	subsection 9.4.1	Piping system redundancy
8	R-SYS-3	Landing gear failure leading to damage on airframe structure causing fuel tank rupture. The escaping gas can be dangerous for the passengers.	2	5	subsection 10.7.3	Fuselage designed to separate between cabin and hydrogen tank.
9	R-SYS-4	Placing the hydrogen tank in the back of the fuselage can cause stability and controllability problems due to high weight concentration in the back of the aircraft, leading to an oversized empennage	3	4	section 9.2 and 9.4.2	High importance of tank mass in material trade-off, Placing hydrogen tank inside bulk head, hence optimizing fuselage layout.
10	R-SYS-5	Shearing-off of the valves on the hydrogen tank, causing a sudden release of hydrogen and possibly moving the tank in opposite direction due to reaction forces.	2	4	section 9.3	Placing the valves on the back of the tank, design of firewall and floor to withstand reaction forces.
11	R-OPS-3	Aircraft stuck on an airport because energy infrastructure is not in place, meaning the aircraft can not refill the tanks at a given airport.	3	4	section 3.1 and 3.3	Keep reserve fuel for 10% extra distance, Design fuel system capable of using different fuels.
12	R-SYS-6	Temperature of compressed hydrogen gets too low when it reaches the engines, resulting in a higher SFC	4	3	subsection 7.4.3	Adding a heat exchanger on the engines which ensure the temperature stays between 150 and 250K.

The technical risk map shown in table 13.4 presents the risk map before mitigation on the left and the risk map after mitigation on the right. The numbers in tables 13.2 and 13.3 correspond to the numbers used in table 13.4.

Table 13.4: Technical risk map before and after mitigation.
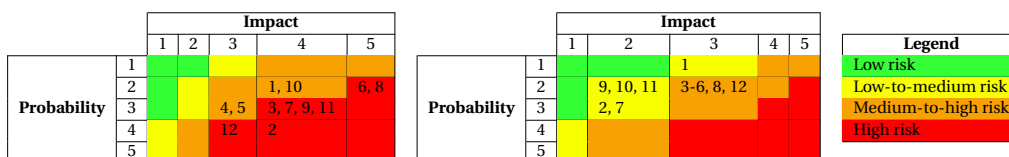
Using the mitigation strategies, none of the risks pose a high risk to the project. More importantly, most of the risks associated with the design relate to materials. Either difficulties arise from a recyclability point of view, or due to the failure of materials caused by impacts that result in tank ruptures. Therefore, multiple materials have been considered for the design of the fuselage, wing and hydrogen tank. For the tank, Kevlar 49 or T800S CFRP can also be used if Hexcel CFRP would be unavailable, adding only 1.5 to 2 tons in weight.

13.4. Flight Testing and Certification

As for every aircraft, a certification process needs to take place and the aircraft needs to be certified by the FAA and EASA authorities. However, before the aircraft can be certified, a prototype has to be built and tested to avoid wasting time during the certification process of the full scale aircraft. During this process, different tests have to performed such as flying with maximum payload, performing takeoff with OEI and testing the maximum available range. All these are standard tests that are required during the certification for all multi-engine aircraft. In the case of the SHOTS aircraft, special attention needs to be given to the engines with the modified combustion chamber and the hydrogen fuel system. Regarding the modified engines, maximum thrust, fuel consumption, gas temperature and emissions need to be tested in an engine testing facility before being mounted on the aircraft. Lastly, certifying the hydrogen tank needs additional resources. As of this moment, no regulations are put in place regarding the usage of such fuel tank or system on-board of an aircraft. Therefore, by the time the SHOTS aircraft will begin testing, either regulations are present or this concept will be used as a baseline to investigate and create standards for the certification of using a hydrogen fuel systems on-board of an aircraft.

13.5. Production Plan

The production of an aircraft is an essential element during the design phase since a good design still needs to be manufactured. The production line is organized as shown in figure 13.5. It is opted to use modern production techniques such as automated tape laying when, for example, fabricating components made out of carbon fiber. Furthermore, the production principle of lean manufacturing should be adhered to, this should minimize both cost and impact on the environment.

Please note that several components are not manufactured by the company but ordered from an external party. Therefore, special attention should be given to this issue since these can impact the production process when delays occur.
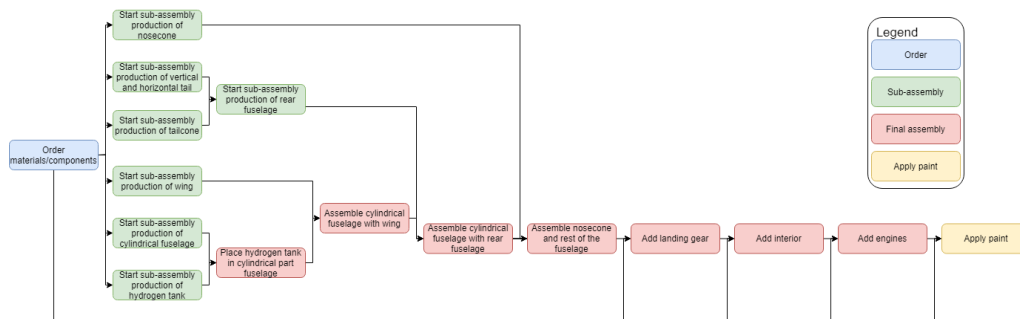

Figure 13.5: Production plan flow chart for the SHOTS aircraft.

The use of a four-panel CFRP fuselage is present in the Airbus A350 XWB, and it offers benefits in terms of production and maintenance costs when compared to an integral barrel section, as well as a 2% decrease in empty weight per seat compared to the Boeing B787 according to Airbus [160]. The same approach is used for manufacturing and assembly of the SHOTS aircraft. A preliminary estimation of the time required to manufacture the CFRP aircraft parts using automated tape laying is made by using an average deposition rate of 17.5 kg/h [161]. From calculations in chapter 10, a total CFRP weight of 5,407 kg is found, thus resulting in a time of 309 hours. It is further assumed that an automated tape laying machine such as one by TORRESLAYUP [161] can function for 12 hours/day. This results in a production time of 26, 13, 9 and 7 days for 1, 2, 3 and 4 machines respectively. A combination of automated tape laying and automated fiber placement is used for production of the Airbus A350 XWB, with a reported

sale of 14 automated fiber placement machines from MTorres to Airbus in 2014 [1].

Since the hydrogen tank is a novel aspect of the design, its attachment to the fuselage needs to be considered. Two circular metal straps will be adhesively bonded to the hydrogen tank at the locations corresponding to the first and last frames of the fuel tank fuselage section. The metal straps and frames at these locations will have attachment points with drilled holes. In this way, the hydrogen fuel tank can be placed inside the fuselage, rotated to align with the frames, and then bolted on either side for a secure attachment. In reality, a separation of 1.7 cm is present between the fuselage and the tank. Therefore, specialized automated tools will be required to ensure that access is possible for removal of the fasteners during maintenance. Blind fasteners with diameters as small as 0.4 cm are available via Monogram Aerospace Fasteners [2]. Nevertheless, a detailed thermal, vibrational and structural analysis needs to be performed in further design stages to ensure the safety of this mechanism. The attachment mechanism is illustrated in figure 13.6. Finally, the fuselage frames have to be designed to withstand the force exerted when hydrogen is released because the valves of the tank fail and the tank moves in the opposite direction as discussed in section 13.3.
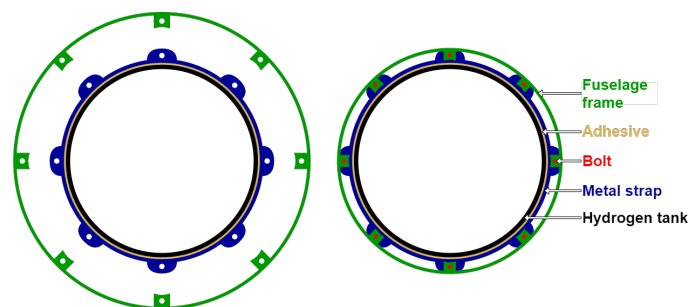

Figure 13.6: Attachment of hydrogen tank to the fuselage (please note that the left image is for illustration of individual attachment points and therefore the two components are displayed on a different scale).

13.6. Operations and Logistics

Any aircraft entering the aviation industry should be compliant with the operational requirements of customers, i.e. airlines. Since the SHOTS aircraft requires hydrogen refueling, this is a major consideration for the operations and logistics. Furthermore, the EOL disposal of the aircraft requires some additional services which will also be addressed in this section.

13.6.1. RAMS Characteristics

RAMS characteristics are of major importance when it comes to the operational life of the aircraft. The following list illustrates what aspects are considered for each of the characteristics:

- Reliability: design reliability and the operational reliability.
- Availability: turnaround time.
- Maintainability: position of engines, number of engines and the general size of the aircraft.
- Safety: crashworthiness, size of the hydrogen tank and position of hydrogen and biokerosene tank.

Regarding the reliability of the SHOTS aircraft, the majority of the aspects are reliable due to the conventional design used. Nevertheless, the modular cabin, hydrogen tank and the combustion chamber modifications lead to a lower reliability when compared to similar aircraft. The modular cabin design will have an influence on the maintenance aspect since the modular design is not meant to be dismantled during operations. The hydrogen tank represents the most unreliable aspect in this list. Mainly due to the fact that high pressure tanks of such dimensions and usage on-board of an aircraft have not been tested nor experimented sufficiently. Finally, the modification of the engines' combustion chamber to burn hydrogen, represents a lower impact on the reliability as these changes can be performed and tested on the ground. Therefore, with vast testing, this change will not have a great impact on the reliability of the aircraft.

Next, for the availability, the refueling time is essential as it dictates the turnaround time of the aircraft. As discussed in section 9.4, the refueling time varies as a function of the refueling method chosen. Since

---

[1] `https://www.composites.media/automated-layup-systems-sweating-assets/` (accessed 29-06-2020)
[2] `https://trsaero.com/monogramaerospace/products/blind-bolts/composi-lok/` (accessed 29-06-2020)

all the other operations, besides the hydrogen refueling, are the same as similar aircraft, only the hydrogen refueling will be discussed here. When the airport infrastructure is not installed with pipelines to refuel the hydrogen tank, trucks must be used. The usage of trucks has the disadvantage of time. Even when four trucks are used in combination with four compressors, the refueling time can reach 1.3 hours. This will therefore result in a low availability of the SHOTS aircraft at the beginning of the aircraft's operational lifetime.

Thirdly, the maintainability is discussed. Compared to similar aircraft, the SHOTS aircraft has two additional engines that will require extra labour to inspect and maintain. Therefore, the amount of maintenance time increases. Furthermore, the combustion chamber redesign will require a different inspection method compared to similar aircraft. Furthermore, the hydrogen tank will require extra attention during maintenance. To be able to maintain the tank, it is required that that the tank can be removed from the fuselage. Even with the implementation of the modular design, to facilitate this process, specialized workers and a different infrastructure is required to maintain the hydrogen tank. Finally, experience with the Boeing 777 has shown that composite parts are less maintenance intensive. It has been demonstrated that the 777's composite tail requires 35% fewer scheduled maintenance labor hours than the Boeing 767 despite its 25% larger size [3]. These benefits come from the increased fatigue and corrosion resistance of composites compared to metal.

The final topic of the RAMS characteristics is the safety of the SHOTS aircraft. The main point of concern is the high pressure hydrogen tank placed in the back of the aircraft. All the other aspects are similar if not equal to similar aircraft. The safety of the hydrogen tank was discussed in section 9.3 where all the different safety risk were analyzed. From this section, it can be found that the main safety issues due to the usage of the hydrogen tank have been covered.

13.6.2. Operations on the ground

The operations on the ground mainly depend on the size of the aircraft and the operations on the apron itself. Aircraft aprons are categorized according to their aerodrome reference code [10], which is in turn categorized according to the wing span of the aircraft. The wing span of the SHOTS aircraft is 35.99 m giving it an aerodrome reference code C. This is fortunate since reference aircraft, like the Airbus A220 and Embraer 195, also have this aerodrome reference code. Therefore, the SHOTS aircraft has the same reliability compared to reference aircraft in terms of apron size and taxiing.

The length of the aircraft is another aspect to consider for ground handling of the aircraft. The length of the SHOTS aircraft is 46.81 m, compared to 41.5 m for the Embraer 195. Unfortunately, the aerodrome reference code is not limited to the length of an aircraft and hence, no further investigation can be conducted into this aspect of the aircraft.

Lastly, the ground operations of the SHOTS aircraft should be compatible with current airport infrastructure as stated by requirement **WFC-OP-01**. Normally, aircraft connect to a jet bridge on the left side of the aircraft while ground equipment, such as baggage handling, has its operational area on the right side of the aircraft. Since the aircraft has a conventional shape and handling procedures, the only element which should be given special attention is the hydrogen refueling. The panel for hydrogen refueling is located at the back of the aircraft, close to the hydrogen tank itself. Since there is no baggage handling at this location (as the location of the regular cargo hold houses the hydrogen tank), there is space for refueling equipment (as much as 4 trucks in total). Special care should be given to operating the APU since the jet blast produced by the APU could have an impact on the relatively large hydrogen refueling truck. Therefore, the refueling trucks should be located on the side of the aircraft for safety.

13.6.2.1. Hydrogen distribution & production

Hydrogen can be produced either centralized at a larger factory, or decentralized at a smaller remote location. Due to the large quantity of fuel required for aircraft, it is opted to produce the hydrogen centralized near the airport at a relatively large facility. There are different production techniques to produce hydrogen, which depend on the type of hydrogen produced. A distinction is made between grey, blue and green hydrogen in order to differentiate their sustainability. The differences between these three types of hydrogen are[4]:

---

[3] https://www.boeing.com/commercial/aeromagazine/articles/qtr_4_06/article_04_2.html(accessed29-06-2020)

[4] https://www.iea.org/commentaries/the-clean-hydrogen-future-has-already-begun (accessed 18-05-2020)

- Grey hydrogen is produced from natural gas and hence, production emits greenhouse gasses.
- Blue hydrogen is produced from fossil fuels, but the emissions are used or captured and stored.
- Green hydrogen is produced from renewable energy sources without emitting carbon emissions.

At the time, the cost of green hydrogen is relatively high. However, it is expected that the cost will drop significantly in the years to come due to the hydrogen industry's rapid expansion. Nevertheless, during the first years of the introduction to the market, it is possible to use blue hydrogen to remain cost-competitive. As soon as the cost of green hydrogen approaches the cost of blue hydrogen, a transition can be made in order to facilitate completely sustainable hydrogen production. The electricity for the green hydrogen production can be supplied by solar panels in the vicinity of the airport or by wind turbines at a more remote location. A feasibility for solar panels and off shore windmills at Amsterdam Schiphol Airport is performed to support the KLM Cityhopper fleet. For solar panels to supply all energy for hydrogen production an area of approximately 6.4 km^2 is required[5]. For wind energy approximately 118 wind turbines are required[6].

13.6.2.2. Refueling

The strategy for the implementation of hydrogen airport infrastructure is twofold and considers the hub(s) of an airline and its destinations separately. An estimate is provided for the required area coverage to produce all the biokerosene to support KLM Cityhopper. It is assumed that the alleged Diesel tree (Copaifera langsdorffii) produces all the fuel [162], in which case approximately 385 km^2 area of land is required[7].

Airline hub(s)

It is expected that airlines buy multiple SHOTS aircraft, which creates opportunity for the airport infrastructure at the airline hub(s). At least half of the aircraft refueling takes place at an airline's hub since contracts are often signed which make the cost of refueling at their hub cheaper than refueling at a destination. Taking the example of the KLM Cityhopper fleet, the destinations are within 2,000 km range from Amsterdam[8], which would mean that the potential of their Embraers is not fully utilized. Only refuelling at Amsterdam Schiphol Airport could thus be a viable strategy.. This is a very big advantage for the implementation of a hydrogen aircraft since this only requires infrastructure to be built at one airport. This is further illustrated in figure 13.7, where the blue dot represents Amsterdam Schiphol Airport and the black dots represent the destinations. The red circle shows a 2,000 km radius from Amsterdam Schiphol Airport. Furthermore, since the hub houses many SHOTS aircraft, it is opted to build refueling infrastructure consisting of pipelines. This greatly reduces the refueling time.
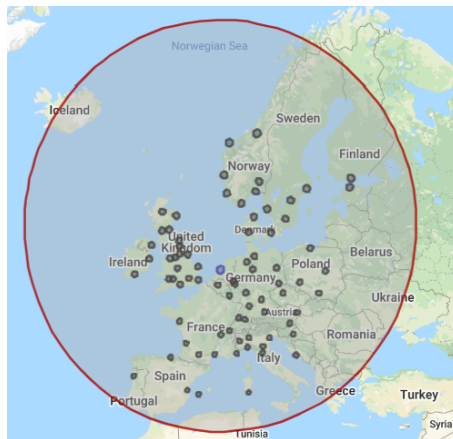

Figure 13.7: Possible deployment of the SHOTS aircraft to be used by KLM Cityhopper.

---

[5]Assumptions: solar intensity 1 kW/m^2, 8 hours of sun per day, solar panel efficiency 20%, electrolysis efficiency 80%, 5000 kg of hydrogen per aircraft per day required, specific energy hydrogen 33.33 kWh/kg, 49 aircraft (fleet size KLM Cityhopper)

[6]Assumptions: 3.6 MW power output per wind turbine (offshore), 24 hours per day energy production, electrolysis efficiency 80%, 5000 kg of hydrogen per aircraft per day required, specific energy hydrogen 33.33 kWh/kg, 49 aircraft (fleet size KLM Cityhopper)

[7]Assumptions: yield per acre per year is 25 barrels, 159 L/barrel, 1 acre = 4046.9 m^2, density jet fuel 0.8 kg/m^3, 16919 kg of biokerosene per aircraft per day required, no losses in fuel anywhere in the process, 49 aircraft (fleet size KLM Cityhopper)

[8]https://www.eraa.org/klm-cityhopper (accessed 17-06-2020)

Destinations

As it is very expensive for airlines to construct pipelines at all of their destinations, it is opted to adopt the airline hub strategy to avoid building any infrastructure at airports within a 2,000 km radius. For the airports beyond that range, refueling trucks can be utilized which have a significantly lower cost than building infrastructure. This does, unfortunately, increase the refueling time significantly depending on the amount of hydrogen required. For lower quantities of hydrogen (up to approximately 1500 kg) refuelling trucks are a very cost competitive option since the refuelling rate only after that point decreases significantly. It should also be noted that this is only an issue on the short term. As the implementation of the SHOTS aircraft progresses, more airports will adopt the hydrogen refueling infrastructure. The reason for this is twofold: airlines require the infrastructure and adopting the change will also help to illustrate the airport's commitment to incorporate sustainability demanded by the public.

13.6.3. Maintenance

An aircraft needs to have certain types of maintenance checks throughout its lifetime. These are classified by A-, B-, C-, and D-checks. A-checks denote the least maintenance with the lowest interval and D-checks denote the most maintenance with the biggest interval. It should be noted that the B-check is mitigated in modern aircraft and is performed stepwise during the A-checks [9]. It is custom to perform the following inspections during the maintenance checks:

- **A-check**: this check should be performed every 8 weeks. Filters need to be checked and possibly changed, hydraulics need to be checked and aircraft emergency equipment should be thoroughly inspected. This check should not take more time than 24 hours.
- **C-check**: this check should be performed approximately every 2 years. Engines need to be checked thoroughly, the hydrogen distribution should be checked and the APU should be tested. The landing gear should also be detached from the aircraft and inspected properly. This check should not take longer than 2-3 weeks.
- **D-check**: this check should be performed approximately every 6 years and takes apart almost the entire aircraft. The hydrogen tank should be detached from the aircraft and properly maintained. The entire interior should also be detached to allow for proper inspection of the aircraft structure. The engines should also be detached from the airframe, tested and inspected at a dedicated facility. This check should not take more time than 2 months.

13.6.4. Operations during flight

Operations during the flight mission do not change significantly compared to current four-engine aircraft. The same procedures apply for OEI conditions et cetera. Special care should be taken when dealing with the hydrogen systems. Therefore, additional sensors should be placed at potential leakage points. This is especially important since the hydrogen tank is placed within the same physical compartment as the passenger cabin, i.e. within the bulkhead.

13.6.5. End-of-Life

EOL is a very important element in the design of the SHOTS aircraft to be properly recycled. Dedicated facilities already exist for dismantling of aircraft such as AELS BV[10] in Twente. At a later stage in the design strategic partners should be found for proper recycling. These companies should be either recycling companies or partners which can use the leftover materials. After the dismantling of the aircraft the recycled materials can be used in various industries ranging from the car industry to oven glove manufacturers. Before recycling materials, the first step would be to re-certify and reuse parts on existing airliners. The main steps for recycling are hence as follows:

1. Remove, recertify and sell the engine.
2. Dismantle components and separate them properly, recertify components where applicable.
3. Segregate the different types of materials left: metals, wires, composites et cetera.
4. Dismantle the frame using cut-by-wire since this has no fire risk and is very clean[11].
5. Ship the components and perform waste recovery.

---

[9] https://www.qantasnewsroom.com.au/roo-tales/the-a-c-and-d-of-aircraft-maintenance/ (accessed 18-06-2020)

[10] https://aels.nl/

[11] Information obtained from Deutschen Gesellschaft für Luft- und Raumfahrt's webinar regarding 'Aircraft recycling and dismantling from design to execution' (accessed 17-06-2020)

The WeFlyCycle Business Model

Now that the conceptual design of the SHOTS aircraft has been finalized, there is the possibility to expand on the sales model. Section 14.1 discusses the business model. The entire development cost of the aircraft is disclosed in section 14.2, followed by section 14.3 which provides an outlook on the expected return on investment.

14.1. Competitive Analysis

An aircraft design should be competitive to similar aircraft in the market. The fact that the SHOTS aircraft is competitive is illustrated in table 14.1.

Table 14.1: Competitiveness of the SHOTS aircraft against its competitors [67] [116] [118] [163].

	Embraer E195-E2	Airbus A220-100	SHOTS-1	SHOTS-2
Pax [-]	132	120	120	120
Range [km]	4,815	6,111	4,399	4350
OEW [kg]	35,700	35,220	47,983	47,983
MTOW [kg]	61,500	60,780	69,310	70,710
Max fuel [kg]	13,690	17,530	2,063/6,890	2,063/8,390
Maximum wing loading [kg/m^2]	565.1	541.2	522.82	533.8
Cruise Mach	0.82	0.78	0.79	0.79
Maximum thrust loading [kg/kN]	294	293.7	256.8	272.9
ROC [m/s]	17.27	17.78	31	29
Takeoff distance [m]	1,970	1,220	1,484	1495.7
Landing distance [m]	1,420	1,357	1,452	1451
Listing price [million USD]	66	81	80	78
Fuel burn [kg/km]	2.77	2.48	2.72*	3.14*
Fuel cost [€/km]	1.42	1.27	1.94**	2.16**
Carbon dioxide emissions [kg/s]	1.950	1.930	1.093	1.345
Nitrogen oxide emissions [kg/s]	0.312	0.296	0.239	0.224
Refuelling time [min]	11.7	8.5	5.9***	7.2***
Turnaround time [min]	18	20	18	18

* *Please note that this is an equivalent fuel burn corrected for the different specific energies. The SHOTS-1 aircraft for example burns 1.51 kg/km of biofuel + 0.47 kg/km hydrogen pressurized at 700 bar (which is the equivalent energy of 1.21 kg/km of kerosene).*

** *Based on the current kerosene jet fuel cost of 0.51 €/kg and an expected green hydrogen cost of 2.5 €/kg by 2030 [164]. However, there are talks of future carbon taxation of kerosene. Together with further reduced cost of hydrogen, the cost equation might balance out.*

*** *Based on 1,500 kg required hydrogen and same refuelling rate as Embraer E195-E2 for biokerosene. Refuelling of biokerosene and hydrogen takes place simultaneously.*

The WeFlyCycle project should be sustainable in the long term, and with typical project costs accruing in the billions, the company cannot afford to deliver an outdated model. Airbus is aiming to be the ultimate replacement model for the aging fleet of Europe and America, while simultaneously buying in on the growing market of India and China. In that regard, its success can be proven by some extraordinary statistics: the aircraft is able to fly medium- to long-haul routes with its 6,111 km range or 8 hours straight with a typical 100-120 seat layout. This effectively makes it suitable to perform trans-Atlantic flights[1]. It has an incredibly low fuel consumption and Airbus managed to get the Airbus A220 certified for steep approach, meaning a glide angle of 5.5°. This will allow the airplane to service smaller, more difficult to operate airports like London City Airport.

This is where the WeFlyCycle project steps in. As of now, the A220 does not have to rival any competitor in the future. Since the range of the A220 is undoubtedly superior to the project goal of 4,000-4,500 km, the SHOTS aircraft has to excel on other levels. The SHOTS aircraft meets the following design specifications:

---

[1]`https://simpleflying.com/airbus-a220-etops-approved/` (accessed 02-05-2020)

- The aircraft has to be delivered not later than 2036. The estimated development time including certification and first delivery is 12 years. An additional 4 years of research will go towards bottlenecks in recycling aerospace materials, with special care taken in composites and aluminum alloys.
- The aircraft design has to have a re-iteration every 4 to 5 years on improved recyclability to increase EOL rest value.
- The operational lifetime of the aircraft has to be minimum 30 years at maximum usage. The total amount of flight cycles will be about 43,800 on an average 4 cycles/day basis or an estimated amount of 131,400 flight hours based on commercial data[2].
- The aircraft will be produced at a minimum rate of 5 aircraft/month, with an option to increase to 10 aircraft/month if the demand is present. This specification stems from similar production rates at Embraer. In 2019, they produced 89 E-jets[3]. If production runs for 20 years, this will result in 1,200 aircraft or 50% of the demand in 120-seat planes in the next 20 years [165]. The aircraft is expected to break even once it has produced 717 aircraft after approximately 12 years for a production rate of 5 aircraft/month or 6 years for a production rate of 10 aircraft/month.
- The aircraft achieves a maximum cruise Mach number of 0.82, similar to speed performance of its competitors. The stall speed does not exceed 190 km/h. Yet, the OEW and MTOW are significantly higher than its competitors.
- The aircraft currently has a higher fuel consumption than the Airbus A220 due to its significantly higher OEW/MTOW ratio. Since SHOTS is a transition aircraft and mainly focused on conveying the safety of hydrogen fuel to the public, this is considered acceptable.
- The aircraft will have a turnaround time of 18 minutes, similar to the Airbus A220 of the Embraer E195-E2. It turns out that hydrogen refueling does not impose restrictions on the turnaround time as discussed in section 13.6.
- The aircraft is able to perform steep approach at a glide angle of 5.5° and land in runways of less than 1,500 m in order to operate on smaller, city-centered airports.
- The aircraft is able to achieve a ROC higher than 17.78 m/s and therefore outperforms the Airbus A220.
- The aircraft complies with the targets of ACARE stated in section 2.2. In 2020, the CO_2 emissions equalled 0.297 kg/km per passenger. SHOTS-1 produces 0.039 kg/km per passenger which is a reduction of 85%. This will give the aircraft a significant advantage over the Airbus A220 when airlines consider renewing their fleet. No information was found on NO_x emissions, yet SHOTS-1 produces 20% less nitrogen oxide compared to the A220, one of the most modern airplanes on the market.

By now it should be clear that WeFlyCycle aims to answer the need for transport amidst increasing medium-sized city connectivity, such as the Asian-Pacific market discussed in section 2.2. Passengers want the airline to adjust to their schedule and not the other way around. This can be achieved by providing high-frequency flights on point-to-point routes with highly fuel efficient airplanes. Besides serving Tier 1 airports, airliners should also be able to serve thinner-populated routes between major business centers. Caution should be taken in following up the developments of Airbus's new hybrid aircraft by 2035. Although Airbus has the strong position at this point in time, it is possible for a newcomer to do well on the market in the future. There will be enough demand to sustain multiple companies.

To conclude, the WeFlyCycle project will offer a product that satisfies the following items:

- An aircraft that is entirely recyclable or manufactured from recycled material.
- An aircraft that flies on greener propulsion than fossil fuels.
- Design that will feel familiar to passengers by focusing on evolution instead of revolution. Yet, with striking new elements that will allow for a general notion of safety and integrity.

The last point basically assures that effort will be put into providing a cabin layout that is spacious and incorporates technological gadgets to induce a feeling of luxury and care. Although the lower range requirement seems a disadvantage at first, it is a necessary claim to allow room for the implementation of a greener propulsion alternative. If the WeFlyCycle project succeeds in delivering a feasible and safe design, one can always reconsider increasing the range performance and eventually provide an extended

---

[2] https://www.planestats.com/bhsn_2019jun (accessed 02-05-2020)
[3] https://leehamnews.com/2020/03/26/embraer-had-a-better-2019-than-2018/ (accessed 02-05-2020)

range version. Moreover, the aircraft is still able to operate across all of Europe and provide multiple flights a day on thinner-populated routes in- and outside the season. North-America will be looking for smaller narrow-bodies as well to connect their large and medium cities as reported earlier.

Lastly, airlines such as Air France-KLM, who have consistently ranked highly on the Dow Jones Sustainability Index[4], will definitely be interested in acquiring this type of aircraft in their fleet. They understand that the customer of tomorrow will be increasingly environmentally critical about air transport services.

A mapping of the stakeholders of this project based on interest and influence is shown in table 14.2.

Table 14.2: Mapping of all stakeholders of the WeFlyCycle project.

	Low Interest	High Interest
High Influence	Regulation Authorities	Manufacturer
Low Influence	Airports Passengers	AFRA Airliners

A stakeholder which is of particular interest for the WeFlyCycle project is Aircraft Fleet Recycling Association (AFRA)[5]. This association represents the international aircraft recycling industry. Since one of the main goals of the WFC project is to create an aircraft which is largely made out of recycled or recyclable materials, AFRA has a great interest in the project. The market for the recycling of aircraft is not very large. Nowadays, most aircraft are dumped at expensive landfills after all valuable or easily recyclable parts and components are stripped off. The airframes, which are often made out of hard to recycle composite materials, are then left in the desert. If an aircraft with increased recyclability value would enter the market, its EOL value would be greater than already existing aircraft. This makes it more profitable to recycle an aircraft which means that this market will grow. In order to consolidate this market even further, companies could look into creating a hybrid recycling market where the aircraft and the automobile industry are working together.

14.2. Cost Breakdown

This section explains how the development cost of the project is estimated and how the unit cost for SHOTS-1 and SHOTS-2 of the SHOTS aircraft is estimated. For the development cost, each subsystem is evaluated and further broken down into several processes. The results are presented in table 14.3 [157]. These costs are broken down into several processes as shown in the columns of the table. All these values have been adjusted to inflation so that they are accurate for the year 2020[6]. To estimate the total development cost the values provided in the last column are multiplied by the weight of each subsystem as calculated in the section 5.3.

Table 14.3: Developing Costs in USD per pound for each subsystem of the aircraft [157].

Development cost [USD/lb]	Engineering	Manufacturing	Tool Design	Tool Fabrication	Support	Total
Wing	9,930.2	2,482.2	2,606.8	8,639.4	1,166.2	24,823.4
Empennage	29,206.8	7,302.4	7,666.4	25,410	3,431.4	73,018.4
Fuselage	17,971.8	4,492.6	4,718	15,636.6	2,111.2	44,930.2
Landing gear	1,398.6	350	366.8	1,216.6	163.8	3,498.6
Aircraft systems	19,212.2	4,803.4	5,042.8	16,714.6	2,256.8	48,029.8
Payload	6,027	1,506.4	1,582	5,244.4	708.4	15,068.2
Engines	4867.8	1216.6	1278.2	4235	571.2	9,168.8

Note that table 14.3 also includes the cost of engine development even though the engines used are PW1700G and CF34-10A. However, since the combustion chamber of the PW1700G needs be developed, it should be taken into account. Since the development cost of just the combustion chamber is impossible to calculate, the development cost for developing the whole engine is used. Hence, it should be kept

---

[4]https://www.airfranceklm.com/en/air-france-klm-group-once-again-world-air-transport-leader-2019-dow-jones-sustainability-index (accessed 04-05-2020)

[5]https://afraassociation.org/

[6]https://www.in2013dollars.com/us/inflation/ (accessed 27-05-20)

in mind that the total development cost of the aircraft is slightly overestimated. Finally, it is calculated that the development cost of this aircraft is $2.59 billion.

Next, the unit cost of manufacturing each aircraft is calculated. Similar to development cost, the unit cost for each subsystem is estimated and added together for the total unit cost. Table 14.4 presents the typical cost per unit mass for every aircraft subsystem in 2020 [157]. This table is used, in combination with class II weight estimations, to calculate the unit cost for each concept. However, this unit cost does not take into account the cost of the hydrogen tank and the engines. The cost for manufacturing the hydrogen tank is estimated to be $628,520 as mentioned in subsection 9.2.3. For the engine costs it varies for SHOTS-1 and SHOTS-2: SHOTS-1 uses all PW1700G which cost $12 million each[7] adding up to $48 million total; SHOTS-2 uses two PW1700G and two CF34-10A engines, with PW1700G costing $12 million and CF34-10A costing $7.3 million as mentioned in section 5.2, adding up to $38.6 million.

Table 14.4: Costs in USD per pound for each subsystem of the aircraft [25].

Subsystem cost [USD/lb]	Labour	Materials	Others	Total
Wing	810	159.4	123.2	1,092.6
Empennage	2146.6	630.2	326.2	3,103
Fuselage	903.1	148.4	137.2	1,188.7
Landing gear	142.3	127.6	22.4	292.3
Aircraft systems	419	118.5	64.4	602
Payload	538.7	130.2	82.6	751.5
Assembly	77.1	5.2	4.2	86.5

The original values in the table are taken from a report from 2002 [157], which does not completely reflect the cost breakdown for SHOTS. First, the values are adjusted for inflation to get the values for 2020. Since 2002 the sustainability has become more and more important, so it is critical that the material waste is reduced as much as possible which leads to reduction of material cost by 7% [8]. Another factor that reduces the manufacturing cost is the implementation of more efficient manufacturing methods. Ensuring that the manufacturing techniques are cost effective and the operation of the factory is also efficient, the labour cost is reduced by 5% [8]. Finally, another factor to be taken into account is the automation of manufacturing processes. As the aviation industry is gradually shifting towards automation[9], manual labour is being substituted with machines. One of the biggest tasks for which robotic arms are being used is the riveting [10], hence making the process faster and more accurate. Furthermore, the automated manufacturing of composite material also plays a role in reducing labour costs. Taking these factors into account as well, the labour cost for building the wings and fuselage reduces by 40% [11].

Taking all these factors into account the values in the table 14.4 are added. The total manufacturing cost of the first unit produced is calculated and then 7% is added to that value as part of contingency management. Finally this gives the first unit cost for SHOTS-1 to be $143.38 millions and $133.7 million for SHOTS-2. The unit costs calculated are however not fixed. As the number of aircraft built increases, the company workers get more and more experience and hence the cost for manufacturing an aircraft decreases. This phenomenon is called the learning curve. To take this into account equation 14.1 is used to calculate the unit cost [157] depending on number of aircraft manufactured. In this equation FU is cost of first product manufactured which is already calculated for SHOTS-1 to be $143.38 millions and $133.7 million for SHOTS-2, Q is the number of aircraft produced and s is the effect of the learning curve.

$$MC = FU \cdot Q^{\frac{\ln(s)}{\ln(2)}} \tag{14.1}$$

The learning curve s used for labour costs is 0.85, whereas for the rest a learning curve of $s = 0.95$ is used [157]. For the engine costs however no learning curve is applied as they are bought from another com-

---

[7] https://www.bloomberg.com/news/articles/2011-12-14/jetblue-to-buy-pratt-whitney-engines (accessed 15-05-2020)

[8] https://www.mckinsey.com/~/media/mckinsey/dotcom/client_service/aerospace%20and%20defense/pdfs/excellence_in_cost_management.ashx (accessed 21-06-2020)

[9] https://insights.globalspec.com/article/10099/automation-in-the-aerospace-industry-the-challenge-and-promise-of-integrating-robots-into-the-production-process (accessed 21-06-2020)

[10] https://www.robotics.org/content-detail.cfm/Industrial-Robotics-Industry-Insights/Aerospace-Manufacturing-on-Board-with-Robots/content_id/5960 (accessed 21-06-2020)

[11] https://reports.nlr.nl/xmlui/bitstream/handle/10921/1484/TP-2018-143.pdf?sequence=1&isAllowed=y#:~:text=Compared%20to%20the%20baseline%20aluminium,and%20reduction%20of%20assembly%20steps. (accessed 21-06-2020)

pany. The *FU* stands for the cost of first unit, so when applying the learning curve for labour costs only the labour costs for the first aircraft is used. *Q* is the number of units produced and *MC* is the manufacturing cost for the *Q*th number of unit. Figures 14.1 and 14.2 show how the aircraft cost decreases as the number of aircraft produced increases.
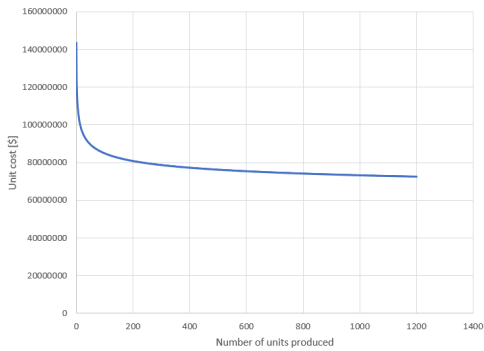

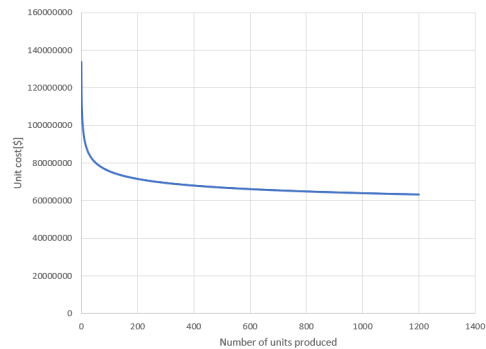Figure 14.1: Unit cost of SHOTS-1 as a function of units produced.

Figure 14.2: Unit cost SHOTS-2 as a function of units produced.

14.3. Return on Investment

Like any industry, the aviation industry attracts investment only if there is a good chance of making profit. This section evaluates the amount of money required to invest and the expected profit at the end of the program.

The first investment is the development cost incurred when developing the aircraft, which is \$2.69 billion. The second cost is the production cost of each aircraft which is clearly illustrated in figures 14.1 and 14.2 and varies with the number of aircraft produced. Therefore, setting the selling price is not very straightforward. If the price is too low, a lot of aircraft will have to be sold to reach the break even point, whereas if the price is too high, not many aircraft will be required to break even but it would be harder to sell an expensive aircraft. Taking into account the competition aircraft Airbus A220 is sold for \$81 million, the selling price should be around this point. Since the upper limit on unit cost is set at 105% of similar aircraft, the selling price for SHOTS-1 is set at \$80 million. Note that there is no contingency required for the selling price since 7% is already added to the manufacturing costs as stated in section 4.1.2. For SHOTS-2, the selling price is set in reference to the selling price for SHOTS-1.

The factors from the customer point of view that affect the price are the ones that affect the income due to the aircraft and the expenses of the aircraft. Since the only difference in the two options are the engines, the income due to the aircraft is not decreased. However, due to increased mass and less efficient engines, the operational cost increases as stated in class II weight estimation in section 5.3. The fuel cost over the lifetime for SHOTS-1 is \$339 million whereas the operational fuel cost for SHOTS-2 is \$380 million. The saving of approximately \$40 million should be reflected in the costs of both aircraft. For this a discounted flow analysis is carried out. Since during the lifetime of SHOTS-2 an extra \$40 million will be spent, the value of that money in present day needs to be calculated. So if the customer pays for example \$1 million right now and invests it somewhere, how much profit can the customer make out of that money during the life time of SHOTS-2? Hence, this profit should correspond with the money saved. In order to calculate the price difference, this profit should be worth around \$40 million at the end of aircraft life cycle. This can be found using equation 14.2.

$$\text{Price difference} = \left(\frac{1}{1+r}\right)^N \cdot (\Delta\text{operational cost}) \tag{14.2}$$

In equation 14.2, *r* is the discount rate and is set at 12% [157]. Moreover, *N* is the number of years the aircraft will fly which is 30 years. The increase in operational cost is \$40 million, however it does not take into account the increase in operational costs due to change in landing fee. Hence, this value is multiplied by a safety factor of 1.5, making it \$60 million. This gives the value of \$2 million, so SHOTS-2 can be sold at \$78 million. From an airline prospective choosing between expensive option and cheaper option boils down to 2 main factors. The first factor is how green the airline is, although both the options perform well, SHOT-1 is still the greener option. Secondly, the economic factor also plays a role, in this

decision. If the airline is short on funds they will go for cheaper option, however if the airline thinks that they can invest this $2 million somewhere else and forecast the overall profit to be more than $40 million(extra fuel cost needed for SHOTS-2) in next 30 years then the airline might opt for SHOTS-2. Using the selling price of $80 million for SHOTS-1 and $78 million for SHOTS-2, and assuming that both of these aircraft will sell equally, the return on investment is shown in figures 14.3a and 14.3b.
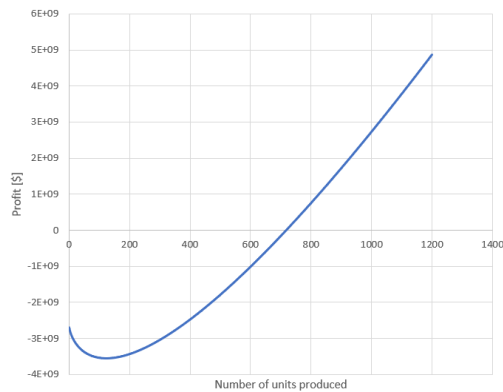
(a) Return on investment as the number of units increase.
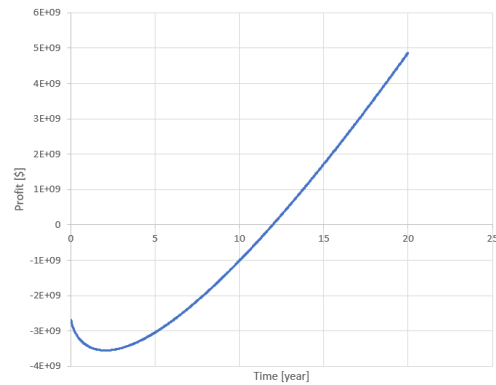
(b) Return on investment at production rate 5 per month as time passes.

From figure 14.3a, it can be seen that the line starts at -$2.69 billion which is the production cost of the aircraft. As the number of aircraft produced increases, the aircraft are sold on a loss for some time since the manufacturing cost is still high. After producing 126 aircraft the total loss is $3.55 billion which is the lowest point of the graph. Once the number of aircraft produced reaches 126, it starts to make profit since the manufacturing cost has decreased below the selling price of the aircraft due to the learning curve. Hence, as the number of aircraft produced increases, the line goes up and at aircraft unit 717 the break even point is reached. Finally the project enters the profit phase and till the production number 1,200 the total profit made is $4.86 billion. Figure 14.3b shows the same return on investment as a function of time. With the lowest possible production rate that is 5 aircraft per month, it will take 12 years to reach the break even point. However if the demand increases the production rate can go up to 10 aircraft per month which will decrease the time needed to reach the break-even point. As it is stated already, the analysis carried out assumes that both the options sell equally. However, in reality that might not be the case. If SHOTS-1 sells more than SHOTS-2 or vice versa it will affect the break even point of this project. To estimate this effect, the extreme case scenarios are chosen to check the break even points as shown in 14.5.

Table 14.5: Break even points for extreme cases: selling only SHOTS-1 or SHOTS-2.

	Break even aircraft number	Break even time [years]
Selling only SHOTS-1	1,111	18.5
Selling only SHOTS-2	502	8.4

Table 14.5 shows that if only SHOTS-1 are sold, the break even point is reached a lot later, which is due to the fact that the profit margin for SHOTS-1 is lower. Whereas for SHOTS-2 the break even point is reached much earlier since the margin is higher. Note that break even time assumes a production rate of 5 aircraft per month. Further analysis is also carried out to check the effect on break even point if the profit margin is kept the same for SHOTS-1 and SHOTS-2. This means it will have no effect if one model sells more than the other. Table 14.6 shows extreme cases. Case 1 shows the selling price for SHOTS-2 if the margin is same as SHOTS-1 for $80 million whereas case 2 shows the highest limit of selling these aircraft above which the requirement **WFC-USER-COST-01** is not met.

Table 14.6: Break even points for extreme cases based on profit margin.

	SHOTS-1 Price [USD]	SHOTS-2 Price [USD]	Break even aircraft number	Break even time [years]
Case 1	80,000,000	70,600,000	1138	19
Case 2	85,000,000	75,600,000	609	10.2

From table 14.5 and 14.6 it can be concluded that even in the worst cases the break even point is below 1,200. However, further market analysis should be carried out to estimate more accurate selling prices. In this way, the selling price of SHOTS-1 and SHOTS-2 can be tweaked to reach a right balance of competitiveness and ensuring the break even point is reached.

Sustainability Compliance Assessment

Sustainability is a significant part of this project. In fact, two of the top-level requirements are primarily concerned with sustainability:

- ***WFC-USER-SUS-01****: The aircraft shall be made of materials which are recycled and/or recyclable.*
- ***WFC-USER-SUS-05****: The propulsion system's energy source shall not rely on fossil fuels.*

The project follows a general strategy which is taken into account by each department throughout the design phase. Moreover, with recyclability being a major part of the project, sustainability is also strongly considered for the EOL phase. It should be noted that the two main sustainability goals of the project which are building the aircraft using recycled and/or recyclable material and using a non-fossil fuel are given priority. Thus, there is more innovation in choice of material and propulsion system. For the other design aspects, off-the-shelf technology is used as much as possible. This choice also decreases the wasted time and resources on testing and certification, thus improving sustainability. Therefore, in further phases of the project using more innovation on aspects such as aerodynamics and stability and control, more sustainability can be achieved as well. An example of this would be to optimize the wing to produce more lift, allowing the reduction of weight and thus fuel consumption. The sustainability of the design throughout the aircraft's life phases is summarized in figure 15.1.
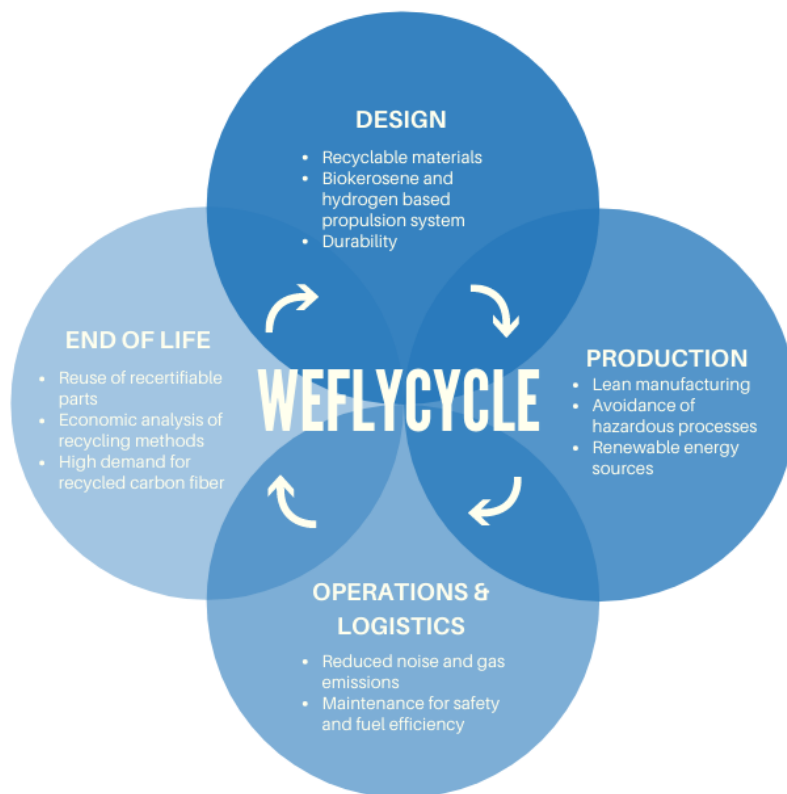

Figure 15.1: Flowchart of sustainability throughout aircraft life phases.

Previously in the report the sustainability within the domain of each department has been discussed. To assess whether the initial goals have been achieved and to determine the actions required in further

phases of the project, a model called Life Cycle Sustainability Assessment (LCSA) is used. This model is based on the fact that sustainability is categorized in three aspects: environmental, social and economic. It gives a trade-off between these three aspects as well as life cycle stages and impacts, products and generations [12]. The method is formulated as follows in equation 15.1.

$$LCSA = LCA + LCC + SLCA \qquad (15.1)$$

LCA is an abbreviation for Life Cycle Assessment and is concerned with the environmental assessment. LCC or Life Cycle Costing is related to economic assessment. This parameter is more than just the economic cost calculation, it also takes into account the operational and EOL phases and hidden costs. Further, SLCA stands for Social Life Cycle Assessment. This method is used to assess the design, production, operations and EOL phases of the design.

15.1. Design and Operations
Sustainability within the design and operations phase of the project is discussed in five categories: material, manufacturing, propulsion, maintenance and budgeting.

15.1.1. Material
A significant goal of the project is the use of recycled and/or recyclable material to build the aircraft. To conduct a LCA, the material choice is considered. Every material choice is made strongly considering this objective, while still adhering to safety requirements. This goal is achieved and it is shown that the aircraft could be recyclable based on the conducted market analysis and material assessment of section 2.1 and chapter 6 respectively.

Further, in order to reduce the environmental impact in LCA, making use of local resources is considered. This has not been entirely achieved since the main focus is on recyclability. It is kept as a recommendation for further phases of the design so as to further reduce the carbon footprint and cost of design and production.

In addition to recyclability, the material durability is strongly considered. The choice of carbon fiber composite for fuselage and wing skins reduces the need for maintenance and inspection. This helps in conducting LCC, since the higher the durability, the longer the lifespan of the material before degrading. Therefore, this calls for a decrease in the cost of maintenance and replacement, as well as reducing the strain on resources. With regards to SLCA, higher durability means a safer aircraft. Additionally, use of local resources will help with thriving local employment and economy, which is recommended for further phases of the project.

15.1.2. Manufacturing
To conduct LCA for manufacturing, adherence to the principle of lean manufacturing[1] is considered. In this way, the use of manufacturing techniques which produce large quantities of waste is avoided. This was achieved in this phase of design. To conduct SLCA, use of manufacturing methods emitting hazardous fumes is to be avoided. Furthermore, use of toxic material is also to be avoided as much as possible. This is considered by avoiding asbestos and chrome-containing paints and coatings which are known to be health hazards. In case no other option is available, use of protection for workers is required[2]. The manufacturing phase is outlined more in detail in the production plan in section 13.5.

Furthermore the manufacturing principle of lean manufacturing will be applied in order to minimize the resources for manufacturing. Nesting shall be used for part production. Additionally, recycling of the used water and use of renewable energy sources for producing electricity[3] is considered. This also helps with economic sustainability.

---

[1] https://searcherp.techtarget.com/definition/lean-production (accessed 19-06-2020)

[2] https://3dinsider.com/3d-printer-fumes/ (accessed 19-06-2020)

[3] https://www.airbus.com/company/sustainability/environment/product-responsibility.html#Lif (accessed 19-06-2020)

15.1.3. Propulsion

The propulsion system is also a significant target of sustainability within the project since use of non-fossil fuel is a top-level requirement. While choosing the engine and fuel this requirement is strongly considered. Firstly, it is decided to use biokerosene and hydrogen as fuel. Biokerosene can already be used in the engines without design changes. However, use of hydrogen calls for altering the combustion chamber. It is chosen to use Lean Direct Injection (LDI C4) as discussed in subsection 7.4.2. Two types of engine, Pratt & Whitney PW 1700G and CF34-10-A, are chosen after a trade-off done in section 5.2. This is mainly done to reduce the unit cost in order to meet requirement **WFC-USER-COST-01**. This helps in achieving economic sustainability.

Another important point to conduct SLCA is to check for noise emission, since this is closely related to people living near the airport. As shown in section 7.5.6 both options of using only PW1700G(SHOTS-1) and using two PW1700G and two CF34-10-A (SHOTS-2) are considered. Both noise emissions are below the level allowed by regulations. However, the second option produces more noise than the first one. Design 2 is chosen despite this based on the fact that it is the cheaper option, and therefore helps with achieving economic sustainability.

The gas emissions are another important criterion in conducting LCA. The CO_2 and NO_x emissions are calculated and then compared to the reference aircraft, Embraer 195-E2. The results are shown in table 15.1.

Table 15.1: Gas emission in kilogram per second by the aircraft.

Gas emitted	SHOTS-1	SHOTS-2	Embraer E195-E2
Carbon dioxide [kg/s]	1.093	1.345	1.95
Nitrogen oxide [kg/s]	0.239	0.224	0.312

Evidently, the aircraft has a significant success in reducing gas emissions relative to competitors. This ensures environmental sustainability and meeting the top-level requirement. Finally, for producing the electricity needed for the ground operation an APU is used which works on biofuel. As a suggestion for the future phases, emissions of this APU can further be reduced by using hydrogen instead.

15.1.4. Maintenance

Maintenance is crucial for sustainability in all three aspects. A properly maintained aircraft has better fuel efficiency, and is therefore more environmentally sustainable. It also reduces the need for part replacement, resulting in more economic sustainability. Finally, it is safe to fly and therefore socially sustainable.

There are four types of maintenance: A-, B-, C- and D-checks. A-checks denote the lowest level of maintenance with smallest time interval and D-checks denote the highest level of maintenance with largest time intervals. These types of maintenance will be done on the aircraft, as explained in Operations and Logistics chapter 13.6.

15.1.5. Budget Allocation

Allocation of resources to different systems of the aircraft is crucial for sustainability of the project, in the sense that a system or subsystem is not compromised due to another system taking up more than its share of resources. Therefore, a budget allocation and contingency management is conducted and it is made certain to stay within the margins. This is achieved as specified by section 4.1.1.

15.2. End-of-life

Another top-level requirement of this project is use of recycled and/or recyclable material. This mostly concerns the EOL solution.

15.2.1. Recyclability

A significant part of the design is concerned with recyclability in each subsystem. To conduct LCA within this domain a few criteria need to be checked. Firstly, during the material selection, the concept of recyclability is a significant criterion that affects the structural design. Therefore, it is ensured that the aircraft is completely recyclable.

It also needs to be ensured that the methods of recyclability are also sustainable. This can be achieved by working with a AFRA [166] credited company, one of which is AELS[4] located in the Netherlands. Working with a local company also further decreases the emissions of transportation. Having AELS as a client also helps with economic and social sustainability. Working with a local company reduces the cost of transportation and further boosts the economy by creating jobs. Lastly, it should be noted that the propulsion system is highly recyclable/reusable.

After the aircraft is disassembled and recycled, the parts can go back to the cycle of production but this does not have to necessarily be within the aerospace industry. There are potential clients in other industries who can make use of the recycled material. In fact, a few of them have been contacted such as Canyon Bicycles in Germany[5], THOR Carbon Bike tuning[6], Fast Forward Wheels[7], Sensa Bikes[8], Carbon Sailing[9] and Specialized[10]. They have all shown interest in using the recycled CFRP and the last company, Specialized, already has a program called fiber recycling which is similar to the one used in the aerospace industry. It should be noted that the challenging part of recyclability in aerospace is not technical but economic feasibility. Therefore, to recycle a part or material, there needs to be a demand for it in the market. It is recommended that more investigation is performed into the value of recycled aerospace CFRP for the sports industry.

Sustainability Overview

An overview of the sustainability performance of the SHOTS aircraft is provided by comparing the two design options to reference aircraft. Figure 15.2 shows four graphs comparing, from left to right, CO_2 emissions, NO_x emissions, noise and selling price of SHOTS-1, SHOTS-2 and reference aircraft. The reference aircraft for the first three is E195-E2 and for the price it is A220. A220 has been chosen instead of E195-E2, as the reference for price, because of a closer price range to SHOTS and hence, a fair comparison. The reference aircraft have been given a score of 1 and the design options are scored relatively to those.

(a) CO_2 emissions.

(b) NO_x emissions.

(c) Noise emissions.

(d) Price
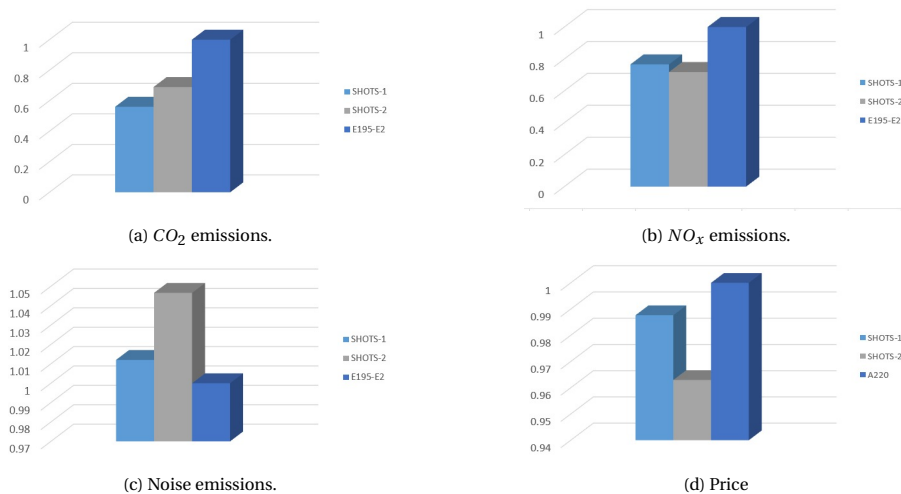
Figure 15.2: Comparison of sustainability parameters with reference aircraft.

---

[4] https://aels.nl/ (accessed 19-06-2020)

[5] https://www.canyon.com/de-de/ (accessed 18-06-2020)

[6] https://www.thorcarbon.eu/ (accessed 18-06-2020)

[7] https://www.ffwdwheels.com/ (accessed 18-06-2020)

[8] https://www.sensabikes.com/ (accessed 18-06-2020)

[9] https://carbonsailing.nl/ (accessed 18-06-2020)

[10] https://www.specialized.com/se/en/carbon-fiber-recycling-program (accessed 18-06-2020)

16

Compliance of Requirements

The requirements previously discussed in the Baseline Report [2] are now shown in table 16.1. Each requirement imposed for SHOTS is checked and three symbols are used to indicate if the requirement is met of not. When a requirement is met, ✓ is used to indicate success. If the requirement is not met or not investigated in the report, ✗ is used. Finally, if the requirement is assessed in the report but further investigation/development is required, ~ is used.

Table 16.1: Compliance of the different requirements.

Requirement ID	Requirement	Compliance	Remarks
WFC-USER-PERF-01.1	The aircraft shall have a range of at least 4000 km at maximum payload.	✓	SHOTS-1 4,399 km SHOTS-2 4,350 km
WFC-USER-PERF-02.1	The aircraft shall be able to transport 120 passengers.	✓	
WFC-PERF-01	The aircraft shall be able to transport all passengers' luggage.	✓	26.7 kg per passenger
WFC-PERF-02	The aircraft shall fly at a cruise altitude of at least 8900 m.	✓	
WFC-PERF-03	The aircraft shall have an OEW/MTOW ratio of less than 0.6, excluding the tank weight from the OEW if hydrogen is used as fuel.	✓	0.49
WFC-PERF-04	The horizontal tail of the aircraft shall be sized to ensure longitudinal stability and controllability for the most aft and forward cg positions encountered during operation.	✓	
WFC-PERF-05	The energy consumption of the aircraft shall be similar to or less than similar existing aircraft.	✓	Better than Embraer E195-E2
WFC-PERF-06	The aircraft shall be able to fly at a maximum cruise Mach number of 0.82.	✓	0.82
WFC-PERF-07	The ROC of the aircraft shall be no less than 17.8 m/s.	✓	SHOTS-1: 31 m/s SHOTS-2: 29 m/s
WFC-PERF-08	The aircraft shall have a stall speed of no more than 190 km/hr.	✓	190 km/hr
WFC-PERF-09	The aircraft shall be able to achieve a glide angle of at least 5.5 degrees.	✓	5.5 degrees
WFC-OP-01	The aircraft configuration shall comply with airport infrastructure present at the beginning of its operational life.	✓	
WFC-OP-02	The runway length of the aircraft during takeoff and landing shall be no more than 1500 m at sea level.	✓	SHOTS-1 Takeoff: 1484 m Landing: 1452 m SHOTS-2 Takeoff: 1495.7 Landing: 1452 m

WFC-OP-03	The aircraft shall be operational for the highest of at least 43800 flights and 109500 flight hours under an operational lifetime of 30 years.	✓	43,800 cycles
WFC-OP-04	The turnaround time of the aircraft shall be less than 40 minutes.	✓	Refueling time will decrease as airports adapt pipeline systems or if refuelling is done at both airport
WFC-OP-05	The hired maintenance crew shall not be 5% more than for maintenance of conventional aircraft.	✓	
WFC-USER-SUS-01	The aircraft shall be made of materials which are recycled and/or recyclable.	~	Dependent on further research and market analysis
WFC-USER-SUS-05	The propulsion system's energy source shall not rely on fossil fuels.	✓	Biokerosene and Hydrogen
WFC-SUS-01	The aircraft noise performance shall comply with the ICAO Annex 16 regulations [167].	✓	SHOTS-1 260.5 EPNdB SHOTS-2 269.4 EPNdB
WFC-SUS-02	The aircraft shall generate less greenhouse gas emissions than similar existing aircraft.	✓	CO_2: SHOTS-1 1.093kg/s SHOTS-2 1.345 kg/s NO_x: SHOTS-1 0.239 kg/s SHOTS-2 0.224 kg/s
WFC-SUS-03	The cabin interior characteristics such as aisle width, seat pitch, cabin height and over-head baggage space shall be similar to existing aircraft.	✓	
WFC-SUS-04	The noise level inside the cabin of the aircraft shall be similar to similar existing aircraft.	✓	84.5 dB
WFC-SUS-05	The noise level outside the cabin of the aircraft during ground operations, takeoff and landing shall be similar to existing aircraft.	✓	88.6 dB and 92.4 dB
WFC-SUS-06	The end-of-life recycling procedures shall be accredited by AFRA.	✓	Use of certified companies
WFC-USER-SF-01.1	The certification of the aircraft shall comply with current safety and reliability requirements as specified in the EASA CS25 regulations [22].	✓	
WFC-SF-01	A factor of safety of 1.5 shall be applied to the prescribed limit load which are considered external loads on the structure.	✓	
WFC-SF-02	The structure shall be able to support ultimate loads without failure for at least 3 seconds [22].	~	Testing required
WFC-SF-03	The aircraft shall use a propulsion technology with a TRL of at least 6, as defined by EU [23].	✓	Combusion chamber has lowest TRL of 7

WFC-SF-04	The aircraft shall have enough reserve energy to fly for 45 minutes at nominal cruise conditions after reaching its destination.	~	Adapted to 10% of range
WFC-SF-06	Manufacturing methods and materials shall ensure the safety of the workers during production and maintenance.	✓	
WFC-USER-COST-01	The unit cost of the aircraft shall not be more than 105 % of similar existing aircraft.	✓	SHOTS-1 USD 80 mil SHOTS-2 USD 78 mil
WFC-COST-01	The overall program cost of the aircraft shall be more than 110 % of similar existing aircraft.	✓	
WFC-PD-01	The aircraft delivery rate shall be at least 5 aircraft/month.	✓	
WFC-PD-01.1	The aircraft delivery rate shall be able to increase to 10 aircraft/month if there is a demand.	✓	
WFC-PD-02	The aircraft shall be operational in 2036.	✓	
WFC-PD-03	The aircraft shall be manufactured according to the lean manufacturing philosophy.	✓	
WFC-PD-04	The assembly methods used for aircraft production shall allow part disassembly and retrofitting.	✓	

17

Conclusion and Recommendations

This report is the result of 10 weeks of work done by 10 Bachelor of Aerospace Engineering students at Delft University of Technology. It has dealt with the detailed design of the winner concept of the Midterm Report [3], the Semi-Hydrogen Operating Turbofan Sustainable (SHOTS) aircraft, which is a hybrid aircraft with a propulsion system based on both biokerosene and hydrogen. The configuration of the aircraft is traditional with low, backward swept wings and four wing mounted engines. Two engines utilize biokerosene and the other two utilize gaseous hydrogen. Two options of the SHOTS aircraft have been designed and analyzed in detail. The final design results are presented in table 17.1.

Table 17.1: Parameters of the SHOTS aircraft.

Parameter	SHOTS-1	SHOTS-2	Parameter	SHOTS-1	SHOTS-2
Wing area [m^2]	132.57	132.57	Engine type [-]	PW1700G	PW1700G/CF34A*
Max wing loading [kg/m^2]	522.82	533.80	Number of engines [-]	4	4
Aspect ratio [-]	9.645	9.645	Max cruise Mach number [-]	0.82	0.82
Wing span [m]	35.99	35.99	Max ROC [km/h]	111.6	104.4
Length [m]	46.81	46.81	Takeoff distance [m]	1484	1495.7
Listing price [million USD]	80	78	Landing distance [m]	1452	1451
Range [km]	4,399	4,350	Stall speed [km/h]	190	190
Pax [-]	120	120	Fuel burn [kg/km]	2.72	3.14
MTOW [kg]	69,310	70,710	Fuel cost [€/km]	1.94	2.16
OEW [kg]	47,983	47,983	Carbon dioxide emissions [kg/s]	1.093	1.345
Max payload [kg]	12,283	12,283	Nitrogen oxide emissions [kg/s]	0.239	0.224
Max fuel [kg]	2,063/6,890	2,063/8,390	Refueling time [min]	5.9	7.2
Max thrust loading [kg/kN]	256.8	272.9	Turnaround time [min]	18	18

* *SHOTS-2 uses two PW1700G and two CF34A engines.*

Most of the top-level requirements set at the beginning of the project have been met:

- ***WFC-USER-PERF-01.1****: The aircraft shall have a range of at least 4000 km at maximum payload.*
- ***WFC-USER-PERF-02.1****: The aircraft shall be able to transport 120 passengers.*
- ***WFC-USER-SUS-05****: The propulsion system's energy source shall not rely on fossil fuels.*
- ***WFC-USER-COST-01****: : The unit cost of the aircraft shall not be more than 105 % of similar existing aircraft*
- ***WFC-USER-SF-01.1****: The certification of the aircraft shall comply with current safety and reliability requirements as specified in the EASA CS25 regulations [22].*

WFC-COST-01 is met only for SHOTS-2. The SHOTS-1 is presented so the client can decide if they prefer to make a higher investment in exchange for lower operational costs. Some requirements, such as **WFC-USER-PERF-SUS-01** regarding 100% recyclability of the aircraft, require further testing to prove the compliance. For future research some further investigation is recommended for the following items:

Hydrogen tank

- More research in the damage tolerance of the hydrogen tank. More specifically, the actual fracture toughness values for the materials being used, taking into account the lay-up. Experimental testing to validate the results of maximum allowable crack length is required to observe the crack propagation modes of different materials.
- Detailed analysis of thermal, vibrational and structural effects of hydrogen fuel tank attachment to the fuselage.
- Design of the frames that support the hydrogen tank to withstand the loads induced by escaping hydrogen due to failure of the valves.

Modular Design

- More research in detaching the rear fuselage to access the hydrogen tank and the stress concentrations that might form.

- Analysis of possible tools to be used for attachment of fasteners for the hydrogen tank attachment and the access for removal. Furthermore, the specific fasteners to be used depend on a detailed analysis of the loading conditions in the hydrogen tank section.

Materials

- Aircraft parts that employ thermoset resin composites could potentially be replaced by thermoplastic composites, which have better recyclability potential. The use of thermoplastic composites has not yet been seen in primary structural parts but investments by Airbus on these materials show that advances are expected [1]. Thermoset composite parts that cannot be repaired could potentially be replaced for thermoplastic composites during the operational life of the aircraft to further improve recyclability. The use of thermoplastic composites could also be applied to rivets. By using similar materials for skin and rivets, the recyclability becomes easier compared to combinations of materials.
- Further research can be done on the use of biocomposites in aircraft parts. Currently, their use is limited to the cabin interior but application to secondary structures can be investigated.
- Contact with material suppliers such as Toray for use of T800S carbon-epoxy composite to obtain accurate values for material cost.

Structures

- More research into drop test, more specifically for the breaking of the rear section of the fuselage and the hydrogen tank to ensure passenger's safety.
- More research into the use of adhesive bonds between stringers and skin panels and how adhesives affect the material properties during a recycling process such as melting aluminum.
- More research in determining material properties of T800S panels to optimize structural dimensions such as required skin thickness of wing panels.
- Optimizing the required skin thickness of the four fuselage panels that are assembled during production. Each panel can be optimized for its critical load case as was done during the design of the Airbus A350 XWB [13].

Production

- Contact with automated tape-laying and automated fiber placement machine suppliers, used for manufacturing of wing and fuselage skin, to better plan the production time and cost.

Recycling

- Further assessment of the recycling processes to be used is required. For now it was mainly considered if some material could be recovered. To achieve a more sustainable design, it is necessary to evaluate the environmental impact of the recycling processes to be used in order to ensure that they are not more harmful than landfilling.
- This report focuses on the use of recyclable materials which are downcycled for use in other industries. However, improvements in recycling processes in the coming years could potentially allow for recycling of niche aerospace materials to be used within the aviation industry over many cycles.
- For aircraft parts that are assumed to be reusable such as engines and landing gear, further research can be done on the recyclability at end of life, as these cannot be reused indefinitely.
- Performing market analysis to investigate the value of recycled CFRP for sports industry. An assessment of the supply chain considering the volume of end-of-life aircraft waste and the specific recycling processes to be used is required. Furthermore, assessment of the relation between recyclate resale value and profit is needed.

Propulsion

- Optimization of the combustion chamber such that the mixing of Hydrogen is even more efficient which will ensure more lean burn resulting in better fuel consumption and lower NO_x emission .
- Design of a hybrid engine that can run on both hydrogen and biofuel to reduce the number of engines and save more weight and cost. Furthermore, this mitigates the risk that only half of the engines can be used because one of the fuels is unavailable.

---

[1] `https://www.airbus.com/newsroom/news/en/2015/01/airbus-focus-on-thermoplastic-composite-materials-brings-environmental-and-production-improvements.html` (accessed 29-06-2020)

Bibliography

[1] Alderliesten, R. "Project Guide Design Synthesis Exercise WeFlyCycle [PDF file]". Design Synthesis Exercise, Delft University of Technology, 2020.

[2] Blomme, A., Pires, D. C., Dekkers, M., Eftekhar, S., García de Quevedo Suero, B., Hamza, S., Janissen, J., Kroon, R., Steenhuizen, V., and Wen, S. "WeFlyCycle AE3200: Baseline Report", Delft University of Technology, 2020.

[3] Blomme, A., Pires, D. C., Dekkers, M., Eftekhar, S., García de Quevedo Suero, B., Hamza, S., Janissen, J., Kroon, R., Steenhuizen, V., and Wen, S. "WeFlyCycle AE3200: Midterm Report", Delft University of Technology, 2020.

[4] Ribeiro, J. S. and de Oliveira Gomes, J. "Proposed framework for end-of-life aircraft recycling," *Procedia CIRP*, Vol. 26, 2015, pp. 311–316. doi: 10.1016/j.procir.2014.07.048.

[5] Overcash, M., Asmatulu, E., and Twomey, J. "Recycling of aircraft: State of the art in 2011," *Journal of Industrial Engineering,* Vol. 2013, No. 960581, 2012, pp. 1–8. doi: 10.1155/2013/960581.

[6] Popescu, V., Vasile, C., Brebu, M., Popescu, G. L., Moldovan, M., Prejmerean, C., Stanulet, L., Trisca-Rusu, C., and Cojocaru, I. "The characterization of recycled PMMA," *Journal of Alloys and Compounds,* Vol. 483, 2009, pp. 432–436. doi: 10.1016/j.jallcom.2008.08.148.

[7] AkzoNobel. "Chrome-free paint systems for General Aviation aircraft [PDF file]". AkzoNobel Aerospace Coatings, 2014.

[8] Simpkin, L. R. J. P. and Rhodes, D. *Civil Jet Aircraft Design.* Arnold, 1999.

[9] ANAC, A. "ICAO Noise Data Base EMBRAER ERJ 190-400", 2019.

[10] International Civil Aviation Organization. "Annex 14 aerodromes: aerodrome design and operations,". Technical report, International Civil Aviation Organization, 2018.

[11] European Environment Agency. "European aviation environmental report 2019", EASA, Eurocontrol, 2019.

[12] Kloepffer, W. "Life Cycle Sustainability Assessment of Products", 2008.

[13] Piquet, B. "Special edition A350XWB Flight Airworthiness Support Technology [PDF File]". Airbus, 2013.

[14] European Commission. *"Annual analyses of the EU air transport market 2016".* Mott Macdonald, 2017.

[15] Wilderer, P. A., Schroeder, E. D., and Kopp, H. *Global Sustainability: The Impact of Local Cultures, A New Perspective for Science and Engineering, Economics and Politics.* John Wiley & Sons, Hoboken, United States, 2006.

[16] Bombardier Commercial Aircraft. "Market forecast 2017-2036", 2017.

[17] Embraer. "Market outlook", 2018.

[18] Costes, B. "PAMELA - Process for advanced management of end of life of aircraft," *Layman Report,* 2007.

[19] Gopalraj, S. K. and Kärki, T. "Review on the recycling of waste carbon fibre/glass fibre-reinforced composites: fibre recovery, properties and life-cycle analysis," *Springer Nature* Vol. 2, March 2020. doi: 10.1007/s42452-020-2195-4.

[20] Sultan, A. A. M. and Mativenga, P. T. "Sustainable location identification decision protocol (SuLIDeP) for determining the location of recycling centres in a circular economy," *Journal of Cleaner Production,* Vol. 223, June 2019, pp. 508–521. doi: 10.1016/j.jclepro.2019.03.104.

[21] International Civil Aviation Organization. Annex 16 - Environmental Protection Volume 1 Aircraft Noise, 2008.

[22] European Union Aviation Safety Agency. "Certification Specifications and Acceptable Means of Compliance for Large Aeroplanes, Amendment 24", 2020.

[23] European Commission. *Technology readiness levels (TRL); Extract from Part 19 - Commission Decision C(2014)4995.* EU, 2014.

[24] Company, M. . "Hydrogen-powered aviation", The Clean Sky 2 JU and FCH 2 JU, 2020.

[25] Hess, R. and Romanoff, H. "Aircraft airframe cost estimating relationships: All mission types", RAND, 1987.

[26] Mooij, E. "Project Management and Systems Engineering in the DSE", DSE Organising Committee, Delft University of Technology, 2019-2020.

[27] Bayle, J., Perreux, D., Chapelle, D., Thiébaud, F., and Nardin, P. "A model to predict the permeation of type IV hydrogen tanks", World Hydrogen Energy Conference, 2010.

[28] Toray Composite Materials America, I. "T800S intermediate modulus carbon fiber", 2018.

[29] Composites, H. "Magnamite PV42/850 product data", 2002.

[30] Marchi, C. "Technical Reference for Hydrogen Compatibility of Materials,". Technical report, Sandia National Laboraties, 2012.

[31] Hua, T. Q., Ahluwalia, R. K., Peng, J. K., Kromer, M., Lasher, S., McKenney, K., Law, K., and Sinha, J. "Technical assessment of compressed hydrogen storage tank systems for automotive applications," *International Journal of Hydrogen Energy,* Vol. 36, No. 4, 2011, pp. 3037–3049. doi: 10.1016/j.ijhydene.2010.11.090.

[32] Alderliesten, R. "Introduction to Aerospace Engineering - Structures and Materials", 2011.

[33] Colozza, A. J. "Hydrogen storage for aircraft applications overview,". Technical report, National Aeronautics and Space Administration, 2002.

[34] Roskam, J. *Airplane Design Part V: Component Weight Estimation.* Design, Analysis and Research Corporation, 5th edition, 2018.

[35] van Heerden, D.-J., , and Curran, R. "Value extraction from end-of-life aircraft," *Encyclopedia of Aerospace Engineering,* 2010, pp. 1–12.

[36] Witik, R. A., Teuscher, R., Michaud, V., Ludwig, C., and Månson, J.-A. E. "Carbon fibre reinforced composite waste: An environmental assessment of recycling, energy recovery and landfilling," *Composites: Part A,* Vol. 49, 2013, pp. 89–99. doi: 10.1016/j.compositesa.2013.02.009.

[37] Nunes, L. J. R., Matias, J. C. D. O., and Catalão, J. P. D. S. *Torrefaction of Biomass for Energy Applications: From Fundamentals to Industrial Scale.* Elsevier Inc., 2017.

[38] Gaustad, G., Olivetti, E., and Kirchain, R. "Improving aluminum recycling: A survey of sorting and impurity removal technologies," *Resources, Conservation and Recycling,* Vol. 58, 2012, pp. 79–87. doi: 10.1016/j.resconrec.2011.10.010.

[39] Mouritz, A. P. *Introduction to Aerospace Materials.* Woodhead Publishing, 2012, Chaps. 8. doi: 10.1016/B978-0-08-102131-6.00002-5.

[40] Mouritz, A. P. *Introduction to Aerospace Materials.* Woodhead Publishing, 2012, Chaps. 11. doi: 10.1016/B978-0-08-102131-6.00002-5.

[41] Mouritz, A. P. *Introduction to Aerospace Materials.* Woodhead Publishing, 2012, Chaps. 9. doi: 10.1016/B978-0-08-102131-6.00002-5.

[42] Ahmad, F., Hong, J.-W., Choi, H. S., Park, S.-J., and Park, M. K. "The effects of stacking sequence on the penetration-resistant behaviors of T800 carbon fiber composite plates under low-velocity impact loading," *Carbon letters,* Vol. 16, No. 2, 2015, pp. 107–115. doi: 10.5714/CL.2015.16.2.107.

[43] van Oudheusden, A. "Recycling of composite materials", Delft University of Technology, 2019.

[44] N.Perry, A.Bernard, F.Laroche, and S.Pompidou. "Improving design for recycling – application to composites," *CIRP Annals,* Vol. 61, No. 1, 2012, pp. 151–154. doi: 10.1016/j.cirp.2012.03.081.

[45] Rybicka, J., Tiwari, A., and Leeke, G. A. "Technology readiness level assessment of composites recycling technologies," *Journal of Cleaner Production* Vol. 112, 2016, pp. 1001–1012. doi: 10.1016/j.jclepro.2015.08.104.

[46] Pimenta, S. and Pinho, S. T. "Recycling carbon fibre reinforced polymers for structural applications: Technology review and market outlook," *Waste Management,* Vol. 31, No. 2, February 2013, pp. 378–392. doi: 10.1016/j.wasman.2010.09.019.

[47] Mouritz, A. P. *Introduction to Aerospace Materials.* Woodhead Publishing, 2012, Chaps. 24. doi: 10.1016/B978-0-08-102131-6.00002-5.

[48] Zhu, G. "Recycling of glass fibre reinforced aluminium laminates and silicon removal from aerospace Al alloy," PhD thesis, Delft University of Technology, Netherlands, October 2012.

[49] Mouritz, A. P. *Introduction to Aerospace Materials.* Woodhead Publishing, 2012, Chaps. 25. doi: 10.1016/B978-0-08-102131-6.00002-5.

[50] Mouritz, A. P. *Introduction to Aerospace Materials.* Woodhead Publishing, 2012, Chaps. 21. doi: 10.1016/B978-0-08-102131-6.00002-5.

[51] Uddin, F. "Flame-retardant fibrous materials in an aircraft," *Journal of Industrial Textiles,* Vol. 45, No. 5, 2014, page 1128–1169. doi: 10.1177/1528083714540700.

[52] Jawaid, M. and Thariq, M. *Sustainable Composites for Aerospace Applications.* Woodhead Publishing, 2018.

[53] Niang, A. "Technical flax as an alternative to glass for seat shells," *Jet Composites Magazine*, Vol. 1, No. 87, 2014, pp. 71–72.

[54] Karakoc, T. H., Ozerdem, M. B., Sogut, M. Z., Colpan, C. O., Altuntas, O., and Açıkkalp, E. *Sustainable Aviation: Energy and Environmental Issues*. Springer, 2016.

[55] Hagnell, M. K. and Åkermo, M. "The economic and mechanical potential of closed loop material usage and recycling of fibre-reinforced composite materials," *Journal of Cleaner Production*, Vol. 223, 2019, pp. 957–968. doi: 10.1016/j.jclepro.2019.03.156.

[56] Polmear, I., Nie, D. S. J.-F., and Qian, M. *Light Alloys: Metallurgy of the Light Metals*. Butterworth-Heinemann, Elsevier, 5th edition, 2017, pp. 157–263.

[57] Meredith, J., Bilson, E., Powe, R., Collings, E., and Kirwan, K. "A performance versus cost analysis of prepreg carbon fibre epoxy energy absorption structures," *Composite Structures*, Vol. 124, 2015, pp. 206–213. doi: 10.1016/j.compstruct.2015.01.022.

[58] Jahan, A. and Edwards, K. L. *Multi-criteria Decision Analysis for Supporting the Selection of Engineering Materials in Product Design*. Butterworth-Heinemann, Elsevier, 2013, pp. 83–104.

[59] Tapper, R. J., Longana, M. L., Norton, A., Potter, K. D., and Hamerton, I. "An evaluation of life cycle assessment and its application to the closed-loop recycling of carbon fibre reinforced polymers," *Composites Part B: Engineering*, Vol. 184, March 2020, pp. 1–10. doi: 10.1016/j.compositesb.2019. 107665.

[60] America, T. C. M. "T800S Technical Data Sheet", 2018.

[61] Dong, P. A. V., Azzaro-Pantel, C., and Cadene, A.-L. "Economic and environmental assessment of recovery and disposal pathways for CFRP waste management," *Resources, Conservation and Recycling, Elsevier*, Vol. 133, 2018, pp. 63–75. doi: 10.1016/j.resconrec.2018.01.024.

[62] Ghavamian, A., Maghami, M. R., Dehghan, S., and Gomes, C. "Concerns of corrosive effects with respect to lightning protection systems," *Engineering Failure Analysis*, Vol. 57, 2015, pp. 434–443. doi: 10.1016/j.engfailanal.2015.08.019.

[63] Roskam, J. *Airplane Design Part I: Preliminary Sizing of Airplanes*. Design, Analysis and Research Corporation, 2nd edition, 1989.

[64] Electric, G. "GE Aviation CF34-10A", 2011.

[65] EASA. "Type certificate data sheet for BR700-710 engines,". Technical report, Rolls-Royce Deutschland Ltd. & Co. KG, Blankenfelde-Mahlow, Germany, 2019.

[66] FAA. "Type certificate data sheet for PW814GA, PW815GA,". Technical report, Pratt & Whitney Canada Corporation, 2017.

[67] Group, J. I. "Jane's All the World's Aircraft: In-Service", 2019.

[68] Bensel, A. "Characteristics of the specific fuel consumption for jet engines", *Department of Automotive and Aeronautical Engineering Hamburg University of Applied Science*, 2018.

[69] Scholz, D. "An optional apu for passenger aircraft,". In *5th Council of European Aerospace Societies Air and Space Conference: Challenges in European Aerospace, Delft*, 2015.

[70] Khandelwal, B., Karakurt, A., Sekaran, P. R., Sethi, V., and Singh, R. "Hydrogen powered aircraft: The future of air transport," *Progress in Aerospace Science*, Vol. 58, 2012, pp. 53–54. doi: 10.1016/j. paerosci.2012.12.002.

[71] Liu, Y., Sun, X., Sethi, V., Nalianda, D., Li, Y.-G., and Wang, L. "Review of modern low emissions combustion technologies for aero gas turbine engines," *Process in Aerospace sciences*, Vol. 94, 2017, pp. 12–45. doi: 10.1016/j.paerosci.2017.08.001.

[72] Marek, C. J., Smith, T. D., and Kundu, K. "Low-emission hydrogen combustors for gas turbines using lean direct injection,". Technical report, National Aeronautics and Space Administration, 2012.

[73] Salaudeen, S. A., Arku, P., and Dutta, A. *Plastics to Energy*. William Andrew, 1st edition, 2019, pp. 269–293.

[74] Beér, J. M. and Lee, K. B. "The effect of the residence time distribution on the performance and efficiency of combustors," *Symposium (International) on Combustion*, Vol. 10, No. 1, 1965, pp. 1187–1202. doi: 10.1016/S0082-0784(65)80255-7.

[75] Dunn-Rankin, D. *Lean Combustion : Technology and Control*. Elsevier Science Publishing Co. Inc., 2007.

[76] Eggels, R. "Gas turbine Combustion Modelling: Lean combustion and fuels", 2008.

[77] Dick, E. *Fundamentals of Turbomachines*. Springer, 2015, page 442.

[78] Dries Verstraete. "The Potential of Liquid Hydrogen for long range aircraft propulsion", Cranfield University School of Engineering, 2009.

[79] Dahl, G. and Suttrop, F. "Engine control and low-NOx combustion for hydrogen fuelled aircraft gas turbines," *International Journal of Hydrogen Energy,* Vol. 23, No. 8, 1998, pp. 695–704. ISSN 0360-3199. doi: 10.1016/S0360-3199(97)00115-8.

[80] Boerner, S., Funke, D.-I. H., Hendrick, P., Recker, E., and Elsing, R. "Development and integration of a scalable low NOx combustion chamber for a hydrogen-fueled aerogas turbine," *EUCASS Proceedings Series,* Vol. 4, 2013, pp. 357–372. doi: 10.1051/eucass/201304357.

[81] Renyu, F. and Man, Z. "Low Emission Commercial Aircraft Engine Combustor Development in China:From Airworthiness Requirements to Combustor Design," *Procedia Engineering,* Vol. 17, 2011, pp. 618–626. doi: 10.1016/j.proeng.2011.10.078.

[82] Tekin, N., Ashikaga, M., Horikawa, A., and Funke, D.-I. H. "Enhancement of fuel flexibility of industrial gas turbines by development of innovative hydrogen combustion systems", April 2019.

[83] Ayed, A., Kusterer, K., Funke, H.-W., Keinz, J., Striegan, C., and Bohn, D. "Experimental and numerical investigations of the dry-low-NOx hydrogen micromix combustion chamber of an industrial gas turbine," *Propulsion and Power Research,* Vol. 4, No. 3, 2015, pp. 123–131. ISSN 2212-540X. doi: 10.1016/j.jppr.2015.07.005.

[84] Ayed, A. Haj, Kusterer, K., Funke, H.-W., Keinz, J., Striegan, C., and Bohn, D. "Improvement study for the dry-low-NOx hydrogen micromix combustion technology," *Propulsion and Power Research,* Vol. 4, No. 3, 2015, pp. 132–140. doi: 10.1016/j.jppr.2015.07.003.

[85] Ayed, A. H., Kusterer, K., Funke, H.-W., Keinz, J., and Bohn, D. "CFD based exploration of the dry-low-NOx hydrogen micromix combustion technology at increased energy densities," *Propulsion and Power Research,* Vol. 6, No. 1, 2017, pp. 15–24. doi: 10.1016/j.jppr.2017.01.005.

[86] Chandrasekaran, N. and Guha, A. "Study of Prediction Methods for NOx Emission from Turbofan Engines," *Journal of Propulsion and Power,* Vol. 28, No. 1, 2012, pp. 170–180. doi: 10.2514/1.B34245.

[87] Turgut, E. and Usanmaz, Ö. "An analysis of altitude wind and humidity based on long-term radiosonde data," *Anadolu University Journal of Science and Technology A - Applied Sciences and Engineering,* Vol. 17, 2016, pp. 830–844. doi: 10.18038/aubtda.279852.

[88] Truman, H. S. "The Pratt & Whitney turbofan ™ engine. Alan Epstein overview. The development of the geared turbofan ™ engine", 2015.

[89] Kyprianidis, K. G., Nalianda, D., and Dahlquist, E. "A NOx emissions correlation for modern RQL combustors," *Energy Procedia,* Vol. 75, 2015, pp. 2323–2330. doi: 10.1016/j.egypro.2015.07.433.

[90] Stanely Smith. Fuel/oil Heat Exchange System for an Engine, 1985.

[91] Corchero, G. and Montañés, J. L. "An approach to the use of hydrogen for commercial aircraft engines", Escuela Técnica Superior de Ingenieros Aeronáuticos, Universidad Politécnica de Madrid, 2004.

[92] Westenberger, A. "Liquid hydrogen fuelled aircraft-system analysis final technical report (published version)", *Airbus Deutschland GmbH*, 2003.

[93] R.Vos, J. "Aerospace Design and System Engineering Elements 1, wing and propulsion system design lecture slides", Delft University of Technology, 2018.

[94] Roling, P. and Vokuijl, M. "Flight mechanics lecture slide: climb and descent", Delft University of Technology, 2019.

[95] Young, T. M. *Performance of the Jet Transport Airplane: Analysis Methods, Flight Operations, and Regulations.* Wiley, 2018, pp. 206–209.

[96] Jr., J. D. *Introduction to flight.* McGraw-Hill, 2016, page 538.

[97] Raymer, D. P. *Aircraft Design: A Conceptual Approach.* American Institute of Aeronautics and Astronautics, 6th edition, 2018.

[98] Depitre, A. "Noise certification workshop", Technical report ICAO, 2006.

[99] Acevedo-Giraldo, D. "Experimental aeroacoustic and aerodynamic analysis of a large-scale flap side-edge model," PhD thesis, March 2019. doi: 10.13140/RG.2.2.30634.98247.

[100] Dickson, N. "Aircraft Noise Technology and International Noise Standards", 2014.

[101] Airbus, A. "Aircraft Noise – Technologies and operations", 2015.

[102] ANAC, A. "ICAO Noise Data Base Airbus A320", 2006.

[103] Zevitas, C. D., Spengler, J. D., Jones, B., McNeely, E., Coull, B., Cao, X., Loo, S. M., Hard, A.-K., and Allen, J. G. "Assessment of noise in the airplane cabin environment," *Journal of Exposure Science & Environmental Epidemiology,* Vol. 28, No. 6, 2018, pp. 568–578. ISSN 1559-0631. doi: 10.1038/s41370-018-0027-z.

[104] Funke, H. H. W., Keinz, J., and Hendrick, P. "Experimental evaluation of the pollutant and noise

emissions of the GTCP 36-300 gas turbine operated with kerosene and with a low NOx micromix hydrogen combustor," *Proceedings of the 7th European Conference for Aeronautics and Space Sciences*, 2017.

[105] General Electric Aviation. GE CF34-10E Data Sheet, 2010.

[106] Oliviero, D. F. "Aerospace Design and Systems Engineering Elements II - AE2111-II: Mobile surfaces of the wing", Delft University of Technology, 2018.

[107] Torenbeek, E. *Advanced Aircraft Design : Conceptual Design, Technology and Optimization of Subsonic Civil Airplanes.* Wiley Publications, Chichester, United Kingdom, 2013.

[108] Vogeltanz, T. "Application for calculation of mean aerodynamic chord of arbitrary wing planform," *AIP Conference Proceedings,* Vol. 1, No. 1738, 2016. doi: 10.1063/1.4951901.

[109] Schiktanz, D. and Scholz, D. "Survey of experimental data of selected supercritical airfoils", Hamburg University of Applied Sciences, 2011.

[110] Drela, M. and Youngren, H. "XFOIL 6.9 User Primer", MIT Aero & Astro and Aerocraft inc., 2001.

[111] Howe, D. *Aircraft conceptual design synthesis.* Professional Engineering Publishing, London, 2000.

[112] Nicolai, L. M. and Carichner, G. *Fundamentals of Aircraft and Airship Design, Volume 1.* American Institute of Aeronautics and Astronautics, Reston, United States, 2010.

[113] Sadraey, M. *Aircraft Design: A Systems Engineering Approach.* Wiley Publications, Chichester, United Kingdom, 2019.

[114] Olivero, F. "Design for Lateral-directional aspects, Design for ground operations", 2020.

[115] Cumpsty, N., Mavris, D., and Kirby, M. "Aviation and the environment: Outlook,". Technical report, International Civil Aviation Organization, 2019.

[116] Airbus. "Airport planning publication APP", Airbus, 2020.

[117] Airbus. "Airport recovery publication ARP", Airbus, 2020.

[118] Embraer. "E-Jets E2 Airport Planning Manual", 2017.

[119] Marin, J. C., Justo, J., París, F., and Cañas, J. "The effect of frequency on tension-tension fatigue behavior of unidirectional and woven fabric graphite-epoxy composites," *Mechanics of Advanced Materials and Structures* Vol. 26, No. 17, 2019, pp. 1430–1436. doi: 10.1080/15376494.2018.1432814.

[120] Amateau, M. F. *Engineering Composite Materials.* Pennsylvania State University, 2003, Chaps. 18.

[121] C.Zweben and Wardle, M. "Flexural fatigue of marine laminates reinforced with woven roving of e-glass and of kevlar 49 aramid,". In *34th Annual Meeting of the SPI Reinforced Plastics/Composites Institute, New Orleans, Louisiana*, 1979. doi: 10.1002/pc.750020204.

[122] Pang, J. C., Li, S. X., Wang, Z. G., and Zhang, Z. F. "General relation between tensile strength and fatigue strength of metallic materials," *Materials Science and Engineering: A,* Vol. 564, 2013, pp. 331–341. doi: 10.1016/j.msea.2012.11.103.

[123] Schijve, J. *Fatigue of Structures and Materials.* Springer Netherlands, 2nd edition, 2009. doi: 10.1016/S0142-1123(03)00051-3.

[124] Wang, W., Yan, W., Duan, Q., Shan, Y., Zhang, Z., and Yang, K. "Study on fatigue property of a new 2.8gpa grade maraging steel," *Materials Science and Engineering: A* Vol. 527, No. 3, 2010, pp. 3057–3063. doi: 10.1016/j.msea.2010.02.002.

[125] Mouritz, A. P. *Introduction to Aerospace Materials.* Woodhead Publishing, 2012, Chaps. 18. doi: 10.1016/B978-0-08-102131-6.00002-5.

[126] Mouritz, A. P. *Introduction to Aerospace Materials.* Woodhead Publishing, 2012, Chaps. 19. doi: 10.1016/B978-0-08-102131-6.00002-5.

[127] Christos, C., Gotsis, P., and Minnetyan, L. "Progressive fracture and damage tolerance of composite pressure vessels," *Journal of Advanced Materials -Covina-,* Vol. 30, 1997.

[128] Wisnom, M. R. and Hallett, S. R. "The role of delamination in strength, failure mechanism and hole size effect in open hole tensile tests on quasi-isotropic laminates," *Composites Part A: Applied Science and Manufacturing,* Vol. 40, No. 4, 2009, pp. 335 – 342. doi: 10.1016/j.compositesa.2008.12.013.

[129] Lucintel. "Growth Opportunities in the Global Carbon Fiber Market 2013-2018,". Technical report, Lucintel – Global Management Consulting & Market Research Firm, November 2012.

[130] Experts, I. "Carbon Fibers & Carbon Fiber Reinforced Plastics - A Global Market Overview,". Technical report, Industry Experts, 2012.

[131] Das, S., Warren, J., West, D., and Schexnayder, S. M. "Global Carbon Fiber Composites Supply Chain Competitiveness Analysis,". Technical report, Clean Energy Manufacturing Analysis Centre, 2016.

[132] Li, T.-T., Wang, R., Lou, C.-W., and Lin, J.-H. "Static and dynamic puncture behaviors of compound fabrics with recycled high-performance Kevlar fibers," *Composites Part B: Engineering,* Vol. 59, March 2014, pp. 60 – 66. doi: 10.1016/j.compositesb.2013.10.063.

[133] Anderson Greenwood, Crosby and Varec products. "Pressure relief valve engineering handbook,". Technical report, Emerson, 2012.

[134] Sapre, S., Pareek, K., Rohan, R., and Singh, P. K. "Investigation of compressed hydrogen refueling process of 60 L type IV tank used in fuel cell vehicles," *Energy Storage,* Vol. 1, No. 6, 2019, page 91. doi: 10.1002/est2.91.

[135] Linde, G. "The ionic compressor IC90 (90 MPa)", 2018.

[136] Maus, S., Hapke, J., Ranong, C. N., Wüchner, E., Friedlmeier, G., and Wenger, D. "Filling procedure for vehicles with compressed hydrogen tanks," *International Journal of Hydrogen Energy,* Vol. 33, No. 17, 2008, pp. 4612–4621. doi: 10.1016/j.ijhydene.2008.06.052.

[137] Bourgeois, T., Ammouri, F., Weber, M., and Knapik, C. "Evaluating the temperature inside a tank during a filling with highly-pressurized gas," *International Journal of Hydrogen Energy,* Vol. 40, No. 35, 2015, pp. 11748–11755. doi: 10.1016/j.ijhydene.2015.01.096.

[138] Klymyshyn, N. "PNNL tank mass calculator for cross comparison of type 1, type 3 and type 4 pressure vessels", 2014.

[139] McWhorter, S. and Ordaz, G. "DOE Fuel Cell Technologies Office Record,". Technical report, USA Department of Energy, 2013.

[140] Galassi, M. C., Baraldi, D., Iborra, B. A., and Moretto, P. "CFD analysis of fast filling scenarios for 70 MPa hydrogen type IV tanks," *International Journal of Hydrogen Energy,* Vol. 37, No. 8, 2012, pp. 6886–6892. doi: 10.1016/j.ijhydene.2012.01.041.

[141] Megson, T. H. G. *Aircraft Structures for Engineering Students.* Elsevier, Amsterdam, 6th edition, 2016. doi: 10.1016/B978-0-08-100914-7.00001-3.

[142] Bauchau, O. A. and Craig, J. I. *Structural analysis: solid mechanics and its applications*, Vol. 1630. Springer, 2009, pp. 173–221. doi: 10.1007/978-90-481-2516-6.

[143] Wu, G. and Wang, J. "The mechanical behavior of glare laminates for aircraft structures," *JOM,* Vol. 57, 2005, pp. 72–79. doi: 10.1007/s11837-005-0067-4.

[144] Childs, T. , Airbus Operations Limited, United Kingdom, US Patent Application for a "Stringer for an aircraft wing and a method of reinforcing thereof", Publication No. US7677496B2, filed 21 Sep. 2007.

[145] Swanson, S. R. and Smith, L. V. "Comparison of the biaxial strength properties of braided and laminated carbon fiber composites," *Composites Part B: Engineering* Vol. 27B, No. 1, 1996, pp. 71–77. doi: 10.1016/1359-8368(95)00008-9.

[146] Toor, P. M. "On damage tolerance design of fuselage structure (longitudinal cracks)," *Engineering Fracture Mechanics,* Vol. 24, No. 6, 1986, pp. 915–927. doi: 10.1016/0013-7944(86)90276-6.

[147] Kumar, G. H. and Praveen, D. N. "Damage tolerance analysis of a fuselage stiffened panel with a broken frame," *International Journal of Innovative Science and Research Technology,* Vol. 2, No. 6, June 2017, pp. 105–110. doi: 10.14741/ijcet/spl.2.2014.106.

[148] Rodi, R. "The residual strength failure sequence in fibre metal laminates,". Technical report, Ph.D. Dissertation, Delft University of Technology, 2012.

[149] Johnson, R. W., Thomson, L. W., and Wilson, R. D. "Study on utilization of advanced composites in fuselage structures of large transports,". Technical report, National Aeronautics and Space Administration, 1985.

[150] Xue, P., Ding, L., Qiao, F., and Yu, X. "Crashworthiness study of a civil aircraft fuselage section," *Latin American Journal of Solids and Structures,* Vol. 11, No. 9, 2014, pp. 1615–1627. doi: 10.1590/S1679-78252014000900007.

[151] Guida, M., Marulo, F., and Abrate, S. "Advances in crash dynamics for aircraft safety," *Progress in Aerospace Sciences,* Vol. 98, 2018, pp. 106–123. doi: 10.1016/j.paerosci.2018.03.008.

[152] Liu, X., Guo, J., Bai, C., Sun, X., and Mou, R. "Drop test and crash simulation of a civil airplane fuselage section," *Chinese Journal of Aeronautics,* Vol. 28, No. 2, 2015, pp. 447–456. doi: 10.1016/j.cja.2015.01.007.

[153] Budynas, R. and Nisbett, K. *Shigley's Mechanical Engineering Design.* McGraw-Hill Education, 2014.

[154] Rice, R. C., Jackson, J. L., Bakuckas, J., , and S.Thompson. "Metallic materials properties development and standardization (MMPDS) scientific report DOT/FAA/AR-MMPDS-01", U.S. Department of Transportation - Federal Aviation Administration - Office of Aviation Research, 2003.

[155] Karal, M. "AST composite wing program: executive summary [PDF File]". National Aeronautics and Space Administration, 2001.

[156] Velicki, A., Yovanof, N., Baraja, J., Linton, K., Li, V., Hawley, A., Thrash, P., DeCoux, S., and Pickell, R. "Damage Arresting Composites for Shaped Vehicles-Phase II Final Report [PDF File]". National Aeronautics and Space Administration, 2011.

[157] Markish, J. "Valuation techniques for commercial aircraft program design," PhD thesis, Massachusetts Institute of Technology, 2002.

[158] America, T. C. M. "T1100G Technical Data Sheet", 2017.

[159] Boeing. "Commercial market outlook 2019-2038 [PDF file]". Boeing, 2019.

[160] Marsh, G. "Airbus takes on Boeing with reinforced plastic A350 XWB," *Reinforced Plastics,* Vol. 51, No. 11, December 2007, pp. 26–27, 29.

[161] Breuer, U. P. *Commercial Aircraft Composite Technology.* Springer International Publishing, Switzerland, 2016. doi: 10.1007/978-3-319-31918-6.

[162] Queensland Government. "Invasive plant risk assessment: diesel tree", 2016.

[163] Embraer. "E195-E2 Fleetsmart [PDF file]". Embraer, 2017.

[164] Van Wijk, A. "Green Hydrogen Economy in the Northern Netherlands", Delft University of Technology, 2018.

[165] Airbus. "Global Market Forecast - Cities, Airports & Aircraft 2019-2038", 2019.

[166] AFRA. "Best management practice for management of used aircraft parts and assemblies and for recycling of aircraft materials", 2016.

[167] ICAO. *Annex 2 - Rules of the Air.* International Civil Aviation Organization, 10th edition, November 2005, pp. 1–74. ISBN 5149548022.

[168] Slingerland, R. "Prediction of tail downwash, ground effect and minimum unstick speed of jet transport aircraft," Master's thesis, University of Technology Delft, 2005.

[169] Phillips, W. F. *Mechanics of Flight.* John Wiley & Sons, 2009.

A

Airfoil Trade-off

For the airfoil trade-off, only supercritical airfoils were considered. The additional remarks on the left of table A.1 provide insight in the selection process.

Table A.1: Complete overview of all the airfoils and their primary characteristics considered in the trade-off.

Remarks	Property	SC(2)-0710	BOEING HSNLF	BOEING BAC AIRFOIL	BOEING 737 OUTBOARD	RAE 5215	GRUMANN K-2	WHITCOMB INTEGRAL SC
High is best	(t/c)	0.1	0.101	0.113	0.108	0.097	0.103	0.11
	Based on Re	1x(10^6)	1x(10^6)	1x(10^6)	1x(10^6)	1x(10^6)	1x(10^6)	1x(10^6)
Close to cruise is best	C_l for AOA = 0	0.52	0.27	0.25	0.15	0.25	0.2	0.43
	AOA for C_l = 0	-4	-2.3	-2.3	-2	-2.2	-1.5	-3
High is best	C_l max	1.57	0.88	1.38	1.35	1.6	1.23	1.65
High is best	AOA for C_l max	11.7	7.5	14	14	14.5	11.5	14
Low is best	C_d min	0.006	0.006	0.007	0.006	0.007	0.006	0.007
Close to cruise is best	C_l of C_d min	0.5	0.44	0.23	0.38	0.2	0.3	0.42
High is best	(C_l/C_d) max	90	80	90	95	82	60	68
Low is best	C_l of (C_l/C_d) max	0.7	0.83	0.85	0.52	1.1	0.76	1.2
	Cruise C_m	-0.12	-0.059	-0.038	-0.026	-0.057	-0.069	-0.115
	Drag bucket starts at C_l	0.1	-0.1	-0.1	0.1	0.05	-0.1	0
	Drag bucket ends at C_l	0.6	0.5	0.3	0.5	0.3	0.3	0.4
	C_L ROC max in the drag bucket?	N	N	N	N	N	N	N
	C_L cruise in the drag bucket?	Y	Y	N	Y	N	N	N

Based on the values provided by table A.1, a weighting matrix was constructed to compare all airfoils and perform a trade-off. The weighting factor ranges from 0 to 3, where 0 is the worst choice and 3 the most optimal choice. To have a fair weighting process, airfoils with similar values for certain properties received the same weighting factor. The value of 0 is assigned when the performance for that property is unacceptable and therefore isn't allowed to attribute to the overall weighting score. The weighting matrix is illustrated in table A.2.

Table A.2: Complete ranking matrix of all the airfoils considered in the trade-off.

Property	SC(2)-0710	BOEING HSNLF	BOEING BAC AIRFOIL	BOEING 737 OUTBOARD	RAE 5215	GRUMANN K-2	WHITCOMB INTEGRAL SC
(t/c)	1	1	3	2	0	1	2
C_l for AOA = 0 AOA for C_l = 0	3	1	1	0	1	0	2
C_l max	2	0	1	1	3	0	3
AOA for C_l max	2	0	3	3	3	2	3
C_d min	3	3	2	3	2	3	2
C_l of C_d min	3	2	0	1	0	0	2
(C_l/C_d) max	2	1	2	3	1	0	0
C_l of (C_l/C_d) max	3	1	1	3	0	2	0
Cruise C_m	3	0	1	2	0	0	0
C_L ROC max in the drag bucket?	0	0	0	0	0	0	0
C_L cruise in the drag bucket?	1	1	0	1	0	0	0
TOTAL	23	10	14	19	10	8	14

Equations for Stability and Control

The following equations are used to determine all parameters in equations 8.41 and 8.44. Equations B.1, B.2, B.4 and B.5 are obtained from Torenbeek [107], equation B.3 is obtained from Slingerland [168] and equations B.6 and B.7 are obtained from Raymer [97].

$$C_{L\alpha_h} = \frac{2\pi A_h}{2 + \sqrt{4 + \left(\frac{A_h \beta}{\eta}\right)^2 \left(1 + \frac{\tan^2 \Lambda_{0.5C_h}}{\beta^2}\right)}} \quad \text{(B.1)}$$

$$C_{L_{\alpha_{A-h}}} = C_{L_{\alpha_w}} \left(1 + 2.15 \frac{b_f}{b}\right) \frac{S_{net}}{S} + \frac{\pi}{2} \frac{b_f^2}{S} \quad \text{(B.2)}$$

$$\frac{d\varepsilon}{d\alpha} = \frac{\frac{0.1124 + 0.1265\Lambda + 0.1766\Lambda^2}{r^2} + \frac{0.1024}{r} + 2}{\frac{0.1124}{r^2} + \frac{0.1024}{r} + 2} \left(\frac{r}{r^2 + m_{tv}^2} \frac{0.4876}{\sqrt{r^2 + 0.6319 + m_{tv}^2}} + \right.$$
$$\left. \left[1 + \left(\frac{r^2}{r^2 + 0.7915 + 5.0734 m_{tv}^2}\right)^{0.3113}\right] \left\{1 - \sqrt{\frac{m_{tv}^2}{1 + m_{tv}^2}}\right\}\right) \frac{C_{L_{\alpha_w}}}{\pi A} \quad \text{(B.3)}$$

$$\bar{x}_{ac} = \bar{x}_{ac_w} - \frac{1.8}{C_{L_{\alpha_{A-h}}}} \frac{b_f h_f l_{f_n}}{S\bar{c}} + \frac{0.273}{1 + \lambda} \frac{b_f c_g (b - b_f)}{\bar{c}^2 (b + 2.15 b_f)} \tan \Lambda_{1/4} + \sum k_n \frac{b_n^2 l_n}{s\bar{c}(c_{L_\alpha})} \quad \text{(B.4)}$$

$$C_{m_{ac}} = C_{m_{0_{airfoil}}} \frac{A \cos^2 \Lambda}{A + 2\cos\Lambda} + \mu_2 \left\{-\mu_1 \Delta C_{l\max} \frac{c'}{c} - \left[C_L + \Delta C_{l\max}\left(1 - \frac{Swf}{S}\right)\right] \frac{1}{8} \frac{c'}{c}\left(\frac{c'}{c} - 1\right)\right\} +$$
$$0.7 \frac{A}{1 + \frac{2}{A}} \mu_3 \Delta C_{l\max} \tan \Lambda_{1/4} - C_L \left(0.25 - \frac{x_{ac}}{\bar{c}}\right) - 1.8\left(1 - \frac{2.5 b_f}{l_f}\right) \frac{\pi b_f h_f l_f}{4S\bar{c}} \frac{C_{L_0}}{C_{L_{\alpha_{A-h}}}} + \Delta C_{m_{ac_{nac}}} \quad \text{(B.5)}$$

$$C_{n_{\beta_{A-h}}} = C_L^2 \left\{\frac{1}{4\pi A} - \left[\frac{\tan\Lambda}{\pi A(A + 4\cos\Lambda)}\right] \cdot \left[\cos\Lambda - \frac{A}{2} - \frac{A^2}{8\cos\Lambda} + \frac{6(\bar{x}_{acw} - \bar{x}_{cg})\sin\Lambda}{A}\right]\right\} - 1.3 \frac{\text{volume}_{fus}}{S_w b}\left(\frac{D_f}{W_f}\right) \quad \text{(B.6)}$$

$$\tau_v = -\frac{1}{C_{L_\alpha}} 0.9 K_f \left(\frac{\partial C_\ell}{\partial \delta_f}\right)_{airfoil} \frac{S_{\text{flapped}}}{S_{\text{ref}}} \cos \Lambda_{\text{H.L.}} \quad \text{(B.7)}$$

$$\sigma_v = -\frac{\kappa_v \kappa_\beta}{\kappa_b} \frac{C_{L_v}}{R_{A_v}} \beta \quad \text{(B.8)}$$

In equation B.1, $\beta = \sqrt{1 - M_h^2}$ and η is assumed to be 0.95 [107]. Furthermore, from Torenbeek [107], C_{L_h} in equation 8.44 is assumed to be -0.8. Finally, the figures required to determine all coefficients are shown below.

Figure B.1: Location of aerodynamic center of wing $\bar{x}_{ac_w}$ as a function of the airspeed and aspect ratio [107].

Figure B.2: Definition of chord ratios [107].

Figure B.3: Graph to determine μ_1 [107].

Figure B.4: Graph to determine μ_2 [107].

Figure B.5: Graph to determine μ_3 [107].

Figure B.6: Definition of aircraft dimensions [107].

Figure B.7: Definitions for lateral stability parameters [107].

Figure B.8: Plain flap deflection effectiveness [97].

Figure B.9: Correction factor K_f [97].

Figure B.10: Graph to determine K_β [169].

Figure B.11: Graph to determine K_v [169].

Figure B.12: Graph to determine K_b [169].

136